LUND UNIVERSITY

Attosecond Wave Packet Metrology

Swoboda, Marko

2010

Link to publication

Citation for published version (APA):
Swoboda, M. (2010). *Attosecond Wave Packet Metrology*. [Doctoral Thesis (compilation), Atomic Physics]. Department of Physics, Lund University.

Total number of authors:
1

General rights
Unless other specific re-use rights are stated the following general rights apply:
Copyright and moral rights for the publications made accessible in the public portal are retained by the authors and/or other copyright owners and it is a condition of accessing publications that users recognise and abide by the legal requirements associated with these rights.
• Users may download and print one copy of any publication from the public portal for the purpose of private study or research.
• You may not further distribute the material or use it for any profit-making activity or commercial gain
• You may freely distribute the URL identifying the publication in the public portal

Read more about Creative commons licenses: https://creativecommons.org/licenses/

Take down policy
If you believe that this document breaches copyright please contact us providing details, and we will remove access to the work immediately and investigate your claim.

LUND UNIVERSITY

PO Box 117
221 00 Lund
+46 46-222 00 00

Attosecond Wave Packet Metrology

Marko Swoboda

Doctoral Thesis
2010

Lund University

ATTOSECOND WAVE PACKET METROLOGY

© 2010 Marko Swoboda
All rights reserved
Printed in Sweden by Media-Tryck, Lund, 2010

Division of Atomic Physics
Department of Physics
Faculty of Engineering, LTH
Lund University
P.O. Box 118
SE–221 00 Lund
Sweden

http://www.atomic.physics.lu.se

ISSN 0281-2762
Lund Reports on Atomic Physics, LRAP-414

ISBN 978-91-628-8021-7

There is a theory which states that if ever anyone discovers exactly what the Universe is for and why it is here, it will instantly disappear and be replaced by something even more bizarre and inexplicable. There is another theory which states that this has already happened.

Douglas Adams

The Restaurant at the End of the Universe

Abstract

Attosecond pulses allow the study of electrons on their natural timescale. They are created from the interaction of atoms with ultrashort, intense laser pulses whose electric field approaches the strength of inner-atomic electric fields. This thesis presents experiments around the generation, characterization and application of attosecond pulses.

First, we study the influence of the atomic generation medium on the temporal properties of attosecond pulses. Their central photon energy can be controlled by using a two-color generation field and by thin-foil filtering techniques tailored to specific spectral bands. With these techniques, broadband attosecond pulses with durations down to 130 as have been measured. To characterize attosecond pulse trains at their birth, we introduce a new method that perturbs the generation laser field with its weak second harmonic. This allows us to assess the influence of the medium in the generation process. We then test the limits of a well-established pulse train characterization method with regard to probe intensity and demonstrate a way to circumvent these limitations.

A second set of experiments uses attosecond pulses to excite atoms and molecules for the creation of ultrashort wave packets. Free electron wave packets can be controlled by an external laser field and driven to scatter off their parent ions. They also carry information on the atomic structure, which enables the phase-resolved characterization of unknown bound wave packets. Exposing molecules to attosecond pulses can trigger dissociation reactions that can be controlled by a delayed probe laser pulse. We present a study of different probe pulse properties and report the observation of attosecond electron dynamics inside a hydrogen molecule.

POPULÄRVETENSKAPLIG SAMMANFATTNING

Det mänskliga ögat är ett utmärkt instrument, men det är inte snabbt. Vi kan se och reagera på rörelse av makroskopiska objekt som oss själva eller fallande träd. Mycket i naturen är dock snabbare än vad våra ögon kan se eller vad vår hjärna kan hantera. Extremt snabba processer kan då tyckas väldigt förbryllande för oss.

Hur lyckas katter att alltid landa på sina fötter? Lämnar hästens hovar marken samtidigt när den galopperar? Att försöka svara på dessa frågor kan anses vara början till ultrasnabb vetenskap. Kulor flyger långsamt jämfört med mikroskopiska rörelser, till exempel atomerna i en molekyl. Men ändå är de lättaste atomkärnor 2000 gånger tyngre än elektronerna som åtföljer den. Massan hos en partikel och den hastighet som den får av en konstant energitillskott är omvänt proportionella. Elektroner rör sig därför på en egen, unik, tidsram som kallas attosekunder. Att studera processer på denna tidskala är vad som har blivit känt som attofysik.

Sju attosekunder är till en sekund som en sekund är till jordens ålder. Elektroner i atomer och molekyler arrangerar sig inom loppet av några attosekunder när de deltar som yttersta elektroner i kemiska reaktioner. Att förstå dessa processer i detalj är därför avgörande för att förstå kemins grunder.

Hur kan man då mäta något på dessa tidsskalor? När man använder ljus, finns det två sätt att utföra en snabb mätning. En kamera med en väldigt snabb slutartid kan exponera filmen endast under mycket korta intervall där slutaren är öppen. Alternativt kan en långsam slutartid användas tillsammans med mycket korta ljusblixtar. Detta är den mätmetod som används i de flesta tidupplösta experiment med en laser: upprepning av en process med varierande fördröjningen mellan initieringen av processen och blixten som fryser bilden. När man använder två laserblixtar för att först starta en särskild dynamik och sedan spela in den med en annan blixt, så pratar man om en pump-prob mätning.

I den här avhandlingen presenteras pump-prob experiment som gjordes för att mäta mycket korta ljusblixtar - kallad attopulser - och hur de påverkar atomer och molekyler. De första tre experimenten visar hur egenskaperna hos dessa attopulser kan ändras med olika metoder. Medium för generering av dessa pulser har ett inflytande på utformningen av dessa blixtar och kan beskrivas i detalj. Färgen på blixtarna kan ändras på två sätt som presenteras därnäst: man kan blanda två olika färger för att skapa pulserna och blandningen kontrollerar slutresultatet. Alternativt kan man använda ett filter, som ett par solglasögon, som bara en viss färg kan passera. Sedan presenteras två olika sätt hur dessa blixtar kan mätas. Först i tur undersöker vi en ny karakteriseringsmetod och sedan tittar vi på begränsningarna hos en redan etablerad metod.

Den andra hälften av den här avhandlingen handlar om hur dessa extremt korta ljusblixtar kan utnyttjas till att initiera olika processer. Först kan elektroner användas för att studera atomen och hur den ser ut, sedan kan man använda attopulser att studera hur elektronerna rör sig. Slutligen kontrollerar och mäter vi sprängningen av en vätemolekyl med dessa attosekundsblixtar.

List of Publications

This thesis is based on the following papers, which will be referred to by their Roman numerals in the text.

I **Macroscopic effects in attosecond pulse generation**
T. Ruchon, C. P. Hauri, K. Varjú, E. Mansten, M. Swoboda, R. López-Martens and A. L'Huillier.
New J. Phys. **10**, 025027 (2008).

II **Spectral shaping of attosecond pulses using two-color laser fields**
E. Mansten, J. M. Dahlström, P. Johnsson, M. Swoboda, A. L'Huillier and J. Mauritsson.
New J. Phys. **10**, 083041 (2008).

III **Broadband attosecond pulse shaping**
E. Gustafsson, T. Ruchon, M. Swoboda, T. Remetter, E. Pourtal, R. López-Martens, Ph. Balcou and A. L'Huillier.
Opt. Lett. **32**, 1353 (2007).

IV **Atomic and macroscopic measurements of attosecond pulse trains**
J. M. Dahlström, T. Fordell, E. Mansten, T. Ruchon, M. Swoboda, K. Klünder, M. Gisselbrecht, A. L'Huillier and J. Mauritsson.
Phys. Rev. A **80**, 033836 (2009).

V **Intensity Dependence of Laser-Assisted Attosecond Photoionization Spectra**
M. Swoboda, J. M. Dahlström, T. Ruchon, P. Johnsson, J. Mauritsson, A. L'Huillier and K. J. Schafer.
Laser Physics **19**, 1591 (2009).

VI **Coherent electron scattering captured by an attosecond quantum stroboscope**
J. Mauritsson, P. Johnsson, E. Mansten, M. Swoboda, T. Ruchon, A. L'Huillier and K. J. Schafer.
Phys. Rev. Lett. **100**, 073003 (2008).

VII **Phase Measurement of Resonant Two-Photon Ionization in Helium**
M. Swoboda, T. Fordell, K. Klünder, J. M. Dahlström, M. Miranda, C. Buth, K. J. Schafer, J. Mauritsson, A. L'Huillier and M. Gisselbrecht.
(2010) *Phys. Rev. Lett., accepted for publication*.

VIII **Attosecond pump-probe electron interferometry**
J. Mauritsson, T. Remetter, M. Swoboda, K. Klünder, A. L'Huillier, K. J. Schafer, O. Ghafur, F. Kelkensberg, W. Siu, P. Johnsson, M. J. J. Vrakking, I. Znakovskaya, T. Uphues, S. Zherebtsov, M. F. Kling, F. Lépine, E. Benedetti, F. Ferrari, G. Sansone and M. Nisoli.
(2010) *arXiv:1001.1085v1 [physics.atom-ph]*.

IX **Ionization and Wave-Packet Dynamics Studied Using Two-Color XUV and IR Pump-Probe Spectroscopy**
F. Kelkensberg, C. Lefebvre, W. Siu, O. Ghafur, T. T. Nguyen-Dang, O. Atabek, A. Keller, V. Serov, P. Johnsson, M. Swoboda, T. Remetter, A. L'Huillier, S. Zherebtsov, G. Sansone, E. Benedetti, F. Ferrari, M. Nisoli, F. Lépine, M. F. Kling and M. J. J. Vrakking.
Phys. Rev. Lett. **103**, 123005 (2009).

X **Electron Localization following Attosecond Molecular Photoionization**
G. Sansone, F. Kelkensberg, J. F. Pérez-Torres, F. Morales, M. F. Kling, W. Siu, O. Ghafur, P. Johnsson, M. Swoboda, E. Benedetti, F. Ferrari, F. Lépine, J. L. Sanz-Vicario, S. Zherebtsov, I. Znakovskaya, A. L'Huillier, M. Yu. Ivanov, M. Nisoli, F. Martín and M. J. J. Vrakking.
(2010) *Nature, accepted for publication*.

ABBREVIATIONS

APT	Attosecond Pulse Train
BBO	Beta Barium Borate
CEO	Carrier Envelope Offset
CPA	Chirped Pulse Amplification
CRAB	Complete Reconstruction of Attosecond Bursts
E-field	Electric field
EWP	Electron Wave Packet
FROG	Frequency-Resolved Optical Gating
FWHM	Full Width at Half Maximum
GD	Group Delay
GDD	Group Delay Dispersion
HHG	High-order Harmonic Generation
IR	Infra-Red
KDP	Potassium Dihydrogen Phosphate
MBES	Magnetic Bottle Electron Spectrometer
R2PI	Resonantly-enhanced 2-Photon Ionization
RABITT	Reconstruction of Attosecond Beating by Interference of Two-photon Transitions
SAP	Single Attosecond Pulse
SFA	Strong Field Approximation
TDSE	Time Dependent Schrödinger Equation
TOF	Time Of Flight
VMIS	Velocity Map Imaging Spectrometer
XUV	eXtreme Ultra Violet

CONTENTS

Papers

CHAPTER 1

INTRODUCTION

The human eye is a remarkable instrument, but it is not fast. We are able to see and react to the motion of macroscopic objects such as ourselves or falling trees. Large parts of nature, however, are much faster than what our eyes can see or what our brains can process. Extremely fast things can seem extremely puzzling to us. How do cats manage to always land on their feet? Do all of a horse's hooves fully leave the ground during gallop? Seeking and finding answers to these questions can be considered as the beginning of ultrafast science. The study of dynamical processes is especially important for the understanding of the microscopic world made of atoms and molecules. Bullets fly slowly compared to the microscopic scale motions of the atoms inside molecules. Still, even the lightest nucleus is 2000 times heavier than the electron that orbits around it. The lighter a particle is, the faster it will move. Compared to atoms which move on a femtosecond timescale[1], electrons move on the attosecond timescale. Studying processes on this timescale has become known as attosecond science.

Figure 1.1. *Image of a bouncing ball, captured with 25 light flashes per second [1].*

Seven attoseconds[2] are to one second as one second is to the age of the Earth. Electrons inside atoms and molecules rearrange in a matter of attoseconds when they participate as outermost electrons in chemical reactions. To understand these processes in detail is therefore crucial to understanding the foundations of chemistry. But how can one measure on these timescales? When using light, there are two ways of performing a fast measurement. A camera with a very fast shutter can expose the film only during the very short interval that the shutter is open. Alternatively, a slow shutter together with very short flashes of light can be used. This concept is illustrated in Figure 1.1, where a se-

[1] One femtosecond is a millionth of a billionth of a second, $1\,\mathrm{fs} = 1 \times 10^{-15}\,\mathrm{s}$.
[2] One attosecond is a billionth of a billionth of a second, $1\,\mathrm{as} = 1 \times 10^{-18}\,\mathrm{s}$.

quence of flashes illuminates the motion of a bouncing ball. The image shows the whole process recorded in a single image, which works because the ball is moving. If the ball stood still, the images from individual flashes would all be superposed and the picture blurred. This can be seen in the turning points of the ball's trajectory, where the images from several flashes overlap. To clearly resolve such cases, one can then record a single image with a single flash and repeat the process many times, but each time triggering the flash a little later after releasing the ball. This is the measurement principle used in many time-resolved experiments with lasers: repetition of a process while varying the delay between the start of the process and the flash recording an image. Using two laser flashes to first trigger the dynamics and then record it with a second flash is called a pump (trigger) and probe (image) measurement.

Pulsed lasers can emit extremely short flashes of light[3]. The relation $\Delta t \Delta\omega \geq 0.44$ defines the ultimate limit. It states that the product of the spectral bandwidth[4] $\Delta\omega = 2\pi\Delta\nu$ and the duration of a laser flash Δt cannot be pushed below a constant of the order of one. Therefore, short pulses need large bandwidths. The entire visible spectrum has a bandwidth[5] of 1.4 eV, enough for pulses of 2.8 fs duration. Clearly, greater bandwidths are needed to access the attosecond domain and measure the dynamics of electrons.

In 1987, two research groups independently observed an effect that came to be known as High-order Harmonic Generation [2, 3]. When an intense laser pulse interacts with a gas, harmonics of the fundamental frequency are observed. The lowest orders quickly decrease in intensity, before a plateau-like region with approximately equal intensity over several harmonic orders occurs. Following the harmonic plateau, the highest harmonic orders then decrease rapidly in intensity, defining a cutoff of the harmonic spectrum.

The physics underlying the formation of these harmonics is well described in terms of a three-step process, introduced with a semi-classical model in 1993 [4–6]. This first description was superseded by a full quantum model in 1994 [7], using Feynman's path integrals to keep a close analogy to the intuitive semi-classical picture. Finally, it was also shown experimentally that these harmonics had good coherence properties [8], which they inherit from the generating laser field. It was predicted that the combined bandwidth of this radiation should allow the production of light pulses in the attosecond regime given a favorable phase relation between the harmonics, called phase locking [9–13]. With the development of suitable detection techniques [14],

[3] Laser *pulses*.

[4] ν is the frequency in Hertz, defined as $\nu = c/\lambda$, where λ is the wavelength, and ω is the angular frequency, measured in units of radians/second.

[5] Bandwidths in energy are given by $\Delta E = \hbar\Delta\omega$.

these pulses were first observed in a train formed by the combination of many harmonics in 2001 [15] and soon thereafter as single pulses of 650 as duration [16]. The first attosecond pulses were generated in Lund in 2003 [17], the year I was an exchange student in Lund, working on a project to optimize harmonic generation from a terawatt laser [18].

1.1 Aim and Outline of this Thesis

When I began as a PhD student in Lund in the spring of 2006, some of the techniques for the generation [19–22] and characterization [17, 23] of attosecond pulses were already established in Lund. Some experiments using these pulses in applications had also been performed [24, 25]. With the European Marie Curie Early Stage Training Site "MAXLAS" as my funding project, the aim was to develop better characterization techniques as well as to demonstrate applications of this new light source. A fruitful collaboration with AMOLF Amsterdam, the MPQ Garching and the Politecnico di Milano provided also access to a facility with the capability of using single attosecond pulses, which was not possible in Lund at that time.

This thesis spans topics ranging from improving the generation of attosecond pulse trains in Lund (Papers **I-III**) and their characterization (Papers **IV** and **V**) to developing applications in a number of experiments (Papers **VI-X**). Paper **I** studies the effects of the generation medium on the attosecond pulse shape, while Paper **II** aims to improve the versatility of the Lund attosecond source using a two-color setup. Paper **III** extends attosecond pulse compression techniques to greater bandwidths, setting a new world record[6] for the shortest attosecond pulse observed on target at that time.

Papers **IV** and **V** are mainly concerned with the characterization of attosecond pulse trains. Paper **IV** presents a study of a novel pulse characterization method [26] that was also compared with the established RABITT[7] method [14, 15] to benchmark the results. The limitations of the RABITT technique with regard to the probing laser intensity are studied in Paper **V**.

Papers **VI** and **VII** present applications of attosecond pulse trains performed in Lund, while Papers **VIII-X** are the result from a series of experimental campaigns performed in Milan within the framework of a European collaboration[8]. In Paper **VI**, free electron wave packets released by ionization of target gas atoms with

[6] At the time: 130 as, today: 80 as.

[7] RABITT is short for the Reconstruction of Attosecond Beating by Interference in Two-photon Transitions.

[8] The whole collaboration consisted of Politecnico di Milano, AMOLF Amsterdam, MPQ Garching, Université de Lyon, Louisiana State University and Lund University.

an attosecond pulse train are driven by an external IR laser field to re-scatter on the atom they originated from. A novel method analogous to the stroboscope used in Figure 1.1 was developed to image this process on attosecond timescales. Paper **VII** shows how high-order harmonic combs can be used as a precise and phase-resolved spectroscopic tool that studies effects of the atomic level structure and its behavior in moderately strong laser fields. Paper **VIII** demonstrates the characterization of bound electronic wave packets by a novel interferometric method. Finally, Papers **IX** and **X** are concerned with the dissociation dynamics of hydrogen and deuterium molecules. In Paper **IX**, the effects of an external laser field on the molecular dissociation dynamics by the process of the bond-softening [27] are studied, with a special focus on the influence of the laser pulse duration. Paper **X** represents one of the first measurements of attosecond electron dynamics in molecules. During the molecular dissociation process set in motion by ionizing a molecule with a single attosecond pulse, a localization of the remaining electron on one or the other nucleus is observed, alternating between both nuclei on attosecond time scales. This localization can be controlled by a delayed IR pulse.

This thesis is structured as follows. This Section concludes with an overview of the different types of wave packets discussed in this thesis. Chapter 2 describes the basic physics of attosecond light pulse generation and provides a description of the experimental setups both in Lund and Milan. In Chapter 3, different methods to characterize attosecond pulses are presented. Chapter 4 explores applications of attosecond pulses where electronic and nuclear wave packets are created and characterized. Finally, Chapter 5 gives a concluding summary and outlook.

1.2 Wave Packets

Three types of wave packets are considered in this thesis. Ultrashort laser pulses and attosecond pulses are optical wave packets. Their properties are determined by the electromagnetic waves that constitute them. Electron wave packets are formed when attosecond pulses or intense laser pulses interact with atoms and propel electrons to excited and unbound states. When an attosecond pulse excites a molecule, a superposition of vibrational and/or rotational states, *i.e.* a nuclear wave packet is created. Nuclear wave packets will be briefly described at the end of this Section.

1.2.1 Optical Wave Packets

An electromagnetic wave is a solution of the wave equations resulting from the Maxwell equations in a medium of electric and

magnetic permeability ε and μ, respectively

$$\nabla^2\mathbf{E} - \frac{\varepsilon\mu}{c^2}\frac{\partial^2\mathbf{E}}{dt^2} = 0, \quad \nabla^2\mathbf{H} - \frac{\varepsilon\mu}{c^2}\frac{\partial^2\mathbf{H}}{\partial t^2} = 0 \tag{1.1}$$

The oscillating quantities for these waves are both the electric field $\mathbf{E}$ and the magnetic flux[9] $\mathbf{H}$.

An optical wave packet can be expressed as a sum of plane waves

$$\begin{aligned} E(z,t) &= \int d\omega A_0(\omega)\exp\left[-i(\omega t - kz)\right] \\ &= \int d\omega A_0(\omega)\exp[i\phi(\omega)]\exp(-i\omega t), \end{aligned} \tag{1.2}$$

where we have used the dispersion relation $k = k(\omega)$ to express kz as the spectral phase $\phi(\omega)$ of the wave packet at a fixed position z. The spectral amplitude function $A_0(\omega)$ defines the spectrum of the wave packet. If $A_0(\omega)$ is non-negligible only for a certain range of frequencies $\Delta\omega$, then $\Delta\omega$ is termed the bandwidth of the wave packet and we can define a mean or central frequency $\tilde{\omega}$, also called the carrier frequency. Conversely, if the wave packet $E(z,t)$ is non-negligible only during a certain interval Δt, then Δt is called the duration of the wave packet. The envelope function $A(z,t) = |E(z,t)|$ of the wave is used to characterize the duration, often by the full-width at half-maximum (FWHM) of the intensity distribution $I(z,t) = |E(z,t)|^2$.

The *group delay* (GD) of a wave packet,

$$\tau_g(\omega) = \left.\frac{\partial\phi(\omega)}{\partial\omega}\right|_{\tilde{\omega}}, \tag{1.3}$$

defines a delay of the frequency components in the wave packet relative to the carrier frequency $\tilde{\omega}$. The change of this delay τ_g, the *group delay dispersion* (GDD), is defined as

$$GDD(\omega) = \left.\frac{\partial^2\phi(\omega)}{\partial\omega^2}\right|_{\tilde{\omega}}. \tag{1.4}$$

The GDD and the group delay τ_g are the two main quantities used to describe the phase properties of attosecond pulses. A constant group delay $\tau_g(\omega)$ simply shifts the wave packet to a later time $t + \tau_g$. A changing τ_g, *i.e.* a $GDD \neq 0$, results in a distortion of the wave packet shape.

The phase properties of a wave packet can also be described in the temporal domain by a temporal phase $\phi(t)$. We can then define

$$\frac{\partial\phi(t)}{\partial t} = \omega(t) \tag{1.5}$$

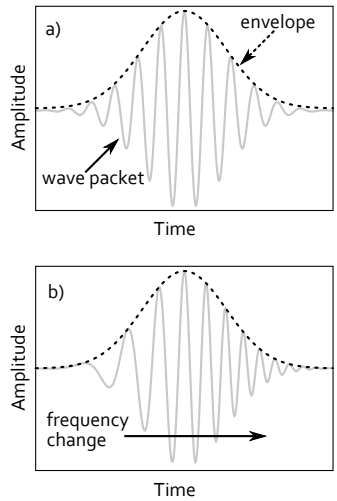

Figure 1.2. *Illustration of optical wave packets, a) without chirp, and b) with chirp, changing its frequency in time, and their envelope function.*

[9] We will disregard $\mathbf{H}$ from here on as the electric field is dominant in the interactions this thesis deals with. Also, we will consider linearly polarized fields (*e.g.* along the *y*-axis), which will be writen as scalar waves propagating along direction z with wave vector k.

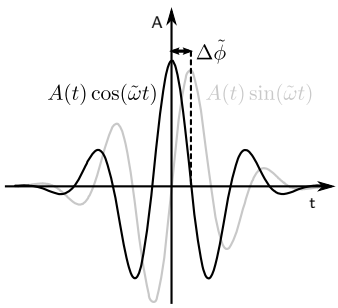

Figure 1.3. *Illustration of two optical wave packets with the same Gaussian envelope $A(t)$ but differing in their CEO-phase by $\Delta\tilde{\phi}$.*

as the *instantaneous frequency* of the wave packet at time t, which is changing with

$$\frac{\partial^2\phi(t)}{\partial t^2} = b(t), \tag{1.6}$$

the *chirp* of the wave packet. We thus see that a chirp $b(t) \neq 0$ corresponds both to a time-dependent frequency of the pulse and a $GDD(\omega) \neq 0$. If $b(t)$ is a constant, this constant b is called the *chirp rate* of the wave packet. Figure 1.2 illustrates two wave packets with envelope $A(t)$ and carrier frequency $\tilde{\omega}$. In Figure 1.2 b), the wave packet has a carrier frequency changing in time $\tilde{\omega} = \tilde{\omega}(t)$, defined by its chirp $\partial^2\phi/\partial t^2$.

The carrier-envelope-offset phase $\tilde{\phi}$ (CEO phase) is the offset of the phase function $\phi(t)$ within an optical wave packet written as

$$E(t) = A(t)e^{i\phi(t)} \tag{1.7}$$

where $A(t)$ is the amplitude envelope function and

$$\phi(t) = \tilde{\omega}t + \tilde{\phi} \tag{1.8}$$

One can thus see that $\tilde{\phi}$ determines the occurrence of the maximum of $E(t)$ under the envelope $A(t)$, as shown in Figure 1.3. Thus follows the name "carrier-envelope *offset*" phase. Figure 1.3 shows two cases, a sine-like pulse where the maximum absolute amplitude of $|E|$ occurs twice and a cosine-like pulse, which only has a single maximum $|E|$. For this thesis, $\tilde{\omega}$ will be used as the attosecond pulse carrier frequency and $\tilde{\phi}$ will be used for the CEO phase of attosecond pulses. The frequency ω_1 is used to denote the angular frequency of the fundamental radiation, together with its CEO phase ϕ_1.

1.2.2 Electronic Wave Packets

Electron waves are defined as solutions to the Schrödinger equation, which represents a wave equation for particles,

$$i\hbar\frac{\partial}{\partial t}\psi(\mathbf{r},t) = \left[-\frac{\hbar^2}{2m}\nabla^2 + V(\mathbf{r},t)\right]\psi(\mathbf{r},t), \tag{1.9}$$

where $V(\mathbf{r},t)$ is the potential that confines the particle and/or defines its interaction [28], m is the particle mass and $\psi(\mathbf{r},t)$ is the wave function, with $|\psi|^2$ describing the probability that the particle be found at location $\mathbf{r}$ at time t. If the potential $V(\mathbf{r},t)$ is zero or negligible, *i.e.* in the case of a free particle, the operator

$$T\psi = -\frac{\hbar^2}{2m}\nabla^2\psi = \frac{\mathbf{p}^2}{2m}\psi \tag{1.10}$$

represents the kinetic energy of the particle and $\mathbf{p}$ is the particle momentum. The particle's wave properties are defined by the angular frequency ω and wave vector $\mathbf{k}$, which is related to $\mathbf{p}$ by

$$\mathbf{p} = \hbar\mathbf{k}, \quad k = |\mathbf{k}| = \frac{|\mathbf{p}|}{\hbar} = \frac{2\pi}{\lambda_B}, \quad \omega = \frac{\hbar k^2}{2m}. \tag{1.11}$$

Thus energy and angular frequency are related by $W = \hbar\omega$ and λ_B is the de-Broglie wavelength of the particle. Similar to light pulses, particle wave packets can be expressed by a sum of plane waves as

$$\psi(\mathbf{r}, t) = (2\pi\hbar)^{-3/2} \int d\mathbf{p} A(\mathbf{p}) \exp i\left[\mathbf{p}\mathbf{r} - Wt/\hbar + \Phi_0(\mathbf{p})\right], \tag{1.12}$$

where W is the energy of the particle, $\Phi_0(\mathbf{p})$ is the phase distribution and the integral is performed over a momentum distribution $\Delta\mathbf{p} = \hbar\Delta\mathbf{k}$. Equation 1.12 represents a Fourier transform from momentum to space. Therefore, if an electron wave packet is fully characterized in momentum and phase, we have access to its spatial properties, conversely.

Attosecond electron wave packets are most commonly created by photoionization of atoms or molecules with attosecond pulses, as sketched in Figure 1.4 a). Perturbation theory allows us to express the probability $P(\mathbf{p}_f)$ that an atom interacting with a wave packet of XUV radiation be ionized and an electron be found in the final state of energy $W_f = \mathbf{p}_f^2/2m_e$, where $\mathbf{p}_f$ is the final state momentum and m_e is the mass of the electron. $P(\mathbf{p}_f)$ is given by the probability amplitude $a(\mathbf{p}_f)$ with $P(\mathbf{p}_f) = |a(\mathbf{p}_f)|^2$. From first-order perturbation theory, we can express $a(\mathbf{p}_f)$ for a pulse of XUV radiation with amplitude $A_{XUV}(t)$ as

$$a(\mathbf{p}_f) = (i\hbar)^{-1} \int_{-\infty}^{+\infty} dt\, \mu_{\mathbf{p}_f g} A_{XUV}(t) \exp\left[i\hbar^{-1}\left(W_f + I_p - \hbar\tilde{\omega}\right)t\right] \tag{1.13}$$

where I_p is the ionization potential of the atom, $\mu_{\mathbf{p}_f g}$ is the transition dipole moment from the ground state to a continuum state characterized by the momentum $\mathbf{p}_f$, and $\tilde{\omega}$ is the XUV carrier frequency. A spectrally broad attosecond pulse can also excite both bound states and continuum states, as shown in Figure 1.4 b). Finally, Fig. 1.4 c) shows a two-photon absorption process combining the absorption of an attsecond optical wave packet and an infrared radiation pulse. These three processes will be explored in this thesis.

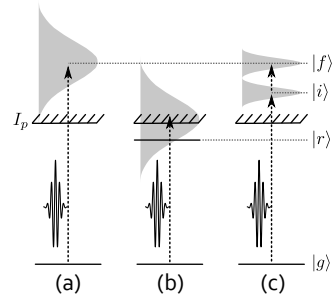

Figure 1.4. *Several pathways to create electron wave packets from optical wave packets. In (a), a broadband attosecond pulse ionizes a system in ground state $|g\rangle$ fully above the ionization threshold I_p to final state $|f\rangle$. In (b), the bandwidth of the attosecond pulse overlaps with I_p, also populating an excited state $|r\rangle$ in the system and in (c) two-photon absorption to a final state $|f\rangle$ occurs through an intermediate state $|i\rangle$.*

1.2.3 Nuclear Wave Packets

In a molecule, all nuclei interact with each other, for example through vibrational and rotational modes. A superposition of

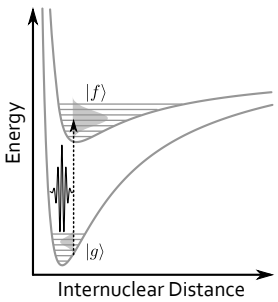

Figure 1.5. *Electronic transition within a molecule. The attosecond pulse propels the electronic ensemble to the excited state and creates a vibrational nuclear wave packet as a superposition of several states in the new potential landscape.*

several such vibrational and rotational states forms a nuclear wave packet. One way to create these wave packets is by absorption of attosecond pulses. This is illustrated in Figure 1.5, where the absorption of an attosecond pulse leads to a transition to an excited electronic state in the molecule and the simultaneous population of several vibrational levels.

The nuclei within a molecule also interact with the molecular electrons leading to additional terms in the Hamiltonian describing the system. The solutions to the Schrödinger equation including this Hamiltonian are the molecular states, described by the molecular wave function $\Psi(\mathbf{R}_n, \mathbf{r}_m)$, depending on the positions of the nuclei $\mathbf{R}_n$ and the electrons $\mathbf{r}_m$. As the complexity of the problem prevents an exact solution, approximations have to be made.

The *Born-Oppenheimer Approximation* (BO) is one such and very fundamental approximation. The mass ratio between electrons and protons is 1:2000 and as a result, nuclear dynamics evolve slowly in comparison to electrons. The BO approximation therefore considers the nuclei fixed in the frame of electronic transitions. As a result, the wave function describing the molecular system can be separated into $\Psi = \psi(\mathbf{R}_n, \mathbf{r}_m)\chi(\mathbf{R}_n)$, with an electronic part ψ and a nuclear part χ. The nuclear positions then act as a parameter for the electron wave function, whose transitions occur for fixed positions. Especially for diatomic molecules, the only nuclear coordinate defining the shape of the potential curve of the electronic wave function is the internuclear separation $R = |\mathbf{R}_1 - \mathbf{R}_2|$. In the BO approximation, electronic transitions occur so that R remains the same. This is also the case in Figure 1.5, where the sudden change of the electronic state leads to a different nuclear potential curve in which an ensemble of vibrational modes are populated.

Transitions which violate the BO approximation are termed non-adiabatic. Transition amplitudes between different electronic states in a molecule are still influenced by the nuclei through the Franck-Condon factor. When the molecule is excited to a different vibrational level in an electronic transition[10] through the absorption of a photon or another process, the transition amplitude scales with the overlap of the nuclear part of the wave functions between both states.

[10] A vibrational and electronic transition is termed *vibronic*.

CHAPTER 2

ATTOSECOND PULSE GENERATION

This Chapter describes the generation of attosecond light pulses. The first Section provides an introduction to the physics of the generation of high-order harmonics, attosecond pulse trains and single attosecond pulses. In the second Section, the experimental realization of these concepts will be presented.

2.1 High-Order Harmonic Generation

The general outline of this Section is illustrated in Figure 2.1, where an intense laser pulse interacts with atoms. First, the response of a single atom to this driving laser is described in Section 2.1.1. Then, we consider effects arising from the emission of an ensemble of atoms, so-called phase matching. As a next step, we describe how a train of attosecond pulses is formed and how it can be shaped using a filtering method. Finally, two cases of nontrivial fundamental laser pulse shapes are described, high-

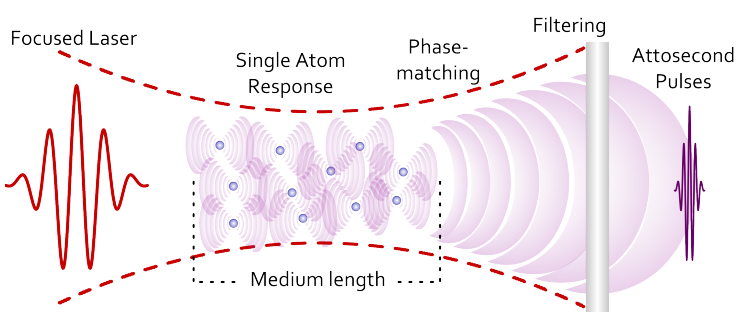

Figure 2.1. *Overview of an experiment in attosecond pulse generation.*

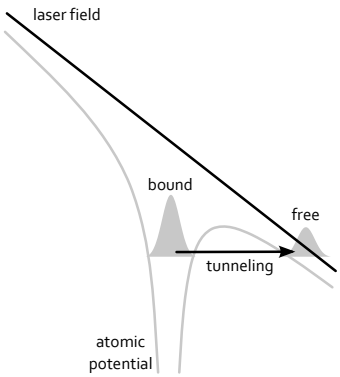

Figure 2.2. *Step 1: The strong electric field of a laser pulse suppresses the atomic potential and allows part of the bound electronic wave function to tunnel into the continuum.*

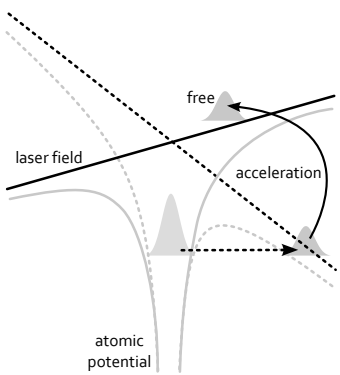

Figure 2.3. *Step 2: The free electron wave packet is accelerated in the laser field.*

order harmonic generation (HHG) with two-color fields and the production of single attosecond pulses (SAPs).

2.1.1 The Single Atom Response

The basic mechanism of HHG can be described by the semi-classical three-step model [5, 6]. For laser pulses that achieve intensities of $10^{13}\,\mathrm{W/cm^2}$ [2] and above, the laser electric field strength becomes comparable to the Coulomb potential in an atom. The atomic potential is then suppressed by the laser field and bound electrons can undergo tunneling transitions to continuum states (Figure 2.2). This is step (1): tunneling.

Step (2) is the acceleration of the free electron in the continuum by the laser electric field (Figure 2.3). How much kinetic energy W_k the electron gains while being driven by the laser field depends on the time of release into the continuum t_i. The electron trajectories following in the continuum can be calculated using the classical Newtonian equations for a charged particle in an electric field. For certain tunneling times t_i, the electron trajectory will cross the origin again, thereby returning to the parent ion. This is illustrated in Figure 2.4, which shows classical trajectories for a range of t_i, color-coded to depict W_k at the return time t_r.

Finally, Step (3) in the three-step model is the radiative recombination of the electron after its excursion at the return time t_r. The kinetic energy W_k is released as a burst of light, with photon energy $W_{ph} = W_k + I_p$ (Figure 2.5).

The laser electric field goes through an extremum every half cycle, and the three-step process occurs twice per laser cycle for as long as the laser electric field amplitude does not change significantly from cycle to cycle. The tunneling ionization probability depends very nonlinearly on the applied electric field strength. This defines a distribution of possible times t_i when the atomic potential is sufficiently suppressed to allow tunneling ionization. An electron released at any t_i will then be accelerated by the instantaneous electric field it experiences from t_i on. The shape of the electric field then determines the distribution of return energies W_k and thus the emitted photon energies resulting from a given interval of tunneling times.

The maximum photon energy obtained by these simple classical considerations is called the cutoff energy W_c and is equal to

$$W_c = I_p + 3.17 U_p, \tag{2.1}$$

with

$$U_p = \frac{e^2}{2 m_e c \epsilon_0} \frac{I}{\omega_1^2} \tag{2.2}$$

being the ponderomotive potential or jitter energy of a free elec-

tron in an external electric field oscillating with frequency ω_1[1] [29–31].

The three-step process is repeated every half cycle of the fundamental laser field and each time it results in the emission of a spectrum spanning up to W_c. The fundamental laser pulse has a duration of 35 fs (FWHM) [2] at a period of $T_1 = 2\pi/\omega_1 = 2.67$ fs. The process can be repeated for more than 10 cycles, corresponding to about 20 possible emission events. The continua from each of these events then interfere and the inverse of their spacing in the temporal domain ($T_1/2$) determines the spacing in the spectral domain ($2\pi/T_1/2 = 2\omega_1$). The frequency spacing combined with inversion symmetry considerations imply that only odd harmonics of the fundamental laser frequency ω_1 are observed. At the photon energies corresponding to even harmonics destructive interference occurs between the emission from subsequent half cycles. To observe even harmonics in the spectrum, an asymmetry between the electric field of two consecutive half cycles must exist. This can be achieved by using two-color HHG (Section 2.1.5). This technique has been used in Papers **II**, **IV**, and **VI**. No harmonics, but a continuum of XUV frequencies is observed if the emission is confined to a single event during the fundamental laser pulse. The generation of these single attosecond pulses is described in Section 2.1.6 and they have been used for experiments in Papers **VIII**,**IX** and **X**.

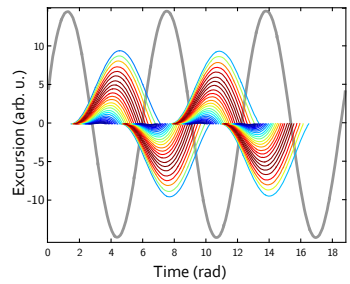

Figure 2.4. *Classical electron trajectories from four half cycles in an infinite driving field, with red representing the highest kinetic energies W_k at the return time t_r and blue representing the lowest kinetic energy.*

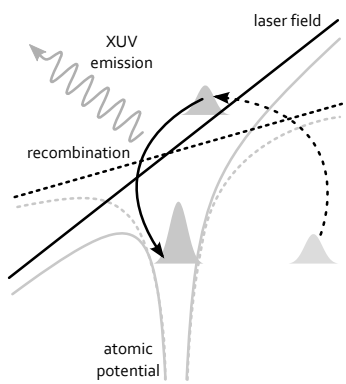

Figure 2.5. *Step 3: The accelerated part of the electron wave packet interferes with the bound part resulting in the emission of XUV light.*

Phase Properties

The time-domain picture of the single atom response provides insight into the spectral phase properties of the emitted radiation. Each frequency component emitted in the course of a half cycle of the laser field originates from a specific return time t_r. A distribution of the emitted energy for a given return time t_r from a classical calculation is shown in Figure 2.6. The frequency variation, or the chirp, of the attosecond pulse is related to this kinetic energy distribution by

$$\tau_g(\omega) = t_r = \left.\frac{\partial \phi}{\partial \omega}\right|_{\tilde{\omega}}, \tag{2.3}$$

with $\omega = W_k/\hbar$. The attosecond pulse spectral phase $\phi(\omega)$ therefore follows from the temporal electron return energy distribution.

[1] From now on, we will use ω_1 to represent the angular frequency of the fundamental IR light, at wavelength $\lambda_1 = 800$ nm.

[2] For the pulses used in Lund. During the experiments in Milan, the pulses were usually few-cycle pulses, varying between 5 and 7 fs duration. Pulse compression techniques have also been used in Lund and are an ongoing effort, but have not played a role in any of the papers in this thesis.

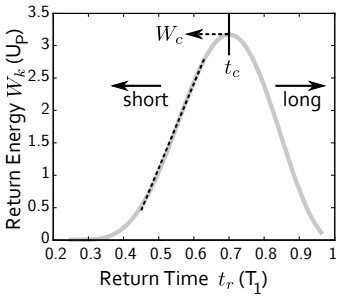

Figure 2.6. *Classical electron return energies W_k over excursion time in the continuum and the separation of the return energies in two branches.*

The Two Trajectories

Figure 2.6 shows the return energy distribution $W_k(t_r)$. The cutoff energy W_c is emitted only at $t_c = 0.7T_1$, but any energy $W_k < W_c$ is emitted twice every half cycle. The electron path leading to the emission event at $t_r > t_c$ is called the long trajectory, since the electron needs a longer excursion to gain a given amount of energy. The long trajectory is characterized by a decreasing return energy with increasing return time, $\partial W_k/\partial t_r < 0$.

The emission event with $t_r < t_c$ is called the short trajectory. The short trajectories show a return energy increasing with return time, that is $\partial W_k/\partial t_r > 0$ so that $\partial\omega/\partial t_r > 0$, or equivalently, $\partial t_r/\partial\omega > 0$, *i.e.* $\partial^2\phi/\partial\omega^2 > 0$. This corresponds to a positive chirp, and over a large range of photon energies in Figure 2.6 it can be approximated to be constant as is indicated by the dashed line. The line gradient then equals the chirp rate of this interval of the emitted spectrum.

The contribution from the long trajectory is usually weak in our experiments. One reason is that phase matching (see Section 2.1.2) is easier to achieve for the short trajectory. The emission from the long trajectories is also spatially more divergent than that from the short trajectories [32], so that it can be reduced by introducing a hard aperture in the beam.

Intensity Dependence

From Equations 2.1 and 2.2 follows that the cutoff energy W_c is a linear function of the generation laser intensity I. Higher intensities lead to higher $\partial W_k/\partial t_r$ and therefore smaller $\partial^2\phi/\partial\omega^2$. This dependence of $\phi(\omega)$ is commonly expressed as an approximate linear dependence [23, 33, 34]

$$\phi(\omega, I) = \alpha I, \text{ with } \alpha(\omega) = \frac{\partial\phi}{\partial I}. \tag{2.4}$$

In summary, the single atom response mostly determines the phase structure of the emitted harmonic radiation. These phase properties result from the emission time distribution $\omega(t_r)$ which is shaped by the different return energies of the electron trajectories during excursion into the continuum.

2.1.2 Phase Matching

The overall harmonic emission will be maximized if the emission from each individual atom in the harmonic generation medium is in phase with all others. In reality, there is a mismatch $\Delta k = k_q - qk_1$ between the wave vector k_1 of the fundamental field and the wave vectors of the generated harmonics k_q due to several effects [35–37].

Free electrons that occur from strong-field ionization processes due to the high laser intensities involved contribute to the phase mismatch Δk by affecting the generation medium dispersion. The free electron density N_e is a function of the laser intensity, as higher intensities increase the ionization probability. The plasma frequency $\omega_p = \sqrt{4\pi e^2 N_e / m_e}$ determines the refractive index of a partially ionized medium for harmonic order q as

$$n_q^e = \sqrt{1 - \left(\frac{\omega_p}{q\omega_1}\right)^2}, \tag{2.5}$$

and we see that the dispersion $n_q^e(\omega)$ is dominated by the effect on the fundamental frequency (ω_1) during propagation. Successful phase matching is achieved when the dispersion of the neutral medium $\partial n/\partial\omega > 0$ is compensated for by the right amount of ionization in the generation medium, because $\partial n_q^e/\partial\omega < 0$.

Additional contributions to the phase mismatch Δk come from the use of focused laser beams in HHG. The laser intensity varies over the laser focus, both along the propagation direction as well as perpendicular to it. These intensity variations lead to a varying amount of free electrons and therefore a varying refractive index, both on- and off-axis[3].

For focused laser beams, the so-called *Gouy-phase* describes the variation of the fundamental phase fronts across the focus [18, 39]

$$\phi_g = k_1 z - \arctan\left(\frac{z}{z_R}\right), \tag{2.6}$$

where the focus is assumed to be located at $z = 0$ and z_R is the Rayleigh range of the focused laser beam, assumed to be Gaussian. Neglecting the Gouy phase of the harmonic field, we see that the phase difference between the harmonic field and the induced polarization [4] at frequency $q\omega_1$ is $-q\phi_g = q\arctan(z/z_R)$ which increases with q and decreases with z_R. The corresponding mismatch is therefore $\Delta k = -q\partial\phi_g/\partial z$ close to $z = 0$.

The single atom response also influences the phase matching conditions. The intensity dependent parameter α from Equation 2.4 describes the influence of the generation intensity on the phase of the single atom response. A non-uniform intensity distribution over the harmonic generation medium therefore translates again to non-optimal phase matching.

The need for high laser intensities to observe HHG implies the use of a focusing element before the generation medium. From our previous considerations, we see that a varying intensity in

[3] This intensity-dependent refractive leads to plasma defocusing, an effect that can be countered by the focusing optical Kerr-effect of the medium. Balancing both effects is used for filamentation in gaseous media [38].

[4] The nonlinear polarization of the generation medium [40].

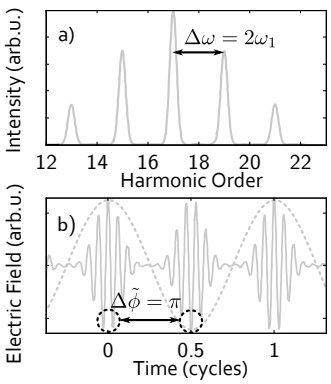

Figure 2.7. *Harmonic spectrum and its coherent sum in the time domain. The harmonics are spaced at $2\omega_1$, leading to a periodicity of a half laser cycle in the resulting APT. Consecutive pulses show a π-shift of their CEO phase $\tilde{\phi}$.*

the medium will lead to an increased mismatch Δk and a reduced harmonic conversion efficiency. This suggests that one way to achieve good phase matching is to reduce intensity variations in the generation medium, for instance by loose focusing geometries. In addition, locating the generation medium behind the focus means

$$\frac{\partial I}{\partial z} < 0 \rightarrow \frac{\partial \phi(I,\omega)}{\partial z} < 0, \tag{2.7}$$

which is then compensated by the Gouy-phase pointing in the opposite direction

$$\frac{\partial \phi_g}{\partial z} > 0. \tag{2.8}$$

This suggests that on-axis phase matching is easier to achieve for a medium placed behind the focus. These are also the normal conditions used in our HHG experiments [18].

Paper **I** examines the influence of phase matching on the attosecond pulse characteristics by a simple model including the absorption of the generated harmonics. It is found that phase matching has an influence on the GDD and the temporal shape of the attosecond pulses. The experiments in Paper **I** study the generation of attosecond pulses at different generation pressures with the result that there is an optimum pressure range with regard to the GDD of the spectrum. This could in principle be used to aid the compression of attosecond pulses to shorter durations. The effect, however, is relatively small compared to the intrinsic GDD from the single atom response or the GDD induced by thin-foil filters.

2.1.3 Trains of Attosecond Pulses

The origins of attosecond pulse trains (APTs) can be viewed either in the temporal or the spectral domain. The process of HHG emits a sequence of short bursts of radiation, coherently driven by the generation laser and with emission events during each laser half cycle. Each of these short bursts is of attosecond duration and their interference leads to the observation of harmonics. Alternatively, the coherent frequency conversion process in the generation medium by a laser pulse of fundamental frequency ω_1 leads to the generation of phase-coupled harmonics. Given the right phase-relation, the sum of these harmonics forms a train of attosecond pulses. Both pictures complement each other since the generation process itself is better understood in the temporal domain, but the concepts of conventional optics and spectral phase $\phi_q(\omega)$ are more easily transferred within the frequency domain. The coherent sum of the electric fields of a range of harmonic frequencies

$$E_{sum}(t) = \sum_q E_q(t) \exp -i(q\omega_1 t + \phi_q(\omega)), \tag{2.9}$$

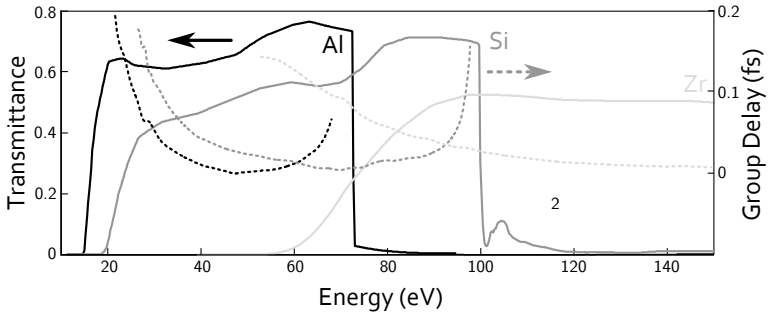

Figure 2.9. *Overview of common thin-foil filter materials, their transmission (solid lines) and induced group delay (dashed lines).*

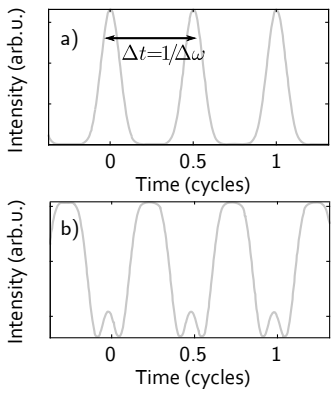

Figure 2.8. *Reconstructed APT temporal intensity profiles, a) for a flat phase, b) with a chirp, increasing the FWHM of the pulses.*

with $E_q(t)$ as the amplitude envelope of the individual harmonic field, forms a periodic interference pattern in time. Figure 2.7 presents a harmonic spectrum ranging from the 13th to the 21st harmonic and the resulting electric field $E_{sum}(t)$ Figure 2.7 b). The resulting temporal intensity distribution $I(t) = |E_{sum}(t)|^2$ (Figure 2.8 a)) corresponds to a train of attosecond pulses, with the duration of a single pulse far below the fundamental laser period (2.6 fs at 800 nm). As a result of the HHG process (Section 2.1.1), the attosecond pulses are spaced at intervals corresponding to the inverse of the harmonic frequency spacing. The CEO phase $\tilde{\phi}$ between two consecutive attosecond pulses in Figure 2.7 shows a π-shift, which is a common property of APTs with two pulses per fundamental laser cycle.

If the harmonic spectral phase $\phi_q(\omega) = 0$ for all q, then the individual pulse duration is only determined by the total bandwidth of the harmonic spectrum. In reality, the phase properties of the harmonics (Section 2.1.1) inherent to the generation process in general lead to longer pulses. Figure 2.8 b) illustrates the intensity profile obtained by including the linear chirp from Figure 2.7 a). The individual pulses are longer than in the ideal case of Figure 2.8 a) and "satellite pulses" have appeared in between. For time-resolved experiments, the shortest possible pulse duration is of importance as it determines the temporal precision of the experiment. This is why ways to compress and shape the APTs are needed.

2.1.4 Filtering

Attosecond pulses exhibit a GDD $\partial^2\phi/\partial\omega^2 \neq 0$. For the commonly used short trajectory it is positive, meaning an increase of the central frequency $\bar{\omega}$ of the pulse over time. Synchronization

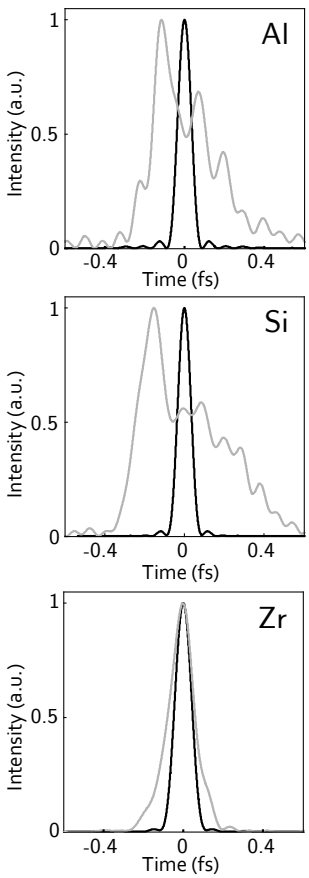

Figure 2.10. *Reconstructed average attosecond pulse shapes for three different filter materials. The Fourier limited pulse shape is shown in gray. Regarding variations of the pulse shape during an APT, see Section 3.1.4.*

of all the frequency components in the spectrum is necessary to obtain the shortest possible pulse duration. To achieve this compression, the lower photon energies must be delayed with respect to the higher ones. Several schemes have been proposed [22, 41–45]. In Paper **III** we use the negative group-delay dispersion exhibited by materials on the low energy side of their transmission window.

Figure 2.9 shows the transmission (solid) and induced group delay (dashed) curves for 200 nm layers of common filter materials. The filtering is achieved by transmission through such a thin foil of material. Zirconium is the material of choice for high photon energies generated in neon, transmitting only above 60 eV but exerting negative GDD up until 120 eV photon energy. Aluminium is the most useful in the region of lower harmonics, until about 50 eV photon energy. This is the spectral range commonly generated from argon gas and Al shows negative GDD over the full range, making it highly suitable for attosecond pulse compression [22]. Al filters are by far the most commonly used filters in Lund and they have been employed in all experiments of the papers in this thesis. The advantage of Si as a filter material lies in its large relevant bandwidth and small induced GD. Paper **III** conducts a thorough study of these filter materials and shows how a 200 nm Zr filter can be used to compress a harmonic comb generated in neon to form an APT with average pulse duration of 130 as and central energy of 80 eV. It should be noted that at the same time the conversion efficiency is reduced by a factor of $\approx$ 100 compared to argon.

The technique of thin-foil filtering compensates the intrinsic positive chirp of the harmonic spectrum only in regions of negative group delay dispersion of the filter material (see Fig. 2.9). The reconstructed average pulses from three different filter materials are shown in Figure 2.10. Using Al, 45 eV bandwidth centered at 50 eV can be achieved. The severe chirp, however, leads to an asymmetric pulse shape which is much longer than the Fourier limit (black line). Using Si, similar problems arise but the central energy (75 eV) is significantly higher than in the Al case. Finally, using a Zr filter, the XUV intensity is temporally confined and close to the Fourier limit. One can therefore conclude that the chief problem in attosecond pulse compression with large bandwidths is the need for a filter with a similarly wide window of negative GDD.

2.1.5 Two-Color Harmonic Generation

The papers **II**,**IV**, and **VI** present experiments where two light fields with frequencies ω_1 and $2\omega_1$ are mixed and used in HHG. The relative phase and intensity of the two fields heavily influences the observed harmonic spectrum [21, 26, 46]. The case of

multiple fields and other frequencies has been considered elsewhere [47–53].

Figure 2.11 presents classical calculations of the electron trajectories in the continuum for a field

$$E_{total} = E_R \sin(\omega_1 t + \phi_1) + E_B \sin(\omega_2 t + \phi_2), \tag{2.10}$$

consisting of a fundamental wave with frequency ω_1 and its second harmonic with frequency $\omega_2 = 2\omega_1$, with electric field amplitudes E_R and E_B, respectively. As was the case in Figure 2.4, the return energy W_k defines the color of the given curve, and dark red represents the highest energies. The intensity ratio R is $R = I_B/I_R = 25\%$, with different relative phase $\Delta\phi_{21} = \phi_2 - \phi_1$ between a) and b). In Figure 2.11 a) $\Delta\phi_{21}$ is chosen such that the symmetry between two half cycles of the fundamental ω_1 field is broken. Higher energies are emitted only once per laser cycle. The result of the broken half cycle symmetry is the appearance of even harmonics in the emission spectrum [21, 47, 54]. Figure 2.11 b) presents a case where the emission events over the course of a fundamental laser cycle yield approximately the same energies, with reduced even harmonics. The presence of even harmonics can to some extent be controlled by the relative phase of both fields [26]. This concept is extensively used in Paper **IV**.

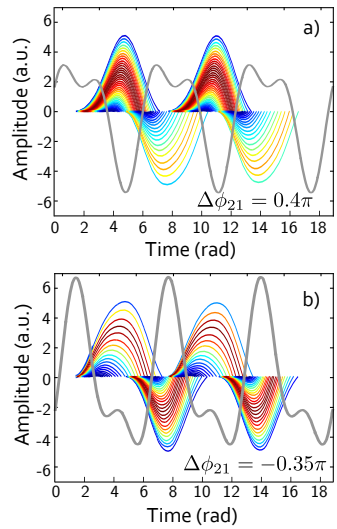

Figure 2.11. *Classical trajectories in a field composed by a fundamental wave and its second harmonic.*

Using two-color fields in HHG also allows us to control the attosecond emission as shown in Figure 2.12 (compare Figures 2.7 and 2.8). In some conditions (Fig. 2.11 a)), the emission is very asymmetric from one half cycle to the next, both in the emitted photon energies and in the generation efficiency in particular. Using spectral and spatial filtering, APTs with only one attosecond pulse per laser cycle can be created. The formation and use of APTs with only one pulse per fundamental laser cycle has been shown in [21] as well as in Papers **II** and **VI**.

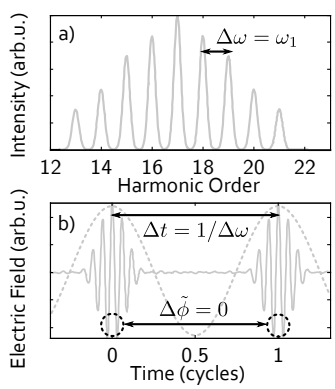

Figure 2.12. *a) Harmonic spectrum spaced by ω_1, which leads to an APT with one pulse per cycle (b). Consecutive pulses have the same CEO phase $\tilde{\phi}$.*

To have only one pulse per cycle is of practical relevance in experiments that demand that each attosecond pulse see the exact same electric field situation as the previous one when overlapped with a probe field matching the generation wavelength $\lambda_1 = 2\pi c/\omega_1$, as is illustrated in Figure 2.12 b). A conventional APT (Section 2.1.3) with two pulses per laser cycle will, when overlapped with a probe field of λ_1, see an opposite electric field between consecutive attosecond pulses in the train (Figure 2.7 b)), leading to a mixture of both configurations in the experimental signal. In addition, with only one pulse per cycle, the CEO phase π-shift between two successive attosecond pulses (see Figure 2.7 compared to 2.12) vanishes, resulting in the same CEO phase $\tilde{\phi}$ for consecutive pulses. As a result, the signal from each individual pulse will be in phase with all other pulses in the train. This property has been used in Paper **VI** and has allowed us to perform a stroboscopic measurement of re-scattering of electron waves on

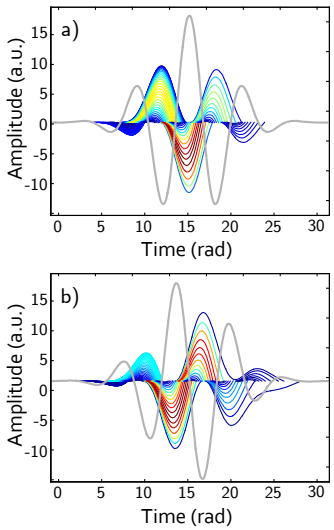

Figure 2.13. *Classical electron trajectories in a few-cycle pulse, color-coded for highest return energy brightest.*

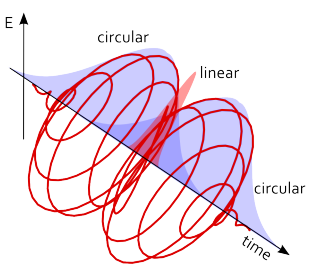

Figure 2.14. *Illustration of two counter-rotating circularly polarized laser pulses forming a short window (marked in red) of linearly polarized radiation, allowing the return of electrons for the production of attosecond pulses only during a single half cycle.*

an atomic potential. The process has been named *quantum stroboscope* to emphasize that amplitudes and not intensities are added constructively. Paper **II** shows how the average attosecond pulse in such an APT can be measured with the streaking-technique (see Section 3.2.1) that is commonly used for the characterization of single attosecond pulses.

2.1.6 Generation of Single Attosecond Pulses

In the case of a few-cycle pulse, the emitted spectrum within a single half cycle is highly dependent on the maximum E-field amplitude. With a laser pulse as short as that shown in Figure 2.13 a), individual half cycles exhibit varying return energy distributions. The emission of the highest photon energies can then be confined to a single half cycle, thus eliminating the harmonic structure from this part of the emission spectrum. Using a low-pass filter, all photon energies being emitted repeatedly can then be excluded, leaving a single attosecond pulse (SAP) [11, 16, 55].

An alternative way to achieve the generation of a single attosecond pulse is by shaping the polarization of the fundamental field [56–59]. One can readily see from classical considerations that during its excursion in the continuum the electron can be made to miss the parent ion if the laser is elliptically polarized. If the polarization state of a fundamental field is varied from elliptical to linear during only one half cycle electron returns will only be possible during this interval. Electrons released by ionization during intervals of elliptical polarization will not be able to return to the parent atom as they are accelerated on a spiral trajectory around the atom. Figure 2.14 shows an example of a short fundamental laser field with such favorable polarization properties. This is the prime technique used for the generation of SAPs in Papers **VIII**,**IX**, and **X**.

An important requirement for the production of SAPs is the control of the CEO phase ϕ_1 of the fundamental laser pulses [60–63], which determines the occurrence of the maximum of the laser electric field under the envelope function. Figure 2.13 b) show the electron trajectories for a "sine" pulse[5]. Obviously, in this case two similar attosecond pulses will be emitted, in contrast to Figure 2.13 a).

2.2 Experimental Realization

In this Section, the experimental setups used in both Lund and Milan are described. Their structure is similar: an oscillator laser, followed by an amplification stage and a harmonic generation

[5] As long as the pulse is not short enough to allow emission only once irrespective of ϕ_1, which is also a possible scenario.

chamber. Once the attosecond pulses have been produced, they are transported into another vacuum chamber and overlapped with a fraction of the generating beam for characterization or application experiments.

2.2.1 Experimental Setup in Lund

The laser system in Lund has changed over the course of this thesis. The components of the laser system mentioned in Figure 2.15 reflect the present state, with major modifications having been undertaken over the years. The first element of the laser system, a Titanium:sapphire-based laser oscillator provides the initial laser pulses for the chirped-pulse amplification (CPA) laser system. Initially, the oscillator was a KM-labs model, using prism compression and a folded cavity arrangement. The maximum achievable bandwidth was about 45 nm, centered at 800 nm central wavelength. This oscillator was later replaced by a Femtolasers *Rainbow* system, using a chirped-mirror technique for dispersion compensation [64, 65] and providing a bandwidth of about 300 nm and duration of approximately 7 fs at about 800 nm central wavelength. In addition, the CEO phase can be stabilized and controlled by an integrated feedback loop, based on a monolithic implementation of difference-frequency generation inside the laser cavity [66]. All the experiments performed in Lund during the course of this thesis (Papers **I** to **VII**), however, did not make use of this option. The main reason is that while the oscillator may have a stable CEO phase, mechanical vibrations and electronic noise in other parts of the laser system would still introduce large errors. Recently, phase-stable operation has also been achieved with our laser system [67].

An Acousto-Optic Programmable Dispersive Filter (AOPDF) (Fastlite *Dazzler*) follows the oscillator and makes it possible to alter the phase properties of the seed pulses from the oscillator and to select a bandwidth of approximately 80 nm to be amplified in the rest of the laser system. With a grating-based, Öffner-type stretcher the seed pulses are stretched to about 200 ps duration. They are then amplified in a regenerative amplifier, with a pulse-picking Pockels-cell reducing the repetition rate of the system to 1 kHz. The pump laser of the amplifier, a diode-pumped, 30 W frequency-doubled Nd:YLF[6] laser was responsible for a break in experiments in Lund for approximately one year during which two models[7] constantly dropped in output power. The problem was solved after changing the chiller aggregate, equipping it with 3 and 5 μm water filters and changing the laser head. During this break, most of the experimental work in Milan was performed.

[6] Neodymium-doped yttrium lithium fluoride.
[7] Photonics Industries International Inc., model DM30.

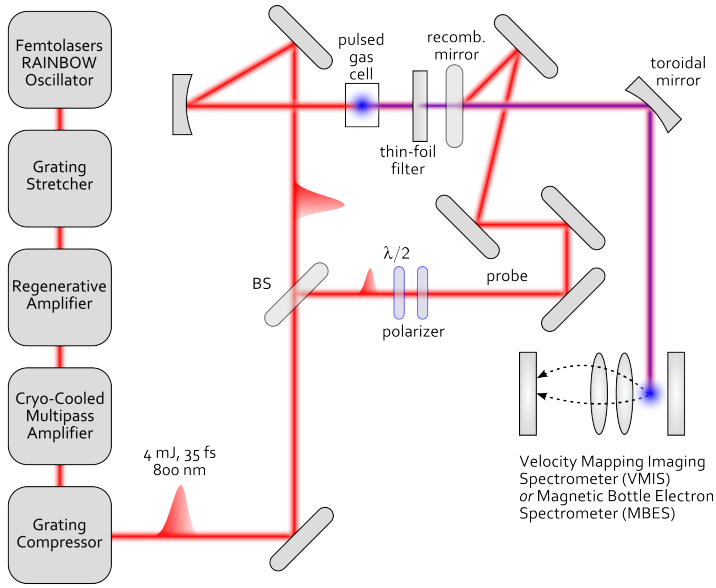

Figure 2.15. *The attosecond interferometer setup in Lund, with a schematic of the laser system arrangement.*

After usually 12 passes in the regenerative amplifier, the average laser power is about 500 mW. The regenerative amplifier has also undergone changes during the course of this work. Most of the optics have changed and the layout has been modified to provide a better contrast, *i.e.* minimized parasitic lasing (amplified spontaneous emission [ASE]). The reduction of the ASE is the main improvement, allowing the further amplification of the laser pulses to energies of up to 8 mJ. This amplification is performed in a cryogenically cooled five-pass amplifier that also represents an upgrade from the initial system where a water-cooled double-pass amplifier was used to boost the final pulse energy before compression. The final pulse compression is performed in a grating-based compressor in an inverse arrangement of the stretcher. The compressor gratings have also been changed during the course of this thesis, being responsible for most of the boost in energy output of the whole laser system. In addition, the telescope inside the compressor was changed to expand the beam to a FWHM of about 1.6 cm to accommodate the higher pulse energies from the new multipass amplifier. The old compressor gratings had a combined transmission of 40% while the new gratings entered operation at an 80% transmission rate. Until now, they have only deteriorated to 75% transmission. This

deterioration behavior is common to such grating-based systems and mostly a result of humidity in the laboratory air, which is hard to prevent in Lund's weather conditions. The introduction of some silica-gel desiccant granulate could not prevent the observed drop in transmission, which may also be partially related to beam alignment issues. After compression, up to 6 mJ energy of phase stable laser pulses have now been demonstrated in this system [67], where regular operation is about 4 mJ. In conclusion, the laser system has changed significantly during this work, from conditions with an average-bandwidth oscillator and 2 mJ output power to a phase-stable system of up to three times the output energy.

Besides its usefulness for dispersion management, the AOPDF can also be used to tune the central wavelength of the laser system. Paper **VII** used this method to vary the carrier frequency of the fundamental laser spectrum, thereby tuning the frequency of the generated high-order harmonics. The tuning was achieved by altering the characteristics of the spectral band selected from the oscillator spectrum. One can shift the center wavelength of the selected 80 nm or introduce a dip in the spectrum at a given wavelength to shift the relative contribution of different wavelengths. As the dielectric optic elements used in the rest of the laser system have a bandwidth far below 80 nm (about 40 nm), shifting the selected spectral window will not greatly alter the final laser wavelength. In addition to the mismatching bandwidths, the gain spectrum of the pumped Ti:Sapphire crystals acts as an additional filter, forcing its characteristics on the final spectrum. This effect is mainly seen as a redshift during amplification, but limits the possible bandwidth as there are a total of 17 passes through Ti:Sapphire-crystals in the entire laser amplification chain. The limited reflection bandwidth of the system optics and the Ti:Sapphire gain profile poses the main limits to the tuning range of the system. Figure 2.16 presents an example of the final laser spectra for different tunings from Paper **VII**.

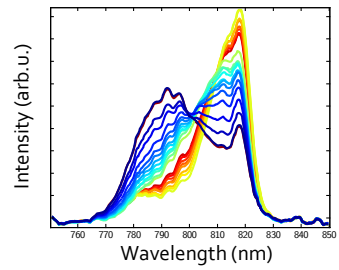

Figure 2.16. *Laser tuning spectra acquired during the experiments of Paper **VII**, showing a shifting center-of-mass of the spectrum.*

The output of the compressor is then split in two parts at a beam splitter, as shown in Figure 2.15. A fraction of 20% acts as a probe pulse for experiments. The remaining 80% are used in high-order harmonic generation. An aperture limits the beam diameter for different experiments. For HHG in argon, an aperture width of 1 cm is common and as neon requires higher intensities in the focus, beam diameters of 15 mm and above have been used. A spherical mirror focuses the laser pulses into a 1-kHz pulsed gas jet released into a gas cell. This presents an upgrade from previous experiments in Lund, all of which were performed with a static pressure cell. The gas cell length can be varied from 3 mm to 10 mm, with the most common length being 6 mm. Several different focal lengths can be used to obtain different generation intensities in the generation cell. The most common ones are 50 cm

(Papers **I**, **II**, **III**, **IV**, **V**, **VI**) and 75 cm (**VII**). A thin-foil filter after the generation blocks the infrared generation pulses. Depending on the filter properties (Section 2.1.4) the harmonic radiation is spectrally filtered and temporally compressed.

The probe beam is sent over a combination of a coarse delay stage with 600 ps range and a piezo-mounted delay stage adjustable to attosecond precision. This delay defines the relative phase between the harmonic radiation and the infrared probe. A combination of a halfwave plate and a thin-film polarizer at Brewster angle can be used to adjust the probe beam intensity. A drilled recombination mirror is used to overlap the probe beam with the XUV. It also acts as an aperture to reduce the signal from the long trajectory (Section 2.1.1). The recombination mirror has a curvature to match the harmonic radiation divergence for generation with $f = 50$ cm focusing. The combined beams are then focused by a toroidal mirror into the detection gas of either a magnetic-bottle electron spectrometer (MBES) or a velocity-map imaging spectrometer (VMIS) [68, 69]. The MBES records the number of electrons after ionization and their time of flight (TOF) in a flight tube and was the main instrument to record electron spectra in Papers **I**, **III**, **IV**, **V** and **VII**. Papers **II** and **VI** used the VMIS, of which an improved model was also used for the experiments performed in Milan, *i.e.* in Papers **VIII**, **IX** and **X**.

2.2.2 Setup for Two-Color Generation

Figure 2.17 shows how the beam splitter in Figure 2.15 was replaced with an interferometric setup for two-color harmonic generation. This setup was used for Papers **II**, **IV** and **VI**. The interferometer allows the adjustment of the relative phase of the fundamental field and its second harmonic, thus providing additional control over the harmonic generation process. Its main function is to spatially and temporally overlap a second harmonic beam with the fundamental laser pulse. The second harmonic is generated in a KDP-crystal, then split off in a dichroic beam splitter. Because type-I phase matching is employed in KDP, the polarization of the second harmonic needs to be rotated by 90 degrees after generation so that the two beams have the same polarization. The coarse relative delay of second harmonic and fundamental beam is adjusted by a delay stage in the blue arm of the Michelson interferometer shown in Figure 2.17.

The fundamental beam has a fraction split off in an additional beam splitter to provide an infrared probe for experiments. A thin glass plate on a rotational stage is used to adjust the relative phase $\Delta\phi$ between the second harmonic and the fundamental with attosecond precision. Finally, both beams are recombined by another dichroic beam splitter. The rest of the setup is similar to Section 2.2.1.

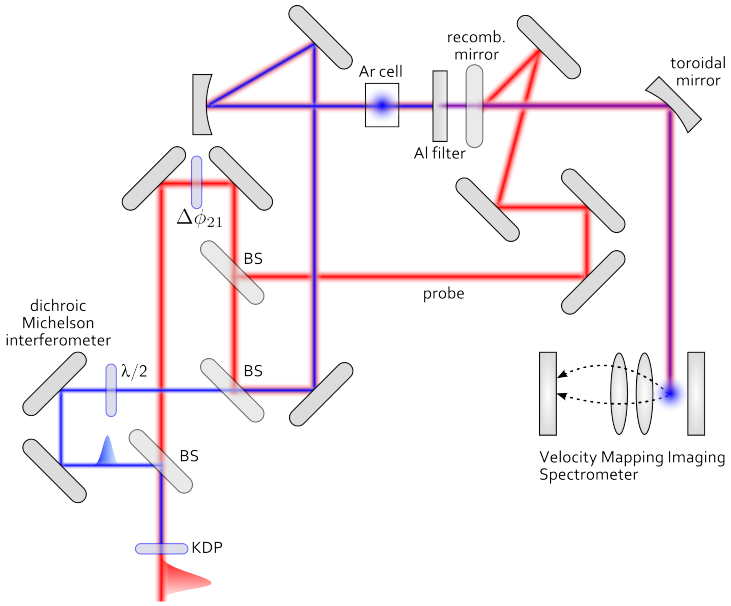

Figure 2.17. *Experimental setup for two-color HHG in Lund. A dichroic Michelson interferometer generates the second harmonic of the fundamental beam, turns its polarization to coincide with the initial state and then allows to precisely tune the relative phase of both laser fields. Their interference in the generation gas induces even harmonics in the generated radiation.*

2.2.3 Experimental Setup in Milan

The experiments of Papers **VIII**, **IX** and **X** were performed in Milan, with Paper **IX** also including data that was recorded in Lund in collaboration with AMOLF Amsterdam already in 2005. The key difference between the experimental setup in Milan and the one in Lund is the possibility to generate single attosecond pulses (SAPs). There are two requirements that have to be met, and one is the phase-stability of the laser system, meaning that its CEO phase is controllable and stable over the course of an experimental scan (typically 30 to 60 min). The second requirement is that few-cycle pulses are needed for the generation of SAPs (Section 2.1.6). This is achieved through self-phase modulation in an argon-filled hollow-core fused silica fiber and subsequent compression by a set of chirped mirrors [70, 71]. The output of the hollow-core fiber has a spectral distribution that is broadest on axis. As a result of this radial spectral distribution, different parts of the beam will be compressed to different durations, dependent on the available bandwidth. A drilled mirror separates

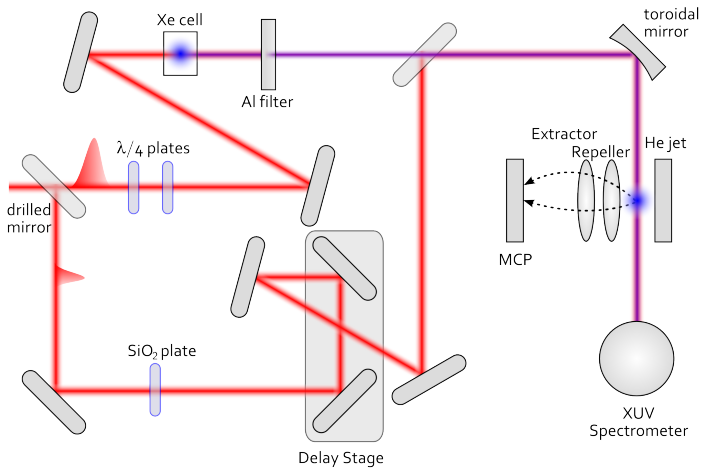

Figure 2.18. *Experimental setup in Milan. The interferometric arrangement generates single attosecond pulses by polarization gating and overlaps them with a few-cycle infrared probe beam for detection in either an XUV spectrometer or a velocity-mapping imaging spectrometer.*

generating and probe pulses. This separation does not induce any additional chirp on the pulses but has different durations as a consequence of the fiber output characteristic. The pulses used in the HHG process are therefore 5 fs long and the probe pulses typically have a duration of 7 fs. The delay of the probe relative to the generated attosecond pulses can be controlled with a precision of 200 as. The piezoelectric attosecond delay stage is inside the vacuum chamber, providing additional stability in a laboratory surrounded by an Italian city and therefore more sources of noise.

The 5 fs generation pulse has its polarization state altered by propagating through two quarter wave plates, leading to a situation as depicted in Figure 2.14, where only a very short window of linear polarization remains in the center of the envelope. The relative orientation of the quarter wave plates allows us to adjust the width of this linear polarization window [56–59].

The probe beam and the generated SAPs are both overlapped in a second drilled mirror and sent into a VMIS, similar to the setup in Lund, with the difference that an XUV photon spectrometer is also attached to the experimental chamber. This allows monitoring the spectrum of the SAPs independently during the experiment.

CHAPTER 3

CHARACTERIZATION OF ATTOSECOND LIGHT PULSES

This Chapter describes various characterization methods for attosecond pulses. The first Section introduces the RABITT method, the main method of measuring the harmonic phase differences in a comb of high-order harmonics. The last Section describes three additional methods: the attosecond AC streak camera, the complete reconstruction of attosecond bursts (CRAB) and the in-situ-characterization method.

3.1 Reconstruction of Attosecond Beating by Interference in Two-Photon Transitions (RABITT)

The RABITT method [15, 22, 72–75] is widely applied for the phase characterization of high-order harmonics and the resulting attosecond pulses. It is a cross-correlation method of a comb of equally spaced high-order harmonics with a fraction of the generating laser pulse. Ionization of atoms with high-order harmonics in the presence of an external laser field will lead to sidebands [76–81] occurring next to the photoelectron peaks originating from the harmonic photons. Each sideband can originate from either emission or absorption of an additional photon. These two pathways to each given sideband state (see Figure 3.1) lead to interference effects that provide access to the phase difference of the ionization pathways [14]. In this thesis, the RABITT technique has been used extensively for the characterization of attosecond pulses in a train. It has been applied to broadband pulses (Paper **III**) and its limitations have been explored in Paper **V**. In addition, an extension of this technique has been used for studies of resonantly enhanced two-photon ionization (R2PI) in Paper **VII**

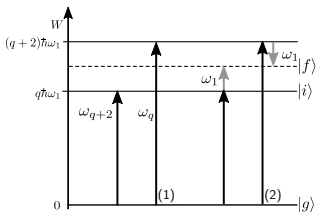

Figure 3.1. *Photon picture of first and second order perturbations used in the RABITT method.*

and is further described in Section 4.2.1. First, we will present the principle of the RABITT technique using a perturbation theory approach [74] before discussing its limitations.

3.1.1 Principle of the RABITT Method

Exposing an atom of ionization potential I_p to high order harmonic radiation, will, for orders with photon energy $q\hbar\omega_1 > I_p$, lead to single photon ionization of target gas atoms and the emission of electrons with kinetic energy $W_e = q\hbar\omega_1 - I_p$. This will lead to a photoelectron spectrum of evenly spaced peaks at $2\hbar\omega_1$ distance. The harmonic intensity is low, allowing the light-matter interaction to be treated as a small perturbation of the atomic system. From first-order perturbation theory (see Section 1.2.2), the probability amplitude for transitions from the ground state $|g\rangle$ to a set of continuum states $|i\rangle$ of energy W_i by absorption of harmonic photons labeled by the order q is described by

$$a_i^{(1)} = (i\hbar)^{-1} \int dt \mu_{ig} A_q(t) e^{i\hbar^{-1}(W_i - I_p - q\hbar\omega_1)t + i\phi_q}, \qquad (3.1)$$

where $\mu_{ig} = \langle i| er |g\rangle$ is the dipole transition matrix element between states g and i, $A_q(t)$ is the amplitude of the qth harmonic and ϕ_q, the harmonic spectral phase.

The addition of a weak probe field can be treated as yet another perturbation. It allows two-photon transitions to states f by absorption of an XUV photon of harmonic q and emission (amplitude a_f^{em}) or absorption (amplitude a_f^{abs}) of a probe laser photon (see Figure 3.1). It is from these two-photon transitions that the sidebands arise. Here, one can disregard the case of first absorbing an IR photon with subsequent absorption of an XUV photon which leads to smaller amplitudes [15]. The amplitude of a given state $|f\rangle$ from absorption is therefore the combination of the amplitudes resulting from emission and absorption

$$a_f^{(2)} = a_f^{abs} + a_f^{em} \qquad (3.2)$$

with

$$\begin{aligned} a_f^{abs}(\tau) &= \sum_i \int \frac{\mu_{fi}\mu_{ig}}{\hbar^{-1}(W_f - I_p - q\hbar\omega_1)} A_q(t) A_1(t-\tau) e^{i\phi^{abs}} dt \qquad (3.3) \\ a_f^{em}(\tau) &= \sum_i \int \frac{\mu_{fi}\mu_{ig}}{\hbar^{-1}(W_f - I_p - (q+2)\hbar\omega_1)} A_{q+2}(t) A_1(t-\tau) e^{i\phi^{em}} dt, \end{aligned}$$

for absorption and emission of a photon, with

$$\begin{aligned} \phi^{abs} &= (W_f/\hbar - I_p/\hbar - q\omega_1)t + \phi_q - \omega_1(t-\tau) \qquad (3.4) \\ \phi^{em} &= (W_f/\hbar - I_p/\hbar - (q+2)\omega_1)t + \phi_{q+2} + \omega_1(t-\tau) \end{aligned}$$

where τ is the relative delay of the XUV and IR fields with envelope functions $A_q(t)$ and $A_1(t)$, respectively. The signal arising from two-photon transitions to state $|f\rangle$ is then proportional to $\left|a_f^{(2)}(\tau)\right|^2$.

An additional phase term comes from the amplitude factors in Equation 3.3. This phase term can be written $\Delta\phi_f^{at} = \phi_+ - \phi_-$ [14, 82], with

$$\phi_\pm = \arg\left[\sum_i \frac{\mu_{fi}\mu_{ig}}{\hbar^{-1}(W_f - I_p - \hbar(q+1\mp1)\omega_1)}\right], \tag{3.5}$$

and is referred to as the *atomic phase*. We can now express the sideband peak signal $S_f(\tau)$ corresponding to absorption of energy $(q+1)\hbar\omega_1$ as

$$S_f(\tau) \propto \cos\left(2\phi_r + \Delta\phi_f^{at} + \Delta\phi_{q,q+2}\right) \tag{3.6}$$

where $\phi_r = \omega_1\tau$, and S_f varies with delay τ and depends on the offsets $\Delta\phi_{q,q+2} = \phi_q - \phi_{q+2}$ and $\Delta\phi_f^{at}$. $\Delta\phi_f^{at}$ is usually small in comparison to $\Delta\phi_{q,q+2}$ but can be calculated from integration of the time-dependent Schrödinger equation [33] or measured [74]. If these atomic phase factors have been determined before or can be considered negligibly small[1], then the only unknown in Equation 3.6 is the harmonic phase difference $\Delta\phi_{q,q+2}$.

Measuring S_f as a function of τ allows us to determine $\Delta\phi_{q,q+2}$ as a function of q by Fourier transform. The Fourier transform contains a DC component and a peak at $2\omega_1$ whose phase is expected to be $\Delta\phi_f^{at} + \Delta\phi_{q,q+2}$. This method is sketched in Figure 3.2, where two sidebands are Fourier-transformed to extract the offset phases $\Delta\phi_{q,q+2}$ and $\Delta\phi_{q+2,q+4}$.

$\Delta\phi_{q,q+2}$ is related to the harmonic group delay sampled at the sideband energies $(q+1)\hbar\omega_1$, by

$$\tau_g((q+1)\omega_1) = \left.\frac{\partial\phi}{\partial\omega}\right|_{(q+1)\omega_1} = \frac{\Delta\phi_{q,q+2}}{2\omega_1}. \tag{3.7}$$

Note that our measurement (Figure 3.2) does not allow us to determine $\tau_g((q+1)\omega_1)$ in absolute value, since the delay τ is only known in relative value. The absolute value of the GD is not needed for the reconstruction of the attosecond pulse (only the GDD matters, see Section 3.1.3). There are, however, experiments, where this absolute delay of generation pulse and harmonics is of interest [23, 83]. The delay between the maximum of the generation pulse envelope and the attosecond XUV burst can be measured by interference of the probe and generation beam during the HHG process [73, 84].

[1] This is the case for transitions to final states far above the threshold, with high W_f

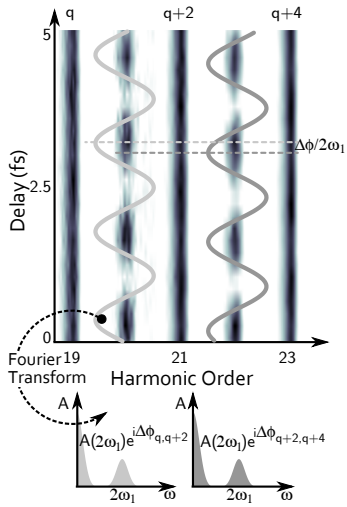

Figure 3.2. *Sketch illustrating the use of the RABITT method: two modulated sidebands, with a phase difference representing the group delay difference between harmonics q, $q+2$ and $q+4$, are Fourier-transformed to yield the phase differences $\Delta\phi_{q,q+2}$ and $\Delta\phi_{q+2,q+4}$ as phase offset at $2\omega_1$ in the Fourier plane.*

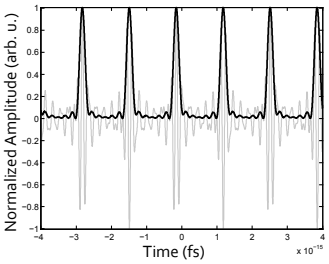

Figure 3.3. *Reconstruction of an APT according to Equation 3.9.*

3.1.2 Atomic Phase Factors

The RABITT method requires that the atomic phase factors are small or can be accurately calculated. Mauritsson *et al.* [85] have calculated the magnitude of ϕ_{fg}^{at} by numerically solving the TDSE. These phase factors can be shown to be related to the scattering phases of the state reached after absorption of one photon [86]. In some cases as in Paper **VII** and in [75], ϕ_{fg}^{at} becomes large. If one of the states i in Equation 3.3 is a resonant state r, then the two-photon transition leading to final state f will experience a π-phase jump [75] (see Section 4.2.1).

The atomic phase is a limitation to the RABITT technique, but it can be used conversely to obtain information on the atomic system. In Paper **VII**, the attosecond chirp information is obtained from the other sideband signals, thus isolating the atomic contribution. Its photon energy and probe laser intensity dependence are then studied in detail. Haessler *et al.* [75] study a "complex resonance" in the ionization of nitrogen molecules by similar techniques.

3.1.3 Reconstruction of Attosecond Pulse Shapes

The aim of the RABITT method is to characterize APTs in phase and amplitude. This is the ultimate goal of all ultrashort pulse measurement techniques, because only the knowledge of both phase and amplitude provides the full picture with respect to the duration and temporal intensity distribution of the pulses. Knowledge of these parameters is important as the pulse duration determines the resolution of ultrafast experiments. The phase is measured by the RABITT technique described above and the amplitude is readily obtained from the harmonic spectrum.

In our experiments, the spectrum is measured by the electron count in an electron spectrometer or by an XUV grating spectrometer (see Section 2.2). When using the photoelectron spectrum, the ionization cross-section σ_q of the target gas has to be taken into account. This exists as tabulated data which can be used to correct the photoelectron spectrum amplitudes [87]. This indirect measurement makes it difficult to draw conclusions on the pulse energy of the APT. The measurement of the conversion efficiency and XUV photon flux requires carefully calibrated detectors, which has not been done in this thesis work [32, 88].

From the measured harmonic spectral phase differences $\Delta\phi_{q,q+2}$ and the relative harmonic spectral amplitudes $A_q = \sqrt{I_q/\sigma_q}$ the average attosecond pulse in an APT can

be reconstructed. We obtain the spectral phase as

$$\phi_q = \begin{cases} 0, & q = q_{min} \\ \sum_{n}^{q} \Delta\phi_{n-2,n}, & q > q_{min} \end{cases} \tag{3.8}$$

where q_{min} is the lowest measured harmonic order[2]. The average intensity profile I_{avg} of such a attosecond pulse then arises from the sum of the individual harmonic fields

$$I_{avg}(t) = \left| \sum_{q} A_q \exp\left[-iq\omega_1 t - i\phi_q\right] \right|^2, \tag{3.9}$$

where the spectral phase ϕ_q defines the relative synchronization of the harmonic components and can greatly influence the pulse shape. Figure 3.3 shows an example of a reconstructed pulse train. The FWHM of the intensity profile $I_{avg}(t)$ defines the pulse duration of the attosecond pulse. An overview of such different average temporal intensity profiles for several different filter materials was given in Figure 2.10.

3.1.4 Pulse to Pulse Variations in RABITT

There are several limits to the validity of RABITT. One is its ability to only measure the average pulse shape of a given APT. To extend the measurement to the pulse-to-pulse variations in the APT [34], a generation intensity dependent measurement has been proposed [23]. A second option which has mainly been used for APTs with few pulses, is the use of a full cross-correlation trace between the APT and the probing field [89–91] (Section 3.2.2).

Equation 3.9 assumes that the individual harmonic fields are infinite in time (*i.e.* monochromatic). In reality, the duration of each harmonic field is shorter than that of the fundamental laser. Therefore, the harmonic amplitude function becomes a function of time $A_q(t)$, with finite duration. The intensity profile $I_{avg}(t)$, as expressed by Equation 3.9, is therefore only an average of all pulses in an APT, each contributing with their respective duration to the shape of the pulse[3].

The limited duration of any harmonic order q stems from the intensity envelope of the fundamental laser pulse. As seen in Section 2.1.1, the harmonic cutoff is dependent on the laser electric field strength seen by the electron during its excursion in the continuum. As a result, lower harmonics have a longer duration because the fundamental laser intensity needed for their generation

[2] q_{min} is usually defined by the used filter material and the I_p of the detection gas. For a correct pulse measurement, $\hbar q_{min}\omega_1$ needs to exceed I_p.

[3] In the spectral domain, a finite duration Δt corresponds to a bandwidth $\Delta\omega$. Equivalently, one can therefore say that the spectra of all attosecond pulses mix to produce the measured average attosecond pulse.

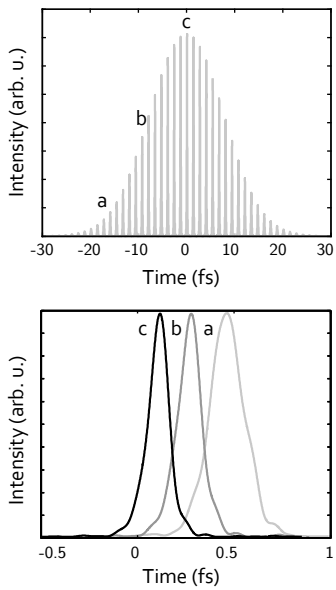

Figure 3.4. *APT reconstructed from RABITT measured in Paper **III**, with pulse to pulse variations used from [23]. A full train is shown, with three different pulses in the train displayed below, showing the greater duration at the wings of the APT.*

persists longer while the fundamental laser pulse interacts with the generation medium. Thus, the highest harmonic orders have the shortest duration. They are emitted at the center of the fundamental pulse, which is used in the generation of SAPs from few-cycle pulses (Section 2.1.6).

In [23], the variation of attosecond pulses within an APT is studied by extending the RABITT method with two improvements. First, the absolute delay of the APT with respect to the fundamental laser envelope maximum is known [73, 84] and second, the RABITT measurements are performed at different generation intensities. Then, a Taylor-expansion of the harmonic phases ϕ_q with respect to their intensity- and q-dependence resolves the pulse-to-pulse variations as higher-order terms in the expansion. The intensity-calibration and the number of intensity-dependent RABITT measurements then determines the precision of the retrieved full pulse train structure. In [23], three measurements were performed, providing the essential information by making reasonable assumptions regarding the fundamental laser pulse shape. Increased knowledge of the fundamental laser pulse shape can further improve the precision.

In Paper **III**, the question of pulse-to-pulse variations arose as well. There, one aim was to produce the shortest attosecond pulses to-date, which then required knowledge of what the measured average pulse shape in the APT meant. The average pulse shape had a duration of 130 as, a world record at that time. It shared this world record for some time with [92], which achieved the same duration with an SAP generated from argon and therefore at a different central photon energy. The method from [23] was used to assess the pulse-to-pulse variations in the APTs generated in Paper **III**. These are the results presented in Figure 3.4. It was found that within the FWHM of the APT, the pulse duration varied from 120 as in the center of the train to 140 as at the half-maximum of the attosecond pulse peak intensity[4]. At 10% of the peak intensity, the pulse duration was 190 as. The study in Paper **III** concluded that using a 500 nm filter of zirconium would be sufficient to push the average pulse duration below 100 as, considered a milestone at that time. Further experiments in this direction were undertaken in the course of this thesis, but proved unsuccessful due to the low filter transmission and sub-optimal performance of the laser system at the time. The race for the first sub-100 as pulse continued thereafter and was finished in 2008 [93].

[4]Using such an APT in experiments, more than 80% of the signal will come from pulses in this part of the train. Therefore, the duration measured by the RABITT method from an APT is a good measure of the experimentally relevant pulse duration.

3.1.5 Limitations of RABITT with High Probe Intensities

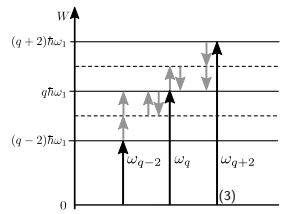

Figure 3.5. *Photon picture of the third perturbation order transitions.*

Another limit to the validity of RABITT arises from the requirement that the probe field should only act as a perturbation to the process as seen in the derivation in Section 3.1.1. For higher probe field intensities, one may need to consider higher orders of perturbation than the second-order used in Section 3.1.1.

Assume that we perform an experiment like RABITT in conditions which exceed the limits prescribed by the description in second order perturbative terms. Instead of a non-perturbative solution [81, 94], one can extend the model by considering an additional order of perturbation. In this case, as depicted in Figure 3.5, the emission or absorption of an additional IR photon becomes possible compared to the two-photon processes used in conventional RABITT, where we considered the transitions $(q \rightarrow q+1)$ and $(q+2 \rightarrow q+1)$. We find that now transitions $(q \rightarrow q+2)$ and $(q+4 \rightarrow q+2)$ become possible. Here, the harmonic number $(q+n)$ denotes a final state reached by the absorption of a single XUV photon. Using the notation from Section 3.1.1, we can then write the third order amplitude of harmonic state q as

$$a_q^{(3)} \approx F(i\hbar)^3 \left[e^{i(2\phi_r+\phi_{q-2})} + 2e^{i\phi_q} + e^{i(-2\phi_r+\phi_{q+2})} \right], \qquad (3.10)$$

where F is an amplitude factor and we have disregarded the atomic phase factors $\Delta\phi_q^{at}$. The total signal $S \propto |a_q^{(3)}|^2$ will then be proportional to

$$\begin{aligned} S(\phi_r) \quad &\propto \quad A\cos\left(4\phi_r + (\Delta\phi_{q-2,q+2})\right) \\ &+ \quad B\cos\left(2\phi_r + (\Delta\phi_{q-2,q})\right) \\ &+ \quad C\cos\left(2\phi_r + (\Delta\phi_{q,q+2})\right), \end{aligned} \qquad (3.11)$$

where A, B and C are constant factors. There are two contributions oscillating at a frequency of $2\omega_1$ and one oscillating with $4\omega_1$. The term oscillating at $4\omega_1$ has as its offset the phase difference $\Delta\phi_{q-2,q+2}$, which allows mapping of the group delay as in the RABITT case. It uses the phase difference of non-consecutive harmonics but yields the same results as shown in Figure 3.7.

We conclude that at higher probe intensities, when the absorption of two IR photons becomes likely, the group delay of the harmonic spectrum can be determined by considering a higher-frequency modulation of the delay-dependent signal. From Figure 3.5 we see that this modulation will be found in the states reached by the absorption of harmonics. We also see that the $2\omega_1$ modulations include several components and therefore become unreliable for the GD measurement.

The previous considerations can be extended to a fourth order of perturbation, as shown in Figure 3.6, with an approximate

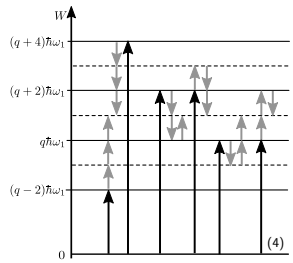

Figure 3.6. *Photon picture of the fourth perturbation order transitions. There are several ambiguous transition pathways to the same final state.*

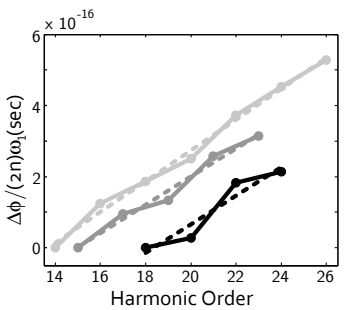

Figure 3.7. *Comparison of RABITT phases measured from higher modulation frequencies. The modulation frequencies are $2\omega_1$ (light gray), $4\omega_1$ and $6\omega_1$ (black). The dashed lines are line fits, indicating that the same GDD was measured each time.*

amplitude as

$$a_{q+1}^{(4)} \approx F\left[e^{i(3\phi_r+\phi_{q-2})} + 3e^{i(\phi_r+\phi_q)} + 3e^{i(-\phi_r+\phi_{q+2})} + e^{i(-3\phi_r+\phi_{q+4})}\right], \tag{3.12}$$

from which we will not write the resulting cross terms. There will be a single component oscillating at $6\omega_1$

$$S \propto \cos\left(6\phi_r + \Delta\phi_{q-2,q+4}\right), \tag{3.13}$$

two components at $4\omega_1$ (originating from $\Delta\phi_{q-2,q+2}$ and $\Delta\phi_{q,q+4}$) and several components with frequency $2\omega_1$ (Figure 3.6).

The possibility of several components contributing to a given modulation frequency is why the RABITT method begins to break down for higher IR intensities. Eventually too many different $\Delta\phi_{m,l}$ will be present in a single final state at the conventional modulation frequency $2\omega_1$, preventing the useful extraction of the harmonic spectral phase differences. Paper **V** studies how this behavior for higher IR intensities introduces errors in the phase measurement, leading to reconstructed pulse shapes that are not physical anymore. Instead of the increasingly unreliable lowest order of modulation, the higher perturbation orders can then be used to obtain an unperturbed measurement of the harmonic chirp rate.

Figure 3.7 shows such a measurement. The phase difference is measured for three different modulation frequencies (varying from gray to black with increasing frequency). The three curves show good agreement and the same chirp rate (gradient) for all three cases. Paper **V** also introduces a more generalized treatment of the observed effects, very similar to the considerations of [95].

3.2 Strong IR Field Cross-Correlation Methods

The RABITT method of the previous Section is not the only method to analyze the phase of attosecond pulses. This Section will introduce three different methods that can also be used. The first method, is the standard method for SAPs. The second method is an extension of the previous one and was used in Papers **VIII**, **IX**, and **X**, allowing full reconstruction of fairly arbitrary pulse shapes. The last method was proposed and demonstrated by [26] and was analyzed in detail in Paper **IV**.

3.2.1 Streaking

The XUV ionization process in the presence of a probe laser field can be treated semiclassically [91]. This is done by dividing the process into two steps, where the ionization by the APT or SAP

is separated from the effect of the probe. An electron is released from an atom at time t_i by single-photon ionization with an initial kinetic energy $W_0 = |\mathbf{p}_0|^2 / 2m_e$ and then accelerated by the probe laser electric field. Here, $\mathbf{p}_0$ is the initial momentum of the electron of mass m_e. The acceleration can then be treated by classical mechanics [96, 97] where the time-dependent momentum $\mathbf{p}(t)$ follows as

$$\mathbf{p}(t) = e\mathbf{A}(t) + [\mathbf{p}_0 - e\mathbf{A}(t_i)], \tag{3.14}$$

with $\mathbf{A}(t)$ as the vector potential of the probe laser. In our experiments laser fields are normally linearly polarized and $\mathbf{A}(t)$ points along the direction of the laser polarization, defining the direction for the gained momentum. One can see that at time $t \gg t_i$, when both pulses have long passed and the electron is detected, the final momentum is

$$\mathbf{p}_f = \mathbf{p}_0 - e\mathbf{A}(t_i). \tag{3.15}$$

This shows that any electron originating at time t_i will have its momentum changed by $e\mathbf{A}(t_i)$ with respect to the probe-field-free case.

Let us now consider an SAP, significantly shorter than the probe period, so that $\mathbf{A}$ can be considered as constant during the duration of the SAP. The final momentum distribution of the photoelectrons as a function of delay (t_i) reproduces the $\mathbf{A}(t)$ of the probe laser pulse over the range of delays scanned. All spectral components within the SAP are released at different $\mathbf{p}_0$ but experience the same vector potential.

The attosecond streak camera method [98] is based on these considerations. Assume an SAP with bandwidth $\Delta\omega$ and duration $\Delta\tau$ being chirped, so that its central frequency $\tilde{\omega}$ changes over $\Delta\tau$ with the chirp rate b. If in addition the SAP is not short enough compared to the variation of the probe laser vector potential $\mathbf{A}(t)$, the frequency $\tilde{\omega}(t)$ will experience different $\mathbf{A}(t)$ over $\Delta\tau$. In the final recorded photoelectron momentum distribution, a distribution of vector potentials $\mathbf{A}(t)$ will then contribute over the pulse duration $\Delta\tau$, thus broadening the momentum distribution compared to the field-free case. The probe field vector potential therefore maps the temporal variation of the SAP central frequency to momentum space. Note that the broadening is in the case where chirp and $\partial\mathbf{A}(t)/\partial t$ are of the same sign, and in the case of opposite sign there will be a narrowing of the momentum distribution. This method is based on the assumption of a fairly well-behaved SAP pulse shape, *e.g.* a Gaussian pulse. It does, however, allow to characterize the chirp rate of the SAP.

Paper **II** presents an implementation of this method not for an SAP but for an APT generated from a two-color field. As seen in Section 2.1.5, an APT with one pulse/laser cycle creates iden-

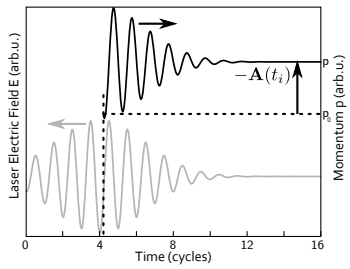

Figure 3.8. *Illustration of the momentum transfer from vector potential* $\mathbf{A}$ *to an electron released at time* t_i *in a laser field* $E(t)$.

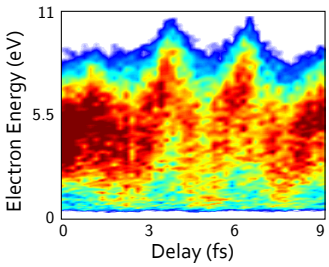

Figure 3.9. *Experimental CRAB spectrogram recorded for Paper **VIII**.*

tical electron wave packets in the probe field, which allows us to employ the attosecond AC streak camera method.

3.2.2 Complete Reconstruction of Attosecond Bursts (CRAB)

The CRAB-method [90, 91] is an extension of the attosecond streak camera method, allowing the full reconstruction of single attosecond pulses or short pulse trains. It has been successfully demonstrated in experiments for SAPs [92, 93, 99, 100] but recently also for APTs [101]. The CRAB-technique originates from the method of Frequency-Resolved Optical Gating (FROG) [102–104], which is used for the characterization of ultrashort laser pulses.

The FROG method is based on a spectrogram, *i.e.* a two-dimensional set of data, which normally is a spectrum recorded as a function of delay. A FROG spectrogram is described by

$$S(\omega,\tau) = \left| \int_{-\infty}^{\infty} dt G(t) E(t-\tau) \exp(i\omega t) \right|^2 , \tag{3.16}$$

where $E(t-\tau)$ is the field to be measured and $G(t)$ is the gating field. The gate may be known or not. It is in fact possible to extract both functions from the spectrogram, in conditions which are then called "blind FROG" [104]. The extraction is normally performed numerically by use of a deconvolution algorithm [102], requiring only a two-dimensional set of amplitude data [105, 106]. The algorithm benefits greatly from one of the two functions being known so that it can be used as an input to the pulse retrieval.

In the case of CRAB, a full trace of delay-dependent photoionization spectra serves as the spectrogram. Here, the IR probe is treated as a time-varying phase gate on the attosecond pulse photoelectron spectrum. In the case of attosecond fields, an equation similar to Eq. 3.16 is obtained from the strong-field approximation [7] for ionization in the presence of a dressing laser field [91]

$$a(\mathbf{p}_f) = -i \int_{-\infty}^{\infty} dt \exp\left[i\zeta(t)\right] \mu_{\mathbf{p}_f g} A_{XUV}(t-\tau) e^{\left[i(W_f+I_p)t - i\hbar\tilde{\omega}(t-\tau)\right]} \tag{3.17}$$

with

$$\zeta(t) = -\int_{t_i}^{\infty} dt' \left(\mathbf{p}\mathbf{A}(t') + \mathbf{A}^2(t')/2 \right), \tag{3.18}$$

and $A_{XUV}(t-\tau)$ as the attosecond pulse envelope. We see that the function $\zeta(t)$ can be identified as a phase gate $G(t)$ as mentioned above. The vector potential of the probe laser field will

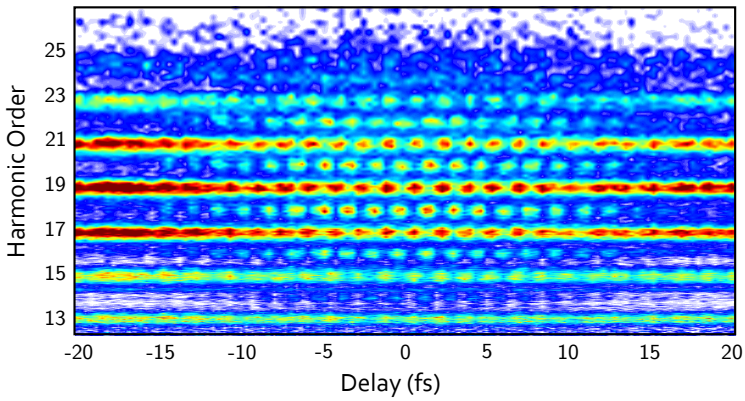

Figure 3.10. *RABITT scan measured using fundamental laser pulses compressed in a hollow-core fiber. The sideband signal extends over ≈ 30 fs, about half of a conventional RABITT performed with the Lund laser system.*

modulate the photoelectron wave packet phase as a gate function with varying delay τ. Despite the phase modulation being lost when only the amplitude square is recorded, two-dimensional deconvolution algorithms (*e.g.* PCGPA[5] [104]) can very efficiently retrieve both functions $E(t)$ and $G(t)$ from the spectrogram.

Figure 3.9 presents one such spectrogram retrieved during the experiments of Paper **VIII**. The pulse duration was found to be $\Delta\tau = 350 \pm 20$ as. With short laser pulses, compressed by a hollow-core fiber and chirped mirrors (described in Section 2.2.3), conditions can approach those considered for short pulse trains in [90]. Experiments with this compression method were performed in Lund in the course of this thesis with the aim of producing SAPs or short pulse trains by polarization gating [107]. These shorter fundamental pulses were used in HHG and as a probe, resulting in the scan shown in Figure 3.10. The signal of sideband 20 - a cross-correlation of the average duration of harmonics 19 and 21 with the IR - has a FWHM of 25 fs. If we consider the sideband signal as an intensity autocorrelation, assuming for simplicity equal length and a Gaussian shape for both the probe pulse and the harmonics, the duration of the IR is about 17 fs.

The retrieval of attosecond pulses using the CRAB method was attempted in the course of this thesis, but the resolution of the data in Figure 3.10 did not prove to be sufficient for useful pulse reconstructions. The algorithm developed in this work was tested on the scan in Figure 3.9 and showed a duration of 400 as,

[5]Principal Component Generalized Projections Algorithm.

a reasonable agreement with the algorithm used in Milan.

3.2.3 *in-situ* Method

The last method presented here probes attosecond pulses while they are generated [26], using two-color HHG (Section 2.1.5) with a very weak blue field ($R = 0.001$). The blue field slightly perturbs the generation by the fundamental laser, with consecutive half IR cycles being affected differently. This difference will then break the symmetry between both half cycles and lead to the onset of weak even harmonics. The magnitude of an individual even harmonic peak depends on the relative phase $\Delta\phi_{21}$ between both fields and scanning $\Delta\phi_{21}$ leads to a modulation of the even harmonic signals. For the even harmonics in the plateau region of the spectrum, the phase of the even harmonic maximum $\Delta\phi_m(q\omega_1)$, with q as the even harmonic number, is related to the distribution of release times $t_r(q\omega_1)$ as [108]

$$t_r(q\omega_1) \approx -\frac{\Delta\phi_m(q\omega_1)}{\omega_1}, \tag{3.19}$$

which is analogous to the considerations for Equation 2.3 and thus yields the GD curve of the even and odd harmonics [108]. This GD curve is, under the assumption of a smooth variation of the harmonic intensity over the spectrum [26], a sampling of the emission times or GD function for the odd harmonics. The method, however, breaks down for harmonics in the cutoff and for the lowest harmonics. Interestingly, it determines the GD of the harmonic emission in the single atom response and does not include effects of phase matching on the temporal properties (see Paper **I**). Phase matching may affect the method validity in conditions of high pressure and long media. This has been investigated in Paper **IV**.

CHAPTER 4

METROLOGY OF ATTOSECOND WAVE PACKETS

This Chapter presents applications of attosecond pulses. Attosecond wave packets, created from the interaction of attosecond light pulses with matter, can be attosecond electron wave packets or vibrational wave packets in molecules. They can be created by excitation with an APT, forming a train of attosecond electron wave packets, or by an SAP leading to the formation of a single attosecond wave packet. These wave packets are then characterized as precisely as possible, both in amplitude and phase, and manipulated by an external laser field.

4.1 Free Attosecond Electron Wave Packets

The simplest attosecond electron wave packets are those above the ionization threshold and created by single-photon absorption. This type of wave packet has been used from the beginning of attosecond physics, primarily for the characterization of attosecond pulses. Free electron wave packets are used both in the RABITT and streaking techniques presented in Sections 3.1.1 and 3.2.1. Here, we concentrate on the properties of the electron wave packets themselves.

4.1.1 Electron Wave Packets in Laser Fields

The attosecond electron wave packets (EWPs) used in this thesis are created by photoionization of matter with attosecond pulses. With Equation 1.13 we see from first-order perturbation theory that the temporal properties of an EWP are defined by the attosecond pulse. This is the foundation of attosecond pulse characterization techniques presented in the previous Chapter. Figure 4.1 a) shows the electron momentum distribution $|a(\mathbf{p})|^2$ from single-

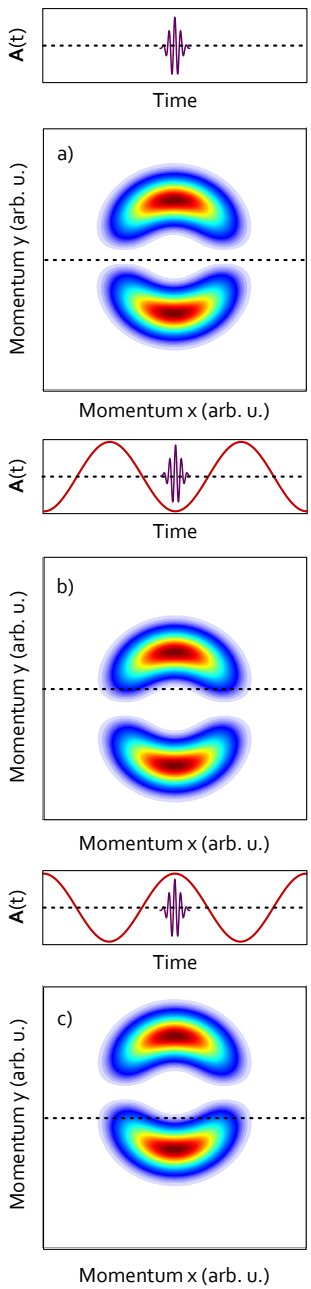

Figure 4.1. *a) Electron momentum distribution $|a(\mathbf{p})|^2$ from an SAP ionizing He, with no IR field present b) with IR, $\mathbf{A}(t) < 0$, c) with IR, $\mathbf{A}(t) > 0$.*

photon ionization of a He atom in its ground state by an SAP centered at a photon energy of 40 eV with 13 eV bandwidth. This creates photoelectrons in a coherent superposition of ϵp final continuum states[1] with a bandwidth corresponding to that of the ionizing radiation. This wave packet shown in Figure 4.1 a) represents the basic wave packet available for experiments with attosecond pulses. For an APT, where a sequence of attosecond pulses of similar bandwidth is spaced at constant temporal intervals, the EWPs created by each individual pulse will interfere with one another. The momentum distribution resulting from ionization of an atom with an APT is shown in Figure 4.2 a).

As seen in Section 3.2.1, the presence of a laser field during ionization allows the transfer of momentum from the laser field to the created EWP, following the instantaneous vector potential $\mathbf{A}(t)$ of the external laser field at the time of ionization (Equation 3.15). Figures 4.1 b) and c) present the momentum distribution from ionization at the two opposing extrema of the vector potential, shifting the whole momentum distribution along the laser polarization direction. The field used in Figures 4.1 and 4.2 is polarized along the y-direction.

For ionization with APTs in the presence of a probe laser field, the situation is complicated by the periodicity of the APT in comparison to the external laser period. Figures 4.2 b) and c) depict two possible scenarios. In the case of Figure 4.2 b), two attosecond pulses per fundamental (and probe) laser cycle lead to a superposition of EWPs with momentum distributions displaced in the opposite direction. These are the experimental conditions used by Remetter *et al.*[25] for momentum shearing interferometry of attosecond EWPs, where the upper and the lower lobes of Figure 4.2 a) can interfere around the zero of p_y. If the APT includes only one attosecond pulse per laser cycle - as in Papers **II** and **VI** (Section 2.1.5) - the momentum distribution as a whole is shifted as in Figure 4.2 c) with the periodicity of the train leading to a modulation of the momentum distribution by interference. These are the conditions of the "quantum stroboscope" [109], where the time spacing between the pulses of the APT matches the frequency of the external field, thus "freezing" the momentum distribution at a given instantaneous vector potential $\mathbf{A}(t + n2\pi/\omega_r)$, with n the number of pulses in the train and ω_r the repetition frequency of the APT. With each pulse being in phase with all others, their created EWPs will add constructively, leading to a total signal proportional to n^2. Paper **VI** demonstrates this method and its use for a time-resolved measurement with APTs. As a result from the fact that all attosecond pulses experience the same vector potential, techniques developed for SAPs can be directly applied in these conditions. Paper **II** shows the application of the attosecond

[1] With angular momentum $\ell = 1$, due to ground state He being $1s$ with $\ell = 0$.

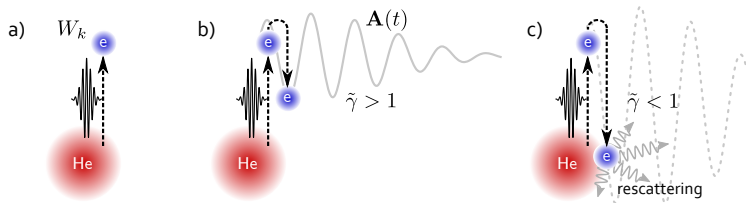

Figure 4.3. *Illustration of ionization of He by an attosecond pulse a) without external laser field, b) in the presence of a weak to moderately strong external laser field, c) in presence of a strong IR field allowing return of the electron and re-scattering.*

AC streak camera technique to measure the GDD of the attosecond pulses.

When the external laser field reaches intensities of $10^{12}\,\mathrm{Wcm}^{-2}$, the laser field transfers a significant amount of momentum to the electrons. This transferred momentum can become sufficient to turn around an electron ejected along the polarization direction of the laser and have its final momentum point in the opposite direction. These are the conditions depicted in Figures 4.1 b), c) and 4.2 c). To better describe these conditions, a $\tilde{\gamma}$-parameter can be defined

$$\tilde{\gamma} = \frac{W_k}{2U_p}, \tag{4.1}$$

with W_k the kinetic energy of the ejected electron without the external laser field and U_p the ponderomotive energy. A $\tilde{\gamma} > 1$ implies that the transferred momentum from the IR field does not exceed the initial momentum gained in the ionization step ($p_k^2/m_e = W_k = q\hbar\omega_1 - I_p$). $\tilde{\gamma} < 1$ means that the electric field of the external probe laser is strong enough to turn electrons of field free ejection energy W_k around and have them pass the original ion.

Figure 4.3 illustrates these possible scenarios. In Fig. 4.3 a), a photoelectron is ejected with an excess kinetic energy of W_k in one direction. In Fig. 4.3 b) and c), the electron is released in presence of an external field at a given instant and then driven by field for the rest of the probe pulse duration. Two probe fields of different amplitude are shown, representing two different $\tilde{\gamma}$ parameters. For $\tilde{\gamma} > 1$ (Figure 4.3 b)), the electron will wiggle in the field, with a minimum kinetic energy of zero and a maximum determined by its acceleration in the electric field. After the pulse has passed, it will be found with a momentum determined by the vector potential at the time of its release and its initial W_k, as in Equation 3.15. For $\tilde{\gamma} < 1$ (Figure 4.3 c)), while the electron

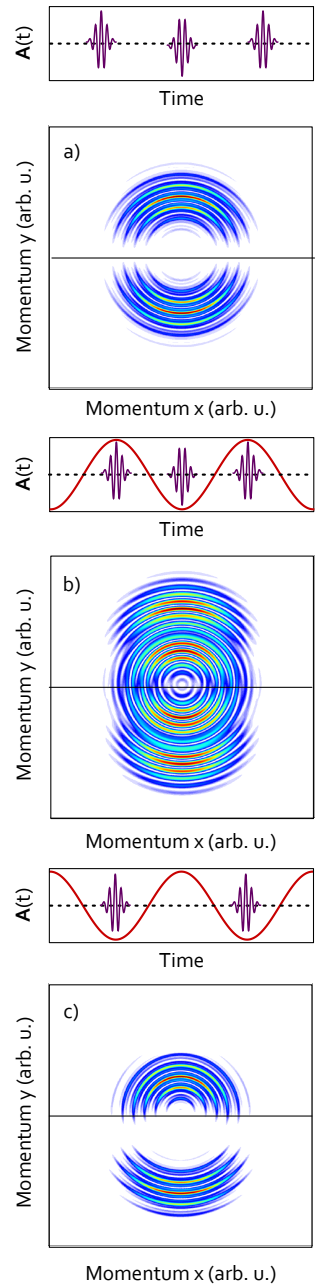

Figure 4.2. *a) $|a(\mathbf{p})|^2$ from a train of pulses, no IR b) with IR, two pulses/cycle, c) with IR, one pulse/cycle.*

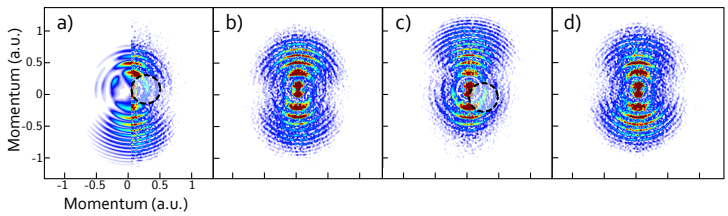

Figure 4.4. *Momentum maps from Paper* ***VI****. The first panel compares theory and experiment, showing re-scattering and excellent agreement. Panel 3 shows again re-scattering, but in the other direction as it represents a vector potential* **A** *shifted by half a laser cycle or* π*.*

wiggles in the field following its release, it will not only return to the parent ion but actually be able to pass it and re-scatter off the atomic potential with a certain probability.

Paper **VI** reaches conditions of $\tilde{\gamma} \approx 0.9$ and records the re-scattering of electrons. It makes use of the quantum stroboscope realized by preparing an APT from two-color HHG (Section 2.1.5). Figure 4.4 shows the photoelectron momentum distributions recorded from helium atoms as measured with a VMIS (Section 2.2.1) in Paper **VI**. Here, a) and c) correspond to the maxima of the vector potential **A** in opposing directions, with a) being split in half at the symmetry axis along the laser polarization for comparison with a TDSE calculation (left side). In both cases, the vector potential **A** is strong enough to turn around the lowest-energy photoelectrons and allow re-scattering. Figure 4.4 b) and d) are recorded at the zero-crossings of the vector potential. We see re-scattering effects appear in a) and c) as minima in the electron signal in the innermost ring from destructive interference between the re-scattered and the unaffected portions of the EWP. It is clearest at about 60° from the vertical axis (highlighted by circle). The calculation in a) shows the re-scattering in greater clarity and confirms the interpretation of our observations.

The experiment in Paper **VI** imaged the re-scattering of returning EWP fractions on the atomic potential for the first time. This provided a proof-of-principle experiment to use of these coherent EWPs for diffraction studies on more complicated systems, similar to other coherent diffraction techniques with either photons or electrons (*e.g.* [110]).

4.2 Metrology of Bound States

Experiments grow in complexity when bound states are involved. Here, the observables are again free electrons, which now carry

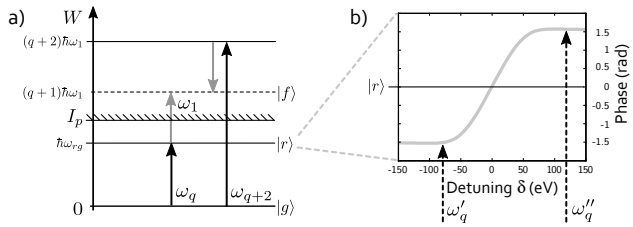

Figure 4.5. *a) Photon picture of the R2PI phase measurement. b) resonance-induced phase change in two-photon ionization from second-order perturbation theory, dependent on detuning δ from a resonance $|r\rangle$.*

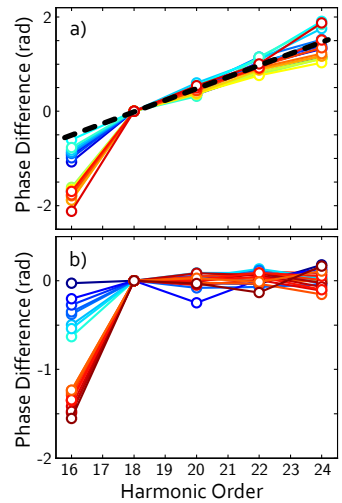

Figure 4.6. *a) Harmonic phase differences measured in He, b) harmonic phase differences corrected for linear chirp fit indicated by dashed line in a).*

information on the intermediate excited states i. Papers **VII** and **VIII** present two experiments aimed at such an intermediate state characterization. Paper **VII** studies the phase effects of a resonant two-photon ionization process and uses it to measure the resonance behavior in the presence of a probe laser field of varying strength. Paper **VIII** aims to fully characterize in amplitude and phase a wave packet comprising several bound states by use of an interferometric method.

4.2.1 Resonant Two-Photon Ionization

The release of an electron by absorption of two photons whose combined photon energy is higher than the binding energy, is called two-photon ionization. This process has a much greater probability amplitude if at least one of the two photons matches a resonant transition in the atom. This process may involve photons of different energies (resonant two-color two-photon ionization) or more generally, more than two photons (resonantly-enhanced multiphoton ionization - REMPI).

The atomic phase factor ϕ_q^{at} from Section 3.1.2 can be greatly affected if the energy of an intermediate state is very close to the photon energy of a harmonic q. The dominant term of the transition amplitude from the ground state to the final state by absorption of the harmonic photon energy and an IR photon energy (Figure 4.5 a)) is proportional to $\mu_{fr}\mu_{rg}/[\omega_{rg} - q\omega_1]$, which diverges for $q\omega_1 = \omega_{rg}$, *i.e.* at resonance. When scanning the excitation frequency through the resonance, this resonant term will change sign, so that the associated atomic phase will undergo a π phase shift. Figure 4.5 b) shows this phase shift as a function of the detuning $\delta = \omega_{rg} - q\omega_1$ using a simple two-level perturbation theory model with radiation fields of 30 fs (IR) and 10 fs (XUV) duration, the latter corresponding to a bandwidth of 180 meV.

Paper **VII** studies the phase of resonant two-photon ionization

(R2PI) of helium via the $1s3p\,^1P_1$ state. The 15$^{\text{th}}$ harmonic, which at a fundamental wavelength of 800 nm has a photon energy of 23.25 eV, is close to the $1s3p$ resonance, which lies 23.087 eV from the ground state. With an ionization potential of 24.58 eV, helium excited in the $3p$ state can then be ionized by absorption of a single IR photon of 1.54 eV photon energy. By changing the fundamental central frequency ω_1 using the DAZZLER (see Section 2.2.1), the detuning δ with respect to the resonance can be varied.

The measurement of the R2PI phase is based upon the superposition of two pathways whose resulting interference pattern provides access to the pathway phase difference. The photon energy of harmonic 17 is high enough to ionize helium and with the presence of the probe field, the absorption of 17$^{\text{th}}$ harmonic photons and simultaneous emission of an IR photon is possible, thus providing a transition pathway to the same final state as the R2PI involving harmonic 15. Since the 15$^{\text{th}}$ harmonic is tuned by changing the fundamental one, all of the involved photon energies will follow and the interference effect will still occur independently of the photon energy. Tuning the relative phase of IR and harmonics, the resulting delay-dependent interference pattern in the electron signal will then have the R2PI phase encoded.

As seen in Section 3.1.1, the interference pattern provides access to the phase difference of both pathways. This phase difference has three different contributions: the harmonic spectral phase difference between the neighboring harmonics, $\Delta\phi_{q,q+2}$, the atomic phase contribution from the two-photon process involving the absorption of an IR photon ϕ_a^{at}, and the two-photon atomic phase contribution associated with the emission of an IR photon, ϕ_e^{at} . With ϕ_a^{at} containing the contribution of the resonance, the other two contributions need to be determined independently to extract ϕ_a^{at}. The group delay of the attosecond pulses can be characterized by a RABITT measurement, excluding the effects of the resonant state. The additional higher harmonic orders in the experiment allow us to perform an accurate measurement of the harmonic chirp. A fit as in Figure 4.6 a) (dashed line) then allows us to assess the group delay contribution in the final state and to remove it from the phase measurement, as is shown in the transition from Figure 4.6 a) to b). The other contribution ϕ_e^{at} is not dependent on the detuning. The remaining term is the contribution resulting from the resonant term, dependent on the detuning, $\phi_a^{at}(\delta)$. To reference the interference pattern between measurements with different detunings δ, this approach requires knowledge of the absolute delay of the involved laser fields, which we do not have. We therefore perform a relative measurement where a detuning-unaffected final state, namely the next higher sideband[2], will serve as a reference for the modulation.

[2]Sideband 18 was used in all experiments with He, and sideband 16 in Ne.

This method allows us to determine the phase of R2PI via the $3p$ state in helium. The results are presented in detail in Paper **VII**. The detuning is varied by changing the laser spectrum, thus tuning the central frequency, or alternatively, by varying the probe intensity, thus shifting the atomic states.

Figure 4.7 presents a chirp-corrected measurement performed in neon, with Ne $2s^2 2p^5 (^2P_{3/2}) 4p$ as the resonant state (gray). The data in black in Figure 4.7 are the chirp-corrected harmonic phase differences measured from argon, and the gray data is from three different detunings δ. The problem, however, is that in contrast to helium, the tuning range of the laser was not sufficient to reach the other side of the resonance and to observe a significant change in the R2PI phase. Also, with a harmonic bandwidth of $\approx$ 150 meV, not only one but several states are populated by the XUV radiation. This is seen clearly from a picosecond-scan of the sideband signal (see Figure 4.8) which shows evidence of beating between two states, so-called quantum beats [111, 112]. One can see from the persistence of sideband 14 over several picoseconds that long lived states are populated. In Figure 4.8, two different detunings δ allow us to selectively populate one or two states, the latter configuration leading to the observed quantum beats which indicate a level splitting of about 14 meV. This suggests that the two populated levels are in the $2s^2 2p^5 (^2P_{3/2}) 4p$ state which shows a splitting of 14.07 meV between states of $J = 1$ and $J = 2$ [113] and lies 20.12 eV from the ground state[3].

Both detunings from Figure 4.8 are displayed with their phases in Figure 4.7. The measurement indicates that each time most of the excitation bandwidth is on low-energy side of the studied resonance. The observation of two simultaneously populated levels underlines the necessity of a higher spectral resolution for such phase-dependent R2PI-studies with closely spaced levels. Fortunately, these are requirements that can be met by using longer pulses for HHG [114]. In principle, this concept can be extended to laser pulses of arbitrary length, thus promising to be useful as a spectroscopic tool.

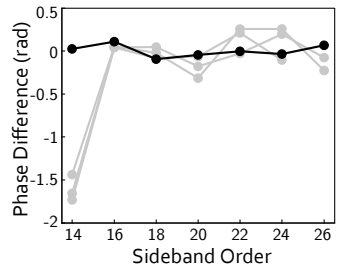

Figure 4.7. *RABITT phases measured in neon, with the difference of the reference phase from argon (triangles) and the phases from neon (circles and dashed lines) being the phase imprint of R2PI.*

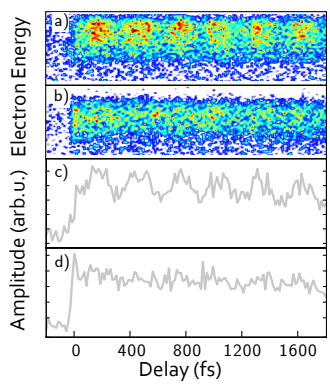

Figure 4.8. *a) Quantum beats between two levels occur at one specific tuning in the sideband signal of neon. b) At a different detuning δ, the quantum beats vanish. c) and d) show the integrated signal of a) and b), respectively.*

4.2.2 Multiple Excited States

The bandwidth of a single attosecond pulse ranges from several electron volts up to tens of electron volts. Such an SAP can then excite not only a single state but a broad and coherent superposition of states, a wave packet. Figure 4.9 illustrates the principle of the experiment in Paper **VIII** which was performed in these conditions. An optical wave packet centered at 28 eV with a bandwidth of 11 eV is used to ionize helium atoms. The attosecond

[3] This corresponds to the 13$^{\text{th}}$ harmonic at 797 nm wavelength, which we could not reach by our tuning method.

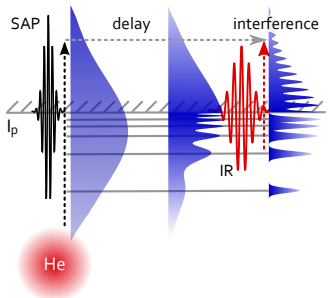

Figure 4.9. *Illustration of the experiment in Paper **VIII**. An SAP creates a superposition of bound and free states that evolve before being probed by a short IR pulse leading to interferences between bound and free fractions in the continuum electron spectrum.*

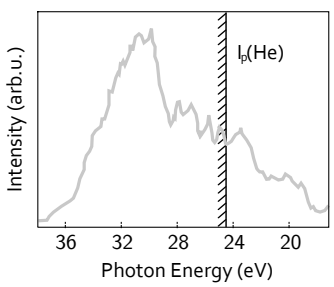

Figure 4.10. *Single attosecond pulse spectrum used in Paper **VIII**.*

pulse spectrum covers several excited states and exceeds the ionization potential, leading to the simultaneous creation of a free and a bound wave packet fraction. After a delay τ, an IR probe pulse ionizes the bound fraction of the wave packet created at $t = 0$ by the SAP, thus leading to interferences with the free portion of the wave packet. Recording the photoelectron spectra over a wide range of delays τ then allows us to fully reconstruct the bound wave packet as will be described below. Figure 4.10 shows an experimental SAP spectrum measured during the experimental campaign in Milan.

Here we explain the essence of the analysis performed in Paper **VIII** both on experimental data and on several numerical wave packets by a simple example. Let us consider a wave packet prepared with the $2p$ and $3p$ state in He and a range of continuum states ϵ, which can be written as

$$\begin{aligned}\Psi(t) &= A_{2p}(t)\Psi_{2p}e^{i(W_{2p}t/\hbar+\varphi_{3p})} + A_{3p}(t)\Psi_{3p}e^{i(W_{3p}t/\hbar+\varphi_{3p})} \\ &+ \int d\epsilon A_{\epsilon p}\Psi_{\epsilon p}e^{i(W_{\epsilon p}t/\hbar+\varphi_{\epsilon})}. \end{aligned} \tag{4.2}$$

The wave packet is characterized by the coefficients $A_i(t)e^{i\varphi_i}$ of a basis set expansion (wave function Ψ_i, energies W_i). An ideal time-resolved measurement should allow us to recover the components of the wave packet and follow their time-dependent evolution.

Let us now consider a final continuum state with energy W_f, reached by direct absorption of the attosecond pulse and by an indirect path through a population of a bound state (of energy W_i) and ionization after delay τ by the IR probe. The phase difference $\Delta\varphi$ accumulated between both pathways during τ is then given by

$$\Delta\varphi = \hbar^{-1}\left[W - W_i\right]\tau. \tag{4.3}$$

Maxima of the observed electron signal will occur at phase differences $\Delta\varphi = 0, 2\pi$ and minima at $\Delta\varphi$ equal to odd multiples of π. As a result, for any fixed W, the electron signal will be periodically modulated with the delay τ with a frequency equal to the energy difference between the final and the bound state.

For higher continuum state energies W, this frequency will be higher, leading to hyperbolic fringes as in Figure 4.11. For electrons originating from different bound states, this fringe pattern will have different modulation frequencies in the same final state. As an illustration, Figure 4.11 a) and b) show the patterns originating from our example of He $2p$ and $3p$. When several bound states are involved, the resulting interferogram consists of wavy hyperbolic-like lines as shown in Figure 4.11 c) and d). The total signal is modulated with a fixed frequency corresponding to the splitting of both initial bound states. This periodic structure is due to quantum beat interference [111, 112].

To extract the participating states, Fourier transforms of the signal $S(\tau, W)$ for a given final state energy W along the delay τ are performed

$$S'(W', W) = \mathcal{F}\left[S(\tau, W)\right] = \int d\tau S(\tau, W) e^{-iW'\tau}. \tag{4.4}$$

This allows us to identify the frequencies $W = W' - W_{2p}$, $W = W' - W_{3p}$ which are straight lines at 45° in the resulting (W', W) diagram (Figure 4.12, $W = W' - W_{2p}$ in the gray outline) as well as $W = W_{2p} - W_{3p}$, which are vertical lines and correspond to quantum beats.

We now show on this simple example with the $2p$ and $3p$ state how to recover the precise composition of the wave packet. The extraction of the time-dependent amplitudes $A_{2p}(t)$ and $A_{3p}(t)$ uses the following method: by selecting the direct-indirect interference of a particular state (as shown by the gray outline for the $2p$ state in Figure 4.12), the inverse Fourier transform $\mathcal{F}^{-1}$ allows us to return to the interferogram $S(\tau, W)$ of the $2p$ state in Figure 4.11 a) (or to Figure 4.11 b), if the other 45° line is selected). If the selected state has a lifetime shorter than the observation window, the amplitude $A_{2p}(t)$ and thus the lifetime can be extracted from the filtered interferogram by means of a shifting window function $\mathcal{G}(\tau)$ as shown in Figure 4.13. A Fourier transform $\mathcal{F}\mathcal{G}(\tau)S(\tau, W)$ as a function of delay τ will then yield a decaying Fourier amplitude $\Re\left\{\mathcal{F}\left[\mathcal{G}(\tau)S(\tau, W)\right]\right\}$ originating from the $2p$ state for all W_f. In Figure 4.13, a lifetime of 5 fs was assumed, as is seen in the amplitude plot.

The extraction of the state phases φ_i presents an additional difficulty: the knowledge of the zero timing $t = 0$ is needed. Figure 4.14 illustrates the method to determine the zero timing and therefore the phase φ_i for any given state with energy W_i. From the spectrogram of Figure 4.14 a), the Fourier transform yields the binding energies of specific states as seen above. A state with energy W_i is selected and provides the phase pattern of the spectrogram $\varphi_{det}(W, \tau)$, which is illustrated in Figure 4.14 b), where it oscillates between 0 and 2π. It can be written as

$$\varphi_{det}(W, \tau) = \varphi_i + (W_i - W)(t - t_0)/\hbar, \tag{4.5}$$

with $\tau = (t - t_0)$. Figure 4.14 c) is a phase-wrapped[4] representation of b). With W_i determined precisely by the Fourier transform, the t_0 can then be determined by differentiating

$$\frac{\partial \varphi_{det}(W, \tau)}{\partial W} = \varphi'_{det}(t - t_0), \tag{4.6}$$

[4]Meaning that once the increasing phase reaches 2π, the further increase is appended beyond 2π and so forth, leading to a phase steadily increasing with τ for a given final state.

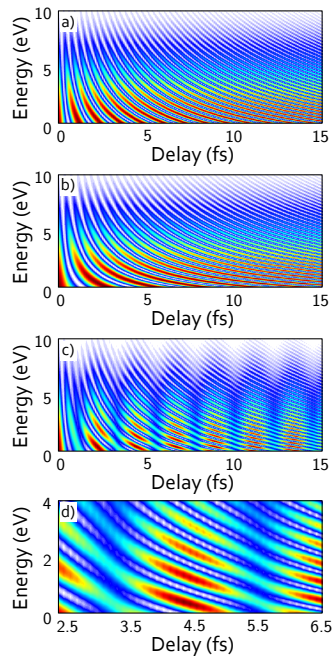

Figure 4.11. *Interference fringe patterns originating from a) the 2p state in Helium, b) the 3p state, and c) their coherent superposition. d) zoom of interference pattern from c).*

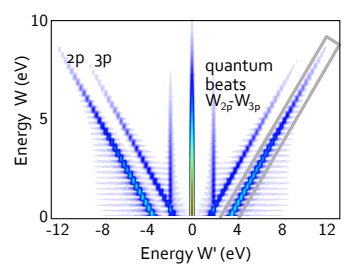

Figure 4.12. *Fourier transform of Figure 4.11 c) along the delay, converting the scale to energy W'.*

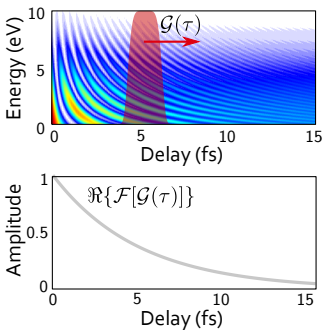

Figure 4.13. *Illustration on how the time-dependent amplitude $A_{2p}(t)$ can be extracted from an interferogram with 5 fs lifetime by shifting a short-time Fourier transform and plotting the amplitude.*

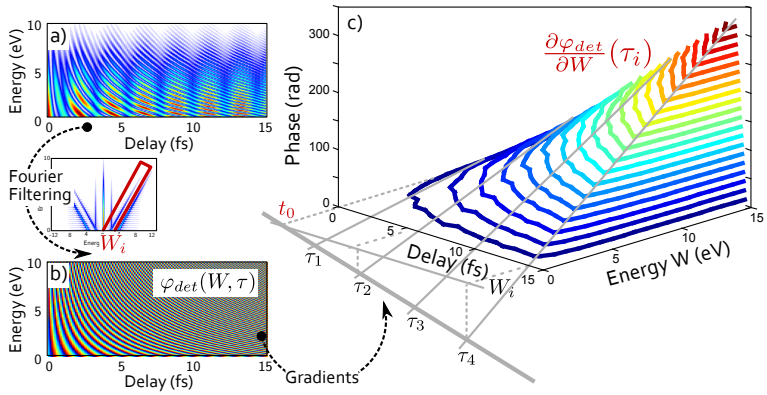

Figure 4.14. *Sketch illustrating the phase determination in Paper **VIII**. From a) the phase $\varphi_{det}(W,\tau)$ is extracted for a state i by Fourier filtering. The Fourier transform also determines the bound state energy W_i. Differentiating the phase $\partial\varphi_{det}/\partial W$ for several $\tau = t - t_0$ allows access to t_0. Thus all unknowns from Equation 4.5 have been determined.*

which yields t_0 as illustrated in Figure 4.14 c). Thus, the two unknowns in Equation 4.5, W_i and t_0, have been determined and allow us to access φ_i. By selecting a different state in the Fourier plane, this method provides access to all phases of all contributing states and works for a time-dependent phase $\varphi_i(t)$ as well.

The experiments and simulations in Paper **VIII** demonstrate the full reconstruction of arbitrary bound wave packets with short-lived states by this method. An additional focus is on the extraction of the quantum beat signal from the experiment by separating various angular components of the photoelectron momentum distributions [115, 116].

4.3 Molecular Wave Packets

Another type of wave packets evolving on short time scales are molecular wave packets. Particularly in hydrogen molecules the nuclei show dynamics on the scale of a few femtoseconds. Following the absorption of attosecond pulses, the molecular electronic ensemble evolves even faster than the molecular nuclear wave packets. Paper **IX** presents a study of nuclear wave packets in hydrogen molecules undergoing dissociative ionization after ionization by attosecond pulses (APTs and SAPs). In Paper **X**, the localization of the molecular electron cloud following photoionization of hydrogen and deuterium molecules by single attosecond pulses is studied. Both experiments study the distribution of

the ejected ions, but in different energy regions and therefore originating from different processes. Dissociation in Paper **IX** occurs with low energy ion ejection by the bond-softening process [27], while the higher ion energies studied in Paper **X** indicate different mechanisms.

4.3.1 Dissociation of H_2 by Bond-Softening

The protons in an H_2 molecule are held together by their electrons. The removal of all or a single electron may lead to the dissociation of the molecule and the ejection of two protons or one proton and a neutral hydrogen atom, respectively. There are numerous dissociation processes that can occur in the interaction of a hydrogen molecule with intense laser fields of longer wavelength or weak short-wavelength pulses [117, 118], such as *e.g.* the double excitation into an auto-ionizing state.

In Paper **IX**, a short XUV burst suddenly removes an electron from H_2 molecules as shown in Figure 4.15, leaving the molecule in an electronic excited state. The H_2^+ ion is created in a coherent superposition of vibrational states. This vibrational wave packet has a "revival" of its amplitude each time all vibrational components are in phase. After a certain delay τ, an infrared probe pulse interacts with the system, allowing transfer between the $1s\sigma_g^+$ and $2p\sigma_u^+$ state. The $2p\sigma_u^+$ state is dissociative and will relax to a H(1s) atom and a proton, as shown in Figure 4.15.

In principle, a high probe intensity or high photon energy of the second pulse could strip the system of its remaining electron. The two fragment protons would then have higher kinetic energy (highest potential curve in Figure 4.15). The main dissociation channel under investigation in Paper **IX**, however, is the process of bond-softening [27] by the IR field, which leads to $H^+ + H(1s)$, and requires lower intensities while yielding low energy fragments. For some internuclear distances, resonant single photon or multiphoton transitions from populated vibrational states to the $2p\sigma_u^+$ state are possible, leading to fragments with different kinetic energies, but with the possibility to even show energies below the energy of a single IR photon. For IR pulses shorter than the vibrational period of the molecule, the ejected proton signal will then give information on the vibrational dynamics of the molecule and the revivals of the wave packet. In addition, the presence of the infrared field modifies the potential curves to allow transitions for different internuclear separations than the ones shown in Figure 4.15. The imprint of the vibrational wave packet on the ion signal is lost however when using infrared pulses longer or comparably long to the vibrational period of the hydrogen molecule. In Paper **IX**, two experiments with different pulse lengths are performed. In one case, an APT generated in Lund and probed with IR pulses of 35 fs duration is used to excite

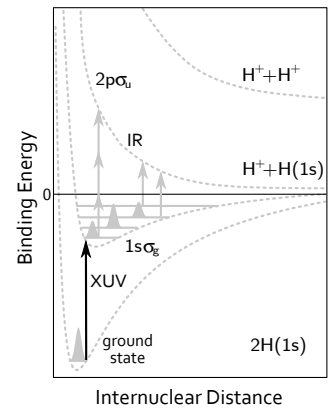

Figure 4.15. *Sketch of the potential situation in Paper **IX**. Adapted from [119]. An XUV pulse forms a vibrational wave packet in an excited state that can then be transferred to higher dissociative states by an IR pulse at certain internuclear distances.*

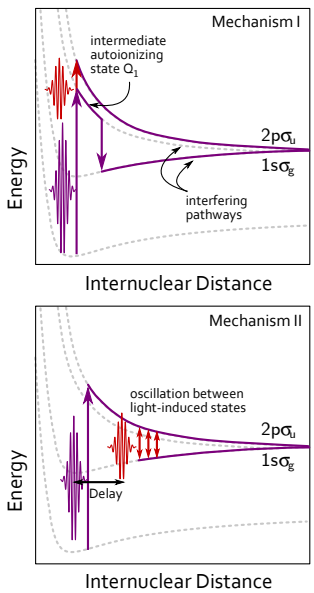

Figure 4.16. *Sketch of the two mechanisms responsible for asymmetry in the ion distribution in Paper* ***X****. Mechanism I occurs in the overlap of the SAP with the IR and Mechanism II with both pulses separated by a delay. In both cases, attosecond oscillations of the ion ejection asymmetry are measured at high ion kinetic energies.*

and dissociate the hydrogen molecules. It is found that the energy of the ejected ions is dependent on the delay between APT and IR, but no vibrational dynamics can be resolved. These results are compared with an experiment performed using an SAP and a 7 fs probe in Milan. There, the vibrational dynamics of the molecule can be resolved and the populated vibrational states uncovered by a Fourier transform. Paper **IX** shows the influence of the pulse duration (in particular of the probe pulse) for unraveling the molecular dissociative dynamics in a two-color pump-probe experiment.

4.3.2 Asymmetry and Localization

Paper **X** studies the dissociation of hydrogen (and its heavier isotope deuterium for experimental reasons) by recording the ionic fragments released from the interaction with a single attosecond pulse and a few-cycle infrared pulse. The difference from Paper **IX** is the considered energy range of the ejected ions and the particular focus on the role played by the electron wave packet on the molecular ion before dissociation. The experiments were performed in Milan with SAPs and a 7 fs IR probe field.

In principle, for an ensemble of randomly oriented molecules, the electron can remain with each individual nucleus after dissociation. Since the interaction is dependent on the laser polarization, molecules with a favorably aligned molecular axis contribute the most. The resulting distribution of ejected H^+ ions should then be symmetric with respect to the laser polarization. An asymmetry in the H^+ ion distribution hints toward a mechanism of localizing the electron on a specific nucleus. There are several mechanisms that allow this symmetry breaking in dissociation to occur.

In Paper **X**, localization of the remaining electron on either of the H-atoms is observed over a large range of delays and fragment energies. It is interpreted by two different mechanisms which are illustrated in Figure 4.16. The first mechanism occurs when the exciting attosecond pulse and the infrared probe pulse overlap. Without the IR, the dissociation of H_2 is the result of populating the $2p\sigma_u^+$ by absorption of an XUV photon, accompanied by the emission of an s-electron. With the addition of the IR, the absorption and emission of several photons allows access to a number of higher ℓ-states. It is then possible that a dissociative wave packet forms in the $1s\sigma_g$ state through the involvement of an autoionizing state $Q_1\,{}^1\Sigma_u^+(1)$, which is accompanied by the emission of a p-electron. This pathway will then interfere with the pathway of s-electron emission. The dissociation by either pathway will then become indistinguishable in the final state, leading to interference and localization, that depends on the relative phase/delay of the SAP and IR. Because this modification of the

continuum wave function is only possible when both pulses overlap, this mechanism does not explain the observed asymmetries at large delays.

The second mechanism does not require the overlap of both pulses. Instead, viewing the delayed IR probe pulse as a static field, it induces quasi-states in the two-level-system of $1s\sigma_g/2p\sigma_u$. These quasi-states resemble localized states between which the electron wave function oscillates during the presence of the IR. Toward the end of the dissociation the molecule is stretched to a degree prohibiting further jumps of the electron and the system remains in one of these states. How many oscillations between both states are possible is therefore dependent on the delay of the IR with respect to the attosecond pulse that initiates the dissociation dynamics. In a way, this is similar to [120], where the temporally localized start of the dissociation process is determined by the electric field maximum and not an attosecond pulse.

Both mechanisms are described in greater detail and with supporting calculations in Paper **X**, demonstrating that attosecond pulses are useful in the study of molecular processes in a pump-probe scheme.

CHAPTER 5

SUMMARY AND OUTLOOK

This thesis presented detailed characterization methods for both attosecond pulses and attosecond wave packets. A study of the properties of the generation medium in high-order harmonic generation and its influence on the shape of the produced attosecond pulses was performed in Paper **I**. Tunability in the generation of attosecond pulses was demonstrated in Paper **II** by using the second harmonic of the fundamental field as a control field. Paper **III** dealt with the generation of attosecond pulses at higher photon energies, greater bandwidths and how these pulses could still be shaped by appropriate filtering techniques. A novel *in-situ* scheme for the characterization of attosecond pulses was introduced in Paper **IV** and Paper **V** studied the probe intensity dependence of the established RABITT method.

A large fraction of the work in this thesis was also devoted to the application of attosecond pulses in various systems. In Paper **VI**, the scattering of free electron wave packets on their original ion was imaged by a novel technique that uses attosecond pulse trains with one pulse per probe field cycle. The work of Paper **VII** allowed us to measure the phase of a resonant two-photon ionization process and to assess the behavior of an excited state dressed by an external laser field. The technique presented in Paper **VIII** aims at a complete characterization of bound wave packets in Helium. The final two Papers, **IX** and **X**, demonstrate how attosecond pulses provide a useful tool in the study of molecular systems. Paper **IX** tested the influence of different infrared pulse shapes on the dissociation dynamics of hydrogen molecules by a mechanism called bond-softening and found few-cycle pulses necessary to resolve the vibrational dynamics in this molecule. Finally, Paper **X** is one of the first time-resolved studies of electron localization and dynamics on attosecond timescales in a molecular system.

The field of attosecond science has undergone a rapid expan-

sion since the year 2006 in which this thesis work began. Significant progress has been seen in the generation of the shortest light pulses, their detection and their use in interactions with matter. These pulses have been applied to novel systems of increasing degrees of complexity. Attosecond sources have seen the breakthrough of the generation of single attosecond pulses in several labs around the world. Currently, single attosecond pulses can be generated by various methods with durations down to 80 as [93]. The use of multicycle generation pulses [46] demonstrated that few-cycle pulses are no longer an absolute requirement. The conditions in which single attosecond pulse emission can occur have also been relaxed by the use of two-color fields [121] or pulses with controlled polarization state [59, 92, 122]. In this thesis, single attosecond pulses were used in the experiments of Papers **VIII**-**X**. The use of several light fields of different wavelength allows to steer harmonic generation [21, 48, 50], a technique that has found wide application and was also employed in Papers **II**,**IV** and **VI**.

At the same time, attosecond pulses need not be generated from gases alone. Alternative sources with unique properties have appeared which also hold the potential to extend the capabilities of attosecond experiments. Free electron lasers, both in the VUV to XUV regime at FLASH in Hamburg and the hard X-ray regime at the LCLS in Stanford have become available for experiments [110, 123, 124]. These sources overlap with the field of attosecond science providing pulses many times more intense and at shorter wavelengths. Yet a drawback remains in the huge technological and experimental efforts required for the construction and maintenance of such machines. High-order harmonic generation from gases was shown to be a viable way to improve the performance of free electron lasers [125]. If used as a seeding pulse to modulate the electron energy distribution inside an undulator, harmonics can be used to improve both the coherence and the temporal properties of the radiation produced by free electron lasers. In addition to sources based on classical accelerator technology, the generation of harmonics from plasmas has also seen great progress [126, 127]. It is now possible to characterize their temporal structure [128], a requirement for the use in time-resolved experiments. This allows the use of some of the advantages of this harmonic generation scheme in experimental arrangements that do not necessarily need high repetition rates or that require higher photon energies. Despite their potential as a future attosecond source, the advantages of attosecond pulse generation in gases, such as high repetition rate, good coherence properties and the requirement of smaller laser systems will ensure the continued usefulness of gas harmonics in the future.

Experiments with attosecond pulses have improved in several ways: the two classic ultrafast methods of autocorrelation [129]

and FROG [92, 93, 100] have been successfully and routinely applied in the attosecond domain and were also used for the characterization of attosecond pulses in Paper **VIII**. Novel methods to directly study the harmonic generation process have been developed [26] and used in Paper **IV**. The gold-standard of attosecond pulse train characterization, the RABITT method, has been studied in further detail in Paper **V**, which tested its behavior in stronger probe fields.

Attosecond experiments in general have also benefited greatly from upgrades in the electron detection equipment. The use of momentum imaging techniques [68] provides additional information, a fact which was extensively used in Paper **VIII**, where it was used to resolve different angular momentum channels in the photoelectron distributions. In addition, almost all other applications of attosecond pulses in this thesis made use of a VMIS, as seen in Papers **II**, **VI**, **IX**, and **X**. As a parallel development, using these techniques in combination with coincidence detection allows a full reconstruction of the participating particle distribution in both time and space [130, 131].

The applications of attosecond pulses are beginning to leave the domain of proof-of-principle experiments as many experimental arrangements have now been demonstrated. This includes the first experiment with a solid-state sample [132] or the direct probing of atomic wave functions [133] during the HHG process. Beyond the characterization of free electrons, bound wave packets attract increasing interest [75, 134]. This is also reflected in the experiments of Papers **VII** and **VIII**, both of which aim at bound states. In the first case, the behavior of a single state is studied, whereas the second experiment allows the full characterization of a nontrivial superposition of states.

Finally, experiments with molecules have attracted a lot of interest. Many of these techniques are based on using the physics of harmonic generation itself [135, 136]. The demonstration of coherent control techniques in the attosecond emission from molecules [83] and the successful demonstration of molecular orbital tomography [137] from aligned molecules indicate that the field is evolving toward attosecond molecular science. In this domain, the control of electron localization in molecular dissociation [120] preceded the molecular attosecond pump-probe experiment shown in Paper **X**.

These studies promise a window to a better understanding of the behavior of electrons inside molecules. Especially the application to electron dynamics inside biomolecules is both promising and not yet realized. In a similar manner, the understanding of electron dynamics within solids and nanostructures generates great interest as smaller structure sizes tend to exhibit greater influence of the wave properties of electrons. At the same time, an inquiry into the origins of the atomic phase is required to better

understand the ionization processes that are at the heart of many attosecond techniques. Additional progress in attosecond science promises to come from improved attosecond sources, such as arbitrarily shaped pulse trains and attosecond wave forms. Also, the synthesis of arbitrary generation fields from several colors should allow full control of electrons during the harmonic generation process. A final challenge to the improvement of attosecond sources is the production of intense attosecond pulses. These would allow the study of nonlinear effects, from which experiments can greatly benefit by improved temporal resolution and better signal-to-noise ratios.

Comments on the Papers

I **Macroscopic effects in attosecond pulse generation**
This paper studies the influence of phase matching on the attosecond pulse shape. It is found both from an analytical model and experiments that macroscopic effects can contribute to the compression of attosecond pulses. I took part in the experiments and contributed to the manuscript.

II **Spectral shaping of attosecond pulses using two-color laser fields**
Tunable attosecond pulse trains are generated from a two-color laser field, consisting of a fundamental field and its second harmonic. Dependent on the relative phase of both fields, the central photon energy from the short trajectory can be adjusted. I contributed to the experiments and to the preparation of the manuscript.

III **Broadband attosecond pulse shaping**
This paper extends the thin-foil-filtering technique developed in Lund to harmonics generated in Ne, demonstrating an APT with an average pulse duration of 130 as by filtering with Zr. A comparison of several filter materials is also performed. This was the first campaign I contributed to after my arrival. I participated in the experiments and helped in the preparation of the manuscript, particularly the assessment of pulse-to-pulse variations.

IV **Atomic and macroscopic measurements of attosecond pulse trains**
Using HHG with a weak second harmonic field, the validity of the novel *in-situ* method is assessed and verified by RABITT measurements. The paper also demonstrates that this method can be used to measure the single atom response in HHG. I contributed to the experiments and the preparation of the manuscript.

V **Intensity Dependence of Laser-Assisted Attosecond Photoionization Spectra**
In this paper, we study the limitations of the RABITT method at high probe field strengths. An extension to the method is proposed, based on higher-order perturbation theory. I was responsible for the experiments, the data analysis and the writing of the manuscript.

VI **Coherent electron scattering captured by an attosecond quantum stroboscope**
We create EWPs by ionization with an APT and then use a strong IR field to drive them back to the atomic potential, where we observe rescattering in the measured electron momentum distributions. I contributed to the experiments, the data analysis and to the manuscript preparation with focus on the figures.

VII **Phase Measurement of Resonant Two-Photon Ionization in Helium**
We use an APT to study phase-resolved resonantly-enhanced two-photon ionization of He. In addition, we study the behavior of an excited state in a dressing laser field. I played a major role in the experimental work, did most of the data analysis and wrote the manuscript.

VIII **Attosecond pump-probe electron interferometry**
In this paper, we use a single attosecond pulse to study a wave packet comprising several bound states. We demonstrate that it is possible to fully characterize unknown wave packets in both amplitude and phase by an interferometric method. I took part in the experiments in Milan and the preparation of the manuscript.

IX **Ionization and Wave-Packet Dynamics Studied Using Two-Color XUV and IR Pump-Probe Spectroscopy**
We study the ultrafast wave packet dynamics leading to the dissociation of hydrogen molecules after their excitation by attosecond pulses and probing with an IR pulse. We also present a comparison of excitation with an APT versus an SAP. I took part in the experiment in Milan and contributed to the manuscript by giving feedback.

X **Electron Localization following Attosecond Molecular Photoionization**
This paper presents the first example of a molecular attosecond pump-probe experiment. An electron localization on an attosecond timescale is measured by an asymmetry in momentum distribution of ions ejected from hydrogen dissociation. I contributed to the experiment in Milan and gave feedback on the manuscript.

Acknowledgments

The completion of this work would not have been possible without the support and help of many people. Not only is experimental physics a very team-oriented effort, but it has also been great to know that I was not in alone facing challenges of any kind.

First and foremost I would like to thank my supervisor, Anne L'Huillier, who has been tremendously inspiring to work with, both in her unfaltering and contagious enthusiasm for physics and in her ability to see the best in everyone. My co-supervisor, Sverker Werin, has been an example with his sympathetically unpretentious lectures and provided a great source of checks and balances during my years in Lund. The head of the Atomic Physics division, Claes-Göran Wahlström, taught me to appreciate the northern Swedish accent and that burning windows can be "one way to learn". His predecessor, Sune Svanberg, with his very physical "full-contact" style of teaching and many unique presentations has been a source of inspiration. They both have shaped the division to become such a great place that I will sorely miss working here.

The attosecond physics group, both past and current members, has always been something to look forward to after vacations. Johan Mauritsson is the best at "making up numbers in his computer" and has at least quadrupled my knowledge of wine. Per Johnsson is always worth to hang around in the lab and at defense parties. Thomas Fordell is the epitome of Finnish cool, blessed with seemingly infinite patience to tickle the laser. Kathrin Klünder was great to share the office with and warned me when I caught the Saxonian flu again. Marcus Dahlström is a bit like Woody Allen, only much funnier. Erik Mansten will drive anything that floats and engineer a "gas-puff" to go with it. Miguel Miranda, the fastest Portuguese around and second half of the laser dream team. Xinkui He is always fun to discuss with, physics or - especially - not. Rafał Rakowski taught me everything I know about the Polish army. Christian Erny shares an interest in business and a passion for boardgames. Eleonora Lorek teaches Swedish to Germans. Mathieu Gisselbrecht is dan-

gerously interesting to talk to, usually whenever you hit a productive spot. Elena Mengotti was always ”mega-jolie”. Thierry Ruchon will get anyone to laugh and has a unique taste in music in the lab. Thomas Remetter is *totalie* serious all the time, seriously. Anders Persson is the laser-whisperer. Emilie Pourtal has always had a mood like noon in the Sahara.

The MAXLAS project has succeeded in providing me with good friends in related fields of science and has been paying my bills for three years, for which I am grateful to the European Union. Guillaume Genoud was a great work-bro and knew from the start that Obama would win. Nino Čutić introduced me to several digital vices and the best comedians I know. Jörg Schwenke has a surprisingly deep knowledge of many rabbit-holes (like SpOn) and endured me during the worst part of this thesis. Jens Uhlig is ready for everything, even sharing a flat with me. Ralf Nüske knows how to ask the right questions and has Wikipedia in his pocket.

I am grateful to Minna Ramkull for the division excursions, the paintings in the coffee room and her endless patience with wrongly filled-in Tur-och-Retur forms. Bertil Hermansson fulfilled exotic PC requests and never forgot to remind me of the Knake-session. I also greatly appreciate the administrative support and number-crunching of Henrik Steen and Harriett Lindahl.

I am also glad to have met all the other great people at Atomic Physics, and not just in the coffee room. I would also like to thank our many collaborators, especially Ken Schafer, whose theoretical support and ideas are found in almost every paper in this thesis. Many of the experiments have been performed in European collaborations. Those whom I would like to thank especially are Philippe Balcou and Rodrigo López-Martens from the LOA Paris, from whom I learned the pressure limits in the MBES.

The largest such campaign was surely was the Milano-collaboration, which was responsible for three papers within this thesis. In Milan, Giuseppe Sansone and Enrico Benedetti sacrificed many of their nights for several months measuring with us, and when they were busy, Mauro Nisoli came to our aid. I would also like to especially thank Marc Vrakking from AMOLF Amsterdam, whose enthusiasm and persistence in the hydrogen experiments led to their extremely successful conclusion. Freek Kelkensberg was always up for interesting discussions and relentlessly worked on manuscripts during the weekends. I would like to thank Matthias Kling for taking the time to share his VMI-wisdom with me and for being available on Skype at 2am. The campaign would also never have been as successful as it was without the help of all the other people I had the pleasure to work with: Federico Ferrari, Wing-Kiu Siu, Thorsten Uphues, Sergey

Zherebtsov and Franck Lépine.

I am also glad to have had the support of many good friends, Mathias Forkmann, Gregor Thoss, Steffen Hahn, Daniel Wollmann, Uli Walker, Br. Viktor Voss, Joe Sasse as well as Stefan Häßler and Sabrina Guillard, who made giving a seminar in Saclay so much more fun.

Zuguterletzt möchte ich meiner Familie danken, meinen Eltern, die mich unablässig unterstützt und sehr geduldig auf meine Anrufe gewartet haben, meinen Brüdern Falk und Jan, sowie Birgit, Sören und Renate mit den Zwillingen, und dem ganzen Clan.
Und schließlich ganz besonders Dir, meiner liebsten Christiane,
Dein M.

REFERENCES

1. Edit by Richard Bartz Michael Maggs. Datei:Bouncing ball strobe edit.jpg (2007). URL http://upload.wikimedia.org/wikipedia/commons/3/3c/Bouncing_ball_strobe_edit.jpg. [Online; accessed 14-January-2010].

2. M. Ferray, A. L'Huillier, X. F. Li, G. Mainfray and C. Manus. *Multiple-harmonic conversion of 1064 nm radiation in rare gases*. J. Phys. B **21**, L31 (1988).

3. A. McPherson, G. Gibson, H. Jara, U. Johann, T. S. Luk, I. A. McIntyre, K. Boyer and C. K. Rhodes. *Studies of multiphoton production of vacuum-ultraviolet radiation in the rare gases*. J. Opt. Soc. Am. B **4**, 595 (1987).

4. K. C. Kulander, K. J. Schafer and J. L. Krause. *Dynamics of short-pulse excitation, ionization and harmonic conversion*. In *Super-Intense Laser-Atom Physics*. Plenum Press, New York (1993).

5. K. J. Schafer, B. Yang, L. F. DiMauro and K. C. Kulander. *Above threshold ionization beyond the high harmonic cutoff*. Phys. Rev. Lett. **70**, 1599 (1993).

6. P. B. Corkum. *Plasma perspective on strong-field multiphoton ionization*. Phys. Rev. Lett. **71**, 1994 (1993).

7. M. Lewenstein, K. C. Kulander, K. J. Schafer and P. H. Bucksbaum. *Rings in above-threshold ionization: A quasiclassical analysis*. Phys. Rev. A **51**, 1495 (1995).

8. H. Merdji, P. Salieres, L. Le Deroff, J. F. Hergott, B. Carre, D. Joyeux, D. Descamps, J. Norin, C. Lynga, A. L'Huillier, C. G. Wahlstrom, M. Bellini and S. Huller. *Coherence properties of high-order harmonics: Application to high-density laser-plasma diagnostic*. Laser Part. Beams **18**, 495 (2000).

9. G. Farkas and C. Tóth. *Proposal for attosecond light pulse generation using laser induced multiple-harmonic conversion processes in rare gases*. Phys. Lett. A **168**, 447 (1992).

10. S. E. Harris, J. J. Macklin and T. W. Hänsch. *Atomic scale temporal structure inherent to high-order harmonic generation*. Opt. Commun. **100**, 487 (1993).

11. P. B. Corkum, N. H. Burnett and M. Y. Ivanov. *Subfemtosecond pulses*. Opt. Lett. **19**, 1870 (1994).

12. M. Ivanov, P. B. Corkum, T. Zuo and A. Bandrauk. *Routes to control of intense-field atomic polarizability*. Phys. Rev. Lett. **74**, 2933 (1995).

13. Ph. Antoine, A. L'Huillier and M. Lewenstein. *Attosecond Pulse Trains Using High-Order Harmonics*. Phys. Rev. Lett. **77**, 1234 (1996).

14. V. Véniard, R. Taïeb and A. Maquet. *Phase dependence of (N+1) - color (N>1) ir-uv photoionization of atoms with higher harmonics*. Phys. Rev. A **54**, 721 (1996).

15. P. M. Paul, E. S. Toma, P. Breger, G. Mullot, F. Augé, Ph. Balcou, H. G. Muller and P. Agostini. *Observation of a train of tttosecond pulses from high harmonic generation*. Science **292**, 1689 (2001).

16. M. Hentschel, R. Kienberger, Ch. Spielmann, G. A. Reider, N. Milosevic, T. Brabec, P. Corkum, U. Heinzmannß, M. Drescher and F. Krausz. *Attosecond metrology*. Nature **414**, 509 (2001).

17. R. López-Martens, J. Mauritsson, P. Johnsson, K. Varju, A. L'Huillier, W. Kornelis, J. Biegert, U. Keller, M. Gaarde and K. Schafer. *Characterization of high-order harmonic radiation on femtosecond and attosecond time scales*. Appl. Phys. B **78**, 835–840 (2004).

18. Stefan Haessler and Marko Swoboda. *Optimization and Application of High-order Harmonics of an Ultrashort Terawatt Laser*. Lund Reports on Atomic Physics **324** (2004).

19. A. Zaïr, O. Tcherbakoff, E. Mével, E. Constant, R. López-Martens, J. Mauritsson, P. Johnsson and A. L'Huillier. *Time-resolved measurements of high order harmonics confined by polarization gating*. Appl. Phys. B **78**, 869 (2004).

20. R. López-Martens, J. Mauritsson, P. Johnsson, A. L'Huillier, O. Tcherbakoff, A. Zair, E. Mevel and E. Constant. *Time-resolved ellipticity gating of high-order harmonic emission*. Phys. Rev. A **69**, 053811 (2004).

21. J. Mauritsson, P. Johnsson, E. Gustafsson, A. L'Huillier, K. J. Schafer and M. B. Gaarde. *Attosecond Pulse Trains Generated Using Two Color Laser Fields*. Phys. Rev. Lett. **97**, 013001 (2006).

22. R. López-Martens, K. Varjú, P. Johnsson, J. Mauritsson, Y. Mairesse, P. Salières, M. B. Gaarde, K. J. Schafer, A. Persson, S. Svanberg, C.-G. Wahlström and A. L'Huillier. *Amplitude and phase control of attosecond light pulses*. Phys. Rev. Lett. **94**, 033001 (2005).

23. K. Varjú, Y. Mairesse, P. Agostini, P. Breger, B. Carré, L. J. Frasinski, E. Gustafsson, P. Johnsson, J. Mauritsson, H. Merdji, P. Monchicourt, A. L'Huillier and P. Salières. *Reconstruction of Attosecond Pulse Trains Using an Adiabatic Phase Expansion*. Phys. Rev. Lett. **95**, 243901 (2005).

24. P. Johnsson, R. López-Martens, S. Kazamias, J. Mauritsson, C. Valentin, T. Remetter, K. Varjú, M. B. Gaarde, Y. Mairesse, H. Wabnitz, P. Salières, Ph. Balcou, K. J. Schafer and A. L'Huillier. *Attosecond Electron Wave Packet Dynamics in Strong Laser Fields*. Phys. Rev. Lett. **95**, 013001 (2005).

25. T. Remetter, P. Johnsson, J. Mauritsson, K. Varjú, Y. Ni, F. Lépine, E. Gustafsson, M. Kling, J. Khan, R. López-Martens, K. J. Schafer, M. J. J. Vrakking and A. L'Huillier. *Attosecond Electron Wave Packet Interferometry*. Nature Phys. **2**, 323 (2006).

26. N. Dudovich, O. Smirnova, J. Levesque, Y. Mairesse, M. Yu. Ivanov, D. M. Villeneuve and P. B. Corkum. *Measuring and controlling the birth of attosecond XUV pulses*. Nature Physics **2**, 781 (2006).

27. P. H. Bucksbaum, A. Zavriyev, H. G. Muller and D. W. Schumacher. *Softening of the H2+ molecular bond in intense laser fields*. Phys. Rev. Lett. **64**, 1883–1886 (1990).

28. B. H. Bransden and C. J. Joachain. *Physics of Atoms and Molecules*. Prentice Hall (2003).

29. T. W. B. Kibble. *Mutual Refraction of Electrons and Photons*. Phys. Rev. **150**, 1060 (1966).

30. P. H. Bucksbaum, R. R. Freeman, M. Bashkansky and T. J. McIlrath. *Role of the ponderomotive potential in above-threshold ionization*. J. Opt. Soc. Am. B **4**, 760 (1987).

31. K Burnett, VC Reed and PL Knight. *Atoms in Ultra-Intense Laser Fields*. J. Phys. B **26**, 561–598 (1993).

32. Xinkui He, M. Miranda, J. Schwenke, O. Guilbaud, T. Ruchon, C. Heyl, E. Georgadiou, R. Rakowski, A. Persson, M. B. Gaarde and A. L'Huillier. *Spatial and spectral properties of the high-order harmonic emission in argon for seeding applications*. Phys. Rev. A **79**, 063829 (2009).

33. J. Mauritsson, P. Johnsson, R. López-Martens, K. Varjú, W. Kornelis, J. Biegert, U. Keller, M. B. Gaarde, K. J. Schafer and A. L'Huillier. *Measurement and control of the frequency chirp rate of high-order harmonic pulses*. Phys. Rev. A **70**, R021801 (2004).

34. K. Varju, Y. Mairesse, B. Carre, M. B. Gaarde, P. Johnsson, S. Kazamias, R. Lopez-Martens, J. Mauritsson, K. J. Schafer, Ph. Balcou, A. L'huillier and P. Saliéres. *Frequency chirp of harmonic and attosecond pulses*. J. Mod. Opt. **52**, 379 (2005).

35. C. Delfin, C. Altucci, F. De Filippo, C. de Lisio, M. B. Gaarde, A. L'Huillier, L. Roos and C. G. Wahlstrom. *Influence of the medium length on high-order harmonic generation*. J. Phys. B **32**, 5397–5409 (1999).

36. L. Roos, E. Constant, E. Mevel, Ph. Balcou, D. Descamps, M. B. Gaarde, A. Valette, R. Haroutounian and A. L´Huillier. *Controlling phase-matching of high-order harmonic generation by manipulating the fundamental field*. Phys. Rev. A **60**, 5010 (1999).

37. E. Constant, D. Garzella, P. Breger, E. Mével, Ch. Dorrer, C. Le Blanc, F. Salin and P. Agostini. *Optimizing High Harmonic Generation in Absorbing Gases: Model and Experiment*. Phys. Rev. Lett. **82**, 1668 (1999).

38. C.P. Hauri, W. Kornelis, F.W. Helbing, A. Heinrich, A. Couairon, A. Mysyrowicz, J. Biegert and U. Keller. *Generation of intense, carrier-envelope phase-locked few-cycle laser pulses through filamentation*. Appl. Phys. B **79**, 673 (2004).

39. O. Svelto. *Principles of Lasers*. Plenum Press, New York (1998).

40. R. W. Boyd. *Nonlinear Optics*. Academic Press (2003).

41. R. Kienberger, E. Goulielmakis, M. Uiberacker, A. Baltuška, V. Yakovlev, F. Bammer, A. Scrinzi, Th. Westerwalbesloh, U. Kleineberg, U. Heinzmann, M. Drescher and F. Krausz. *Atomic transient recorder*. Nature **427**, 817 (2004).

42. A. Wonisch, Th. Westerwalbesloh, W. Hachmann, N. Kabachnik, U. Kleineberg and U. Heinzmann. *Aperiodic nanometer multilayer systems as optical key components for attosecond electron spectroscopy*. Thin Solid Films **464-465**, 473–477 (2004).

43. A.-S. Morlens, R. López-Martens, O. Boyko, Ph. Zeitoun, Ph. Balcou, K. Varjú, E. Gustafsson, T. Remetter, A. L'Huillier, S. Kazamias, J. Gautier, F. Delmotte and M.-F. Ravet. *Design and characterization of extreme-ultraviolet broadband mirrors for attosecond science*. Opt. Lett. **31**, 1558 (2006).

44. E. Gustafsson, T. Ruchon, M. Swoboda, R. López Martens, Ph. Balcou and A. L'huillier. *Broadband attosecond pulse shaping*. Opt. Lett. **32**, 1353–1355 (2007).

45. Kyung Taec Kim, Kyung Sik Kang, Mi Na Park, Tayyab Imran, G. Umesh and Chang Hee Nam. *Self-Compression of Attosecond High-Order Harmonic Pulses*. Physical Review Letters **99**, 223904 (2007).

46. P. Tzallas, E. Skantzakis, C. Kalpouzos, E. P. Benis, G. D. Tsakiris and D. Charalambidis. *Generation of intense continuum extreme-ultraviolet radiation by many-cycle laser fields*. Nature Physics **3**, 846 (2007).

47. M. D. Perry and J. K. Crane. *High-order harmonic emission from mixed fields*. Phys. Rev. A **48** (1993).

48. E. Goulielmakis, V. S. Yakovlev, A. L. Cavalieri, M. Uiberacker, V. Pervak, A. Apolonski, R. Kienberger, U. Kleineberg and F. Krausz. *Attosecond Control and Measurement: Lightwave Electronics*. Science **317**, 769–775 (2007).

49. H. Merdji, T. Auguste, W. Boutu, J. P. Caumes, B. Carré, T. Pfeifer, A. Jullien, D. M. Neumark and S. R. Leone. *Isolated attosecond pulses using a detuned second-harmonic field*. Opt. Lett. **32**, 3134 (2007).

50. C. Vozzi, F. Calegari, F. Frassetto, L. Poletto, G. Sansone, P. Villoresi, M. Nisoli, S. De Silvestri and S. Stagira. *Coherent continuum generation above 100 eV driven by an ir parametric source in a two-color scheme*. Phys. Rev. A **79**, 033842 (2009).

51. L. E. Chipperfield, J. S. Robinson, J. W. G. Tisch and J. P. Marangos. *Ideal waveform to generate the maximum possible electron recollision energy for any given oscillation period*. Phys. Rev. Lett. **102**, 063003 (2009).

52. Weiyi Hong, Qingbin Zhang, Zhenyu Yang and Peixiang Lu. *Electron dynamic control for the quantum path in the midinfrared regime using a weak near-infrared pulse*. Physical Review A (Atomic, Molecular, and Optical Physics) **80**, 053407 (2009).

53. Rui-Feng Lu, Hai-Xiang He, Ya-Hui Guo and Ke-Li Han. *Theoretical study of single attosecond pulse generation with a three-colour laser field*. J. Phys. B **42**, 225601 (5pp) (2009).

54. U. Andiel, G. D. Tsakiris, E. Cormier and K. Witte. *High-order harmonic amplitude modulation in two-colour phase-controlled frequency mixing*. Europhys. Lett. **47**, 42 (1999).

55. I.P. Christov, M.M. Murnane and H.C. Kapteyn. *High-harmonic generation of attosecond pulses in the single cycle regime*. Phys. Rev. Lett. **78**, 1251 (1997).

56. C. Altucci, C. Delfin, L. Roos, M. Gaarde, A. L'Huillier, I. Mercer, T. Straczewski and C.-G. Wahlström. *Frequency-resolved time-gated high-order harmonics*. Phys. Rev. A **58**, 3934 (1998).

57. A. Baltuška, Th. Udem†, M. Uiberacker, M. Hentschel, E. Goulielmakis, Ch. Gohle†, R. Holzwarth†, V. S. Yakovlev, A. Scrinzi, T. W. Hänsch and F. Krausz. *Attosecond control of electronic processes by intense light fields*. Nature **421**, 611 (2003).

58. M. Kovacev, Y. Mariesse, E. Priori, H. Merdji, O. Tcherbakoff, P. Monchieourt, P. Breger, E. Mevel, E. Constant, P. Salieres, B. Carre and P. Agostini. *Temporal confinement of harmonic emission by polarization gating*. Eur. Phys. J. D **26**, 79 (2003).

59. I. J. Sola, E. Mével, L. Elouga, E. Constant, V. Strelkov, L. Poletto, P. Villoresi, E. Benedetti, J.-P. Caumes, S. Stagira, C. Vozzi, G. Sansone and M. Nisoli. *Controlling attosecond electron dynamics by phase-stabilized polarization gating*. Nature Physics **2**, 319 (2006).

60. L. Xu, Ch. Spielmann, A. Poppe, T. Brabec, F. Krausz and T. W. Hänsch. *Route to phase control of ultrashort light pulses*. Opt. Lett. **21**, 2008 (1996).

61. Th. Udem, R. Holzwarth and T. W. Hänsch. *Optical frequency metrology*. Nature **416**, 233 (2002).

62. D. J. Jones, S. A. Diddams, J. K. Ranka, A. Stentz, R. S. Windeler, J. L. Hall and S. T. Cundiff. *Carrier-envelope phase control of femtosecond mode-locked lasers and direct optical frequency synthesis*. Science **288**, 635 (2000).

63. A. Apolonski, A. Poppe, G. Tempea, Ch. Spielmann, Th. Udem, R. Holzwarth, T. W. Hänsch and F. Krausz. *Controlling the phase evolution of few-cycle light pulses*. Phys. Rev. Lett. **85**, 740 (2000).

64. R. Szipöcs, K. Ferencz, Ch. Spielmann and F. Krausz. *Chirped multilayer coatings for broadband dispersion control in femtosecond lasers*. Opt. Lett. **19**, 201 (1994).

65. R. Szipöcs and A. Köházi-Kis. *Theory and design of chirped dielectric laser mirrors*. Appl. Phys. B **65**, 115 (1997).

66. Takao Fuji, Jens Rauschenberger, Alexander Apolonski, Vladislav S. Yakovlev, Gabriel Tempea, Thomas Udem, Christoph Gohle, Theodor W. Hänsch, Walter Lehnert, Michael Scherer and Ferenc Krausz. *Monolithic carrier-envelope phase-stabilization scheme*. Opt. Lett. **30**, 332–334 (2005).

67. T. Fordell, M. Miranda, A. Persson and A. L'Huillier. *Carrier-envelope phase stabilization of a multi-millijoule, regenerative-amplifier-based chirped-pulse smplifier system*. Opt. Express **17**, 21091–21097 (2009).

68. A. T. J. B. Eppink and D. H. Parker. *Velocity map imaging of ions and electrons using electrostatic lenses: Application in photoelectron and photofragment ion imaging of molecular oxygen*. Rev. Sci. Instr. **68**, 3477 (1997).

69. M. J. J. Vrakking. *An iterative procedure for the inversion of two-dimensional ion/photoelectron imaging experiments*. Rev. Sci. Instr. **72**, 4084 (2001).

70. M. Nisoli, S. De Silvestri and O. Svelto. *Generation of high energy 10 fs pulses by a new pulse compression technique*. Appl. Phys. Lett. **68**, 2793 (1996).

71. M. Nisoli, S. Stagira, S. De Silvestri, O. Svelto, S. Sartania, Z. Cheng, M. Lenzner, Ch. Spielmann and F. Krausz. *A novel-high energy pulse compression system: generation of multigigawatt sub-5-fs pulses*. Appl. Phys. B **65**, 189 (1997).

72. H. G. Muller. *Reconstruction of attosecond harmonic beating by interference of two-photon transitions*. Appl. Phys. B **74**, 17 (2002).

73. Y. Mairesse, A. de Bohan, L. J. Frasinski, H. Merdji, L. C. Dinu, P. Monchicourt, P. Breger, M. Kovačev, R. Taïeb, B. Carré, H. G. Muller, P. Agostini and P. Salières. *Attosecond synchronization of high-harmonic soft X-rays*. Science **302**, 1540 (2003).

74. K. Varjú, P. Johnsson, R. López-Martens, T. Remetter, E. Gustafsson, J. Mauritsson, M. B. Gaarde, K. J. Schafer, Ch. Erny, I. Sola, A. Zaïr, E. Constant, E. Cormier, E. Mével and A. L'Huillier. *Experimental Studies of Attosecond Pulse Trains*. Las. Phys. **15**, 888–898 (2005).

75. S. Haessler, B. Fabre, J. Higuet, J. Caillat, T. Ruchon, P. Breger, B Carré, E. Constant, A. Maquet, E. Mével, P. Salières, R. Taïeb and Y. Mairesse. *Phase-resolved attosecond near-threshold photoionization of molecular nitrogen*. Phys. Rev. A **80**, 011404 (2009).

76. P. Agostini, F. Fabre, G. Mainfray, G. Petite and N. K. Rahman. *Free-Free Transitions Following Six-Photon Ionization of Xenon Atoms*. Phys. Rev. Lett. **42**, 1127 (1979).

77. T. E. Glover, R. W. Schoenlein, A. H. Chin and C. V. Shank. *Observation of Laser Assisted Photoelectric Effect and Femtosecond High Order Harmonic Radiation*. Phys. Rev. Lett **76**, 2468 (1996).

78. J. M. Schins, P. Berger, P. Agostini, R. C. Constantinescu, H. G. Muller, A. Bouhal, G. Grillon, A. Antonetti and A. Mysyrowicz. *Cross-correlation measurements of femtosecond extreme-ultraviolet high-order harmonics*. J. Opt. Soc. Am. B **13**, 197 (1996).

79. V. Véniard, R. Taïeb and A. Maquet. *Two-Color Multiphoton Ionization of Atoms Using High-Order Harmonic Radiation*. Phys. Rev. Lett. **74**, 4161 (1995).

80. H. R. Reiss. *Effect of an intense electromagnetic field on a weakly bound system*. Phys. Rev. A **22**, 1786 (1980).

81. L. B. Madsen. *Strong-field approximation in laser-assisted dynamics*. Am. J. Phys. **73**, 57 (2005).

82. E. S. Toma and H. G. Muller. *Calculation of matrix elements for mixed extreme-ultraviolet-infrared two-photon above-threshold ionization of argon*. J. Phys. B **35**, 3435 (2002).

83. W. Boutu, S. Haessler, H. Merdji, P. Breger, G. Waters, M. Stankiewicz, L. J. Frasinski, R. Taieb, J. Caillat, A. Maquet, P. Monchicourt, B. Carre and P. Salieres. *Coherent control of attosecond emission from aligned molecules*. Nature Physics **4**, 545–549 (2008).

84. S. Haessler. *Generation of Attosecond Pulses in Atoms and Molecules*. PhD thesis Université Paris-Sud 11 (2009).

85. J. Mauritsson, M. B. Gaarde and K. J. Schafer. *Accessing properties of electron wave packets generated by attosecond pulse trains through time-dependent calculations*. Phys. Rev. A **72**, 013401 (2005).

86. K. Klünder and *et al. manuscript in preparation* (2010).

87. B.L. Henke, J.C. Davis, E.M. Gullikson and R.C.C. Perera. A Preliminary Report on X-Ray Photoabsorption Coefficients and Atomic Scattering Factors for 92 Elements in the 10-10,000 eV Region. Lawrence Berkeley National Laboratory (1988).

88. M Schultze, E Goulielmakis, M Uiberacker, M Hofstetter, J Kim, D Kim, F Krausz and U Kleineberg. *Powerful 170-attosecond XUV pulses generated with few-cycle laser pulses and broadband multilayer optics*. New Journal of Physics **9**, 243 (2007).

89. J Mauritsson, P Johnsson, R López-Martens, K Varj ú, A L'Huillier, M B Gaarde and K J Schafer. *Probing temporal aspects of high-order harmonic pulses via multi-colour, multi-photon ionization processes*. J. Phys. B **38**, 2265 (2005).

90. Y. Mairesse and F. Quéré. *Frequency-resolved optical gating for complete reconstruction of attosecond bursts*. Phys. Rev. A **71**, 011401(R) (2005).

91. F. Quéré, Y. Mairesse and J. Itatani. *Temporal characterization of attosecond XUV fields*. J. Mod. Opt. **52**, 339 (2005).

92. G. Sansone, E. Benedetti, F. Calegari, C. Vozzi, L. Avaldi, R. Flammini, L. Poletto, P. Villoresi, C. Altucci, R. Velotta, S. Stagira, S. De Silvestri and M. Nisoli. *Isolated single-cycle attosecond pulses*. Science **314**, 443 (2006).

93. E. Goulielmakis, M. Schultze, M. Hofstetter, V. S. Yakovlev, J. Gagnon, M. Uiberacker, A. L. Aquila, E. M. Gullikson, D. T. Attwood, R. Kienberger, F. Krausz and U. Kleineberg. *Single-Cycle Nonlinear Optics*. Science **320**, 1614 (2008).

94. M. Lewenstein, P. Salières and A. L'Huillier. *Phase of the atomic polarization in high-order harmonic generation*. Phys. Rev. A **52**, 4747 (1995).

95. V. Roudnev and B. D. Esry. *General Theory of Carrier-Envelope Phase Effects*. Phys.l Rev. Lett. **99**, 220406 (2007).

96. T. F. Gallagher. *Above-Threshold Ionization in Low-Frequency Limit*. Phys. Rev. Lett. **61**, 2304 (1988).

97. P. B. Corkum, N. H. Burnett and F. Brunel. *Above-threshold ionization in the long-wavelength limit*. Phys. Rev. Lett. **62**, 1259 (1989).

98. J. Itatani, F. Quéré, G. L. Yudin, M. Yu. Ivanov, F. Krausz and P. B. Corkum. *Attosecond Streak Camera*. Phys. Rev. Lett. **88**, 173903 (2002).

99. He Wang, Michael Chini, Sabih D Khan, Shouyuan Chen, Steve Gilbertson, Ximao Feng, Hiroki Mashiko and Zenghu Chang. *Practical issues of retrieving isolated attosecond pulses*. J. of Phys. B **42**, 134007 (12pp) (2009).

100. I. Thomann, A. Bahabad, X. Liu, R. Trebino, M. M. Murnane and H. C. Kapteyn. *Characterizing isolated attosecond pulses from hollow-core waveguides using multi-cycle driving pulses*. Opt. Express **17**, 4611–4633 (2009).

101. Kyung T. Kim, Kyung S. Kang, Mi N. Park, Tayyab Imran, G. Umesh and Chang H. Nam. *Comparison of RABITT and FROG measurements in the temporal characterization of attosecond pulse trains* (2007).

102. R. Trebino and D. J. Kane. *Using phase retrieval to measure the intensity and phase of ultrashort pulses: frequency-resolved optical gating*. J. Opt. Soc. Am. A **10**, 1101 (1993).

103. R. Trebino, K. W. DeLong, D. N. Fittinghoff, J. Sweetser, M. A. Krumbügel and B. Richman. *Measuring ultrashort laser pulses in the time-frequency domain using frequency-resolved optical gating*. Rev. Sci. Instrum. **68**, 1 (1997).

104. Rick Trebino. *Frequency-resolved optical gating: the measurement of ultrashort laser pulses*. Kluwer Academic Publishers (2000).

105. J. R. Fienup. *Reconstruction of a complex-valued object from the modulus of its Fourier transform using a support constraint*. J. Opt. Soc. Am. A **4**, 118–123 (1987).

106. R. P. Millane. *Multidimensional phase problems*. J. Opt. Soc. Am. A **13**, 725–734 (1996).

107. E. P. Månsson. *Temporal gating of attosecond pulse trains*. Lund Reports on Atomic Physics **403** (2008).

108. J. M. Dahlström, T. Fordell, E. Mansten, T. Ruchon, M. Gisselbrecht, K. Klünder, M. Swoboda, A. L'Huillier and J. Mauritsson. *Atomic- and macroscopic measurements of attosecond pulse trains*. Phys. Rev. A **80**, 033836 (2009).

109. J. Mauritsson, P. Johnsson, E. Mansten, M. Swoboda, T. Ruchon, A. L'Huillier and K. J. Schafer. *Coherent Electron Scattering Captured by an Attosecond Quantum Stroboscope*. Phys. Rev. Lett. **100**, 073003 (2008).

110. Henry N. Chapman, Stefan P. Hau-Riege, Michael J. Bogan, Sasa Bajt, Anton Barty, Sebastien Boutet, Stefano Marchesini, Matthias Frank, Bruce W. Woods, W. Henry Benner, Richard A. London, Urs Rohner, Abraham Szoeke, Eberhard Spiller, Thomas Moeller, Christoph Bostedt, David A. Shapiro, Marion Kuhlmann, Rolf Treusch, Elke Ploenjes, Florian Burmeister, Magnus Bergh, Carl Caleman, Goesta Huldt, M. Marvin Seibert and Janos Hajdu. *Femtosecond time-delay X-ray holography*. Nature **448**, 676–679 (2007).

111. J N Dodd, R D Kaul and D M Warrington. *The modulation of resonance fluorescence excited by pulsed light*. Proceedings of the Physical Society **84**, 176–178 (1964).

112. S. Haroche, J. A. Paisner and A. L. Schawlow. *Hyperfine Quantum Beats Observed in Cs Vapor under Pulsed Dye Laser Excitation*. Phys. Rev. Lett. **30**, 948–951 (1973).

113. Yu. Ralchenko, Kramida, J. A.E., Reader and NIST ASD Team. NIST Atomic Spectra Database (version 3.1.5), [Online]. National Institute of Standards and Technology, Gaithersburg, MD (2008). Available: http://physics.nist.gov/asd3 [2010, January 23].

114. F. Brandi, D. Neshev and W. Ubachs. *High-Order Harmonic Generation Yielding Tunable Extreme-Ultraviolet Radiation of High Spectral Purity*. Phys. Rev. Lett. **91**, 163901 (2003).

115. Gustavo A. Garcia, Laurent Nahon and Ivan Powis. *Two-dimensional charged particle image inversion using a polar basis function expansion*. Rev. Sci. Instrum. **75**, 4989–4996 (2004).

116. M. J. J. Vrakking. *Abel inversion of 2D velocity map images using a Legendre polynomial expansion*. Not published (2008).

117. A Giusti-Suzor, F H Mies, L F DiMauro, E Charron and B Yang. *Dynamics of H2+ in intense laser fields*. Journal of Physics B: Atomic, Molecular and Optical Physics **28**, 309–339 (1995).

118. J H Posthumus. *The dynamics of small molecules in intense laser fields*. Reports on Progress in Physics **67**, 623–665 (2004).

119. A. Rudenko, Th. Ergler, B. Feuerstein, K. Zrost, C.D. Schröter, R. Moshammer and J. Ullrich. *Real-time observation of vibrational revival in the fastest molecular system*. Chem. Phys. **329**, 193 – 202 (2006). Electron Correlation and Multimode Dynamics in Molecules - (in honour of Lorenz S. Cederbaum).

120. M. F. Kling, Ch. Siedschlag, A. J. Verhoef, J. I. Khan, M. Schultze, Th. Uphues, Y. Ni, M. Uiberacker, M. Drescher, F. Krausz and M. J. J. Vrakking. *Control of Electron Localization in Molecular Dissociation*. Science **312**, 246 (2006).

121. Yu Oishi, Masanori Kaku, Akira Suda, Fumihiko Kannari and Katsumi Midorikawa. *Generation of extreme ultraviolet continuum radiation driven by a sub-10-fs two-color field*. Opt. Express **14**, 7230–7237 (2006).

122. H. Mashiko, S. Gilbertson, C. Li, S. D. Khan, M. M. Shakya, E. Moon and Z. Chang. *Double optical gating of high-order harmonic generation with carrier-envelope phase stabilized lasers*. Phys. Rev. Lett. **100**, 103906 (2008).

123. V Ayvazyan, *et al. First operation of a free-electron laser generating GW power radiation at 32 nm wavelength*. Eur. Phys. J. D **37**, 297–303 (2006).

124. Press release, *New Era of Research Begins as World's First Hard X-ray Laser Achieves "First Light" (2009)*. URL http://home.slac.stanford.edu/pressreleases/2009/20090421.htm. accessed 21/01/2010.

125. G. Lambert, T. Hara, D. Garzella, T. Tanikawa, M. Labat, B. Carre, H. Kitamura, T. Shintake, M. Bougeard, S. Inoue, Y. Tanaka, P. Salieres, H. Merdji, O. Chubar, O. Gobert, K. Tahara and M. E. Couprie. *Injection of harmonics generated in gas in a free-electron laser providing intense and coherent extreme-ultraviolet light*. Nature Physics **4**, 296–300 (2008).

126. B. Dromey, M. Zepf, A. Gopal, K. Lancaster, M. S. Wei, K. Krushelnick, M. Tatarakis, N. Vakakis, S. Moustaizis, R. Kodama, M. Tampo, C. Stoeckl, R. Clarke, H. Habara, D. Neely, S. Karsch and P. Norreys. *High harmonic generation in the relativistic limit*. Nature Physics **2**, 456–459 (2006).

127. C. Thaury, F. Quere, J.-P. Geindre, A. Levy, T. Ceccotti, P. Monot, M. Bougeard, F. Reau, P. D'Oliveira, P. Audebert, R. Marjoribanks and P. H. Martin. *Plasma mirrors for ultrahigh-intensity optics*. Nature Physics **3**, 424–429 (2007).

128. Y. Nomura, R. Hörlein, P. Tzallas, B. Dromey, S. Rykovanov, , Zs. Major, J. Osterhoff, S. Karsch, L. Veisz, M. Zepf, D. Charalambidis, F. Krausz and G. D. Tsakiris. *Attosecond phase locking of harmonics emitted from laser-produced plasmas*. Nature Physics **5**, 124 (2009).

129. Yasuo Nabekawa, Toshihiko Shimizu, Yusuke Furukawa, Eiji J. Takahashi and Katsumi Midorikawa. *Interferometry of Attosecond Pulse Trains in the Extreme UltravioletWavelength Region*. Phys. Rev. Lett. **102**, 213904 (2009).

130. P. Eckle, M. Smolarski, P. Schlup, J. Biegert, A. Staudte, M. Schöffler, H. G. Muller, R. Dörner and U. Keller. *Attosecond angular streaking*. Nature Physics **4**, 565 – 570 (2008).

131. M. Meckel, D. Comtois, D. Zeidler, A. Staudte, D. Pavicic, H. C. Bandulet, H. Pepin, J. C. Kieffer, R. Dorner, D. M. Villeneuve and P. B. Corkum. *Laser-Induced Electron Tunneling and Diffraction*. Science **320**, 1478–1482 (2008).

132. A. L. Cavalieri, N. Müller, Th. Uphues, V. S. Yakovlev, A. Baltuška, B. Horvath, B. Schmidt, L. Blümel, R. Holzwarth, S. Hendel, M. Drescher, U. Kleineberg, P. M. Echenique, R. Kienberger, F. Krausz and U. Heinzmann. *Attosecond spectroscopy in condensed matter*. Nature **449**, 1029 (2007).

133. D. Shafir, Y. Mairesse, D. M. Villeneuve, P. B. Corkum and N. Dudovich. *Atomic wavefunctions probed through strong-field light–matter interaction*. Nature Physics (2009).

134. P. Johnsson, J. Mauritsson, T. Remetter, A. L'Huillier and K. J. Schafer. *Attosecond Control of Ionization by Wave-Packet Interference*. Phys. Rev. Lett. **99**, 233011 (2007).

135. S. Baker, J. S. Robinson, C. A. Haworth, H. Teng, R. A. Smith, C. C. Chirila, M. Lein, J. W. G. Tisch and J. P. Marangos. *Probing proton dynamics in molecules on an attosecond time scale*. Science **312**, 424 (2006).

136. B. K. McFarland, J. P. Farrell, P. H. Bucksbaum and M. Gühr. *High Harmonic Generation from Multiple Orbitals in* N_2. Science **322**, 1232 (2008).

137. S. Haessler, J. Caillat, W. Boutu, C. Giovanetti-Teixeira, T. Ruchon, T. Auguste, Z. Diveki, P. Breger, A. Maquet, B. Carre, R. Taieb and P. Salieres. *Attosecond imaging of molecular electronic wavepackets*. Nature Physics **advance online publication** (2010).

Papers

PAPER I

Macroscopic effects in attosecond pulse generation

T. Ruchon, C. P. Hauri, K. Varjú, E. Mansten, M. Swoboda,
R. López-Martens and A. L'Huillier.

New J. Phys. **10**, 025027 (2008).

New Journal of Physics
The open-access journal for physics

Macroscopic effects in attosecond pulse generation

T Ruchon[1], C P Hauri[2], K Varjú[1], E Mansten[1], M Swoboda[1], R López-Martens[2] and A L'Huillier[1,3]

[1] Department of Physics, Lund University, PO Box 118, SE-221 00 Lund, Sweden
[2] Laboratoire d'Optique Appliquée, École Nationale Supérieure des Techniques Avancées (ENSTA)–École Polytechnique CNRS UMR 7639, 91761 Palaiseau, France
E-mail: anne.lhuillier@fysik.lth.se

New Journal of Physics **10** (2008) 025027 (10pp)
Received 8 October 2007
Published 29 February 2008
Online at http://www.njp.org/
doi:10.1088/1367-2630/10/2/025027

Abstract. We examine how the generation and propagation of high-order harmonics in a partly ionized gas medium affect their strength and synchronization. The temporal properties of the resulting attosecond pulses generated in long gas targets can be significantly influenced by macroscopic effects, in particular by the intensity in the medium and the degree of ionization which control the dispersion. Under some conditions, the use of gas targets longer than the absorption length can lead to the generation of compressed attosecond pulses. We show these macroscopic effects experimentally, using a 6 mm-long argon-filled gas cell as the generating medium.

Contents

[3] Author to whom any correspondence should be addressed.

© IOP Publishing Ltd and Deutsche Physikalische Gesellschaft

1. Introduction

The generation of attosecond pulses from high-order harmonics conversion in gases requires that the harmonics selected in a given bandwidth are synchronized [1]. In general, this condition is only met naturally in the cut-off region [2, 3]. In the plateau region, the variation of the harmonic spectral phase tends to ruin the attosecond structure. Indeed, interferences between contributions from different quantum paths responsible for the harmonic emission [4, 5] lead to multiple pulses every half laser cycle while the variation of the accumulated phase along a given quantum path from one harmonic to the next results in a significant temporal chirp [6]. To compensate for the multiple pulse structure, the short quantum path is usually selected by phase matching or spatial filtering [7, 8]. To eliminate the phase variation accumulated for the short quantum path, post-compression techniques have been proposed, based on broadband multilayer mirrors [9], metallic filters [8, 10, 11] or plasma media [6]. These techniques, however, reduce the number of photons available, and must be designed specifically for each spectral region.

For the generation of attosecond pulses in nonlinear media, both the individual single-atom response and phase-matching effects for the set of selected harmonics must be taken into account. These effects are naturally included in complete calculations solving the Schrödinger and Maxwell equations [5, 12, 13]. For the optimization of the strength of individual harmonics careful studies of phase-matching conditions have been carried out [14]–[18]. However, the influence of these macroscopic effects on the relative spectral phase of several consecutive harmonics, and consequently on the temporal shape of attosecond pulses has not so far been scrutinized. In fact, the remarkable agreement between measurements of spectral phases and the predictions coming from the single-atom dipole phase [6] seems to indicate that the macroscopic response should not influence the temporal properties of attosecond pulses, at least under the experimental conditions hitherto investigated.

In this paper, we theoretically examine the influence of the macroscopic response on the dispersion and the temporal properties of the attosecond pulses. For targets with lengths longer than the coherence and absorption lengths of the generation process, we show how dispersion in neutral and ionized media indeed influences the spectral phase of attosecond pulses through phase-matching effects. We demonstrate this effect experimentally, by measuring the harmonic group delay for different pressures in a 6 mm-long argon-filled gas cell.

2. Theory

We consider a coherent sum of consecutive odd harmonics (from q_i to q_f) generated when a strong laser field interacts with a gas. The electric field resulting from the superposition of these harmonics can be written as $\mathcal{E}(t, z') \propto \sum_{q=q_i}^{q_f} \mathcal{E}_q(t, z')$, where $\mathcal{E}_q$ is the electric field of the qth harmonic, t is time and z' is the abscissa of the observation point, supposed to be far away from the generating medium (see figure 1). Using an integral formalism, $\mathcal{E}_q(t, z')$ can be simply calculated by integrating the nonlinear polarization, $\mathcal{P}_q$, induced in the medium at position z and at time $t - \ell_q(z, z')/c$, where $\ell_q(z, z')$ is the optical path of harmonic q from z to z'. In a one-dimensional approximation, valid for loose focusing geometries,

$$\mathcal{E}_q(t, z') = \mathcal{A} \int \mathcal{P}_q\left(t - \frac{\ell_q(z, z')}{c}, z\right) \mathrm{d}z, \tag{1}$$

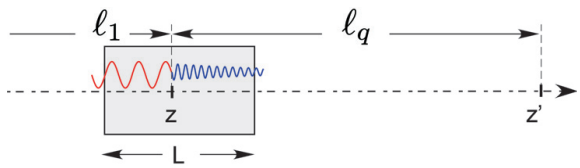

Figure 1. Notation used for the theory.

where $\mathcal{A}$ is a constant and where the integration is taken over the medium. Writing the electric field of the fundamental $\mathcal{E}_1(t,z) = \exp(\mathrm{i}\omega(t-\ell_1(-\infty,z)/c))$, we get $\mathcal{P}_q(t,z) \propto \mathcal{N} d_q \exp(\mathrm{i}q\omega(t-\ell_1(-\infty,z)/c))$ where d_q is the single atom dipole moment, $\mathcal{N}$ the atomic density, ω the laser frequency and $\ell_1(-\infty,z)$ is the optical path of the fundamental from $-\infty$ up to z. Equation (1) can then be written

$$\mathcal{E}_q(t,z') = \mathcal{A}\mathrm{e}^{\mathrm{i}q\omega t}\int \mathcal{N} d_q \mathrm{e}^{-\mathrm{i}q\omega(\ell_1(-\infty,z)+\ell_q(z,z'))/c}\mathrm{d}z. \tag{2}$$

To gain some physical insight into this equation, we consider for simplicity a homogeneous medium of length L and a collimated geometry. The absorption of the fundamental is considered to be extremely small and not taken into account, while absorption at the frequency of the qth harmonic is denoted κ_q. The imaginary part of the wavevector of harmonic q (resp. of the fundamental) is denoted k_q (resp. k_1). In the following, we introduce the phase mismatch Δk_q equal to $k_q - qk_1$. Equation (2) becomes

$$\mathcal{E}_q(t,z') = \mathcal{A}\mathrm{e}^{\mathrm{i}q\omega t - \mathrm{i}\langle\phi_q\rangle}\,\mathrm{e}^{-\kappa_q L/2}\,\mathcal{N} d_q \frac{\mathrm{e}^{(\mathrm{i}\Delta k_q+\kappa_q)L/2} - \mathrm{e}^{-(\mathrm{i}\Delta k_q+\kappa_q)L/2}}{\mathrm{i}\Delta k_q + \kappa_q}, \tag{3}$$

where $\langle\phi_q\rangle = qk_0z' - qk_0L + qk_1L/2 + k_qL/2$ (with $k_0 = \omega/c$), is an average phase for the qth harmonic. The amplitude of the electric field at frequency $q\omega$ depends on two complex quantities: $d_q = |d_q|\exp\mathrm{i}\phi_q^{\mathrm{mic}}$ describes the single atom response, while

$$F_q = \mathrm{e}^{-\mathrm{i}\langle\phi_q\rangle}\,\mathrm{e}^{-\kappa_q L/2}\,\frac{\mathrm{e}^{(\mathrm{i}\Delta k_q+\kappa_q)L/2} - \mathrm{e}^{(-\mathrm{i}\Delta k_q-\kappa_q)L/2}}{\mathrm{i}\Delta k_q + \kappa_q} = |F_q|\mathrm{e}^{\mathrm{i}\phi_q^{\mathrm{mac}}} \tag{4}$$

includes macroscopic effects such as phase matching, absorption of the neutral medium and effects due to ionization.

ϕ_q^{mac} simplifies in some limiting cases. First, if there is no absorption $\phi_q^{\mathrm{mac}} = \langle\phi_q\rangle$ which has a simple physical explanation: in this case, on average, the emitters are situated in the center of the cell, at $z = L/2$. The phase in z' is then expected to be the sum of the phase if no medium was present (qk_0z'), plus the extra phase due to the medium. This latter phase is the difference between the average phase of a photon emitted through upconversion at $z = L/2$ ($qk_1L/2 + k_qL/2$) minus the propagation in vacuum over the length L (qk_0L). Now when absorption is taken into account, the average emitter is shifted towards the end of the medium. This appears as a correction given by the last term in equation (4). The phase of the harmonics can be written:

$$\phi_q = \phi_q^{\mathrm{mic}} - \langle\phi_q\rangle + \arctan\frac{\tan L/2L_q^{\mathrm{coh}}}{\tanh L/2L_q^{\mathrm{abs}}} - \arctan\frac{L_q^{\mathrm{abs}}}{L_q^{\mathrm{coh}}}, \tag{5}$$

where $L_q^{\rm abs} = \kappa_q^{-1}$ are the absorption lengths and $L_q^{\rm coh} = \Delta k_q^{-1}$ are the coherence lengths. The two last terms are corrective terms that, as expected from the above analysis, vanish when no absorption is present, and cancel out when the length of the medium is short compared to both the absorption and coherence lengths.

The opposite limit also has a quite simple physical explanation: when the medium is long compared to the absorption length, only the emitters situated in the last portion of the cell will contribute. In this case, the harmonic phase (equation (5)) simplifies into $\phi_q = \phi_q^{\rm mic} - \langle\phi_q\rangle + \Delta k_q L/2 - \arctan\frac{L_q^{\rm abs}}{L_q^{\rm coh}}$. $-\langle\phi_q\rangle - \Delta k_q L/2 = qk_0 z' - qk_0 L + qk_1 L$ would be the accumulated phase if the emitters were all situated at the exit of the medium. A correction to this extreme case comes as $-\arctan\frac{L_q^{\rm abs}}{L_q^{\rm coh}}$. It does not include any term proportional to the length of the medium. We then come to the somewhat surprising conclusion that it is not only the real part of the index that governs the dispersion, but the absorption plays a role as well. This conclusion follows from the fact that only the photons emitted over a distance $L_q^{\rm abs}$ exit the medium and therefore contribute to the electric field of harmonic q. On average, the photons at frequency $q\omega_0$ are emitted at a fraction of the absorption length inside the medium. Their phase thus depends on the absorption properties of the gas, which vary with the harmonic order.

3. Numerical results

In figure 2(a), we show the variation of Δk_q due to neutral atom dispersion [19] in a 20 mbar Ar target (blue circles) and due to free electron dispersion (green squares), as given by the plasma dispersion formula, assuming 7% ionization of the medium, over a (continuous) frequency range spanning from the 11th to the 30th harmonic of 800 nm radiation. This degree of ionization in argon corresponds to optimized phase-matching conditions where the dispersion of neutral atoms cancels that of free electrons for most of the bandwidth considered (see below). Figure 2(b) shows the two relevant lengths of the problem, namely the absorption and coherence lengths. Both are of the order of some millimeters for this ionization rate. Figure 2(c) shows their ratio together with the last term of equation (5). It becomes apparent that the overall shape rather follows the absorption length. In addition, the curvature due to this term, which gives the GDD (group delay dispersion)[4], is negative. This is plotted in figure 2(d), together with the second derivative of $\phi_q^{\rm mic}$ [20], and that of the second to last term of equation (5). In the case of a long cell, this last term does not contribute to the global GDD as discussed above. Interestingly, the macroscopic and microscopic GDD are then opposite in sign, and therefore (partly) compensate one another, leading possibly to shorter attosecond pulses.

This suggests that pure macroscopic effects, such as the length of the cell or the pressure, play a role in the structure of attosecond pulse trains. We first investigate, for a given pressure, how the length of the cell influences the dispersion in realistic cases. In figures 3(a) and (b), we plot the phase-matching factor $|F_q|$ (a) and the GDD$= \partial^2\phi_q/\partial q^2$ (b) versus the length of the cell and the 'harmonic order', q, for the same conditions as in figure 2, i.e. 20 mbar Ar, with 7% ionization. We here included the microscopic response by using the dipole moment intensities

[4] All through the paper, we call GDD the second derivative of the phase versus the harmonic order. It is a dimensionless quantity that should be multiplied by the square of the fundamental angular speed to get the usual GDD in fs^2.

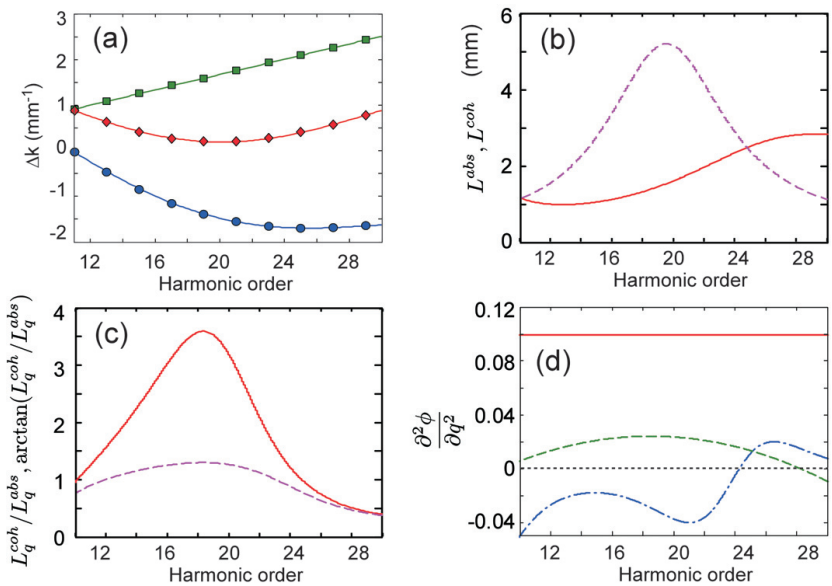

Figure 2. (a) Phase mismatch versus harmonic order due to the electrons (green squares), the neutral atoms (blue circles) and their sum (red diamonds). (b) Coherence (dashed, violet) and absorption (red, solid) lengths versus harmonic order, in millimeter. (c) Ratio of the coherence length over the absorption length (red, solid) and its arc tangent (violet, dashed). (d) GDD induced by the dipole phase (red, solid), arctan $\frac{\tan L/2L_q^{\mathrm{coh}}}{\tanh L/2L_q^{\mathrm{abs}}}$ (green, dashed) and $-\arctan\frac{L_q^{\mathrm{abs}}}{L_q^{\mathrm{coh}}}$ (blue, dashed dot).

calculated by integrating the time-dependent Schrödinger equation in argon [21] and dipole phases ϕ_q^{mic} characteristic of the shortest quantum path [22]. The resulting microscopic GDD for the short quantum path is constant and equals 0.1. This is the GDD obtained for very short cell lengths in figure 3. Now, when the cell length increases, the GDD for the first harmonics decreases (figure 3(b)), resulting in better synchronization. At the same time, for the higher harmonics (approximately above the 23rd), macroscopic effects induce an irregular GDD. In the case where phase matching is not optimized, for example, for higher ionization rates (14%), both $|F_q|$ (figure 3(c)) and the GDD (figure 3(d)) exhibit pronounced oscillations as a function of medium length. The amplitude oscillations, well known in nonlinear optics under the name of Maker fringes, result from the fact that interferences between harmonic fields generated in different parts of the medium strongly depend on the length of the medium. As expected, the GDD exhibits similar oscillations. We here envision possibilities to control the attosecond pulse duration in conditions where individual harmonics are not perfectly phase matched.

Figure 4(a) presents the temporal properties of attosecond pulses obtained by superimposing harmonics 11–31 for cell lengths varying from 0 to 20 mm and ionization rates from 0 to 14%. In this calculation, the Rayleigh range was chosen to be extremely long in order to unravel the specific effects of dispersion, thus discarding possible geometrical effects. The

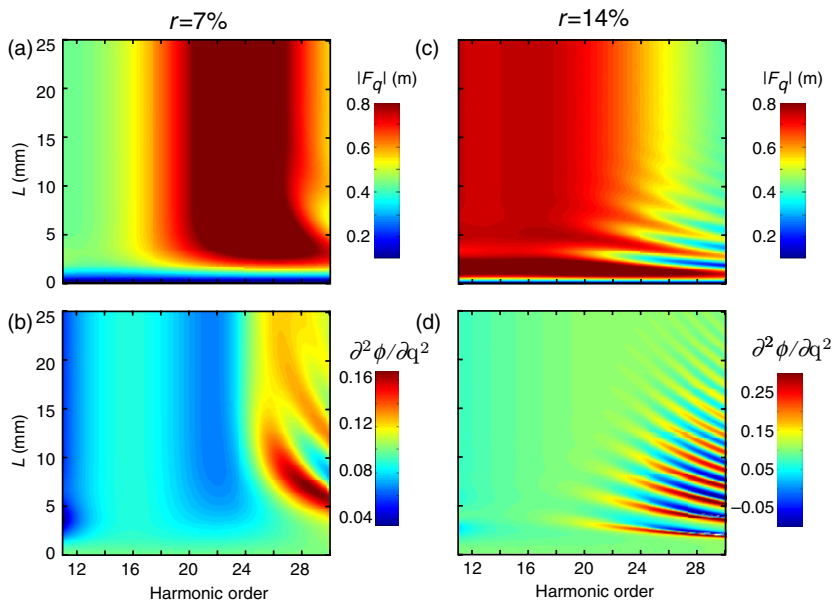

Figure 3. Amplitude of the phase-matching factor $|F_q|$ versus the length of the cell and the harmonic order for (a) 7% and (c) 14% ionization. (b) Macroscopic group delay dispersion, i.e. $\partial^2\phi_q^{\mathrm{mac}}/\partial q^2$ versus L and q for (b) 7% and (d) 14% ionization. It was calculated using an Ar pressure of 20 mbar.

laser intensity and pulse duration are those leading to a given ionization rate which is specified on the vertical axis. To give a better description of the temporal profile than the full width at half maximum (FWHM), we use the second-order moment defined as

$$\bar{\tau} = \left[\frac{1}{W}\int_{-\infty}^{\infty} t^2 I(t)\mathrm{d}t - \frac{1}{W^2}\left(\int_{-\infty}^{\infty} t I(t)\mathrm{d}t\right)^2\right]^{1/2}, \tag{6}$$

where W is the integral of the intensity profile $I(t)$, i.e. the energy fluence. Second-order moments are equal to 42% of the FWHM for Gaussian pulses and increase rapidly as the contrast of the pulses decreases. If no macroscopic effects were considered one would get the pulse duration given by the $L = 0$ limit. The main effect shown in figure 4(a) is that there is a region of medium lengths and ionization rates where the temporal profiles of the generated attosecond pulses are optimized. This happens for lengths larger than the average absorption length (L_{23}^{abs} is indicated by the red dashed line) and for ionization rates in the range of 5–7%. The white-dashed lines show the coherence length (abscissa) for the 23rd harmonic as a function of ionization rate (ordinate). The shortest pulses are here obtained for optimized phase-matching conditions where the coherence length is going to infinity and for medium lengths typically longer than twice the absorption length. Figure 4(b) shows the intensity in the attosecond pulse for the same generation conditions. The optimum efficiency corresponds to the shortest duration, i.e. to

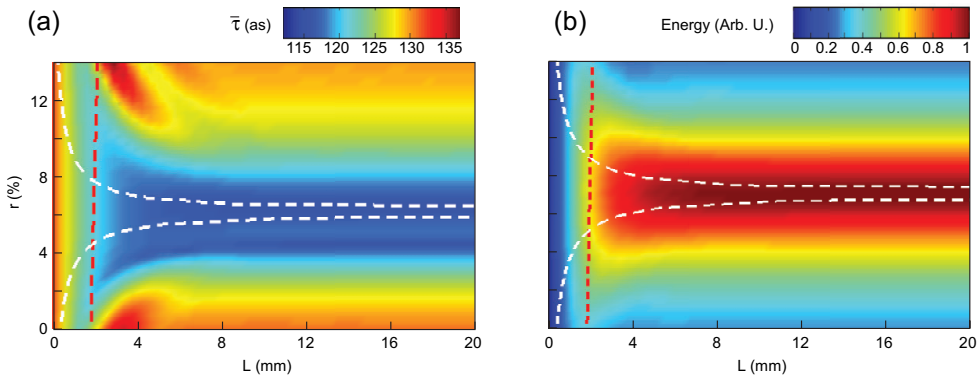

Figure 4. (a) Second-order moments of the attosecond pulses reconstructed from the superposition of harmonics 11–31 for ionization ratio from 0 to 14% and cell length from 0 to 20 mm. The white (resp. red) dashed line represents the coherence (resp. absorption) length of harmonic 23rd. (b) Energy of the attosecond pulse for the same range of parameters.

the best phase-matching conditions. We also verified that more refined calculations taking into account the (weak) z-dependence of the dipole moment and phase as well as the Gouy phase did not significantly change our results.

Finally, we have studied the influence of the pressure on the temporal structure of the attosecond pulses. The cell was assumed to be 6 mm long. In figure 5, the GDD is plotted versus the harmonic order for 7 and 14% ionization rate, and versus the pressure. The conclusions follow those made exploring the effect of the length of the cell: (i) macroscopic effects tend to reduce the GDD for the lower-order harmonics and (ii) they lead to an irregular structure for the highest ones.

4. Experimental results

To show experimentally the influence of macroscopic effects on the spectral phase of attosecond pulses, we generated harmonics in a 6 mm long, 500 μm wide cylindrical cell, using a loose focusing geometry and varied the pressure in the generating cell. From figure 3, this cell length is likely to give the most striking effects. The 1 kHz titanium sapphire laser of the Lund High-Power Laser Facility, with 2.3 mJ pulse energy, 8 mm beam diameter and 35 fs pulse duration was focused by a $f = 75$ cm curved mirror to an intensity of 1.6×10^{14} W cm^{-2}. The gas cell was pulsed at 1 kHz with a piezo-electric valve, letting the gas in through a 1 mm hole drilled in the middle of the cell. Since no direct measurement of the pressure in the cell could be done, we indicate in the following the background pressure in the chamber. The beam waist was estimated to $\approx 100\,\mu$m, i.e. roughly eight times smaller than the tube diameter, thus avoiding any guiding by the tube. Finally, a hard aperture allowed us to filter the short quantum path contribution to the high harmonic emission [8] and a 200 nm-thick Al filter was used to eliminate the fundamental laser field.

IOP Institute of Physics DEUTSCHE PHYSIKALISCHE GESELLSCHAFT

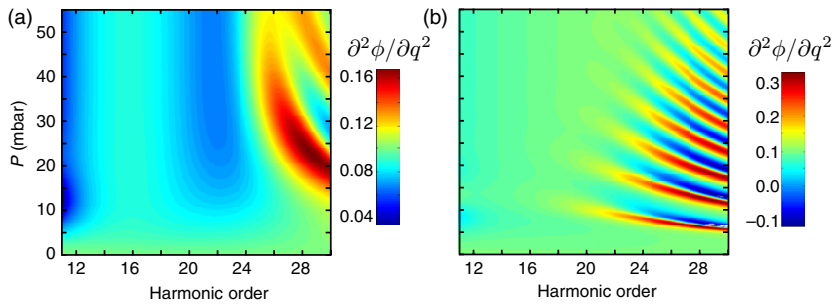

Figure 5. Macroscopic group delay dispersion, i.e. $\partial^2\phi_q^{\mathrm{mac}}/\partial q^2$ versus P and q for (a) 7% and (b) 14% ionization. The nonlinear medium is argon at 20 mbar.

Our attosecond pulses were characterized using the RABITT method (reconstruction of attosecond beating by interferences of two-photon transitions) [1]. The laser beam was split into two arms to perform an XUV+IR pump–probe cross correlation. The main fraction of the pulse energy went into the pump arm where attosecond pulses were generated, as described above. The small part of the laser beam, sent into the delayed probe arm, was recombined with the XUV pump immediately after the spatial filter, using the coated surface of the aperture to reflect the probe beam. The recombined beams were then focused into a magnetic bottle electron spectrometer, filled with argon at a detection pressure of $1\text{–}10 \times 10^{-5}$ mbar. We have taken data for eight different pressures, adjusted through the voltage on the piezo-electric valve. Each experiment lasted about 15 min and no significant variations of the laser parameters have been noticed in the 3 h needed for the collection of the data. In addition, we have checked, by varying the pressure in the detection chamber and by varying the intensity in the probe beam, that neither nonlinear effects nor higher-order processes were present during the detection, allowing a robust RABITT reconstruction.

In figure 6(a), we show the phase differences between two subsequent harmonics (modulo 2π for each point and with an arbitrary offset for the whole set, which is not measurable in our set-up). We observe the main features predicted by the theoretical analysis: (i) increasing the pressure first decreases the group delay (see figure 6(b)) and (ii) irregularities mainly affect the highest part of the spectrum. This latter effect can be quantified making a linear fit of sets of four consecutive harmonics across the range covered and plotting the standard deviation (σ) value of these fits versus the mean harmonic order of this set (see figure 6(c)). The variation of pressure also led to a change in spectral bandwidth, which partly compensated the flattening of the group delay. Consequently, the pulse width was found to vary nonmonotonically with pressure between typically 270–360 as. The shortest pulse duration (270 as, corresponding to a 195 as second moment) was obtained for a pressure of 5 mbar, which gives the highest harmonic intensity.

5. Conclusion

In conclusion, we have shown that phase matching plays a significant role in the GDD of high-order harmonics and in the temporal shaping of attosecond pulses. A theoretical description has been provided which points out the importance of absorption and ionization effects. We find

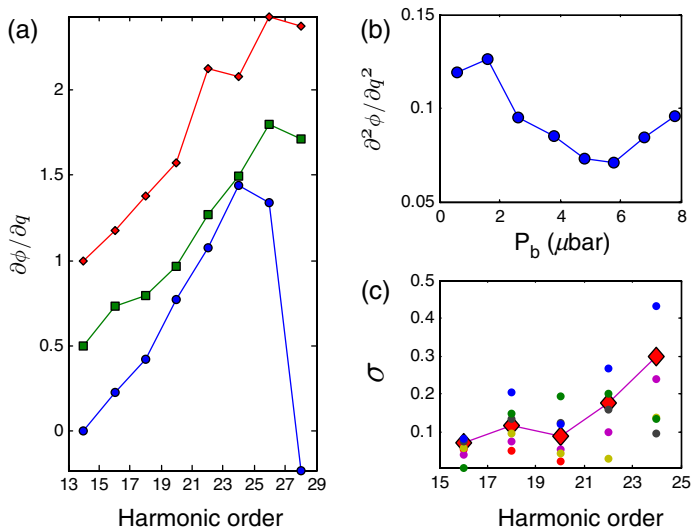

Figure 6. (a) Group delays measured for three different pressures in the generation cell, increasing from the bottom curve to the top one. (b) Slopes of the curves (GDD) calculated on the first four harmonics for eight different pressures in the generation cell (the abscissa gives the background pressure in the generation chamber). (c) Sigmas of linear fits taken over sets of four consecutive harmonics. The abscissa give the central harmonic for one set, each color for the scatter points give the sigmas for one pressure in the generation cell. The solid line shows their average.

that, in general, i.e. in conditions where phase matching is optimized for most of the spectral bandwidth of the attosecond pulses, propagation and phasematching effects lead to a small compression of attosecond pulses compared to the predictions of the single atom response. This is due to the spectral variation of the absorption length, leading, in the absorption limit, to a signification variation of the accumulated phase and henceforth to a negative GDD. The amount of chirp is approximately a factor of ten less than that due to the single response and of opposite sign. Experiments, performed in normal pressure conditions in argon, using a simple few millimeter long gas cell, confirm these predictions. The use of more advanced gas targets should lead to self-compressed attosecond pulses by adjusting the ionization rate and the pressure profile along the propagation axis [18, 23].

Acknowledgments

This research was supported by the Integrated Initiative of Infrastructure LASERLAB-EUROPE (RII3-CT-2003-506350) within the 6th European Community Framework Programme, the Marie Curie Research Training Network XTRA (MRTN-CT-2003-505138), the Swedish Research Council and the Knut and Alice Wallenberg Foundation. TR is supported by a Marie

Curie Intra-European fellowship (MEIF-CT-2006-040577). KV is currently at the Department of Optics and Quantum Electronics, University of Szeged, Hungary, supported by a Magyary Zoltań Postdoctoral Fellowship. We are grateful to Bertrand Carré and Claes-Göran Wahlström for fruitful discussions.

References

[1] Paul P M, Toma E S, Breger P, Mullot G, Augé F, Balcou Ph, Muller H G and Agostini P 2001 Observation of a train of attosecond pulses from high harmonic generation *Science* **292** 1689
[2] Kienberger R *et al* 2004 Atomic transient recorder *Nature* **427** 817
[3] Mairesse Y *et al* 2004 Optimization of attosecond pulse generation *Phys. Rev. Lett.* **93** 163901
[4] Antoine Ph, L'Huillier A and Lewenstein M 1996 Attosecond pulse trains using high-order harmonics *Phys. Rev. Lett.* **77** 1234
[5] Gaarde M B and Schafer K J 2002 Space-time considerations in the phase locking of high harmonics *Phys. Rev. Lett.* **89** 213901
[6] Mairesse Y *et al* 2003 Attosecond synchronization of high-harmonic soft x-rays *Science* **302** 1540
[7] Salières P *et al* 2001 Feynman's path-integral approach for intense-laser–atom interactions *Science* **292** 902
[8] López-Martens R *et al* 2005 Amplitude and phase control of attosecond light pulses *Phys. Rev. Lett.* **94** 033001
[9] Morlens A-S *et al* 2006 Design and characterization of extreme-ultraviolet broadband mirrors for attosecond science *Opt. Lett.* **31** 1558
[10] Kim K T, Kim C M, Baik M-G, Umesh G and Nam C H 2004 Single sub-50-attosecond pulse generation from chirp-compensated harmonic radiation using material dispersion *Phys. Rev.* A **69** 051805
[11] Sansone G *et al* 2006 Isolated single-cycle attosecond pulses *Science* **314** 443–6
[12] Gaarde M B and Schafer K J 2006 Generating single attosecond pulses via spatial filtering *Opt. Lett.* **31** 3188
[13] Christov I P, Murnane M M and Kapteyn H C 1998 Generation and propagation of attosecond x-ray pulses in gaseous media *Phys. Rev.* A **57** R2285
[14] L'Huillier A, Schafer K J and Kulander K C 1991 Theoretical aspects of intense field harmonic-generation *J. Phys. B: At Mol. Opt. Phys.* **24** 3315–41
[15] Constant E, Garzella D, Breger P, Mével E, Dorrer Ch, Le Blanc C, Salin F and Agostini P 1999 Optimizing high harmonic generation in absorbing gases: model and experiment *Phys. Rev. Lett.* **82** 1668
[16] Kazamias S, Douillet D, Weihe F, Valentin C, Rousse A, Sebban S, Grillon G, Augé F, Hulin D and Balcou Ph 2003 Global optimization of high harmonic generation *Phys. Rev. Lett.* **90** 193901
[17] Kazamias S, Douillet D, Weihe F, Valentin C, Rousse A, Sebban S, Grillon G, Augé F, Hulin D and Balcou Ph 2003 Global optimization of high harmonic generation *Eur. Phys. J.* D **90** 193901
[18] Zhang X, Lytle A L, Popmintchev T, Zhou X, Kapteyn H C, Murnane M M and Cohen O 2007 Quasi-phase-matching and quantum-path control of high-harmonic generation using counterpropagating light *Nat. Phys.* **3** 270–5
[19] L'Huillier A, Li X F and Lompré L A 1990 Propagation effects in high-order harmonic generation in rare gases *J. Opt. Soc. Am.* B **7** 527–36
[20] Varju K *et al* 2005 Frequency chirp of harmonic and attosecond pulses *J. Mod. Opt.* **52** 379–94
[21] Gaarde M B and Schafer K J 2000 Calculations of resonant, multiphoton population transfer in potassium atoms at long wavelengths *Phys. Rev.* A **62** 053411
[22] Lewenstein M, Salières P and L'Huillier A 1995 Phase of the atomic polarization in high-order harmonic generation *Phys. Rev.* A **52** 4747
[23] Kosuge A, Sekikawa T, Zhou X, Kanai T, Adachi S and Watanabe S 2006 Frequency-resolved optical gating of isolated attosecond pulses in the extreme ultraviolet *Phys. Rev. Lett.* **97** 263901

PAPER II

Spectral shaping of attosecond pulses using two-color laser fields

E. Mansten, J. M. Dahlström, P. Johnsson, M. Swoboda, A. L'Huillier and J. Mauritsson.

New J. Phys. **10**, 083041 (2008).

New Journal of Physics
The open-access journal for physics

Spectral shaping of attosecond pulses using two-colour laser fields

E Mansten[1,3], J M Dahlström[1], P Johnsson[1,2], M Swoboda[1], A L'Huillier[1] and J Mauritsson[1]

[1] Department of Physics, Lund University, P O Box 118, SE-221 00 Lund, Sweden
[2] FOM Institute for Atomic and Molecular Physics (AMOLF), Kruislaan 407, 1098 SJ Amsterdam, The Netherlands
E-mail: erik.mansten@fysik.lth.se and johan.mauritsson@fysik.lth.se

New Journal of Physics **10** (2008) 083041 (10pp)
Received 14 May 2008
Published 28 August 2008
Online at http://www.njp.org/
doi:10.1088/1367-2630/10/8/083041

Abstract. We use a strong two-colour laser field composed of the fundamental (800 nm) and the second harmonic (400 nm) of an infrared (IR) laser field to generate attosecond pulses with controlled spectral and temporal properties. With a second-harmonic intensity equal to 15% of the IR intensity the second-harmonic field is strong enough to significantly alter and control the electron trajectories in the generation process. This enables us to tune the central photon energy of the attosecond pulses by changing the phase difference between the IR and the second-harmonic fields. In the time domain the radiation is emitted as a sequence of pulses separated by a full IR cycle. We also perform calculations showing that the effect of even stronger second-harmonic fields leads to an extended tunable range under conditions that are experimentally feasible.

[3] Author to whom any correspondence should be addressed.

© IOP Publishing Ltd and Deutsche Physikalische Gesellschaft

Contents

1. Introduction

Attosecond pulses represent the sharpest instruments available to study ultrafast dynamics [1]. These pulses are formed when a strong laser field interacts with a gaseous medium and the underlying physics is well described by the three step model. In this model the electron tunnels through the atomic potential, which is distorted by the strong laser field (I); gets accelerated by the field in the continuum (II); and may recombine with its parent ion (III) emitting the accumulated excess energy as a burst of extreme ultra-violet (XUV) light [2, 3]. For multi-cycle pulses, the repetition of the process, combined with the inversion symmetry of the atomic potential, leads in the time domain to a train of attosecond pulses separated by half a laser cycle and in the spectral domain to odd harmonics of the laser frequency. Spectral and temporal control of the attosecond pulse generation requires shaping of the generating laser field on a sub-cycle level. One example of such sub-cycle control is the use of phase stabilized few-cycle laser pulses [4], where the short pulse duration leads to a change in the field amplitude between consecutive half-cycles. Another, more elaborate, method is to use pulses with a time-varying polarization [5]–[7]. These methods allow control to be exerted by changing the carrier envelope phase of the laser pulse, in particular leading to the generation of single attosecond pulses [7, 8]. The technique with time-varying polarization also gives control of the photon energy of the pulses [9].

An alternative approach to control the sub-cycle field structure and thereby the electron dynamics is to mix the fundamental infrared (IR) field with its second harmonic [10]–[12]. The combined field can be written as: $E(t) = E_\omega[\sin(\omega t) + \sqrt{\mathcal{R}}\sin(2\omega t + \varphi)]$, where $\sqrt{\mathcal{R}} = E_{2\omega}/E_\omega$ is the ratio between the two field amplitudes $E_{2\omega}$ and E_ω, ω is the IR frequency, and φ a controllable phase difference between the fields, see figure 1(a). The shape and strength of the combined field in consecutive IR half-cycles differ beyond the simple sign change that occurs in a one colour field. The electron trajectories are also altered and instead of the normal two trajectories with excursion times (τ) shorter than one IR period (T), we now get four [12], as illustrated in figure 1(b). Two of these trajectories (a short and a long) come from ionization during the half-cycle when the electric field is strong and recombination during the weaker half-cycle, we will refer to these as high → low trajectories. The other two trajectories start when the field is weak and return during the stronger half-cycle (low → high) with the result that the harmonic emission from these trajectories reaches high photon energies but the yield can be orders of magnitude weaker than the emission from the high → low trajectories due to the difference in ionization probability. Schemes to use the low → high trajectories for isolated attosecond pulse generation have been proposed [13, 14]. We instead use the high → low trajectories which give much higher conversion efficiencies. In previous work, we

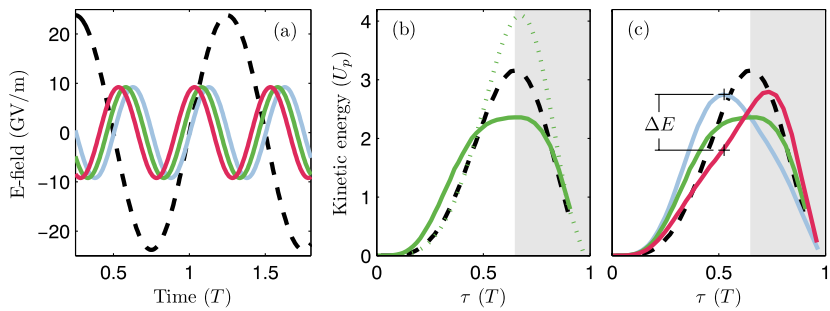

Figure 1. (a) IR field (dashed black) ($I = 7.5 \times 10^{13}\,\mathrm{W\,cm^{-2}}$) and second-harmonic fields with $\mathcal{R} = 15\%$. The phase differences for the three second-harmonic fields are $\varphi = 0$ rad (ice-blue), $\varphi = 0.6$ rad (green) and $\varphi = 1.2$ rad (red). The resulting E field is the sum of the IR and one of the 2ω fields. The timescale units are IR periods (T). (b) Return energy for the high $\rightarrow$ low and low $\rightarrow$ high trajectories calculated using classical mechanics for $\varphi = 0.6$ in solid and dotted green, respectively. Long trajectories are in the shaded regions, $\tau > 0.65T$. (c) High $\rightarrow$ low return for the three phases shown in (a). The dashed black curves in (b) and (c) show the return energy for a one-colour IR field. The kinetic energy of the electrons is given in units of the ponderomotive energy U_p for the IR field. τ is the time the electron spends in the continuum from ionization to recombination and ΔE is the tunable energy range.

have demonstrated that adding a second harmonic with a relative intensity of $\mathcal{R} = 10\%$ will induce a sufficiently strong variation between consecutive IR-half-cycles to efficiently cancel the generation every second half-cycle, which results in the generation of an attosecond pulse train (APT) with only one pulse per IR cycle [12]. In combination with the polarization gating technique mentioned above this can lead to the generation of isolated attosecond pulses [15].

In this paper we show that the field structure *within* each half-cycle can be controlled by using an even stronger blue field. The generated APT still consists of one pulse per IR cycle and the signature of the additional control is that central energy of the attosecond pulses can be tuned by changing φ. We demonstrate that already $\mathcal{R} = 15\%$ is sufficient to tune the peak of the harmonic spectrum between 23 and 29 eV. We also perform calculations to investigate the influence of higher field strengths. We find that the tunable range can be extended to $2.5U_\mathrm{p}$, U_p being the ponderomotive energy of the IR, for $\mathcal{R} = 50\%$ and by carefully choosing the conditions a narrow frequency range can be selected and further enhanced.

In figure 1(c), we plot the return energy as a function of return time for the high $\rightarrow$ low trajectories for three different values of φ together with the return energy for a one colour driving field. For a one colour driving field the highest return energy (cut-off) corresponds to an excursion time (τ) of $0.65T$ where T is the period of the IR field [16]. Trajectories with longer excursion times result in more divergent harmonic emission and can hence be strongly reduced after the generation using an aperture [17]. For the two-colour field we will continue to use $\tau = 0.65T$ to distinguish between short and long trajectories since the divergence of

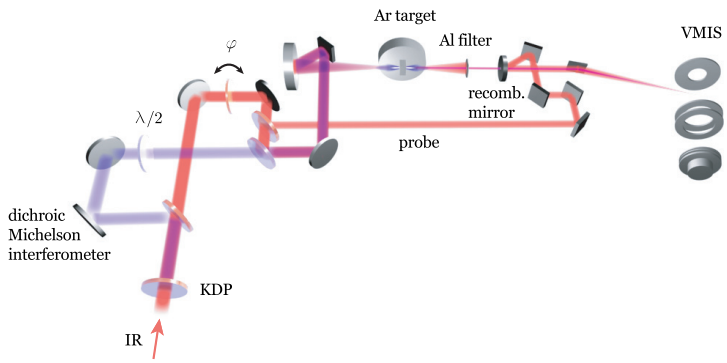

Figure 2. Experimental setup for two-colour generation and characterization of APTs.

the emission mainly depends on the time spent in the continuum. The highest energy reached during the short (high → low) trajectory depends strongly on the relative delay between the two fields, φ, figure 1(c). We find both experimentally and theoretically that we get most of the emission where the slope of the return energy curve decreases. In some cases the curve goes through a maximum at this point (figure 1(c) blue curve). By selecting only the emission from the short, high → low trajectories we thus get a pulse train with only one pulse per cycle and a central energy that can be tuned by changing the delay between the two fields. The central energies of spectra calculated within the strong field approximation (SFA) for the same parameters are marked with + in figure 1(c) and the energy difference between the two markers i.e. the tunable range is denoted ΔE.

2. Experimental method

The setup used to generate the attosecond pulses and characterize their spectral and temporal properties is schematized in figure 2. Incoming 35 fs, 800 nm, 2 mJ laser pulses are sent through a 0.6 mm KDP (potassium dihydrogen phosphate), type I crystal for second-harmonic generation. The IR and the generated second-harmonic radiation (blue) are separated in a dichroic interferometer where the phase difference between the two colours, φ, can be adjusted. Before the IR and the blue are combined at the exit of the interferometer, the polarization of the blue is made parallel with the IR and a fraction of the IR is split off as a probe. After the interferometer the two-colour field is focused into a 1 kHz pulsed Ar gas-target to generate harmonics, which are filtered spectrally and spatially. The spectral filtering is done using a 200 nm thick aluminium (Al) transmission filter that blocks the two-colour driving field and the low-order harmonics and improves the synchronization of the transmitted harmonics [18]. The filter does not significantly affect the shape of the high harmonic spectrum as the transmission

of Al is rather constant in the studied spectral region (20–40 eV)[4]. The emission is spatially filtered using a 1.5 mm aperture, located 400 mm from the laser focus, which efficiently blocks the more divergent contributions from the long trajectories [19]. The spatial filter serves the dual purpose of being a recombination mirror. The back side is a convex mirror off which the probe is reflected and made collinear with the XUV light.

The harmonic emission and the co-propagating probe are focused into an atomic Ar beam inside a velocity map imaging spectrometer (VMIS) [20]. The VMIS projects the 3D momentum distribution of the ejected photoelectrons onto a micro-channel plate detector coupled to a phosphor screen, which is read out by a CCD camera. From the measured 2D projection, the full 3D momentum distribution of the photoelectrons can be unambigously retrieved using an iterative inversion algorithm [21], and from this the photoelectron and corresponding photon spectra shown below can be easily extracted. With the probe present at the time of ionization the energy distribution of the electrons can be shifted as a function of XUV–probe delay [22]–[24]. The shift in momentum is proportional to the vector potential of the probe field, $A(t)$, at the time of ionization, $\Delta p = -eA(t_i)$. The streaking of the photoelectrons allows us to recover the duration of the attosecond pulses [25] since the pulse periodicity is matched exactly to a full IR cycle and consecutive ionization events are identical for a multi-cycle laser [26]. The strength of the probe field has to be chosen below that necessary to turn the photoelectrons around and thereby induce coherent electron scattering [26] in order not to perturb the temporal characterization. Coherent electron scattering occurs when the dimensionless parameter $\tilde{\gamma} = \sqrt{\frac{\hbar\omega_c - I_p}{2U_p}}$ is less than 1, where $\hbar\omega_c$ is the central energy of the XUV light and I_p is the ionization potential of the target atom. In the experiment $\tilde{\gamma} = 3.7$ and no electron–ion interaction is expected.

3. Results

Experimental results showing spectral shaping are presented in figures 3(a) and (c). In (a) harmonic spectra are plotted as a function of φ, for an IR intensity estimated to be $7.5 \times 10^{13}\,\mathrm{W\,cm^{-2}}$ and $\mathcal{R} = 15\%$. The odd and even harmonics have comparable strengths and oscillate with φ with a period of π. The positions of the oscillation maxima depend strongly and almost linearly on the harmonic order. As a consequence, the central frequency can easily be varied simply by changing φ. The measured tunability extends over 6 eV, limited mainly by the target gas (Ar) and the intensities used. The tunable range, ΔE, can be increased by increasing the IR intensity while keeping $\mathcal{R}$ fixed. Higher intensity might demand a target gas with higher ionization potential. For a fixed $\mathcal{R}$, ΔE is proportional to U_p and thus the intensity. For the intensity we use in the calculations and experiment presented in figures 1 and 3, $\Delta E \approx U_p$.

We also perform a temporal measurement at a phase φ marked with green in figure 3(a). The phase was chosen to be within the range where the APT consists of one pulse per IR cycle, i.e. between the ice-blue and red lines. In figure 4, the presence of the probe shifts the photoelectron distribution. The on-axis photoelectron spectra are plotted as a function of the XUV–probe delay in (a) together with an angular distribution in (b), taken at the XUV–probe delay indicated by the white line in (a), where streaking is maximized. The fact that the energy transfer in (a) is either upward or downward proves that we only have one attosecond pulse per IR cycle. The phase of the attosecond pulses can be retrieved either by considering the

[4] Center for X-Ray Optics, Lawrence Berkley National Laboratory.

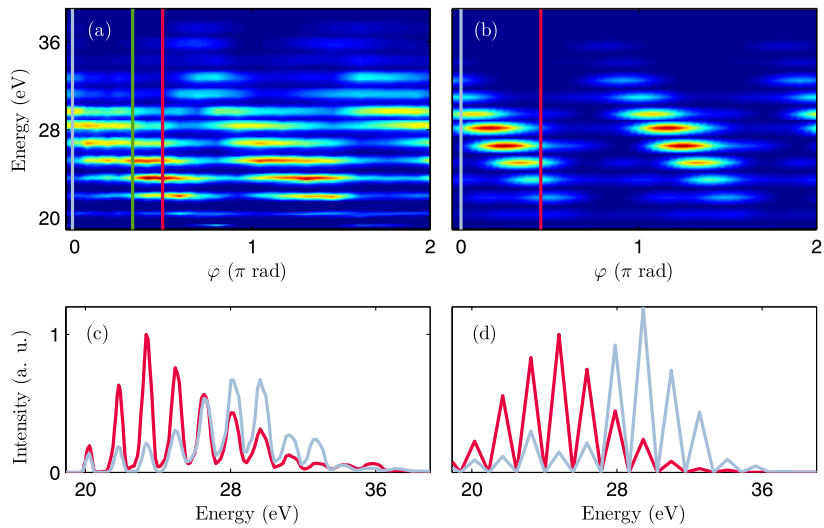

Figure 3. (a) and (b) photon energies as a function of φ, (a) an experimental scan and (b) a calculated scan where only short trajectories are included. (c) and (d) spectra for minimum and maximum energy taken at the relative phases marked with ice-blue and red lines in the scans, (c) experimental and (d) calculated. The green line in (a) indicates the relative phase for which the pulse duration was measured.

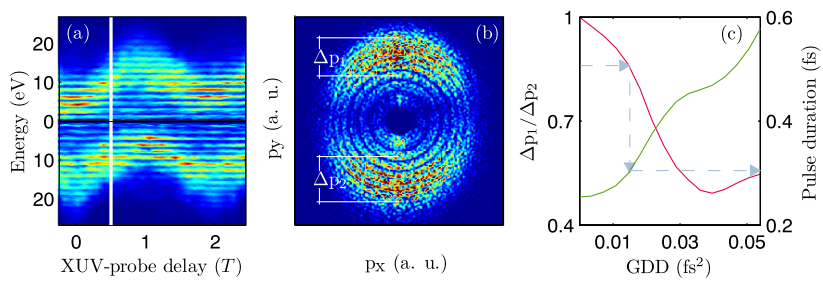

Figure 4. (a) Electron energy distribution along the polarization axis as a function of XUV–probe delay. (b) Electron momentum distribution at the XUV–probe delay when streaking is maximized. The probe-field is polarized along the y-axis. (c) Momentum asymmetry as a function of GDD, red curve and left y-axis, and pulse duration as a function of GDD, green curve and right y-axis. The ice-blue arrows point out the path starting from the measured $\Delta p_1/\Delta p_2$ to the retrieved GDD where it meets the red curve and the pulse duration where it meets the green curve.

full scan [27] (figure 4(a)) or the up/down asymmetry, $\Delta p_1/\Delta p_2$, of the angular distribution at XUV–probe delays corresponding to maximum streaking i.e. when $A(t) = 0$ at the time of ionization (figure 4(b)). We choose the latter technique which in principle can be used to measure the pulse-duration of the attosecond pulses with a single shot. Electrons leaving the atom upward and downward to the probe polarization direction are affected differently by the probe field [22]. In figure 4(b) the upward electrons get a more narrow distribution than the downward electrons ($\Delta p_1 < \Delta p_2$). For each combination of harmonic spectrum and probe intensity the ratio $\Delta p_1/\Delta p_2$ depends on the group delay dispersion (GDD) of the attosecond pulses in a unique way. The probe intensity can be extracted from the maximum momentum shift in the scan. For our measured harmonic spectrum and probe intensity we calculate, using the SFA, how the electron distributions change with GDD. This allows us to deduce $\Delta p_1/\Delta p_2$ as a function of GDD (figure 4(c) red line). The variation of the pulse duration with GDD is indicated by the green line. From our experimentally measured ratio, $\Delta p_1/\Delta p_2 = 0.85$, we obtain a GDD of 0.015 fs^2 and a pulse duration of 300 as. The negative GDD of the Al-filter compresses the pulse from 450 as towards the transform limit of 250 as.

Our theoretical calculations consist of solving the time-dependent Schrödinger equation within the SFA [28]. The atomic dipole $\langle x(\omega)\rangle$ from the calculations is converted to an intensity spectrum by taking the product $\omega^4|\langle x(\omega)\rangle|^2$. Experimentally, contributions from the short trajectories can be selected through phase matching and spatial filtering [29]. To mimic this effect in the single atom calculations we restrict the SFA integration to include only the excursion times with: $0 < \tau < 0.65T$. Comparing calculations and experiment, in figure 3, we find a good agreement between the experimental (a) and the calculated (b) spectra. Note that the calculations, based on a continuous driving field, give information about the intensity but not the shape of individual harmonics. The experimental results together with the calculations confirm the idea of sub-cycle control induced by the second-harmonic field. The probability for ionization and return of the electron wave packet is increased over a certain energy range close to the highest detected energy. This energy range can be tuned by changing the phase difference φ.

We investigate theoretically how the sub-cycle control can be improved by increasing $\mathcal{R}$ even further. The situation where $\mathcal{R} = 25\%$ and $\varphi = 0.6$ (see figure 5) stands out in particular since the electron is pulled back with an almost constant energy over an extended period of time, $\sim T/4$, i.e. there are many sub-cycle tunnelling times that lead to the same final energy (figure 5(b)). This results in a significant enhancement of the harmonic emission at that particular energy. The intensity within the enhanced energy region is well above the already strong harmonics for $\varphi = 0$ and 1.2 rad in figure 5(c).

For $\mathcal{R} > 25\%$, the electron is pulled back to the atom in a more complex way and the return energies are now highly dependent on φ. In figure 6(b), the calculated return energy is plotted as a function of τ for three phase differences. We note that the energy curve can peak twice; once for $0 < \tau < 0.65T$ and another time for $0.65T < \tau < T$. The highest obtainable energy within the short and long trajectory integration windows vary in opposite ways with φ. This results in a central photon energy that decreases with φ for the short trajectories and increases for the long trajectories, see figures 6(a) and (c). Under these conditions, 2×10^{14} W cm^{-2}, $\mathcal{R} = 50\%$, the tunable range is increased and we find that it is feasible to tune the energy over $2.5U_p$.

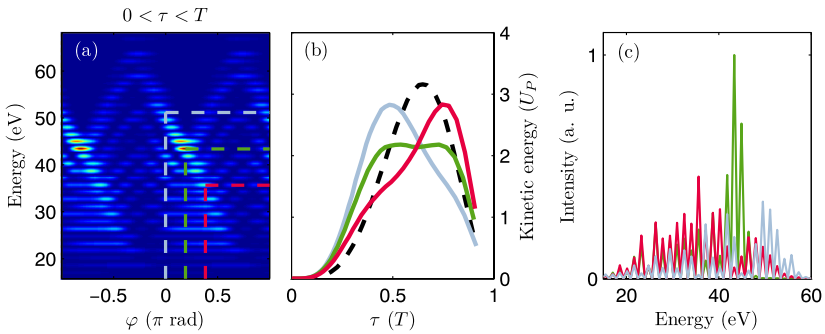

Figure 5. (a) A calculated scan of φ including the phases presented in (b) and (c). The calculations are done for an IR intensity of 2×10^{14} W cm^{-2} and $\mathcal{R} = 25\%$. (b) Kinetic energy of the returning electrons for the three φ-values shown in figure 1, $\varphi = 0$ rad (ice-blue), $\varphi = 0.6$ rad (green) and $\varphi = 1.2$ rad (red). (c) Harmonic spectra showing the enhanced emission at 42 eV corresponding to the flat region in the return energy curve (b).

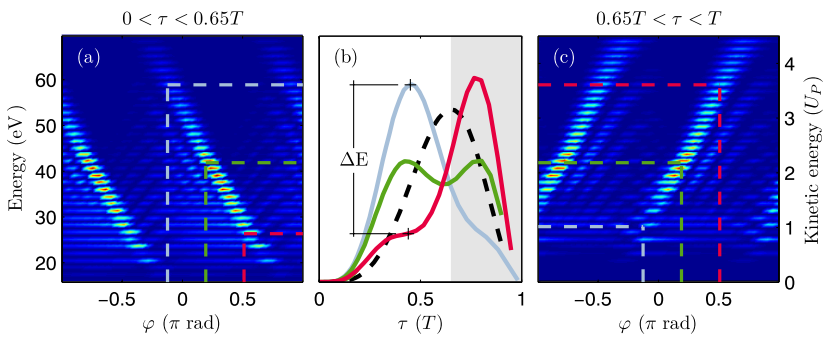

Figure 6. Calculations for an IR intensity of 2×10^{14} and $\mathcal{R} = 50\%$. (a) SFA calculations including short trajectories, $0 < \tau < 0.65T$. (b) Electron return energies for $\varphi = -0.4$ rad (ice-blue), $\varphi = 0.6$ rad (green) and $\varphi = 1.6$ rad (red). (c) SFA calculations for long trajectories, $0.65T < \tau < T$. The φ-values used to calculate the return energies are indicated in the scans by the vertical dashed lines. The horizontal dashed lines mark the peak of the spectra and connect the peak to the return energy curves.

4. Conclusion

We have shown that by altering the driving laser field on a sub-cycle level using a two-colour laser field, we can control the spectral properties of the generated APT by varying the phase difference φ between the IR and its second harmonic. With this method we have extended the spectral control beyond that of transmission filters. For applications this will be very useful as the photon energy of the emitted attosecond pulses can be tuned close to or just below the

ionization potential of a target gas to study below threshold ionization [30]. For almost all values of φ one pulse per IR cycle is generated. For a sequence of pulses the central frequency can be tuned by varying φ except for a narrow transition φ-region where two pulses per cycle are generated. In the same manner, isolated attosecond pulses generated by a two-colour field can be tuned in frequency by varying φ within the range where only one pulse is generated. By increasing the second-harmonic intensity compared to the experiment presented here, we predict that the tunable frequency range can be extended further and provide a flexible attosecond source to meet future needs.

Acknowledgments

This research was supported by the Marie Curie Early Stage Training Site (MAXLAS), the Integrated Initiative of Infrastructure LASERLAB-EUROPE (RII3-CT-2003-506350) within the 6th European Community Framework Programme, the Knut and Alice Wallenberg Foundation, the Crafoord Foundation and the Swedish Research Council.

References

[1] Paul P M, Toma E S, Breger P, Mullot G, Augé F, Balcou Ph, Muller H G and Agostini P 2001 Observation of a train of attosecond pulses from high harmonic generation *Science* **292** 1689
[2] Schafer K J, Yang B, DiMauro L F and Kulander K C 1993 Above threshold ionization beyond the high harmonic cutoff *Phys. Rev. Lett.* **70** 1599
[3] Corkum P B 1993 Plasma perspective on strong-field multiphoton ionization *Phys. Rev. Lett.* **71** 1994
[4] Baltuška A *et al* 2003 Attosecond control of electronic processes by intense light fields *Nature* **421** 611
[5] Ivanov M, Corkum P B, Zuo T and Bandrauk A 1995 Routes to control of intense-field atomic polarizability *Phys. Rev. Lett.* **74** 2933
[6] Sola I J *et al* 2006 Controlling attosecond electron dynamics by phase-stabilized polarization gating *Nat. Phys.* **2** 319
[7] Sansone G *et al* 2006 Isolated single-cycle attosecond pulses *Science* **314** 443–6
[8] Hentschel M, Kienberger R, Spielmann Ch, Reider G A, Milosevic N, Brabec T, Corkum P, Heinzmann U, Drescher M and Krausz F 2001 Attosecond metrology *Nature* **414** 509
[9] Sansone G, Benedetti E, Vozzi C, Stagira S and Nisoli M 2008 Attosecond metrology in the few-optical-cycle regime *New J. Phys.* **10** 025006
[10] Perry M D and Crane J K 1993 High-order harmonic emission from mixed fields *Phys. Rev.* A **48** R4051–4
[11] Eichmann H, Egbert A, Nolte S, Momma C, Wellegehausen B, Becker W, Long S and McIver J K 1995 Polarization-dependent high-order two-color mixing *Phys. Rev.* A **51** R3414
[12] Mauritsson J, Johnsson P, Gustafsson E, L'Huillier A, Schafer K J and Gaarde M B 2006 Attosecond pulse trains generated using two color laser fields *Phys. Rev. Lett.* **97** 013001
[13] Pfeifer T, Gallmann L, Abel M J, Neumark D M and Leone S R 2006 Single attosecond pulse generation in the multicycle-driver regime by adding a weak second-harmonic field *Opt. Lett.* **31** 975
[14] Merdji H, Auguste T, Boutu W, Caumes J P, Carr B, Pfeifer T, Jullien A, Neumark D M and Leone S R 2007 Isolated attosecond pulses using a detuned second-harmonic field *Opt. Lett.* **32** 3134–6
[15] Mashiko H, Gilbertson S, Li C, Khan S D, Shakya M M, Moon E and Chang Z 2008 Double optical gating of high-order harmonic generation with carrier-envelope phase stabilized lasers *Phys. Rev. Lett.* **100** 103906
[16] Krause J L, Schafer K J and Kulander K C 1992 High-order harmonic generation from atoms and ions in the high intensity regime *Phys. Rev. Lett.* **68** 3535
[17] Bellini M, Lyngå C, Tozzi A, Gaarde M B, Delfin C, Hänsch T W, L'Huillier A and Wahlström C-G 1998 Temporal coherence of ultrashort high-order harmonic pulses *Phys. Rev. Lett.* **81** 297

[18] López-Martens R *et al* 2005 Amplitude and phase control of attosecond light pulses *Phys. Rev. Lett.* **94** 033001
[19] Gaarde M B and Schafer K J 2006 Generating single attosecond pulses via spatial filtering *Opt. Lett.* **31** 3188
[20] Eppink A T J B and Parker D H 1997 Velocity map imaging of ions and electrons using electrostatic lenses: application in photoelectron and photofragment ion imaging of molecular oxygen *Rev. Sci. Instrum.* **68** 3477
[21] Vrakking M J J 2001 An iterative procedure for the inversion of two-dimensional ion/photoelectron imaging experiments *Rev. Sci. Instrum.* **72** 4084
[22] Kienberger R *et al* 2004 Atomic transient recorder *Nature* **427** 817
[23] Johnsson P *et al* 2005 Attosecond electron wave packet dynamics in strong laser fields *Phys. Rev. Lett.* **95** 013001
[24] Remetter T *et al* 2006 Attosecond electron wave packet interferometry *Nat. Phys.* **2** 323
[25] Itatani J, Quéré F, Yudin G L, Ivanov M Yu, Krausz F and Corkum P B 2002 Attosecond streak camera *Phys. Rev. Lett.* **88** 173903
[26] Mauritsson J, Johnsson P, Mansten E, Swoboda M, Ruchon T, L'Huillier A and Schafer K J 2008 Coherent electron scattering captured by an attosecond quantum stroboscope *Phys. Rev. Lett.* **100** 073003
[27] Mairesse Y and Quéré F 2005 Frequency-resolved optical gating for complete reconstruction of attosecond bursts *Phys. Rev.* A **71** 011401
[28] Lewenstein M, Balcou Ph, Ivanov M Yu, L'Huillier A and Corkum P B 1994 Theory of high-order harmonic generation by low-frequency laser fields *Phys. Rev.* A **49** 2117
[29] Antoine Ph, L'Huillier A and Lewenstein M 1996 Attosecond pulse trains using high-order harmonics *Phys. Rev. Lett.* **77** 1234
[30] Johnsson P, Mauritsson J, Remetter T, L'Huillier A and Schafer K J 2007 Attosecond control of ionization by wave-packet interference *Phys. Rev. Lett.* **99** 233011

PAPER III

Broadband attosecond pulse shaping

E. Gustafsson, T. Ruchon, M. Swoboda, T. Remetter, E. Pourtal, R. López-Martens, Ph. Balcou and A. L'Huillier.

Opt. Lett. **32**, 1353 (2007).

June 1, 2007 / Vol. 32, No. 11 / OPTICS LETTERS **1353**

Broadband attosecond pulse shaping

E. Gustafsson,[1,*] T. Ruchon,[1] M. Swoboda,[1] T. Remetter,[1] E. Pourtal,[1] R. López-Martens,[2] Ph. Balcou,[2] and A. L'Huillier[1]

[1]*Department of Physics, Lund University, P.O. Box 118, 221 00 Lund, Sweden*
[2]*Laboratoire d'Optique Appliquée, Ecole Nationale Supérieure des Techniques Avancées, Ecole Polytechnique CNRS UMR 7639, 91761 Palaiseau, France*
[*]*Corresponding author: erik.gustafsson@fysik.lth.se*

Received December 7, 2006; revised February 7, 2007; accepted March 8, 2007;
posted March 8, 2007 (Doc. ID 77774); published April 20, 2007

We use semiconductor (Si) and metallic (Al, Zr) transmission filters to shape, in amplitude and phase, high-order harmonics generated from the interaction of an intense titanium sapphire laser field with a pulsed neon gas target. Depending on the properties of the filter, the emitted attosecond pulses can be optimized in bandwidth and/or pulse length. We demonstrate the generation of attosecond pulses centered at energies from 50 to 80 eV, with bandwidths as large as 45 eV and with pulse durations compressed to 130 as.
© 2007 Optical Society of America
OCIS codes: 120.5050, 320.7160.

The characteristic plateau region of high-order harmonic spectra, produced when an atom is exposed to an intense laser field, spans a large spectral width ranging from the ultraviolet to the soft x-ray. In general, the different frequency components in the harmonic spectrum are not perfectly synchronized. The harmonic emission corresponding to the shortest quantum path, selected for the production of attosecond pulses, exhibits a significant positive chirp [1,2]. The production of attosecond pulses of durations below 200 as requires the filtering of a given bandwidth in the plateau region and synchronization of the selected spectral components.

Transmission filters, which exhibit negative group delay dispersion (GDD) in the low-energy part of their spectral window, can compensate for the positive chirp of attosecond pulses [3]. Previously, we have obtained pulses of 170 as duration, using argon as the generating medium and thin aluminum films to filter out and spectrally rephase high-order harmonics [2]. These pulses, resulting from the synchronization of about 10 consecutive harmonics, were centered around 30 eV and were about 1.2 cycles long. The same technique was recently used to shape harmonic emission generated in Ar with ellipticity-gated few-cycle laser pulses [4], leading to the generation of isolated 130 as pulses [5]. Multilayer mirrors can also be employed to shape the harmonic emission. The amplitude and phase properties of the mirror reflection can be tailored by the layer structure [6–8].

In the present work, semiconductor (Si) and metallic (Al, Zr) transmission filters enabled us to shape the harmonic emission from neon over a broad bandwidth up to photon energies of 100 eV. We were able to generate attosecond pulses with the largest bandwidth (45 eV) using an Al filter, the shortest Fourier-transform-limited duration (75 as) using a Si filter, and the shortest duration (130 as) using a Zr filter.

Our setup for broadband attosecond pulse generation and characterization is described elsewhere [9]. We use a 1 kHz titanium sapphire laser, with 2 mJ pulse energy and a pulse duration of 35 fs. The laser beam is split into two arms to perform an XUV+IR pump–probe cross correlation. The main fraction of the pulse energy (1.5 mJ) goes into the pump arm where attosecond pulses are generated (see Fig. 1). The laser is focused with $\sim f/50$ optics into a Ne gas cell, leading to the generation of much higher harmonic orders than in Ar [2]. An iris immediately before the focusing mirror provides an easy way to vary the energy and the divergence of the beam in the focus, enabling us to adjust the cutoff energy. The intensity at the focus was estimated to be about 3×10^{14} W cm^{-2} when Si was used, 4.5×10^{14} W cm^{-2} using Al, and 8×10^{14} W cm^{-2} with Zr. To maximize the XUV harmonic flux, we use a 1 kHz pulsed valve [10], providing high pressure in the 6 mm long gas target while keeping low background pressure in the vacuum chamber. A pair of silica plates, antireflection coated for 800 nm, separates the IR field from the harmonic emission, thus protecting the filters from exposure to a high laser flux. The top layer of the antireflection coating is fused silica (SiO_2), which has a high reflectance for grazing incidence XUV radiation [11]. The reflectance curve and the group delay (GD) added by the silica plates are shown in Fig. 2 (dashed curves) [12]. The GD stays constant except around 100 eV, where Si starts absorbing. Finally, the emission is shaped by the transmission filters and a hard

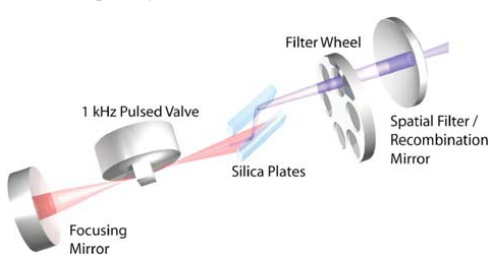

Fig. 1. (Color online) Setup for high-order harmonic generation and pulse shaping. The high-order harmonics are generated in a 6 mm long Ne gas target filled by a 1 kHz pulsed valve. A pair of silica plates reflects XUV radiation and transmits IR. The XUV light is shaped by 200 nm thick transmission filters mounted on a motorized filter wheel and spatially filtered through a hard aperture.

0146-9592/07/111353-3/$15.00 © 2007 Optical Society of America

1354 OPTICS LETTERS / Vol. 32, No. 11 / June 1, 2007

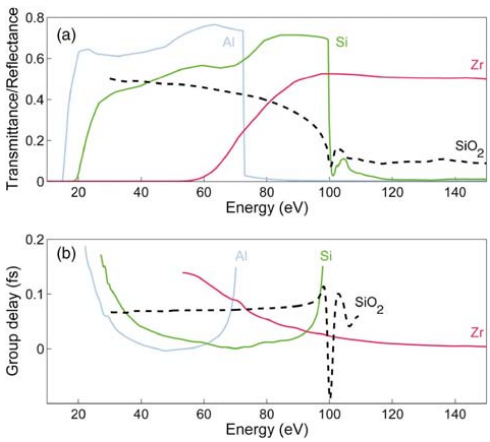

Fig. 2. (Color online) (a) Transmittance through the 200 nm thick filters and reflectance off the silica (SiO_2) plates. (b) GD added by the filters and the reflection off the pair of silica plates. The GD curves are displaced along the GD axis to fit in the plot window.

aperture, which filters the short quantum path contribution to the high-harmonic emission [2]. The small part of the laser beam sent into the probe arm is recombined with the XUV pump immediately after the spatial filter (see Fig. 1), using the back of the aperture to reflect the probe beam. The recombined beams are then focused into a magnetic bottle electron spectrometer where a target gas (Ne) is photoionized.

Our attosecond pulses are characterized using the RABITT method (Reconstruction of Attosecond Beating by Interferences of Two-photon Transitions), based on XUV+IR cross correlation [13]. The cross-correlation signal is provided by sidebands in the electron spectra arising from absorption of XUV radiation plus additional absorption or emission of one IR photon. The sideband intensities oscillate with pump–probe delay. A Fourier analysis of the sideband modulation allows us to determine the GD of the created electron wave packets and, after taking into account the influence of ionization, the GD of the attosecond pulses [9]. The electric field of the average pulse in the train can be reconstructed from the GD and the harmonic spectrum.

The filters, made of Si, Al, or Zr, with 200 nm thickness, act as bandpass filters in different photon energy regions. Their properties, calculated from tabulated refractive index data [11,14], are presented in Fig. 2. Surface oxidation alters the value of their transmittance, especially on the red side [9]. However, neither the spectral window nor the GDD are significantly affected. The GDD varies from negative at the onset of filter transmission to positive on the high-energy side of the bandpass region, close to the next absorption band. To achieve pulse compression, the generated harmonic emission and the filter properties must be matched. In particular, it is important to avoid having harmonic emission in the high-energy part of the bandpass region where the GDD is positive: this is achieved either by locating the harmonic cutoff before the GDD becomes positive or by cutting off the harmonic emission with another filter (e.g., silica plates). Suitable energy ranges are 20 to 60 eV (Al), 25 to 90 eV (Si), and 70 to 160 eV (Zr).

The results of our experiments are presented in Fig. 3. The plots on the left side show the measured spectrum (light gray), the measured GD (curve with circles), and the GD calculated by subtracting the effect of the filter (curve with triangles), while those on the right side show reconstructed pulses using the measured GD (darker curve) and in the Fourier limit (lighter curve). The variation in the slopes of the three curves with triangles is mainly due to the different laser intensities in the three cases.

Si filtering leads to attosecond pulses centered at 75 eV, with a large bandwidth (30 eV). The similarities between the measured and calculated GD curves in Fig. 3(a) indicate that Si mainly acts as a spectral filter, blocking the remaining IR and lower-order harmonics without adding much GDD. A reconstruction of the average pulse intensity profile in the train is plotted by the darker curve in Fig. 3(b). The temporal profile is asymmetric, the width at half-maximum is 365 as, while the Fourier-transform limit is 75 as (lighter curve).

The spectrum transmitted through the Al filter is very uniform, covering a 45 eV spectral range centered around 50 eV [Fig. 3(c)]. For low energies the

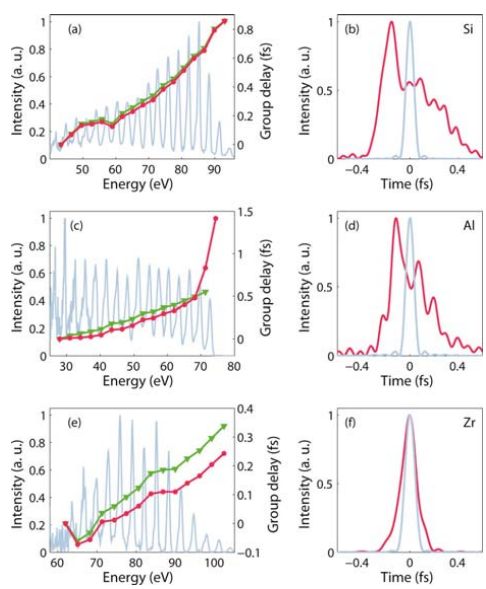

Fig. 3. (Color online) Broadband attosecond pulse shaping with Si, Al, and Zr filters. (a), (c), (e) Harmonic spectrum (light curves); group delay before (curves with triangles) and after transmission through different filters (curves with circles). (b), (d), (f). Reconstructed pulses (darker curves) and bandwidth-limited pulses (lighter curves).

filter barely affects the GD of the measured pulses, but close to the absorption edge the filter adds a rapid phase variation, causing a relatively long pulse duration, thereby underscoring the need to significantly turn off the emission before the absorption band. The Fourier limit pulse width was in this case 80 as, while the retrieved pulse length was 270 as [Fig. 3(d)].

Finally, short pulses centered at high energy were obtained by using high laser intensity combined with Zr filtering. The spectral bandwidth was limited by Zr on one side and by the silica plates on the other, leading to a nice bell-shaped spectrum [Fig. 3(e)] around 80 eV. The negative GDD of Zr in this spectral region provided compression down to 130 as [Fig. 3(f)]. We also analyzed the structure of the corresponding attosecond pulse train and, in particular, the pulse-to-pulse variation using the method described in [15]. The pulse duration varies from 120 as at the center of the train intensity envelope down to 130 as at half-maximum and 200 as at one tenth of the maximum. The bandwidth limit of the Zr shaped pulses was 95 as, and it should be possible to get close to the Fourier limit using thicker Zr filters. Calculations done for our experimental conditions show that we should obtain pulse lengths down to 100 as by shaping with a 500 nm Zr filter.

In conclusion, we demonstrate broadband pulse shaping of high-order harmonic radiation over a wide range of energies, using metallic and semiconductor filters. We are able to produce pulses with large bandwidths (up to 45 eV), centered around 50, 70, and 80 eV, depending on the filter used and with durations from 365 as down to 130 as. We believe that these filters will become an essential part of future attosecond XUV beamlines.

We thank Per Johnsson, Johan Mauritsson, Katalin Varjú, and Christoph Hauri for help regarding the experimental setup and analysis tools. This research was supported by the Integrated Initiative of Infrastructure LASERLAB-EUROPE (RII3-CT-2003-506350) within the 6th European Community Framework Programme, the Marie Curie Research Training Network XTRA (MRTN-CT-2003-505138), the Swedish Science Council, and the Knut and Alice Wallenberg Foundation.

References

1. Y. Mairesse, A. de Bohan, L. J. Frasinski, H. Merdji, L. C. Dinu, P. Monchicourt, P. Breger, M. Kovačev, R. Taïeb, B. Carré, H. G. Muller, P. Agostini, and P. Salières, Science **302**, 1540 (2003).
2. R. López-Martens, K. Varjú, P. Johnsson, J. Mauritsson, Y. Mairesse, P. Salières, M. B. Gaarde, K. J. Schafer, A. Persson, S. Svanberg, C.-G. Wahlström, and A. L'Huillier, Phys. Rev. Lett. **94**, 033001 (2005).
3. K. T. Kim, C. M. Kim, M.-G. Baik, G. Umesh, and C. H. Nam, Phys. Rev. A **69**, 051805 (2004).
4. I. J. Sola, E. Mével, L. Elouga, E. Constant, V. Strelkov, L. Poletto, P. Villoresi, E. Benedetti, J.-P. Caumes, S. Stagira, C. Vozzi, G. Sansone, and M. Nisoli, Nat. Phys. **2**, 319 (2006).
5. G. Sansone, E. Benedetti, F. Calegari, C. Vozzi, L. Avaldi, R. Flammini, L. Poletto, P. Villoresi, C. Altucci, R. Velotta, S. Stagira, S. D. Silvestri, and M. Nisoli, Science **314**, 443 (2006).
6. A. Wonisch, T. Westerwalbesloh, W. Hachmann, N. Kabachnik, U. Kleineberg, and U. Heinzmann, Thin Solid Films **464–465**, 473 (2004).
7. R. Kienberger, E. Goulielmakis, M. Uiberacker, A. Baltuška, V. Yakovlev, F. Bammer, A. Scrinzi, T. Westerwalbesloh, U. Kleineberg, U. Heinzmann, M. Drescher, and F. Krausz, Nature **427**, 817 (2004).
8. A.-S. Morlens, R. López-Martens, O. Boyko, P. Zeitoun, P. Balcou, K. Varjú, E. Gustafsson, T. Remetter, A. L'Huillier, S. Kazamias, J. Gautier, F. Delmotte, and M.-F. Ravet, Opt. Lett. **31**, 1558 (2006).
9. K. Varjú, P. Johnsson, R. López-Martens, T. Remetter, E. Gustafsson, J. Mauritsson, M. B. Gaarde, K. J. Schafer, C. Erny, I. Sola, A. Zaïr, E. Constant, E. Cormier, E. Mével, and A. L'Huillier, Laser Phys. **15**, 888 (2005).
10. E. Gustafsson and T. Ruchon, Lund Reports on Atomic Physics LRAP-366 (Division of Atomic Physics, Lund Institute of Technology, 2006).
11. http://www.cxro.lbl.gov.
12. M.-H. Chiu, J.-Y. Lee, and D.-C. Su, Appl. Opt. **38**, 4047 (1999).
13. P. M. Paul, E. S. Toma, P. Breger, G. Mullot, F. Augé, P. Balcou, H. G. Muller, and P. Agostini, Science **292**, 1689 (2001).
14. D. Y. Smith and E. D. Palik, *Handbook of Optical Constants of Solids* (Academic, 1985), Vol. 1.
15. K. Varjú, Y. Mairesse, P. Agostini, P. Breger, B. Carré, L. J. Frasinski, E. Gustafsson, P. Johnsson, J. Mauritsson, H. Merdji, P. Monchicourt, A. L'Huillier, and P. Salières, Phys. Rev. Lett. **95**, 243901 (2005).

PAPER IV

Atomic and macroscopic measurements of attosecond pulse trains

J. M. Dahlström, T. Fordell, E. Mansten, T. Ruchon, M. Swoboda, K. Klünder, M. Gisselbrecht, A. L'Huillier and J. Mauritsson.

Phys. Rev. A **80**, 033836 (2009).

Atomic and macroscopic measurements of attosecond pulse trains

J. M. Dahlström,[1] T. Fordell,[1] E. Mansten,[1] T. Ruchon,[2] M. Swoboda,[1] K. Klünder,[1] M. Gisselbrecht,[1,3] A. L'Huillier,[1] and J. Mauritsson[1]

[1]*Department of Physics, Lund University, P.O. Box 118, SE-221 00 Lund, Sweden*

[2]*DSM, Service des Photons, Atomes et Molcules, CEA-Saclay, 91191 Gif sur Yvette, France*

[3]*UMR8624, LIXAM, CNRS–Université Paris Sud, Bat. 350, 91405 Orsay, France*

(Received 12 May 2009; published 25 September 2009)

We characterize attosecond pulses in a train using both the well established "reconstruction of attosecond beating by interference of two-photon transitions" (RABITT) technique and the recently demonstrated *in situ* method, which is based on a weak perturbation of the harmonic generation process by the second harmonic of the laser field. The latter technique determines the characteristics of the single atom emission, while RABITT allows one to measure attosecond pulses "on target." By comparing the results of the two methods, the influence of propagation and filtering on the attosecond pulses can be extracted.

DOI: 10.1103/PhysRevA.80.033836 PACS number(s): 42.65.Ky, 32.80.Qk, 32.80.Rm

I. INTRODUCTION

Attosecond pulse trains (APTs) are created when intense infrared (ir) laser pulses interact with a gas of atoms or molecules [1]. The characteristics of the attosecond pulses depend both on the quantum-mechanical single atom dynamics as well as on macroscopic effects due to propagation in the nonlinear medium [2]. Under normal experimental conditions, the pulse train contains two pulses per cycle of the laser field [3–5]. The properties of these pulses can be modified by transmission through filters [6] or reflection by gratings and/or multilayer mirrors [7]. Several techniques to characterize attosecond pulse trains have been proposed, each with specific advantages and limitations. In this paper we concentrate on analyzing and comparing two of these techniques: the reconstruction of attosecond beating by interference of two-photon transitions (RABITT) [1] and a two-color *in situ* method [8], which uses a weak perturbation of the high-order harmonic generation (HHG) by the second harmonic of the fundamental laser field. Both techniques aim to characterize the average attosecond pulse structure in an APT.

Figure 1 illustrates schematically the difference between these two techniques. RABITT allows us to determine the *final* structure of the attosecond pulses after propagation in the gas cell and filtering. The attosecond pulses are characterized "on target," i.e., in the chamber where they can be used for applications. The RABITT scheme is implemented by ionizing an atomic gas with the APT in presence of a synchronized weak ir field. The perturbation due to the ir field results in sidebands in the photoelectron spectra as shown in Fig. 2(a). Information about the structure of the attosecond pulses can then be obtained by studying the intensity oscillations of these sidebands with respect to the subcycle delay between the probe field and the APT.

The *in situ* method measures the single atom emission from the individual atoms. In contrast to RABITT, the *initial* shape of the attosecond pulses, before propagation and filtering, is now measured [Fig. 1]. This is important for applications that are conducted in the generation process itself, e.g., the tomography of electronic orbitals [9]. The presence of a weak second harmonic (blue) field in the generation chamber leads to the generation of even harmonics as shown in Fig. 2(b) [10]. The harmonic generation process is nonlinear beyond the perturbative regime, which results in comparable probabilities for the processes shown in Fig. 2(b) even though the number of ir photons absorbed differs by 4. Information about the initial properties of the attosecond pulse is obtained by studying the intensity oscillations of the even harmonics with respect to the phase between the ir and the blue field.

In this paper we present a detailed theoretical and experimental comparison between the two characterization methods. Implementing both schemes allows us to measure both the initial and final shapes of the attosecond pulses. From these measurements the influence of propagation as well as

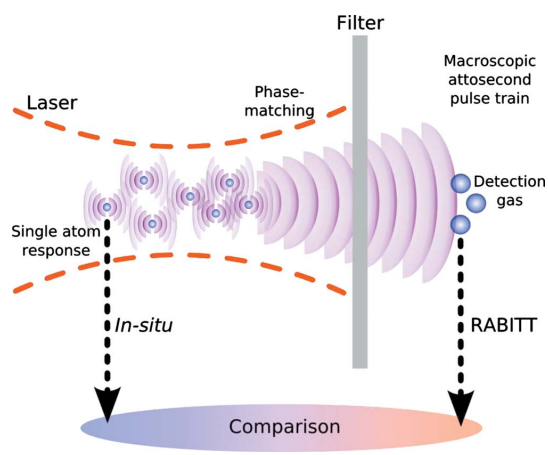

FIG. 1. (Color online) Cartoon illustrating the differences between the two characterization methods. The *in situ* method measures the single atom emission, while the RABITT scheme determines the corresponding attosecond pulses "on target." The influence of phase matching and filtering on the attosecond pulses can be deduced through the implementation of both methods on the same HHG setup.

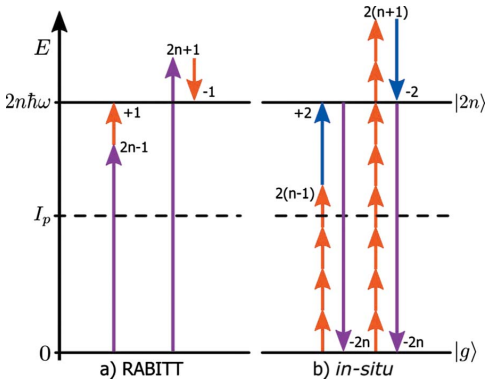

FIG. 2. (Color online) Energy diagrams associated with the two characterization methods. (a) Sidebands are created through the absorption and emission of an ir photon (ω_R) in the RABITT method. (b) Even harmonics are produced in the *in situ* method due to the presence of a weak blue field ($2\omega_R$). Attosecond pulses are characterized by studying the interferences arising from the degenerate ways of reaching the sidebands or even harmonics.

filtering can be determined. The paper is composed as follows: Sec. II reviews the theory of the two characterization methods, Sec. III gives an overview of the experimental setup, Sec. IV presents results from both methods at low gas generation pressure, Sec. V discusses the reasons for the difference observed at higher gas pressures, and Sec. VI summarizes the paper with an outlook.

II. THEORY

The electric field of an attosecond pulse can be written as $\tilde{E}(t)=\tilde{\Lambda}(t)\exp[i\tilde{\phi}(t)]$, where $\tilde{\Lambda}(t)$ and $\tilde{\phi}(t)$ represent the temporal envelope and phase, respectively. It can also be described through its Fourier transform

$$E(\omega)=\Lambda(\omega)\exp[i\phi(\omega)] \tag{1}$$

$$=\int dt\tilde{\Lambda}(t)\exp[i\tilde{\phi}(t)-i\omega t], \tag{2}$$

where $\Lambda(\omega)$ and $\phi(\omega)$ are the spectral envelope and phase. The Fourier integral in Eq. (2) can be approximated using the saddle point method when the linear part in the temporal phase cancels the Fourier component,

$$\left.\frac{d\tilde{\phi}}{dt}\right|_{t=t'(\omega)}-\omega=0, \tag{3}$$

and the quadratic part of the temporal phase is large,

$$\left.\left|\frac{d^2\tilde{\phi}}{dt^2}\right|\right|_{t=t'(\omega)}\gg 0. \tag{4}$$

Note that the temporal phase must be expanded at different times for different Fourier components, i.e., the saddle point time is a function of frequency, $t'(\omega)$. The saddle point approximation yields

$$E(\omega)\approx\left.\sqrt{\frac{2\pi}{\left|\frac{d^2\tilde{\phi}}{dt^2}\right|}}\tilde{\Lambda}(t)\exp\left[i\tilde{\phi}(t)-i\omega t\pm\frac{i\pi}{4}\right]\right|_{t=t'(\omega)}, \tag{5}$$

where the positive (negative) phase factor corresponds to a positive (negative) chirp which is the case for attosecond pulses from the short (long) branch. The spectral phase is approximately equal to

$$\phi(\omega)=\tilde{\phi}(t'(\omega))-\omega t'(\omega)\pm\frac{\pi}{4} \tag{6}$$

and its first derivative is

$$\frac{d\phi}{d\omega}=-t'(\omega), \tag{7}$$

which is obtained using the chain rule and Eq. (3). We can, therefore, interpret the group delay (GD=$-d\phi/d\omega$) as the time when the temporal phase oscillates as ω. A deeper analysis is needed if Eqs. (3) and (4) are not satisfied, which is the case of frequencies above the harmonic cutoff.

We define the relative timing of spectral components (or relative group delay) as

$$t^{(rel)}(\omega,\omega_0)=t'(\omega)-t'(\omega_0)=-\frac{d\phi}{d\omega}+\left.\frac{d\phi}{d\omega}\right|_{\omega_0}, \tag{8}$$

where $t^{(rel)}(\omega,\omega_0)$ is the time it takes for the attosecond pulse to go from oscillating at ω_0 to oscillating at ω. The reference frequency, ω_0, is arbitrarily chosen to be the lowest frequency of the pulse.

In the present work performed with relatively long (multicycle) driving pulses, the emission spectrum contains peaks at harmonic frequencies. In what follows, we use the following notation for the spectral phase $\Phi_n=\phi(n\omega_R)$, where n is the harmonic number and ω_R is the angular frequency of the ir laser field.

A. RABITT

The sidebands that appear in the RABITT method can be understood through the use of second-order perturbation theory [1]: absorption of a high-order harmonic photon followed by absorption or emission of an ir photon. Interferences occur between the different quantum paths that lead to the same sideband [Fig. 2(a)]. If we assume that the competing quantum paths have the same amplitude, then the intensity of the sideband varies as

$$I_{2n}(\varphi)\propto 1+\cos[2\varphi-\Delta\Phi_{2n}-\Delta\Phi_{2n}^{at}], \tag{9}$$

where φ is the phase of the probe field oscillations relative to the attosecond pulses, $\Delta\Phi_{2n}=\Phi_{2n+1}-\Phi_{2n-1}$ is the difference between the phases of the corresponding harmonics, and $\Delta\Phi_{2n}^{at}$ is the difference in atomic phase for the corresponding energies [11]. The atomic phase is neglected in the following because it only has a small effect on the final result in the spectral region that we consider. The first derivative of the

spectral phase can then be determined using the approximate relation

$$\left.\frac{d\phi}{d\omega}\right|_{2n\omega_R} \approx \frac{\Delta\Phi_{2n}}{2\omega_R}. \tag{10}$$

The final shape of an average attosecond pulse in the APT can be reconstructed using Eq. (10) combined with a measurement of the spectrum [12]. The aim of this paper is, however, not to reconstruct attosecond pulses but rather to study how the corresponding relative timing is affected by macroscopic dispersion in the generation cell. Using Eqs. (8)–(10), the relative timing can be written as a function of experimental observables as

$$t_{final}^{(rel)}(\omega,\omega_0) \approx -\frac{1}{\omega_R}[\varphi_{min}(\omega)-\varphi_{min}(\omega_0)], \tag{11}$$

where $\varphi_{min}(\omega)$ is the relative phase between the probe and the APT that minimizes the sideband intensity, $I_{2n}[\varphi_{min}(\omega)]=0$, for $\omega=2n\omega_R$. The subscript final is used to indicate that this is the final state of the pulse as it is detected on target.

B. *In situ*

We will now derive an analog to Eq. (11) for the *in situ* method, where the relative timing of the initial attosecond pulses is determined from the oscillation of the induced even harmonics. Using the strong field approximation (SFA), the Fourier components of the HHG dipole can be approximated as [13]

$$\vec{x}_n \propto \int dt d\tau d^3\vec{p}\, \exp\left[\frac{iS(\vec{p},t,\tau)}{\hbar} - in\omega_R t\right], \tag{12}$$

where $\vec{p}$ is the canonical (drift) momentum, τ is the time between tunneling and recombination, S is the quasiclassical action, and n is the harmonic order. Finding the stationary points of the quasiclassical action and then applying the saddle point approximation five times reduce the integrals in Eq. (12) to a sum of discrete contributions, each corresponding to a quasiclassical trajectory [5,14]. In the limit of a vanishing ionization potential, the quasiclassical trajectories become classical and the quasiclassical action becomes the classical action,

$$S[x(t,t')] = \int_{t-\tau(t)}^{t} dt' \left\{\frac{mv(t,t')^2}{2} + qx(t,t')E(t')\right\}, \tag{13}$$

where x, v, m, and q are the position, velocity, mass, and charge of the electron, respectively. We label the electron trajectories as $x=x(t,t')$, where t is the return time and t' is the integration variable for the action. The electron is released from the atom at time $t-\tau$ and accelerated by the laser field, E, until it returns and recombines with the atom at time t. In the one-color HHG, where $E=E_R=E_{R0}\sin(\omega_R t)$, the process is repeated with an alternating sign every half period, $x_R(t,t')=-x_R(t+T_R/2,t'+T_R/2)$, since $E_R(t')=-E_R(t'+T_R/2)$. The action is, however, the same, $S_R(t)=S_R(t+T_R/2)$.

Adding a weak blue field, $E=E_R+E_B$, $E_B=E_{B0}\sin(2\omega_R t+\varphi)$, induces a small change in the trajectories and the accumulated action. We treat the blue field as a perturbation and expand the trajectory,

$$m\frac{d^2}{dt^2}\sum_{n=0}^{\infty}\lambda^n x^{(n)} = qE_R + \lambda qE_B, \tag{14}$$

where λ is the usual perturbation parameter. The zeroth-order solution is the same as in the one-color case, $x^{(0)}=x_R$, and the first-order solution is purely given by the blue field, $x^{(1)}=x_B$. Higher orders, $n>1$, are equal to zero. We expand the action as $S=S^{(0)}+\lambda S^{(1)}+\lambda^2 S^{(2)}$. The zeroth-order action is the same as in the one-color case, $S^{(0)}=S_R$. The first-order action, $S^{(1)}=\sigma$, is composed of three cross terms that can be rewritten using a few partial integrations,

$$\sigma = \int_{t-\tau}^{t} dt'\{mv_R v_B + qx_R E_B + qx_B E_R\} \tag{15}$$

$$= q\int_{t-\tau}^{t} dt' x_R E_B, \tag{16}$$

where the following boundary conditions are used: $x_R(t,t)=x_R(t,t-\tau)=v_R(t,t-\tau)=x_B(t,t)=0$. It is interesting to note that σ can be written as an integral over the unperturbed trajectory, x_R, and the blue field (or as an integral over the trajectory perturbation, x_B, and the red field). Unlike S_R, the first-order action changes sign between opposite half cycles of the ir field, $\sigma(t)=-\sigma(t+T_R/2)$, which reflects the fact that the electron is now moving differently in the two half cycles, $x(t,t')\neq -x(t+T_R/2,t'+T_R/2)$. The second order action is given purely by the blue field, $S^{(2)}=S_B$, and it has, therefore, the same sign in opposite half cycles of the ir. The sum of the contributions from the zeroth and the second order is labeled as $\Sigma=S^{(0)}+S^{(2)}$.

The integrals of Eq. (12) are evaluated for the two-color case using the saddle point solutions for the ir field only, i.e., we assume that σ and S_B are slowly varying compared to S_R. Only the two stationary points corresponding to the short branch of trajectories in two neighboring half cycles of the fundamental are used, in accordance with the experiment where the long branch has been removed using spatial filtering in a narrow aperture. The contributions from the first-order action can be combined using Euler's formula. The HHG dipole takes the following form for the odd harmonics:

$$\vec{x}_{n=2N+1} \propto \cos\left[\frac{\sigma_n}{\hbar}\right]\exp\left[\frac{i\Sigma_n}{\hbar} - in\omega_R t_n\right], \tag{17}$$

where the first-order change in action, σ_n, leads to a change in dipole amplitude. In the limit of a vanishing blue field, we recover the one-color case: $\cos(\sigma_n/\hbar)\to 1$ and $\Sigma_n \to S_{Rn}$. The HHG dipole for the even harmonics takes the following form:

$$\vec{x}_{n=2N} \propto \sin\left[\frac{\sigma_n}{\hbar}\right]\exp\left[\frac{i\Sigma_n}{\hbar} - in\omega_R t_n\right], \tag{18}$$

where the amplitude again is dependent on the change in action. The even harmonics vanish if there is no blue field since $\sin(\sigma_n/\hbar)\to 0$. The intensities of the odd and even har-

monics vary out of phase: the odd harmonics decrease when the even harmonics increase. A weak blue field implies that $\sin(\sigma_n/\hbar) \approx \sigma_n/\hbar$. In this regime the even harmonic amplitudes grow linearly with the applied blue field and oscillate with the relative phase, φ. It is in this regime that an *in situ* measurement can be carried out.

Using Eq. (16), we seek the relative phase, $\varphi_{min}(t)$, that induces no even harmonic amplitude,

$$\sigma(t,\varphi_{min}(t)) = q\int_{t-\tau(t)}^{t} dt' x_R(t,t') E_B(t',\varphi_{min}(t)) = 0, \tag{19}$$

where the return time, $t=t(\omega)$, is a saddle point solution to Eq. (12) and, therefore, a function of frequency [in close analogy with Eqs. (3) and (4)]. We find excellent agreement with the pioneering work of Dudovich *et al.* [8] using unperturbed classical trajectories in Eq. (19). The solution, $\varphi_{min}(t)$, is expanded to first order around the central return time, $t_c = 0.35T_R$,

$$\varphi_{min}(t) - \varphi_{min}(t_c) \approx -(1+\xi)\omega_R(t-t_c), \tag{20}$$

where $\xi \approx -0.06$ is the "systematic scaling difference" between φ_{min} and $\omega_R t$. Our numerical linearization of $\varphi_{min}(t)$ in Eq. (20) depends on the choice of t_c: ξ varies from 0.1 (in the shortest return) to 0 (in the cutoff regime). It is, however, the scaling around the central return time (central frequency) that is most appropriate for calculating the initial properties of the entire attosecond pulse. Using Eqs. (8) and (20), we find the following simple relation between the oscillations in the even harmonics and the relative emission time from the atom:

$$t_{initial}^{(rel)}(\omega,\omega_c) \approx -\frac{\gamma}{\omega_R}[\varphi_{min}(t(\omega)) - \varphi_{min}(t(\omega_c))], \tag{21}$$

where $\gamma = 1/(1+\xi) \approx 1.06$ is a correction factor. Equation (21) resembles Eq. (11) from the RABITT section in both form and interpretation. The even harmonic oscillations are mapping out the relative emission times from the atom much like the sidebands in a RABITT scan map out the relative arrival times on target. In contrast to RABITT, the *in situ* method needs a correction factor, γ, which is slightly larger than one for the short branch of trajectories. The validity of Eq. (21) is limited to the high-order harmonic plateau where the constant amplitude approximation [Eq. (12)] and the linearization of $\varphi_{min}(t)$ [Eq. (20)] are sound. The *in situ* method can also be applied to the second (long) branch of trajectories. The correction factor for the long branch is $\gamma \approx 0.88$ for $t_c = 0.55T_R$.

We want to stress that the *in situ* method is *not* a direct measure of the emission time (or the group delay) because $\varphi_{min}(t)$ is not related to the return time in a trivial way [Eq. (19)]. In fact, one could also interpret the *in situ* method as a measurement of the continuum time which is an equally good parameter of the process.

All technical details aside, we have found that the *in situ* method produces traces of oscillating even harmonics which, to reasonable agreement, can be treated as RABITT scans. In the following, we will present data which are uncorrected,

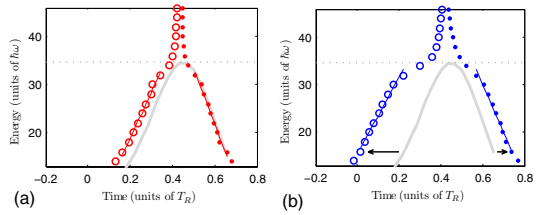

FIG. 3. (Color online) (a) The single atom response of the short (○) and the long (●) branches are calculated using SFA for a typical ir intensity, $I_R = 2\times10^{14}$ W/cm^2. The group delays, $-d\phi/d\omega$, of both branches are in good agreement with the simple classical model (gray line). The group delay branches merge beyond the cutoff (dotted line). (b) The numerical *in situ* scans generated using SFA with a weak blue field, $I_B/I_R = 0.1\%$, show qualitative agreement for both the short (○) and the long (●) branches with the simple classical model (gray line).

$\gamma = 1$, verifying numerically and experimentally the validity of $\gamma \approx 1$ for harmonics in the plateau. Unlike RABITT, the *in situ* method is not limited to sampling the relative timing at only even harmonic energies. The oscillations in the odd harmonic energies [Eq. (17)] can be treated in a similar way, thus doubling the number of sampling points for the relative timing compared to RABITT.

C. Numerical SFA calculation

We perform a numerical experiment using SFA to verify the analytical work presented in Sec. II B for an ir intensity of $I_R = 2\times10^{14}$ W/cm^2. Our numerical calculations are based on Eq. (13) in [5] where the saddle point approximation is done only over $\vec{p}$ space. The integration over continuum time, τ, and actual time, t, is done numerically. This allows us, in a simple way, to access either branch of trajectories by numerically restricting the integral over the continuum time, τ. We calculate the single atom response for the short branch of trajectories by restricting the continuum time integral to $0 < \tau < 0.65T_R$. Then we calculate the response from the long branch of trajectories by restricting the continuum time integral to $0.65T_R < \tau < T_R$. The corresponding group delays are calculated numerically from the first derivative of the spectral phase of the short branch dipole [Fig. 3(a), ○] and the long branch dipole [Fig. 3(a), ●]. The time-energy curves are compared to a simple classical model [Fig. 3(a), gray line], consisting in finding the classical kinetic return energy for a classical electron in a sinusoidal electric field, $E(t) = E_0 \sin\omega t$, which starts and returns to the origin, and then adding the ionization energy.

Next, we perform the numerical *in situ* measurement by calculating the single atom response from the same ir field plus a weak blue field with a relative intensity of $I_B/I_R = 0.1\%$. The phase of the blue field, φ, is then shifted relative to the ir and the atomic response is calculated again. As expected, we obtain weak oscillations in the even harmonics which vary with respect to φ. The relative phases, φ_{min}, that minimize the even harmonic signal are extracted from the short branch [Fig. 3(b), ○] and the long branch [Fig. 3(b),

●]. We find that the *in situ* method produces time-energy slopes [lines in Fig. 3(b)] that are in qualitative agreement with the simple classical model [Fig. 3(b), gray line] for harmonics below the cutoff [Fig. 3(b), dotted line]. There is, however, an absolute time difference between $-\varphi_{min}/\omega_R$, and the (unshifted) simple classical model [Fig. 3(b), gray line]. A careful study of the numerical experiment indicates that the *in situ* measurement suffers from a small systematic deviations from the group delay which can be attributed to the correction factor, γ. We stress that all data presented in Fig. 3(b) are uncorrected, i.e., $\gamma=1$.

A larger and possibly more interesting systematic deviation between the group delay and the *in situ* method arises for harmonics close to and beyond the cutoff [Figs. 3(a) and 3(b), dotted line]. This deviation occurs in a spectral region where Eqs. (3) and (4) are questionable and it is, therefore, more difficult to interpret the deviation. It is clear, however, that the *in situ* measurement is not a direct measurement of the group delay (or the relative timing) of the attosecond pulses and that a deeper analysis is needed for understanding the behavior beyond the cutoff.

The numerical experiment is repeated at progressively higher relative intensities to investigate the robustness of the *in situ* method. We observe the depletion of the odd harmonics, as expected from Eq. (17). The information retrieved from the even harmonics is intact as long as $I_B/I_R<1\%$ for $I_R=2\times10^{14}$ W/cm^2. Increasing the relative intensity further results in an invalid *in situ* measurement.

III. EXPERIMENTAL SETUP

The experimental work is carried out at the Lund Laser Center (LLC) using a kHz Ti-sapphire chirped pulse amplified laser operating at a wavelength of 800 nm (ir). The pulseenergy is 2 mJ and the pulse length is 35 fs. The APTs are generated by focusing the ir laser pulses into a synchronized pulsed argon gas cell [15]. Having a pulsed gas cell allows us to maintain a low average background pressure in the generation chamber while the effective gas pressure in the gas cell is high. We do not measure the instantaneous generation pressure in the gas cell but it is reasonable to assume that it scales with the average background pressure in the generation chamber.

We use aluminum filters after the HHG to

(i) remove the remaining ir and the low-order harmonics in the pump line and

(ii) compress the pulses in the APT.

Eliminating the intense ir beam after the generation cell is important since neither of the characterization schemes work if there is a strong ir field present in the detection process. The individual filters are 200 nm thick and the number of filters used can be changed using a motorized filter holder [6]. Being able to change the number of filters is important in order to access the effect of filters on the attosecond pulses [3]. The attosecond pulses are finally detected using a magnetic bottle electron spectrometer (MBES). The detection gas is argon which allows us to study the high-order harmonics from the plateau and cutoff regions.

In the RABITT method the ionization step in the MBES is perturbed by a synchronized weak ir probe field, which is coupled into the MBES using a Mach-Zehnder interferometer [Fig. 4(a)]. The relative phase, φ, between the APT and the ir is controlled using a piezoelectric translation stage in the interferometer. A typical RABITT scan is shown in Fig. 4(b).

In the *in situ* method the ir pulse is used to generate a second harmonic field (blue) with a 1.3-mm-thick potassium dideuterium phosphate (KDP) type-I crystal. The ir and the blue field are synchronized before the generation chamber using a three-dimensional dichroic interferometer [Fig. 4(c)]. A glass plate in the interferometer enables control of the relative phase, φ, between the ir and the blue fields. The interferometer is engineered so that the polarizations of the recombined red and blue fields are parallel [16]. A typical *in situ* scan is shown in Fig. 4(d). Using Eqs. (11) and (21), we know that the information about the attosecond pulses is derived in the same way from both methods, while the physical interpretation of the two measurements differs.

IV. PROOF OF PRINCIPLE FOR *IN SITU* MEASUREMENTS

In this section, we study the properties of an APT using both the RABITT and the *in situ* method. A direct comparison of the two measurements is not meaningful since attosecond pulses are probed at different times. Two main effects influence the properties of the attosecond pulses:

(i) dispersion from the Al filters;

(ii) phase matching in the generation cell.

To avoid effects due to phase matching as much as possible [2,17], we perform the measurement at the lowest possible pressure, corresponding to a background pressure of $P_G\approx1.5$ μbar. At this pressure, the high-order harmonic signal is weak but still stable enough for both characterization methods to work. The results from the RABITT method are shown in Fig. 5(a) and the results from the *in situ* method are shown in Fig. 5(b).

The change in relative timing induced to an attosecond pulse propagating through one aluminum filter, $\Delta t_{\mathrm{Al}}^{(rel)}(\omega,\omega_0)$, can be determined using two RABITT measurements,

$$\Delta t_{\mathrm{Al}}^{(rel)}(\omega)=t_{final_2}^{(rel)}(\omega)-t_{final_1}^{(rel)}(\omega), \tag{22}$$

where $t_{final_1}^{(rel)}$ is the relative timing of the attosecond pulse having passed one filter and $t_{final_2}^{(rel)}$ is the relative timing after passing two filters. Note that we now drop the notation for the reference frequency since it is $\omega_0=14\omega_R$ for all experimental data. We have verified that $\Delta t_{\mathrm{Al}}^{(rel)}(\omega)$ agrees with the GD deduced from the refractive index of aluminum [18]. Assuming that the two filters are identical we can calculate the relative timing of the attosecond pulse before passing the filter(s),

$$t_{final_0}^{(rel)}(\omega)=t_{final_1}^{(rel)}(\omega)-\Delta t_{\mathrm{Al}}^{(rel)}(\omega). \tag{23}$$

The "unfiltered" relative timing of attosecond pulses [Fig. 5(a), ○] is in good agreement with the simple classical model (gray line) for an effective intensity of $I_R\approx1$

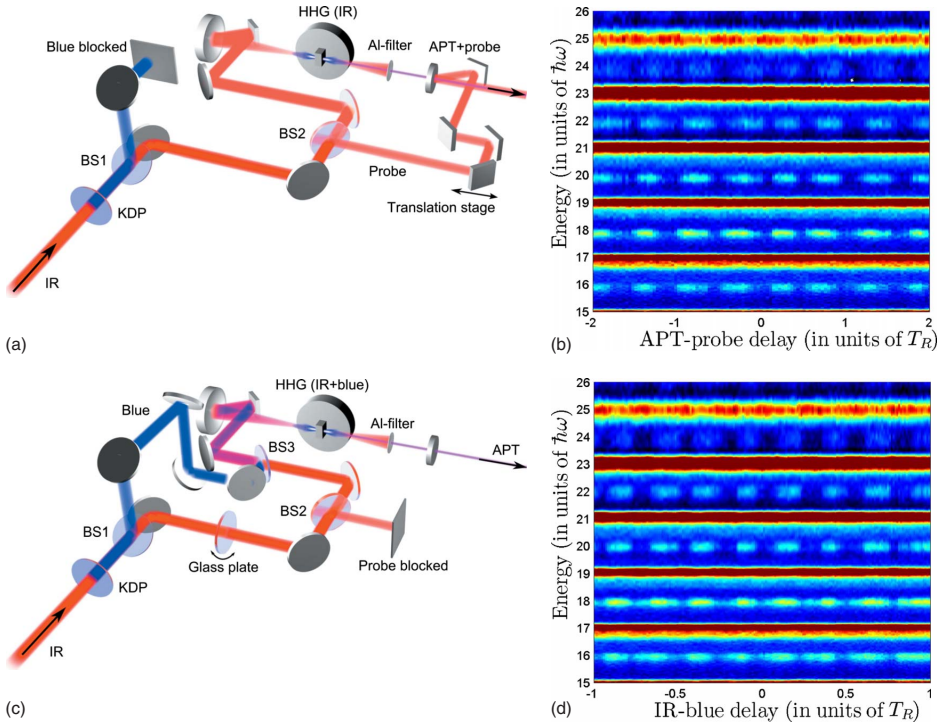

FIG. 4. (Color online) (a) In RABITT mode the blue field (from KPD) is split off (BS1) and blocked. A weak ir probe field is created (BS2) and delayed on the subcycle scale using a translation stage. The APT is generated from the intense ir pulses [HHG (ir)] in a synchronized pulsed gas cell. The intense ir field is eliminated using aluminum filter(s). The APT and the probe are recombined (APT +probe) using a mirror with a narrow aperture. The APT passes through the aperture while the probe is reflected on the mirror. The temporally overlapping APT and probe field are then focused using a toroidal mirror and detected using an electron spectrometer (not shown). (b) The RABITT scan is recorded using an electron spectrometer with subcycle synchronization of the APT and the probe in the detection chamber. (c) In *in situ* mode the ir and the blue field (from KDP) are separated (BS1) into a dichroic interferometer. The ir field is delayed on the subcycle scale using a glass plate (which can be tilted) before it is recombined with the blue field (BS3). The probe is blocked (after BS2). The APT is generated from intense ir pulses in the presence of a weak blue field [HHG (ir+blue)] in a synchronized pulsed gas cell. The ir and blue fields are eliminated using aluminum filter(s). The APT is detected using an electron spectrometer (not shown) after passing a narrow aperture. (d) The *in situ* scan is recorded using an electron spectrometer with subcycle synchronization of the ir and the blue fields in the generation cell [HHG (ir+blue)]. The color scale in (b) and (d) is saturated so that the interferometric beating is more clearly seen.

$\times 10^{14}$ W/cm^2. This intensity corresponds to a cutoff at harmonic (23), which agrees well with spectral measurements taken without the probe field present.

Having estimated the initial state of the attosecond pulses using the RABITT method, we now proceed with the *in situ* scheme. One important advantage of the *in situ* scheme is that all information is imprinted spectrally, which makes it possible to analyze attosecond processes with great accuracy using a photon spectrometer rather than an electron spectrometer. In this paper, however, we use the same MBES as for the RABITT so that a straightforward comparison of the two schemes is made.

The *in situ* measurements are taken immediately after their respective RABITT measurements for one and two aluminum filters [Fig. 5(b)]. The HHG conditions, therefore, have little time to evolve when changing schemes (a few seconds). The filters should not influence the *in situ* measurement because the information is imprinted spectrally already in the HHG process. Using the *in situ* scheme, we should ideally obtain identical information regardless of the number of filters. The measurements again nicely follow the classical model for $I=1\times10^{14}$ W/cm^2 (gray curve). We determine the initial relative timing, $t^{(rel)}_{initial}(\omega)$, and compare it to the relative timing obtained with the RABITT method, $t^{(rel)}_{final_0}(\omega)$, in Fig. 5(c). The corresponding group delay dispersion (GDD) is calculated by fitting a line to the relative timing using sidebands and even harmonics (14)–(22),

$$-\left.\frac{d^2\phi}{d\omega^2}\right|_{18\omega_R} \approx \begin{cases} 2.31\times10^4 \text{ as}^2/\text{rad} & \text{(RABITT)} \\ \gamma\times 2.24\times10^4 \text{ as}^2/\text{rad} & (\textit{in situ}), \end{cases} \tag{24}$$

with a root mean square deviation of approximately 23 as for

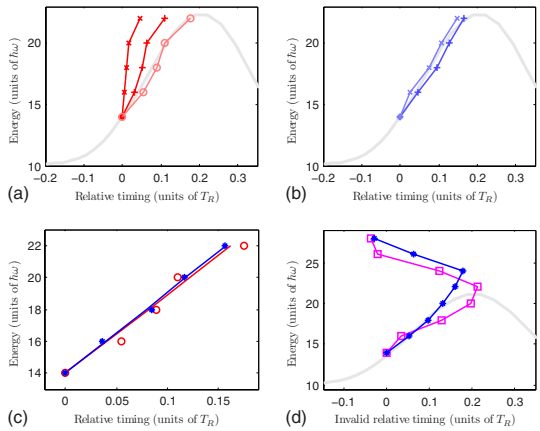

FIG. 5. (Color online) (a) RABITT measurements with one (+) and two (×) aluminum filters are used to determine the relative timing of the unfiltered attosecond pulses (○). All temporal measurements are presented as relative timings with reference to harmonic (14). (b) *In situ* measurements with one (+) and two (×) aluminum filters. The data are uncorrected, γ=1. The simple classical model (I_R=1×10^{14} W/cm^2) [(a) and (b) gray curve] is plotted for reference. (c) Unfiltered RABITT measurement (red, ○) compared to the average *in situ* measurement (blue, *). (d) A slight increase in the blue intensity (blue, *) has a small effect on the measurement in the harmonic plateau [harmonics (14)–(24). Increasing the blue intensity further (pink, □) results in an invalid measurement. The simple classical model (I_R=0.9×10^{14} W/cm^2) (gray line) is plotted for reference.

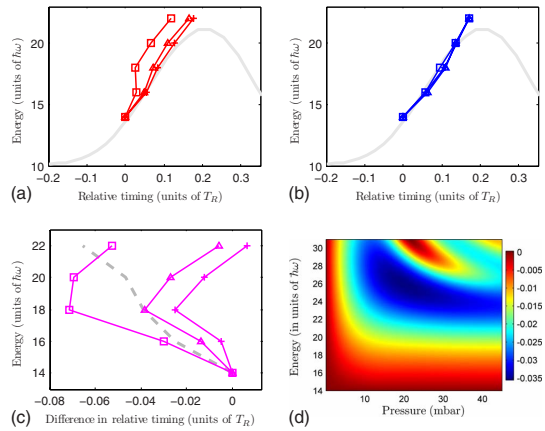

FIG. 6. (Color online) (a) Relative timing measurements from RABITT for a variety of high background pressures in the generation chamber: 5×10^{-3} (×), 6×10^{-3} (△), and 7×10^{-3} (□) mbar (the exact instantaneous pressure in the gas cell is unknown). The effect of the Al filter has been subtracted. At high pressures there is an increased deviation from the simple classical model (I_R=0.9×10^{14} W/cm^2) (gray curve). (b) The corresponding *in situ* measurements are mostly unaffected by the increased pressure. The data are not corrected, γ=1. (c) The difference in relative timing, $\Delta t^{(rel)}_{macro}(\omega, P_G)$ (pink ×, △, and □), is interpreted as the macroscopic delay due to phase matching in the gas cell. The symbols correspond to the same pressures as in the figures above. The delay from phase matching has approximately the same magnitude as an aluminum filter (gray dashed curve). (d) The relative timing due to phase matching (false color in units of T_R) is calculated using a one-dimensional model [17] for pressures ranging from 0 to 100 mbar. The intensity used in the model is 1.25×10^{14} W/cm^2 and the duration of the pulse is 35 fs. The length of the cell is modeled as 5 mm.

the corresponding difference in relative timing. We treat the *in situ* data as a RABITT scan, and the numerical value of the GDD must, therefore, be multiplied by the correction factor, γ. The experiment shows that the correction factor is close to unity for the short branch, as expected from the theory section. The good agreement between these measurements shows that either the RABITT or the *in situ* method can be used to characterize the APTs at low generation pressures for energies in the central and upper regions of the harmonic plateau.

It is tempting to increase the intensity of the blue field so that the even harmonics become stronger and more visible. We use an adjustable aperture in the blue arm of the three-dimensional dichroic interferometer so that the intensity of the blue field can be increased while all other experimental parameters are constant. It has been demonstrated that an increased blue intensity will alter the quasiclassical trajectories in the HHG process [19,20], but a systematic study of how the *in situ* method breaks down has not yet been reported. Even harmonic oscillations appear *beyond the cutoff* for a slight increase in the blue intensity. The information extracted from these oscillations show strong deviations with the expected group delays, while the information from the plateau region remains rather accurate [Fig. 5(d), *]. Even harmonic oscillation beyond the cutoff regime should, therefore, not be included in our simple interpretation [Eq. (21)] of the *in situ* method. The experimental results at high photon energy are in qualitative agreement with the numerical calculations of the long branch shown in Fig. 3(b) shifted by half their period. At moderately higher blue intensities we observe a shift of the modulations in the plateau [Fig. 5(d), □]. This shows that the *in situ* method now predicts the wrong relative timing for the initial attosecond pulses also in the plateau region and that the relative intensity must be reduced.

V. COMPARISON OF RABITT AND *IN SITU* MEASUREMENTS AT HIGHER PRESSURE

We now study how the phase of the attosecond pulses is modified due to a higher gas pressure in the generation chamber. It has recently been shown that in some conditions an increasing gas pressure can lead to a compression of the attosecond pulses [17]. The effect predicted theoretically was, however, small and difficult to demonstrate experimentally. Here, combined measurements using the RABITT and the *in situ* method allow us to unambiguously extract the contribution of phase matching to the temporal structure of attosecond pulses.

RABITT results obtained at different pressures are shown in Fig. 6(a). The data are collected with one aluminum filter,

but the effect of this filter is removed using Eq. (23). The corresponding *in situ* measurements are shown in Fig. 6(b). The *in situ* measurements are mostly insensitive to the increased gas pressure, while the RABITT measurements are deformed in a nontrivial way. Deviations in relative timing for attosecond pulses due to the macroscopic propagation through the gas cell can be extracted by subtracting the final and initial relative timings,

$$\Delta t^{(rel)}_{macro}(\omega, P_G) = t^{(rel)}_{final_0}(\omega, P_G) - t^{(rel)}_{initial}(\omega, P_G), \qquad (25)$$

where we have explicitly written P_G to indicate that the macroscopic effects depend on the gas pressure. In $t^{(rel)}_{initial}(\omega, P_G)$, the P_G dependence refers to a possible change in the fundamental field in the nonlinear medium that could affect the single atom response. The results are shown in Fig. 6(c), together with the effect of a 200 nm Al filter (gray). Macroscopic effects introduce a (nontrivial) negative relative timing, first decreasing then increasing with frequency. The corresponding induced GDD might help to compensate for the single atom GDD for low orders, but for higher orders the GDD is increased. These results agree well with those presented in [17].

To understand the origin of the macroscopic group delay, we perform a simple model calculation [17,21]. We consider for simplicity a one-dimensional approximation along the propagation axis z, a homogeneous medium of length L, and a collimated geometry. In this simple case, the contribution of the single atom response and of propagation can be separated and the effect of propagation both on the phase (or more exactly phase variation) and amplitude of the nth harmonic can be described by

$$F_n = \frac{1 - \exp[(-i\Delta k_n - \kappa_n)L]}{i\Delta k_n + \kappa_n} = |F_n| \exp[i\phi_n^{mac}]. \qquad (26)$$

The phase mismatch Δk_n is equal to $k_n - nk_1$, where k_n and k_1 denote the wave vector of harmonic n and the fundamental, respectively. Absorption at the nth harmonic frequency is described by κ_n. The macroscopic phase can be written as

$$\phi_n^{mac} = -\arctan\left[\frac{\sin[\Delta k_n L]}{\cos[\Delta k_n L] - \exp[\kappa_n L]}\right] - \arctan\left[\frac{\Delta k_n}{\kappa_n}\right]. \qquad (27)$$

Figure 6(d) presents in color its derivative as a function of harmonic order and pressure. These results show a variation in the phase derivative that qualitatively agrees with the measured one. For a given pressure >20 mbar, the induced GD is negative, showing a decrease at low orders, a minimum around the 23rd harmonic, followed by an increase. We stress that this satisfactory agreement is obtained with a simple model, not including the geometric phase due to focusing or two-dimensional effects. Combined RABITT and *in situ* measurements provide a way to really unravel the effect of propagation in the generation of attosecond pulses.

VI. CONCLUSIONS

We have performed a proof of principle experiment for the *in situ* scheme by comparing it to the well established RABITT method. We have found excellent agreement between the methods at low generation gas pressures when the macroscopic phase matching plays a negligible role.

We have found that it is not possible to use the *in situ* scheme to predict the final relative timing of the average attosecond pulses if the generation pressure is high or if it passes through some unknown dispersive material. It is equally important to realize that accurate single atom measurements cannot be conducted at high generation gas pressures with the RABITT scheme. In a RABITT measurement there will always be a trade off between the number of harmonic photons generated and their phase perturbation from propagation through the generation cell.

The advantages and disadvantages of the two schemes become quite clear when the generation pressure is high and one could argue that *both* schemes are needed for a more complete understanding of the attosecond pulse production and propagation.

ACKNOWLEDGMENTS

We thank Lou DiMauro for valuable comments on this work. This research was supported by the Marie Curie programmes (MAXLAS, ATTOCO) of the European Union, the European and Swedish Reseach Councils and the Kunt and Alice Wallenberg Foundation.

[1] P. M. Paul *et al.*, Science **292**, 1689 (2001).
[2] M. B. Gaarde, J. L. Tate, and K. J. Schafer, J. Phys. B **41**, 132001 (2008).
[3] R. López-Martens *et al.*, Phys. Rev. Lett. **94**, 033001 (2005).
[4] Y. Mairesse *et al.*, Science **302**, 1540 (2003).
[5] M. Lewenstein, P. Balcou, M. Y. Ivanov, A. LHuillier, and P. B. Corkum, Phys. Rev. A **49**, 2117 (1994).
[6] E. Gustafsson *et al.*, Opt. Lett. **32**, 1353 (2007).
[7] A.-S. Morlens *et al.*, Opt. Lett. **31**, 1558 (2006).
[8] N. Dudovich *et al.*, Nat. Phys. **2**, 781 (2006).
[9] J. Itatani *et al.*, Nature (London) **432**, 867 (2004).
[10] Even harmonics are not generated if there is no blue field present due to parity conservation.
[11] J. Mauritsson, M. B. Gaarde, and K. J. Schafer, Phys. Rev. A **72**, 013401 (2005).
[12] Except for the carrier envelope phase of the attosecond pulse.
[13] M. Lewenstein, P. Salières, and A. L'Huillier, Phys. Rev. A **52**, 4747 (1995).
[14] P. Salières *et al.*, Science **292**, 902 (2001).
[15] D. Proch and T. Trickl, Rev. Sci. Instrum. **60**, 713 (1989).
[16] J. Mauritsson, J. M. Dahlström, and T. Fordell, J. Phys. B **42**, 134003 (2009).
[17] T. Ruchon *et al.*, New J. Phys. **10**, 025027 (2008).

[18] O. E. Martinez, J. P. Gordon, and R. L. Fork, J. Opt. Soc. Am. B **1**, 1003 (1984).
[19] J. Mauritsson, P. Johnsson, E. Gustafsson, A. LHuillier, K. J. Schafer, and M. B. Gaarde, Phys. Rev. Lett. **97**, 013001 (2006).
[20] E. Mansten *et al.*, New J. Phys. **10**, 083041 (2008).
[21] E. Constant, D. Garzella, P. Breger, E. Mevel, C. Dorrer, C. Le Blanc, F. Salin, and P. Agostini, Phys. Rev. Lett. **82**, 1668 (1999).

PAPER V

Intensity Dependence of Laser-Assisted Attosecond Photoionization Spectra

M. Swoboda, J. M. Dahlström, T. Ruchon, P. Johnsson, J. Mauritsson, A. L'Huillier and K. J. Schafer.

Laser Physics **19**, 1591 (2009).

ISSN 1054-660X, Laser Physics, 2009, Vol. 19, No. 8, pp. 1591–1599.
© Pleiades Publishing, Ltd., 2009.
Original Russian Text © Astro, Ltd., 2009.

ATTOSECOND PULSES

Intensity Dependence of Laser-Assisted Attosecond Photoionization Spectra[1]

M. Swoboda[a, *], J. M. Dahlström[a], T. Ruchon[a, c], P. Johnsson[a], J. Mauritsson[a], A. L'Huillier[a, **], and K. J. Schafer[b]

[a] *Department of Physics, Lund University, P.O. Box 118, Lund, 22100 Sweden*
[b] *Department of Physics and Astronomy, Louisiana State University, Baton Rouge, Louisiana 70803-4001, USA*
[c] *CEA-Saclay, DSM, Service des Photons, Atomes et Molécules, Gif sur Yvette, 91191 France*
*e-mail: marko.swoboda@fysik.lth.se
**e-mail: anne.Lhuillier@fysik.lth.se
Received March 20, 2009; in final form, March 24, 2009

Abstract—We study experimentally the influence of the intensity of the infrared (IR) probe field on attosecond pulse train (APT) phase measurements performed with the RABITT method (Reconstruction of Attosecond Beating by Interference in Two-Photon Transitions). We find that if a strong IR field is applied, the attosecond pulses will appear to have lower-than-actual chirp rates. We also observe the onset of the streaking regime in the breakdown of the weak-field RABITT conditions. We perform a Fourier-analysis of harmonic and sideband continuum states and show that the mutual phase relation of the harmonics can be extracted from higher Fourier components.

PACS numbers: 32.80.Fb, 32.80.Rm, 33.20.Xx, 33.60.+q, 42.65.Ky

DOI: 10.1134/S1054660X09150390

I. INTRODUCTION

Laser-assisted ionization processes provide an elegant tool to study dynamics and details of atomic and molecular systems [1–3]. For time-dependent measurements, the assisting laser needs to be synchronous to the ionization event on a time scale shorter than that of the process to be resolved. A number of experiments in the past years have shown that the attosecond (as) time scale is routinely accessible and laser-assisted ionization processes have become the chief tool for experiments in the field of attosecond science [1–6].

The emission of a comb of high-order harmonics when an atomic medium is exposed to a driving intense laser field is well understood. The resulting attosecond pulse trains (APT) [7, 8] provide a premier tool to controllably ionize atomic media [5, 9] and it is important to determine their characteristics, both amplitude and phase. This can be done by cross-correlation with an IR probing field under stable interferometric conditions. Using weak infrared (IR) fields, this is often done with the Reconstruction of Attosecond Beating by Interference of Two-Photon Transition (RABITT) method [7], while the AC-Streak camera method [10, 11], using stronger IR fields, has mainly been applied to the characterization of isolated attosecond pulses. A special case is the full characterization method FROG-CRAB (Frequency-Resolved Optical Gating-Complete Reconstruction of Attosecond Bursts), which is based on an iterative deconvolution of a time-frequency spectrogram [12, 13]. In this paper, we study the transition from the weak to the strong field regime, and the effect of the probe field strength on the validity of the characterization.

In Section 2, the experimental setup and performed experiments will be presented. We perform in Section 3 a conventional analysis of the data in the RABITT regime, studying specifically the probe intensity dependence of the phase measurement. A Fourier-series approach (Section 4) allows us to see the fingerprints of processes with more than one contributing IR photons and provides a more general description of our delay-dependent laser-assisted photoionization spectra.

2. EXPERIMENT

2.1. Setup

The experiments were performed at the High Power Laser Facility of the Lund Laser Centre. We use a 1 kHz chirped-pulse-amplification (CPA) titanium-sapphire based laser system, providing 2 mJ 30 fs pulses centered around 800 nm. The pulses are focused into an Ar gas cell, pulsed at 1 kHz, to generate high-order harmonics, which then propagate through silica plates and a thin Al-foil to filter the harmonics to form a well-defined APT (cf. Fig. 1). The APT is then recombined with an IR probe beam in a Mach–Zehnder-type interferometer. In the last step of the interferometer, the APT is passed through a drilled mirror while the IR is reflected on the back side of the

[1] The article is published in the original.

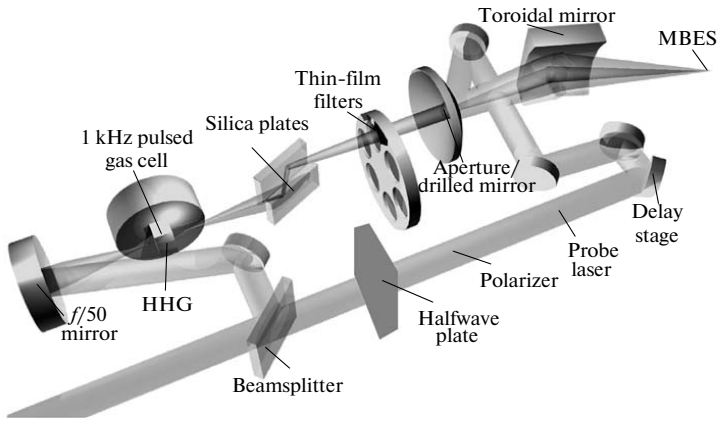

Fig. 1. Setup for the experiment: a 2 mJ, 30 fs laser pulse is split into a probe and a pump arm. The larger part is used in high-order harmonic generation while a fraction travels through a delay stage to serve as probe pulse. The generated harmonics are filtered spectrally and spatially by silica plates, a thin-film metallic filter and an aperture, before recombining with the probe using a drilled mirror and being focused into the detection gas of a magnetic bottle electron spectrometer.

mirror. Both beams are focused into the detection gas of a magnetic-bottle electron spectrometer (MBES) with the help of a toroidal mirror. Using a combination of half-wave plate and polarizer in the probe beam, the pulse energy of the IR can be varied continuously between 5 and 100 μJ. As all focusing parameters are kept constant, any change in the probe pulse energy will directly result in a proportional change of the IR intensity in the detection region of the MBES. The MBES has a 2π acceptance angle and a maximum energy resolution of about 100 meV.

The relative delay of IR probe and APT can be adjusted on two time scales. Using a motorized translation stage in the probe arm we can vary the delay in the range of one femtosecond to several picoseconds. To accurately resolve attosecond processes, a delay stage with a piezoelectric crystal is used to change the relative phase of the two beams with a precision of a few tens of as. This stability allows us to perform interferometry of two-photon pathways as in the RABITT characterization scheme, as shown below. It is also crucial for the use of the AC streak camera method, where the relative phase of the two beams has to be stable with similar precision.

2.2. Delay-Dependent Two-Color Photoionization Spectra

In the experiments presented here, the resulting photoelectron spectra from an IR probe and XUV field were recorded. A shift in the relative delay of the two fields induces a change in the observed spectrum, and recording the spectra at different subcycle delays allows us, in some conditions, to determine the temporal structure of the XUV emission.

Figure 2 shows the seven scans that constitute our experimental results. From left to right, the probe pulse energy changes by a factor of 20, ranging from 5 to 100 μJ. At the lowest intensity, the presence of a weak IR field leads to weak sidebands between the odd harmonic orders. These sidebands originate from $\omega_n + \omega_R$ and $\omega_n - \omega_R$ two-photon transitions [14], where ω_R is the IR photon frequency and $\omega_n = n\omega_R$, with n being an odd integer, see Fig. 3a. The two possible pathways to each final state lead to the observed interference pattern. This pattern is repeated every IR half-cycle, $T_R/2$, reproducing the frequency of the attosecond pulse periodicity. This probe intensity regime is commonly referred to as the RABITT regime.

With increasing IR intensity, the amplitude of the sidebands becomes comparable to direct photoionization by the harmonics (see, e.g. sideband 22 in Figs. 2d–2g). These two-photon processes induce a depletion of the peaks at odd harmonic energies, at the delays where the sidebands are maximum. The cutoff region is first affected by depletion since the strength of continuum-continuum transitions rapidly increases with the energy of the initial state (Figs. 2b and 2c at harmonic 25 and above). For a probe pulse energy of 40 μJ (Fig. 2d), depletion effects become visible even in the low energy region (see harmonic 19 to 23 in Figs. 2d–2g).

At the higher probe intensities (Figs. 2d–2g), processes involving more than one IR photon become significant. This is the so-called streaking regime, where the AC-streak camera becomes the preferred charac-

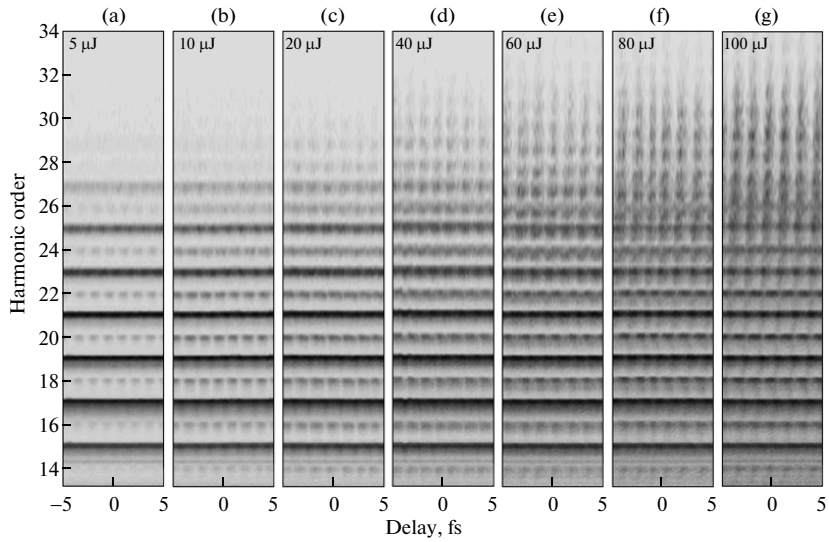

Fig. 2. XUV photoionization spectra, recorded for varying sub-cycle delay between IR and XUV field. The corresponding probe pulse energies are written in the upper part of the figures. A change of this energy translates proportionally to a change of the probe intensity. The zero delay indicates the delay at which the maxima of the IR pulse and the APT coincide.

terization method [10, 11, 13]. The streaking regime is clearly entered in the last two of the scans in Fig. 2, the cutoff being increased by as much as seven IR photons (from harmonic 27 and above). Note that the electron signal is still showing discrete IR photon energy spacing because of the periodicity of photoionization from the sequence of attosecond pulses.

3. ANALYSIS OF THE EXPERIMENT

3.1. Reconstruction of Attosecond Beating by Interference in Two-Photon Transitions (RABITT)

We now analyze the results in Fig. 4 (same as Fig. 2a) within a perturbation theory framework. Here, we will consider the photoionization of the detection gas by the APT as a first-order perturbation and the onset of the sidebands and the RABITT modulation as a perturbation of the second order. This is a good description of two-color photoionization at low IR intensities.

Contributions to the final state probability amplitudes of order N can be obtained from those of order $(N-1)$ through the following equation [15, 16]:

$$a_m^{(N)}(t) = \frac{1}{i\hbar}\sum_f\sum_l \int_0^t dt' \mu_{m,l} E(\omega_f) a_l^{(N-1)}(t') e^{i(\omega_{ml}-\omega_f)t'}, \quad (1)$$

where l is the index of the respective contributing states, ω_f are the frequencies acting on the atom and m denotes the final state. The effect of the IR on the ground state is negligible. The population of continuum states after perturbing the system with a harmonic frequency can be approximated by

$$a_n^{(1)}(t) = \frac{\mu_{n,g} E(\omega_n)}{i\hbar} t, \quad (2)$$

where $\mu_{n,g}$ is the transition dipole matrix element from the ground to the continuum state, and t the interaction time, approximately a measure of the pulse duration. The population of the sideband state $(n-1)$ can be expressed as

$$\begin{aligned} a_{n-1}^{(2)}(t) &= \frac{1}{(i\hbar)^2}\frac{t^2}{2}[\mu_{n-1,n-2}\mu_{n-2,g}E(\omega_R)E(\omega_{n-2}) \\ &\quad + \mu_{n-1,n}\mu_{n,g}E(-\omega_R)E(\omega_n)] \\ &\approx M\frac{E_{R0}E_{X0}}{(i\hbar)^2}\frac{t^2}{2}[e^{i(\phi_R+\phi_{n-2})} + e^{i(-\phi_R+\phi_n)}], \end{aligned} \quad (3)$$

where the factor M represents a combination of the various transition dipole moments, which we approximate as equal for both quantum paths, and E_{R0}, E_{X0} are the amplitudes of the IR and XUV fields. The sideband intensity will finally oscillate

$$I_{n-1}^{(2\omega)}(\varphi) \propto \cos(2\phi_R + \Delta\phi_{n-2,n}), \quad (4)$$

with $\phi_R = \omega_R\tau$, τ being the delay between the XUV and the IR fields. $\Delta\phi_{n-2,n}$ is the phase difference between the harmonic spectral phases ϕ_{n-2} and ϕ_n. This allows

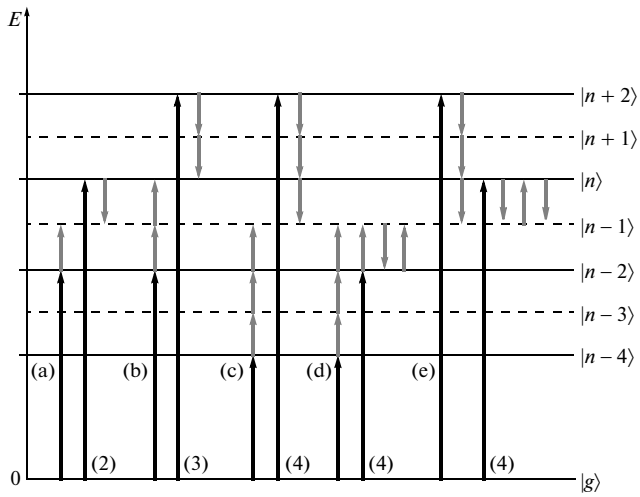

Fig. 3. Sketch over possible transitions involving single harmonic- and multiple IR photons. (a) Shows the RABITT transition, which couples two harmonic photons with an energy difference of $2\omega_R$ to a final state with energy $(n-1)\omega_R$. (b) Shows that the absorption/emission of two IR photons leads to a similar coupling with odd final energy $n\omega_R$. (c) Illustrates that yet another IR photon can be used to couple harmonic photons that are $6\omega_R$ apart in an even final energy $(n-1)\omega_R$. (d, e) Shows that three IR photons will also couple new harmonics that are $2\omega_R$ apart in even final energy $(n-1)\omega_R$, which will distort the information from the RABITT signal in (a).

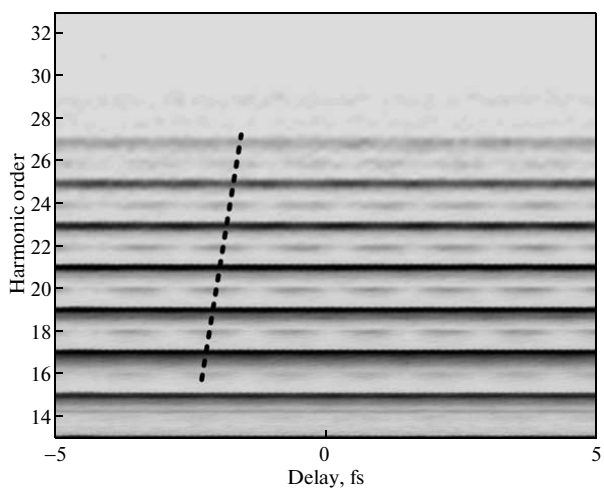

Fig. 4. Delay-dependent photoionization spectrum in the RABITT regime, measured at 5 μJ probe pulse energy. The dashed line indicates the sideband maxima.

us to obtain the phase difference $\Delta\phi_{n-2,n}$ from a Fourier transform of the spectrum over delay.

Using the obtained phase, we can reconstruct a pulse shape as in Fig. 5. The Fourier limit for our spectrum is 160 as. Due to the chirp rate of 18400 as^2 we obtain an average pulse duration of 440 as FWHM. This method of measuring APTs has been successfully employed in a number of experiments [7, 8, 17]. The

high chirp rate and asymmetric pulses come as no surprise as only one thin aluminum filter was employed to counter the intrinsic chirp of the HHG process. The addition of more filters would help to approach the Fourier limit and further compress the pulses [17, 18]. The RABITT method provides access to the relative phase difference of presumably monochromatic harmonics [7, 14]. The measured phase difference is equal to the group delay (GD) over the spectrum of the APT, and an integration allows us to reconstruct an average attosecond pulse in the train. Such a retrieved pulse represents a good approximation for pulses within the FWHM of the APT, accounting for about 90% of the signal from experiments with such trains. There are extensions and implementations of the method that yield more information on the full structure of the APT [19, 20].

3.2. Intensity Dependence of RABITT Signal

The influence of an intense probe field on the measured spectral phase was studied by progressively increasing the IR intensity and recording the delay-dependent photoionization spectra. Figure 6 shows the phase differences $\Delta\phi_{n-2,n}$ evaluated according to the method outlined above, for varying probe intensities. It is clear that the slope is decreasing with increasing intensity, as if the chirp rate was lower, even though the actual APT remained the same.

As a consequence of the phase variation with intensity shown in Fig. 6, the reconstructed pulses will appear more compressed at higher probe intensities, which is a pure artifact of the increased IR intensity. The RABITT analysis relies heavily on the presence of a single IR photon contributing to the final state as to allow only the phase difference of the neighboring harmonics to be measured. Higher-order processes perturb the RABITT signal, as will be discussed in more detail in Section 4.

3.3. Streaking

We now consider briefly the regime of high probing intensities (Fig. 7, same as Fig. 2g) where the interaction between photoelectrons and probing laser field can be understood by simple classical arguments. In this regime, an electron is released into the continuum at a given ionization time t_i due to photoionization by an attosecond pulse. It will gain an additional momentum proportional to the IR vector potential $\mathbf{A}(t_i)$ at the time of ionization. This momentum shift imparted by the IR probe is therefore dependent on the relative delay between the two fields. With APTs generated by two-color fields, or with single attosecond pulses, the pulse properties (duration and chirp) can be extracted from analyzing the streaking trace and the pulse(s) can be reconstructed [10, 11, 13]. In the case of an APT with two pulses per cycle, the situation is more complex and a reconstruction of the attosecond pulses

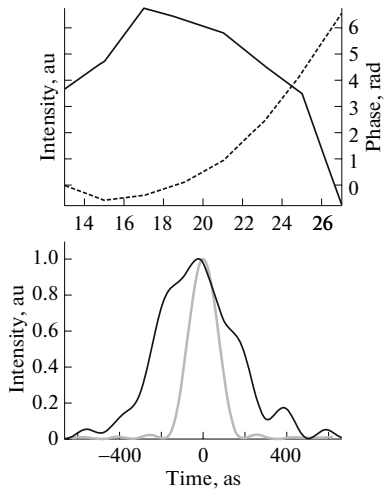

Fig. 5. Reconstruction of average pulse in the pulse train, measured by the RABITT method. The upper panel shows the harmonic intensities (solid line) and integrated spectral phase (dashed line). Using these intensities and phase, one can reconstruct the pulse shape as in the lower panel. The Fourier limited pulse shape is shown as dashed.

from the experimental data is more difficult, since the sign of the probe field reverses for consecutive pulses. Without going further with the analysis of our experimental data, we note that the chirp of our attosecond pulses, however, is clearly visible in the high energy region of the spectrum (see dashed line in Fig. 7). The onset of the streaking regime also explains the observed phase shift of the sideband orders close to the cutoff in Fig. 6. In the perturbative regime and, for simplicity, in absence of attosecond chirp, the maxima of the sidebands occur at the maxima of the probe laser electric field. At moderate probe intensity, depletion of the harmonic states will lead to maxima of the harmonics shifted by $\pi/2$ with respect to the sidebands, thus corresponding to the zeros of the electric field. At high energy, electron peaks, coming from direct electrons being streaked by the probe field, will therefore be maxima at the zeros of the electric field, thus shifted by a factor $\pi/2$ from the sidebands.

4. FOURIER DECOMPOSITION OF THE PHOTOELECTRON SPECTRA

4.1. Perturbation Theory Analyzis

To better understand the influence of a high IR intensity on a RABITT measurement, we extend the analyzis performed in the previous section, based on perturbation theory to the next orders. The third order of perturbation includes components coupling the

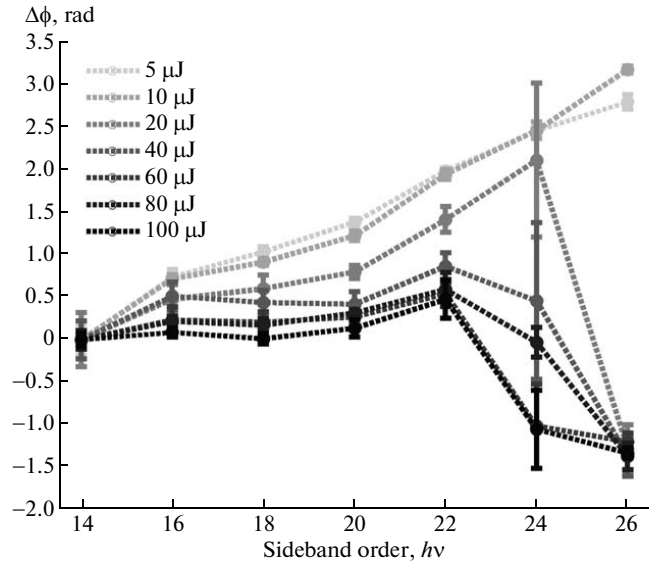

Fig. 6. Phase differences Δϕ measured over the harmonic spectrum, for different probe pulse energies. Higher probe intensities result in a flatter measured spectral phase in the plateau region (order 14–22).

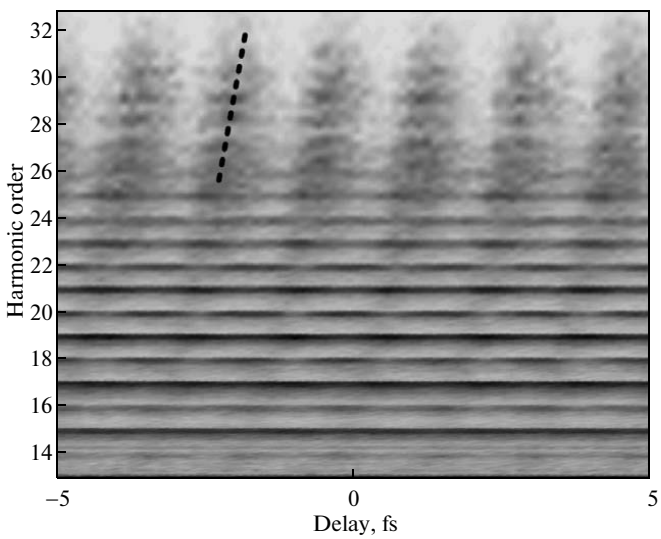

Fig. 7. Delay-dependent photoionization spectrum in the streaking regime, measured at 100 μJ probe pulse energy.

states $(n + 2)$ and $(n - 2)$ to the harmonic (n) state by two IR photon absorption or emission (Fig. 3b):

$$a_n^{(3)} = \frac{1}{(i\hbar)^3}\frac{t^3}{6} \times [\mu_{n,n-1}\mu_{n-1,n-2}\mu_{n-2,g}E(\omega_R)E(\omega_R)E(\omega_{n-2}) + \mu_{n,n-1}\mu_{n-1,n}\mu_{n,g}E(\omega_R)E(-\omega_R)E(\omega_n) + \mu_{n,n+1}\mu_{n+1,n}\mu_{n,g}E(-\omega_R)E(\omega_R)E(\omega_n) + \mu_{n,n+1}\mu_{n+1,n+2}\mu_{n+2,g}E(-\omega_R)E(-\omega_R)E(\omega_{n+2})] \approx M\frac{E_{R0}^2 E_{X0}}{(i\hbar)^3}\frac{t^3}{6}[e^{i(2\phi_R+\phi_{n-2})} + 2e^{i\phi_n} + e^{i(-2\phi_R+\phi_{n+2})}]. \quad (5)$$

This term gives rise to oscillations at frequencies $4\omega_R$, $2\omega_R$, and to a constant term. The intensity of the $4\omega_R$ modulation at the harmonic energy $n\omega_R$ is

$$I_n^{(4\omega)}(\phi_R) \propto \cos(4\phi_R + \Delta\phi_{n-2,n+2}) \quad (6)$$

which is similar to Eq. (4). The next order of perturbation leads to a $6\omega_R$ component in the sideband states and the next to an $8\omega_R$ component in the harmonic states. Higher IR intensities lead to new couplings of states lying further apart and thus higher modulation frequencies.

Figure 3 illustrates how the number of pathways that lead to a given modulation frequency is unique only under certain restrictions. Even numbers of contributing IR photons couple to harmonic states while odd numbers couple to sideband states. The $4\omega_R$ frequency is meaningful only in the harmonic final states, as shown in Eq. (5) and the phase difference that can be determined is that between harmonic states $(n - 2)$ and $(n + 2)$. A Fourier transform that isolates this component will allow us to access to the spectral phase in the same way as with the conventional RABITT, looking at the $2\omega_R$ modulation in the sideband states. Experimentally, due to the resolution of our scans, the $6\omega_R$ component is the highest resolvable. It is already close to the Nyqvist limit, with only three to four data points per period.

Figure 8 shows a comparison of the group delay obtained over the spectrum for three different modulation frequencies. The usual RABITT is based on the 5 μJ-scan, the phases of the $4\omega_R$-modulation were obtained at 20 μJ, and the $6\omega_R$-modulation was present for the central harmonics in the 80 μJ-scan. Excellent agreement was found between the chirp rates obtained with the different methods. Our results are also consistent with previous experiments [8, 17]. From the $2\omega_R$-measurement we obtain a chirp rate of 18400 as^2 or—in terms of a group delay—an emission time difference $\Delta t_e = \Delta\phi/(2\omega_R) = 87$ as. This is very similar to 16800 as^2 ($\Delta t_e = 79$ as) obtained from the $4\omega_R$-component in the harmonics. The slope of the phase difference in the $6\omega_R$-component is also in good agreement with 16900 as^2 chirp rate or a Δt_e of 80 as.

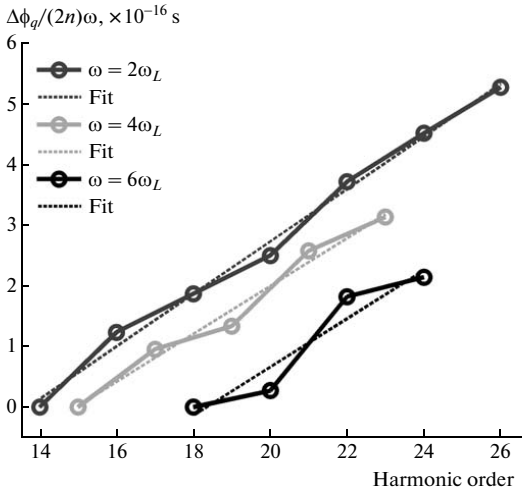

Fig. 8. Comparaison of the obtained phase differences for three different frequency components present in the experimental electron signal. The conventional RABITT includes contribution from sidebands 14 to 26. The $4\omega_R$-component has been extracted from harmonics 15 to 23 and the $6\omega_R$-modulation was obtained from sidebands 18 to 24. The curves have been shifted for better comparison.

4.2. Generalization

Because of the analogy between the conventional RABITT and the possibility to extract the same information from higher components we will now introduce a more general expression for the delay dependence of our photoelectron spectrum. This expression will hold beyond the breakdown of the perturbation picture. The amplitude of any photoelectron peak in the spectrum is periodic with delay ϕ_R between the IR and XUV fields. It can therefore be expressed as a discrete Fourier series:

$$S(\phi_R, I_R) = \sum_{k=-\infty}^{\infty} \tilde{S}_k(I_R)e^{i\phi_R 2k} = \sum_{k=0}^{\infty} S_k(\phi_R, I_R) \quad (7)$$

with $\tilde{S}_k^* = \tilde{S}_{-k}$. Considering only the $k = \pm 1$ contributions we have

$$S_1(\phi_R, I_R) = \tilde{S}_1(I_R)e^{i\phi} + \tilde{S}_1^*(I_R)e^{-i\phi} = 2\left|\tilde{S}_1(I_R)\right|\cos(2\phi_R + \arg(\tilde{S}_1(I_R))), \quad (8)$$

which is the common RABITT case, for low IR intensity, with $\arg(\tilde{S}_1(I_R)) = \Delta\phi_{n-1}$. For higher IR intensi-

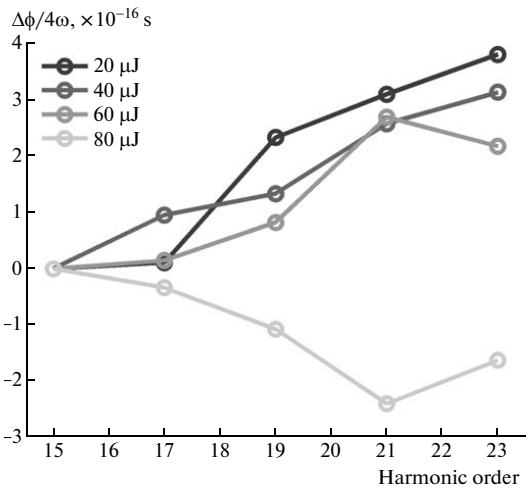

Fig. 9. Intensity dependence of the measured phase from the $4\omega_R$ component in the harmonics. The measured chirp rate over the spectrum shows good agreement at 40 μJ with the $2\omega_R$-measurement from the sidebands. It breaks down at higher probe energy.

ties, higher order terms contribute, the argument will change and higher order terms of the sum $\tilde{S}_k(I_R)$ will grow revealing higher contributing frequencies. In the case of $k = 2$,

$$S_2(\phi_R, I_R) = 2\left|\tilde{S}_2(I_R)\right|\cos(4\phi_R + \arg(\tilde{S}_2(I_R))), \quad (9)$$

which can readily be identified as the $4\omega_R$ component with an argument of $\Delta\phi_{n-2,n+2}$ for a suitable probe intensity. Figures 3d–3e show the effect of the participation of three IR photons, and how two non-surrounding harmonics contribute their phase difference to sideband $n - 1$, destroying the unique source of the $2\omega_R$ modulation. Thus $\arg(\tilde{S}_1(I_R))$ changes and the phase observed in the RABITT analysis varies with IR intensity.

At the same order of perturbation, a $6\omega_R$ modulation can be constructed with three IR photons coupling harmonic $n - 4$ and $n + 2$ to sideband $n - 1$ (cf. Fig. 3d). For sufficiently high intensity, the number of contributing IR photons is $\geqslant 1$, resulting in a great number of frequencies added to form the delay-dependent signal in the sideband. More and more harmonics contribute to the phase, which becomes flat. The oscillation does not uniquely depend on the adjacent orders anymore—the requirement for RABITT. This is the streaking regime, where the classical limit is reached.

As we previously studied the effect of the IR intensity on the phase measurement in the conventional RABITT method, we perform a similar analysis for our measurements with the $4\omega_R$ component. Figure 9 shows the intensity dependence of the harmonic phase measured in this component. We find that at 20 to 60 μJ the phase is meaningful compared with the conventional measurement. The measurement at 80 μJ is showing a similar characteristic flattening of the phase as the conventional RABITT. The $4\omega_R$ breakdown occurs for much higher probe intensities. In this case the number of contributing photons becomes so high that $\arg(\tilde{S}_2(I_R))$ is affected by ambiguous coupling of states. The analyzis of this $4\omega_R$ component provides an additional check on the measured phase from conventional RABITT method. This allows us to assess whether the probe intensities in any experiment have been too high by comparing the $2\omega_R$ with the $4\omega_R$ components and possibly even higher orders.

5. CONCLUSIONS

We have studied the influence of IR probe intensity in two-color XUV photoionization experiments. In the laser-assisted ionization process that is at the heart of the RABITT method for characterizing APTs, the probe intensity needs to be maintained at levels which only perturb the process very slightly. A high probe intensity will greatly alter the measured phase relation of the individual high-order harmonics, making it appear flat over the spectrum, as if the pulses were compressed. RABITT is only valid in the limit of weak IR intensity.

In a next step, the increasing number of contributing IR photons was tracked down by Fourier-analysis of sideband and harmonic states. As an increasing number of photons allows to couple states further and further away, higher modulation frequencies occur. The $4\omega_R$ component of the harmonic states allows us to obtain their mutual phase relation. Also in this case an increasing IR intensity started to affect the phase measurement making the pulses appear artificially compressed. We believe these experiments will allow the scientific community to gain a better understanding of the IR intensity dependence of laser-assisted ionization of a gas using high-order harmonics.

ACKNOWLEDGMENTS

This paper is dedicated to the memory of N.B. Delone, who was a father of this exciting field of research “atoms in strong laser fields,” with the first “multiphoton ionization” (1965) and “multielectron multiphoton ionization” (1975) experimental results. This research was supported by the Marie Curie Intra-European Fellowship (Attotech), the Marie Curie Early Stage Training Site (MAXLAS), the Knut and Alice Wallenberg Foundation, the Swedish Research Council, and the National Science Foundation (Grant no. PHY-0701372).

REFERENCES

1. A. L. Cavalieri, N. Mller, T. Uphues, V. S. Yakovlev, A. B. Caronka, B. Horvath, B. Schmidt, L. Blmel, R. Holzwarth, S. Hendel, M. Drescher, U. Kleineberg, P. M. Echenique, R. Kienberger, F. Krausz, and U. Heinzmann, "Attosecond Spectroscopy in Condensed Matter," Nature **449**, 1029–1032 (2007).
2. M. Drescher, M. Hentschel, R. Kienberger, M. Uiberacker, V. Yakovlev, A. Scrinzi, T. Westerwalbesloh, U. Kleineberg, U. Heinzmann, and F. Krausz, "Time-Resolved Atomic Inner-Shell Spectroscopy," Nature **419**, 803 (2002).
3. J. Mauritsson, P. Johnsson, E. Mansten, M. Swoboda, T. Ruchon, A. L'Huillier, and K. J. Schafer, "Coherent Electron Scattering Captured by an Attosecond Quantum Stroboscope," Phys. Rev. Lett. **100**, 073003 (2008).
4. E. Goulielmakis, M. Uiberacker, R. Kienberger, A. Baltuska, V. Yakovlev, A. Scrinzi, T. West- erwalbesloh, U. Kleineberg, U. Heinzmann, M. Drescher, and F. Krausz, "Direct Measurement of Light Waves," Science **305**, 1267 (2004).
5. P. Johnsson, J. Mauritsson, T. Remetter, A. L'Huillier, and K. J. Schafer, "Attosecond Control of Ionization by Wave-Packet Interference," Phys. Rev. Lett. **99**, 233011 (2007).
6. T. Remetter, P. Johnsson, J. Mauritsson, K. Varjú, Y. Ni, F. Lépine, E. Gustafsson, M. Kling, J. Khan, R. López-Martens, K. J. Schafer, M. J. J. Vrakking, and A. L'Huillier, "Attosecond Electron Wave Packet Interferometry," Nature Phys. **2**, 323 (2006).
7. P. M. Paul, E. S. Toma, P. Breger, G. Mullot, F. Augé, P. Balcou, H. G. Muller, and P. Agostini, "Observation of a Train of Attosecond Pulses from High Harmonic Generation," Science **292**, 1689 (2001).
8. Y. Mairesse, A. de Bohan, L. J. Frasinski, H. Merdji, L. C. Dinu, P. Monchicourt, P. Breger, M. Kovacev, R. Tai'eb, B. Carré, H. G. Muller, P. Agostini, and P. Salieres, "Attosecond Synchronization of High-Harmonic Soft X-rays," Science **302**, 1540 (2003).
9. O. Guyiétand, M. Gisselbrecht, A. Huetz, P. Agostini, R. Taieb, A. Maquet, B. Carre, P. Breger, O. Gobert, D. Garzella, J.-F. Hergott, O. Tcherbakoff, H. Merdji, M. Bougeard, H. Rottke, M. Bottcher, Z. Ansari, and P. Antoine, "Evolution of Angular Distributions in Two-Colour, Few-Photon Ionization of Helium," J. Phys. B: At. Molec. Opt. Phys. **41**, 051002 (2008).
10. J. Itatani, F. Quéré, G. L. Yudin, M. Y. Ivanov, F. Krausz, and P. B. Corkum, "Attosecond Streak Camera," Phys. Rev. Lett. **88**, 173903 (2002).
11. R. Kienberger, M. Hentschel, M. Uiberacker, C. Spielmann, M. Kitzler, A. Scrinzi, M. Wieland, T. Westerwalbesloh, U. Kleineberg, U. Heinzmann, M. Drescher, and F. Krausz, "Steering Attosecond Electron Wave Packets with Light," Science **297**, 1144 (2002).
12. Y. Mairesse and F. Quéré, "Frequency-Resolved Optical Gating for Complete Reconstruction of Attosecond Bursts," Phys. Rev. A **71**, 011401(R) (2005).
13. G. Sansone, E. Benedetti, F. Calegari, C. Vozzi, L. Avaldi, R. Flammini, L. Poletto, P. Villoresi, C. Altucci, R. Velotta, S. Stagira, S. D. Silvestri, and M. Nisoli, "Isolated Single-Cycle Attosecond Pulses," Science **314**, 443–446 (2006).
14. V. Véniard, R. Taieb, and A. Maquet, "Phase Dependence of $(N + 1)$-Color $(N > 1)$ IR-UV Photoionization of Atoms with Higher Harmonics," Phys. Rev. A **54**, 721 (1996).
15. J. J. Sakurai, *Modern Quantum Mechanics* (Addison-Wesley, New York, 1994).
16. R. W. Boyd, *Nonlinear Optics* (Academic, New York, 2003).
17. R. López-Martens, K. Varjú, P. Johnsson, J. Mauritsson, Y. Mairesse, P. Salières, M. B. Gaarde, K. J. Schafer, A. Persson, S. Svanberg, C.-G. Wahlström, and A. L'Huillier, "Amplitude and Phase Control of Attosecond Light Pulses," Phys. Rev. Lett. **94**, 033001 (2005).
18. K. Varjú, P. Johnsson, R. López-Martens, T. Remetter, E. Gustafsson, J. Mauritsson, M. B. Gaarde, K. J. Schafer, C. Erny, I. Sola, A. Zaïr, E. Constant, E. Cormier, E. Mével, and A. L'Huillier, "Experimental Studies of Attosecond Pulse Trains," Laser Phys. **15**, 888–898 (2005).
19. K. Varjú, Y. Mairesse, P. Agostini, P. Breger, B. Carré, L. J. Frasinski, E. Gustafsson, P. Johnsson, J. Mauritsson, H. Merdji, P. Monchicourt, A. L'Huillier, and P. Salières, "Reconstruction of Attosecond Pulse Trains Using an Adiabatic Phase Expansion," Phys. Rev. Lett. **95**, 243901 (2005).
20. J. Mauritsson, P. Johnsson, R. López-Martens, K. Varjú, A. L'Huillier, M. B. Gaarde, and K. J. Schafer, "Probing Temporal Aspects of High-Order Harmonic Pulses via Multi-Colour, Multi-Photon Ionization Processes," J. Phys. B **38**, 2265 (2005).

PAPER VI

Coherent electron scattering captured by an attosecond quantum stroboscope

J. Mauritsson, P. Johnsson, E. Mansten, M. Swoboda, T. Ruchon, A. L'Huillier and K. J. Schafer.

Phys. Rev. Lett. **100**, 073003 (2008).

PRL 100, 073003 (2008) PHYSICAL REVIEW LETTERS week ending 22 FEBRUARY 2008

Coherent Electron Scattering Captured by an Attosecond Quantum Stroboscope

J. Mauritsson,[1,2] P. Johnsson,[1,3] E. Mansten,[1] M. Swoboda,[1] T. Ruchon,[1] A. L'Huillier,[1] and K. J. Schafer[2]

[1]*Department of Physics, Lund Institute of Technology, P. O. Box 118, SE-221 00 Lund, Sweden*

[2]*Department of Physics and Astronomy, Louisiana State University, Baton Rouge, Louisiana 70803-4001, USA*

[3]*FOM-Institute AMOLF, Kruislaan 407, 1098 SJ Amsterdam, The Netherlands*

(Received 15 November 2007; published 21 February 2008)

We demonstrate a quantum stroboscope based on a sequence of identical attosecond pulses that are used to release electrons into a strong infrared (IR) laser field exactly once per laser cycle. The resulting electron momentum distributions are recorded as a function of time delay between the IR laser and the attosecond pulse train using a velocity map imaging spectrometer. Because our train of attosecond pulses creates a train of identical electron wave packets, a single ionization event can be studied stroboscopically. This technique has enabled us to image the coherent electron scattering that takes place when the IR field is sufficiently strong to reverse the initial direction of the electron motion causing it to rescatter from its parent ion.

DOI: 10.1103/PhysRevLett.100.073003 PACS numbers: 32.80.Rm

The basic properties of atoms, molecules, and solids are governed by electron dynamics which take place on extremely short time scales. To measure and control these dynamics therefore requires ultrafast sources of radiation combined with efficient detection techniques. The realization of extreme ultraviolet (XUV) attosecond (1 as = 10^{-18} s) pulses [1,2] has, for the first time, made direct measurements of electron dynamics possible [3–5]. Pioneering experiments utilizing the fast varying electric fields of femtosecond infrared (IR) laser pulses have demonstrated that temporally localized electron wave packets (EWPs) can be used to study molecular structures and dynamics [6–8]. In these experiments, subfemtosecond EWPs are generated through tunnel ionization twice per optical cycle near the maxima in the laser's oscillating electric field. They are subsequently accelerated by the same laser field and may be driven back to their parent ion for further interaction. This basic sequence of events, which is the essence of strong field physics, is very versatile and leads to many different phenomena [9,10]. The only control knob in these experiments, however, is typically the laser intensity, which must be quite high in order to ensure a reasonable probability of tunneling through the Coulomb barrier.

Further control of the electron dynamics requires that the creation and acceleration of the EWPs are decoupled; this is not possible using tunneling ionization since the same laser field governs both events. Decoupling can be achieved by using XUV attosecond pulses to create temporally localized EWPs through single photon ionization at a well defined phase of a synchronized IR field which drives the dynamics from that point forward. These attosecond EWPs are distinctly different from their tunnel ionization counterparts. They are born at the center of the potential well with properties that are directly inherited from the XUV pulses, which can be tailored in time and frequency [11–15]. They can also have a nonzero velocity, and their subsequent dynamics can be controlled by choosing the phase and amplitude of a synchronized IR field appropriately. In particular, the laser field needed to drive these EWPs back to the potential is usually weaker than the laser field needed to form tunnel EWPs, leading to much less distortion of the properties to be studied.

Here, we demonstrate an attosecond quantum stroboscope capable of capturing electron motion on a subfemtosecond time scale. This technique is based on a sequence of identical attosecond pulses [11] which are synchronized with an IR laser field. The pulse to pulse separation in the train is tailored to exactly match an optical cycle of the laser field, and the electron momentum distributions are detected with a velocity map imaging spectrometer (VMIS) [16,17]. This technique has enabled us to image the coherent scattering of electrons that are driven back to the ion by the laser field following their ionization. We envision that coherent electron scattering from atoms, molecules, and surfaces captured by the attosecond quantum stroboscope will complement more traditional scattering techniques [18,19] since it provides high temporal as well as spatial resolution [20].

To understand the principle of the quantum stroboscope and its application to coherent electron scattering, we use a simple classical model, where the atomic potential is omitted, to describe the motion of an electron that is released in a laser field [21]. If the electron is created at rest at time t_0 in a linearly polarized laser field with $\mathbf{E}(t) = \hat{\mathbf{y}}E_0 \sin(\omega t)$, it will at a later time t have a momentum

$$\mathbf{p}(t, t_0) = \frac{eE_0\hat{\mathbf{y}}}{\omega}[\cos(\omega t_0) - \cos(\omega t)], \qquad (1)$$

where e is the electron charge. Equation (1) is useful to describe tunneling wave packets, which are born at rest, but not sufficient to describe EWPs that are created via photoabsorption from attosecond pulses since they will have an initial momentum $\mathbf{p}_0 = \sqrt{2mW}\hat{\mathbf{u}}$, where $W = E_{\mathrm{XUV}} - I_p$ is the kinetic energy, m the mass of the electron, I_p the ionization energy, and $\hat{\mathbf{u}}$ is the initial direction of the

 © 2008 The American Physical Society

outgoing electron. Introducing the dimensionless parameter $\tilde{\gamma} = \sqrt{W/2U_p}$ [22], where the quiver energy $U_p = e^2E_0{}^2/4m\omega^2$, Eq. (1) is generalized to

$$\mathbf{p}(t, t_0) = \frac{eE_0}{\omega}\{[\cos(\omega t_0) - \cos(\omega t)]\hat{\mathbf{y}} + \tilde{\gamma}\,\hat{\mathbf{u}}\}. \quad (2)$$

Equation (2) describes the wiggling motion of the electron while it is in the laser field. We detect the final (drift) momentum:

$$\mathbf{p_f}(t_0) = \frac{eE_0}{\omega}[\cos(\omega t_0)\hat{\mathbf{y}} + \tilde{\gamma}\,\hat{\mathbf{u}}]. \quad (3)$$

In order to observe coherent scattering, the electron, once released, must pass the ion core at least once. From Eq. (3), the final momentum will be zero or opposite to the initial momentum, for certain time delays, if $\hat{\mathbf{u}} \parallel \hat{\mathbf{y}}$ and $\tilde{\gamma}$ is smaller than or equal to 1. When $\tilde{\gamma} = 1$, the momentum transferred by the field to the electrons is such that only electrons that are born exactly at times when $\mathbf{E}(t) = 0$ will return to the ion since the net transfer of momentum from the laser field (proportional to the vector potential of the field) is maximized for these times. For smaller $\tilde{\gamma}$-values, the momentum transfer is larger, which means that the initial direction of the electron can be reversed for a range of initial times. $\tilde{\gamma} = 1$ therefore marks the boundary, in this simple model, between "strong" and "weak" field continuum dynamics for the electron. For a 800 nm laser wavelength, $\tilde{\gamma} = 1$ can be obtained with $I = 1 \times 10^{13}$ W/cm^2 and $W = 1.2$ eV. This intensity is an order of magnitude smaller than that needed for tunnel ionization.

The principle of the quantum stroboscope technique used to capture the electron motion is illustrated in Figs. 1(a) and 1(b). A sequence of identical attosecond pulses are used to release electrons into an IR laser field exactly once per laser cycle. The EWPs disperse as they fly towards the detector where their momentum distribution is recorded. Consecutive EWPs will therefore overlap and interfere. Since the impulse imparted to the electron by the IR field depends on when the ionization occurs [23–25], each phase of the oscillating laser field yields a unique final momentum distribution. When the attosecond pulse periodicity matches the IR optical cycle, the created EWPs are affected identically by the IR field, with the result that the dynamics of individual events can be studied stroboscopically. In contrast, if ionization occurs over the whole IR cycle, or even at as few as 2 times during the cycle, the resulting momentum distribution will be smeared out and show interference fringes that depend on the different ionization times [26]. The quantum stroboscope shares two important features with a conventional stroboscope: First, we can freeze the periodically varying momentum distribution at a single phase of the IR field, and capture the entire time-dependent distribution by varying the XUV-IR delay. Second, by repeating the process periodically, the measured signal is stronger than what we would measure

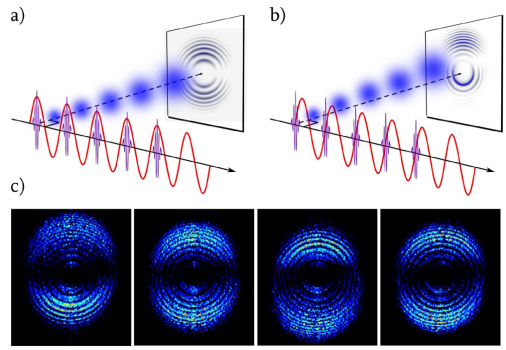

FIG. 1 (color online). (a), (b) An APT is used to ionize the target atoms once per cycle of an IR laser field. When the EWPs are created at the maxima of the IR electric field (a), the net transfer of momentum is zero, and the resulting momentum distribution is symmetric relative to the plane perpendicular to the laser polarization. When the EWPs instead are created at the zero-crossings of the IR electric field (b), the momentum distribution is shifted by the field along the direction of the laser polarization. (c) Experimental results obtained in Ar at four different XUV-IR delays are shown. From left to right, the images correspond to the XUV-IR delays $t_0 = 0$, $\pi/2\omega$, π/ω, $3\pi/2\omega$ for an IR intensity of 5×10^{12} W/cm^2.

with a single pulse. In the quantum stroboscope, the signal is further enhanced due to the coherence of the process, in that a train of N pulses yields fringes that are N^2 times brighter than the signal from an isolated pulse. The quantum stroboscope technique thus provides a complementary approach to the use of isolated attosecond pulses, in particular, suitable for experiments where a high signal to noise ratio is required.

In a first experimental demonstration of this technique, we use pulses with a 300 as duration and a central energy of 24 eV to ionize argon in the presence of an IR laser field with an intensity of 5×10^{12} W/cm^2. The attosecond pulse train (APT) was generated from a two-color laser field consisting of the IR field and its second harmonic to ensure that the XUV pulses were separated by one full optical cycle [11]. Four stroboscopic images taken at different XUV-IR delays (t_0) are presented in Fig. 1(c) (a complete movie spanning one full optical cycle is available in Ref. [27]). The clear up or down asymmetry in the momentum distributions confirms that each image corresponds to ionization at one particular phase of the IR field so that the momentum distribution is shifted up or down in the direction of polarization of the IR field. These results illustrate that the two essential aspects of stroboscopic imaging mentioned above are fulfilled: the electron momentum distribution is "frozen" at a given phase of the IR field, and the signal strength is enhanced by the repetition of the process. The interference fringes, which are evenly

PRL 100, 073003 (2008) PHYSICAL REVIEW LETTERS week ending 22 FEBRUARY 2008

spaced one IR photon apart in energy, show a decreasing spacing when plotted as a function of momentum as in Fig. 1. The position of these fringes does not shift as a function of XUV-IR delay, which shows that we are imaging a train of identical EWPs spaced one IR cycle apart. In addition, the fringe positions depend only on the IR intensity. The quantum stroboscope is therefore self-calibrating since the only unknown parameter, the IR intensity, can be read directly from the interference pattern. In this experiment $\tilde{\gamma} = 3.7$; *i.e.*, the field strength was not sufficient with respect to the initial energy of the electrons to reverse their initial velocity and coherent electron scattering is therefore not expected to be observed.

To understand what we can expect from experiments that guide ionized electrons to rescatter off the ion core, we have performed a series of calculations in helium by numerically integrating the time-dependent Schrödinger equation (TDSE) [28,29]. In Fig. 2, we show the influence of $\tilde{\gamma}$ on momentum distributions obtained at the XUV-IR delay leading to the maximum momentum transfer. The white circles in each panel indicate the range of momenta predicted by Eq. (3) if there is no rescattering from the ion [23]. When the intensity is increased, the downward momentum region extends outside the white circle, which indicates that electrons whose initial direction has been reversed have scattered off the atomic potential and that they have gained extra momentum in the same direction as their initial direction [30,31]. Another interference pattern is readily seen, with maximum along the polarization axis and minima at approximately 30° from the polarization axis (region II). This interference occurs between the ''direct'' outgoing EWP and the ''rescattered'' one. This interference is similar to the holographic imaging proposed by Spanner and co-workers using above threshold ionization [32]. When $\tilde{\gamma} = 0.86$, a larger portion of the EWP scatters of the potential, and the scattered electrons can be seen as jets along the polarization direction. A more detailed analysis of these effects is outside the scope of this Letter and will be discussed in a forthcoming theoretical paper.

To experimentally image coherent electron scattering with the quantum stroboscope, we ionize helium atoms with $E_{\mathrm{XUV}} = 25.8$ eV ($W = 1.2$ eV) and an IR intensity $I = 1.2 \times 10^{13}$ W/cm^2. In this case, $\tilde{\gamma} \approx 0.9$; *i.e.*, the laser field is sufficiently strong to drive the electrons back to the ion core for some XUV-IR delays. Compared to argon, the helium momentum distributions are expected to be more peaked along the laser polarization direction, since the excited EWP is entirely in an $m = 0$ state, whereas for argon, there is a mixture of $m = 0$ and $m = 1$ states, and the latter has no amplitude along the polarization axis. This makes helium a better candidate to observe electron scattering since the electrons along the polarization direction have the highest probability to scatter off the potential. Four experimental momentum distributions recorded at different XUV-IR delays are presented in Fig. 3. When the XUV-IR timing is set to maximize the momentum transfer from the IR field in the upwards (panel 1) or downwards (panel 3) directions, we see a clear signature of rescattering, manifested by a significant increase of low-energy electrons in the direction opposite to the momentum transfer from the IR field [33]. The experimental results are compared with theoretical calculations in the first panel of Fig. 3, and the agreement is excellent with all the substructures well reproduced. We believe that this is the first evidence for coherent electron scattering of attosecond EWPs created by single photon ionization.

In this Letter, we have demonstrated an attosecond quantum stroboscope capable of imaging the electron momentum distribution resulting from a single ionization event. We have also used it to guide ionized electrons back to their parent ions and to image the coherent electron scattering. The basic technique we have demonstrated is very versatile and may be altered in a number of potentially

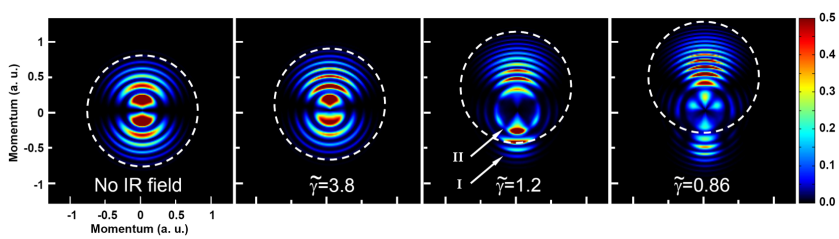

FIG. 2 (color online). Theoretical results obtained by integrating the TDSE are shown (from left to right) for IR intensities equal to zero, 1×10^{12} W/cm^2, 1×10^{13} W/cm^2, and 2×10^{13} W/cm^2 for the XUV-IR delay which corresponds to the maximum momentum transfer. The white circles are positioned at the highest energy electrons in the field free case (panel 1) and shifted by the amount of momentum added by the IR field in the other panels. If no post-ionization interaction between the electron and the atom occurs, the momentum distributions would remain within the circles. Two features are highlighted in panel three, which is calculated at an intermediate intensity where $\tilde{\gamma} = 1.2$, by white arrows: (I) electrons that have scattered off the core appearing outside the white circle in the downward direction and (II) interference minima in the momentum distribution. The interference minima occur in the region where the rescattered and direct electrons overlap.

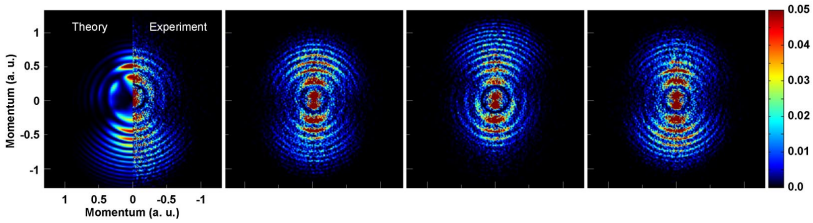

FIG. 3 (color online). Experimental results obtained in helium at an intensity of 1.2×10^{13} W/cm^2 are shown. The results are distinctively different from those taken in argon (Fig. 1). With this higher intensity, more momentum is transferred to the electrons, and in combination with the lower initial energy, some electrons return to the atomic potential for further interaction. In the first panel, we compare the experimental results (right) with theoretical calculations (left) obtained for the same conditions. The excellent agreement is the strongest evidence for coherent scattering effects in the experiment. All the substructures are well reproduced except for the highly saturated innermost peak in the experiment, which most likely is due to above threshold ionization of residual water in the experimental chamber.

useful ways. For example, the guiding field could be a replica of the two-color driving field we used to make the attosecond pulses. This would provide additional control over the return time and energy of the electrons. Using a longer wavelength driving laser [34] would lengthen the time between attosecond pulses, allowing more time for internal dynamics initiated by the launch of the EWP to develop before being probed by the returning electron. We envision that controlled, coherent scattering such as we have demonstrated will enable time resolved measurements with very high spatial resolution in atoms and molecules or at surfaces.

This research was supported by the Marie Curie Intra-European Fellowship (Attotech), the Marie Curie Research Training Networks (XTRA), the Marie Curie Early Stage Training Site (MAXLAS), the Integrated Initiative of Infrastructure LASERLAB-EUROPE within the 6th European Community Framework Programme, the Knut and Alice Wallenberg Foundation, the Crafoord Foundation, the Swedish Research Council, and the National Science Foundation (Grant No. PHY-0701372).

[1] P. M. Paul *et al.*, Science **292**, 1689 (2001).
[2] M. Hentschel *et al.*, Nature (London) **414**, 509 (2001).
[3] M. Drescher *et al.*, Nature (London) **419**, 803 (2002).
[4] R. Kienberger *et al.*, Nature (London) **427**, 817 (2004).
[5] E. Goulielmakis *et al.*, Science **305**, 1267 (2004).
[6] H. Niikura *et al.*, Nature (London) **417**, 917 (2002).
[7] J. Itatani *et al.*, Nature (London) **432**, 867 (2004).
[8] T. Kanai, S. Minemoto, and H. Sakai, Nature (London) **435**, 470 (2005).
[9] K. J. Schafer *et al.*, Phys. Rev. Lett. **70**, 1599 (1993).
[10] P. B. Corkuum, Phys. Rev. Lett. **71**, 1994 (1993).
[11] J. Mauritsson *et al.*, Phys. Rev. Lett. **97**, 013001 (2006).
[12] R. López-Martens *et al.*, Phys. Rev. Lett. **94**, 033001 (2005).
[13] E. Gustafsson *et al.*, Opt. Lett. **32**, 1353 (2007).
[14] G. Sansone *et al.*, Science **314**, 443 (2006).
[15] I. J. Sola *et al.*, Nature Phys. **2**, 319 (2006).
[16] M. J. J. Vrakking, Rev. Sci. Instrum. **72**, 4084 (2001).
[17] A. T. J. B. Eppink and D. H. Parker, Rev. Sci. Instrum. **68**, 3477 (1997).
[18] J. Miao, P. Charalambous, J. Kirz, and D. Sayre, Nature (London) **400**, 342 (1999).
[19] H. N. Chapman *et al.*, Nature Phys. **2**, 839 (2006).
[20] H. Niikura and P. B. Corkum, Adv. At. Mol. Opt. Phys. **54**, 511 (2007).
[21] T. F. Gallagher, Phys. Rev. Lett. **61**, 2304 (1988).
[22] G. Lagmago Kamta and A. F. Starace, Phys. Rev. A **68**, 043413 (2003).
[23] J. Itatani *et al.*, Phys. Rev. Lett. **88**, 173903 (2002).
[24] R. Kienberger *et al.*, Science **297**, 1144 (2002).
[25] P. Johnsson *et al.*, Phys. Rev. Lett. **95**, 013001 (2005).
[26] K. C. Kulander, K. J. Schafer, and J. L. Krause, in *Atoms in Intense Laser Fields* (Academic Press, San Diego, 1992).
[27] See EPAPS Document No. E-PRLTAO-100-004808 for a movie spanning one full optical cycle. For more information on EPAPS, see http://www.aip.org/pubservs/epaps.html.
[28] J. L. Krause, K. J. Schafer, and K. C. Kulander, Phys. Rev. Lett. **68**, 3535 (1992).
[29] T. Remetter *et al.*, Nature Phys. **2**, 323 (2006).
[30] O. Smirnova, S. Patchkovskii, and M. Spanner, Phys. Rev. Lett. **98**, 123001 (2007).
[31] A. K. Kazansky and N. M. Kabachnik, J. Phys. B **40**, 2163 (2007).
[32] M. Spanner, O. Smirnova, P. B. Corkum, and M. Y. Ivanov, J. Phys. B **37**, L243 (2004).
[33] We note that there is an up/down asymmetry even for the XUV-IR delays where no net momentum is transferred to the electrons. We attribute this asymmetry partially to a small frequency modulation on the attosecond pulses and partially to the distortion of the atomic potential.
[34] P. Agostini and L. F. DiMauro, Rep. Prog. Phys. **67**, 813 (2004).

Paper VII

Phase Measurement of Resonant Two-Photon Ionization in Helium

M. Swoboda, T. Fordell, K. Klünder, J. M. Dahlström, M. Miranda, C. Buth, K. J. Schafer, J. Mauritsson, A. L'Huillier and M. Gisselbrecht. (2010) *Phys. Rev. Lett., accepted for publication*.

Phase Measurement of Resonant Two-Photon Ionization in Helium

M. Swoboda,[1] T. Fordell,[1] K. Klünder,[1] J. M. Dahlström,[1] M. Miranda,[1,2]
C. Buth,[3,4] K. J. Schafer,[3,4] J. Mauritsson,[1] A. L'Huillier,[1,*] and M. Gisselbrecht[1]

[1]*Department of Physics, Lund University, P.O. Box 118, 22100 Lund, Sweden*
[2]*Departamento de Física, Universidade do Porto, Rua do Campo Alegre 687, 4169-007 Porto, Portugal*
[3]*Department of Physics and Astronomy, Louisiana State University, Baton Rouge, Louisiana 70803, USA*
[4]*PULSE Institute, SLAC National Accelerator Laboratory, Menlo Park, California 94025, USA*

We study resonant two-color two-photon ionization of Helium via the 1s3p $^1P_1$ state. The first color is the 15$^{\text{th}}$ harmonic of a tunable titanium sapphire laser, while the second color is the fundamental laser radiation. Our method uses phase-locked high-order harmonics to determine the *phase* of the two-photon process by interferometry. The measurement of the two-photon ionization phase variation as a function of detuning from the resonance and intensity of the dressing field allows us to determine the intensity dependence of the transition energy.

Multicolor resonant ionization is at the heart of numerous and diverse applications in fundamental and applied sciences. Examples are studies of very high Rydberg states [1], investigations of biomolecules [2] and specific selection of radioactive species [3]. In the simplest scheme, resonantly-enhanced two-photon ionization (R2PI) occurs via the absorption of two photons, generally of different colors, one tunable (ω_1) used to scan across a resonant state (r), and the second (ω) ionizing from the excited state. In traditional R2PI, the *yield* of the produced ion species is recorded as a function of laser wavelength, and the position and shape of the observed resonance provides information on the underlying electronic and rovibrational structures. These studies rely on spectroscopic information using narrow-bandwidth lasers, which do not allow any temporal resolution. Here, we present an ultrafast time-resolved-technique to retrieve also the *phase* of R2PI when sweeping through the resonance. We demonstrate it by studying R2PI of He via the 1s3p ^{1}P$_1$ state which lies 23.087 eV above the ground state.

The basic principle of our experiment is illustrated in Fig. 1. We study the interference between two pathways to the same ionized final state (f_1), one through the resonance with absorption of two photons with frequency ω_1 and ω, and the second through a continuum path, using a third color (ω_2), involving absorption of a photon with frequency ω_2 and emission of a photon with frequency ω. The phase of the R2PI is encoded in the modulation of the photoelectron signal S_{f_1} as a function of the delay τ between the (ω_1,ω_2) fields and the ω field [Fig. 1 (b)]. When the energy of the exciting radiation ω_1, and thus the detuning from the resonance is changed, the phase variation of the resonant transition leads to a measurable shift of the S_{f_1} oscillation. This phase shift needs to be referenced against another modulation S_{f_2} that is independent of the resonance and thus providing a *clock* to our measurement. A process providing an independent modulation requires a fourth color (ω_3) and involves another final state (f_2) (see Fig. 1).

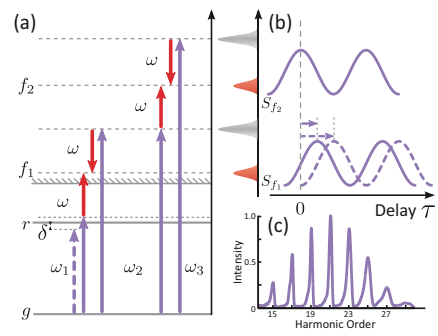

FIG. 1: (color online) a) Schematic diagram illustrating the phase measurement of R2PI. The dashed and solid ω_1 lines represent two excitation energies on either side of the resonance. The photoelectron peaks used in the measurement are S_{f_1} and S_{f_2}. b) Illustration of modulated sideband signals S_{f_1} and S_{f_2}. Two S_{f_1} modulations are indicated, corresponding to the two excitation energies in a). c) Experimental harmonic spectrum used in the measurements.

An essential requirement for our measurement is the use of phase-locked radiation fields with commensurate frequencies, and a temporal precision better than the periodicity of the interference signal, in our case 1.3 fs. Another requirement, is a high spectral resolution for the excitation of a narrow resonance. These requirements can be simultaneously fulfilled [4] by using the high-order harmonic frequency combs produced when an intense laser field interacts with a gas of atoms or molecules [5]. As is now well understood [6, 7], harmonics arise due to interferences between attosecond pulses produced by tunnel ionization, acceleration of the created wave packet in the field and recombination back to the ground state at each half cycle of the laser field. The spectral width of the individual harmonics is thus related to the number of attosecond pulses, and decreases as the laser pulse dura-

tion increases [8]. In this process, a comb of phase-locked harmonics of odd order is generated.

In the present work, we use high-order harmonics generated in Ar to study R2PI of He via the 1s3p $^1P_1$ state [9]. In contrast to the similar "reconstruction of attosecond bursts by interference of two-photon transition" (RABITT) technique, which is used for the determination of the pulse duration of attosecond pulses [10, 11], the influence of the attosecond pulse characteristics on the measurements is here removed [12]. Emphasis is put on the determination of the R2PI phase [13] as a function of detuning from the resonance. The detuning is varied by changing the fundamental wavelength (around 805 nm) or alternatively by increasing the fundamental intensity. We apply these measurements to determine the intensity dependence of the energy of the $1s^2 \rightarrow 1s3p$ transition, and interpret the results using theoretical calculations consisting of solving the time-dependent Schrödinger equation (TDSE) in conditions close to the experimental ones [14].

Our experiments were performed with a 1-kHz 35-fs 4-mJ Titanium-Sapphire laser system. An acousto-optic programmable dispersive filter (DAZZLER) was used to change the central wavelength between 802.5 and 809.3 nm, while maintaining the spectral width of the amplified pulses approximately equal to 25 nm. High-order harmonics were generated in a pulsed Ar gas cell, filtered using a spatial aperture and a 200-nm thick Al thin film [15], and focused by a toroidal mirror into a vacuum chamber containing an effusive He gas jet. A magnetic bottle electron spectrometer (MBES) allowed us to record and analyze in energy the ejected electrons. Part of the laser field was extracted before the generation of harmonics, and recombined downstream collinearly with the harmonics, after a variable time delay that could be adjusted with sub-100-as precision [12].

A comb of about seven phase-locked harmonic fields [Fig. 1 c)], corresponding in the time domain to a train of attosecond pulses of 260 as duration, was thus sent into the interaction chamber together with the dressing field at frequency ω with an adjustable phase φ (or time $\tau = \varphi/\omega$) delay. In addition, a halfwave plate and polarizer in the dressing IR field arm allowed precise control of the pulse energy and therefore the intensity in the interaction region of the MBES. The detuning was determined from $\delta = 15hc/\lambda_0 - E_{3p}$, where E_{3p} is 23.087 eV and λ_0 is the barycenter of the fundamental frequency spectrum, shifted to the blue by $\delta\lambda \simeq 3.5$ nm to account for the blueshift from free electrons in the generation gas [16, 17]. The dressing laser intensity was determined by measuring the energy shifts of the photoelectron peaks of harmonics 17 to 23 in the presence of the laser field, which is simply equal to the ponderomotive energy $U_p \approx 6.0I$ eV where the intensity I is in units of 10^{14}Wcm^{-2} for a laser wavelength of 800 nm [18, 19].

Figure 2 (a,b) presents electron spectra as a function of delay between the harmonics and the dressing field, obtained for two different detunings. Electrons are observed at energies corresponding to one-photon absorption of the harmonics (from the 17$^{\text{th}}$) and at "sideband" energies due to two-photon ionization processes, which we label by the corresponding net number of infrared photons (16, 18 etc.). These sideband peaks strongly oscillate with the delay at a frequency equal to 2ω. The oscillations of sidebands 18, 20, 22 and 24 do not depend on the detuning, while sideband 16 is strongly affected by it. A Fourier transform of the sideband signal over about 10 fs (four cycles) allows us to determine the relative phases of the sideband oscillations with a precision of 0.1 rad. The phases are plotted in Fig. 2 (c) for the two cases shown in (a,b).

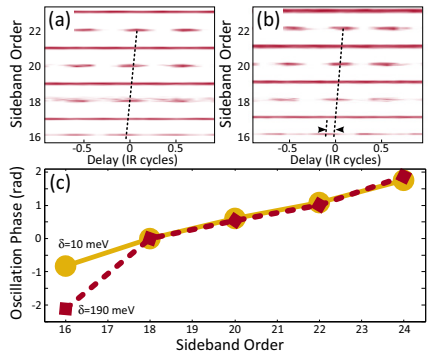

FIG. 2: (color online) Electron spectra as a function of delay for detunings δ =10 meV(a) and δ =190 meV(b). The oscillation of the 16$^{\text{th}}$ sideband depends on the detuning while the others do not (see dashed line) (c) Phase of the oscillations of the sideband peaks in light orange for (a) and dark red for (b). The two results have been superposed at sideband 18.

The relationship between the R2PI phase and the experimental results in Fig. 2 can be understood within second-order perturbation theory [10, 12]. Using the notation from Fig. 1, the photoelectron signal S_{f_1} can be expressed as

$$S_{f_1} = |a_1^a + a_2^e|^2 \tag{1}$$

where a_1^a and a_2^e are the two-photon probability amplitudes with the superscript a or e referring to an absorption or emission of an ω photon and with the subscript 1 or 2 referring to absorption of an ω_1 or ω_2 photon. Introducing φ_1 and φ_2 as the phases of the radiation fields, as well as φ_1^a and φ_2^e as the phase terms involved in the two-photon transitions, Eq. (1) becomes

$$\begin{aligned} S_{f_1} &= \left| |a_1^a| e^{i\varphi_1^a + i\varphi_1 + i\varphi} + |a_2^e| e^{i\varphi_2^a + i\varphi_2 - i\varphi} \right|^2 \\ &= |a_1^a|^2 + |a_2^e|^2 + 2\,|a_1^a a_2^e| \cos\left(\varphi_1^a - \varphi_2^e + 2\varphi + \varphi_1 - \varphi_2\right). \end{aligned} \tag{2}$$

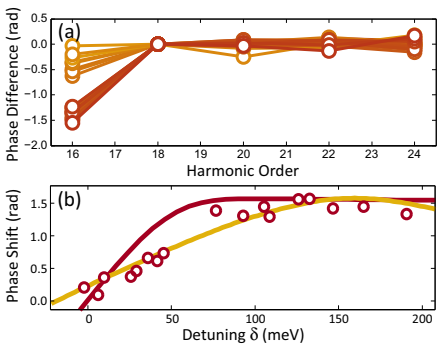

FIG. 3: (color online) a) Measured sideband phases corrected for the attosecond group delay and normalized at zero for sideband 18. Different detunings are indicated by the color code (going from 11 meV below the resonance (dark red) to 190 meV above the resonance (light orange)) b) Measurements (circles) of the R2PI phase as a function of detuning. The dark red line indicates results of a simple perturbative model while the light orange line shows results of simulations based on solving the TDSE.

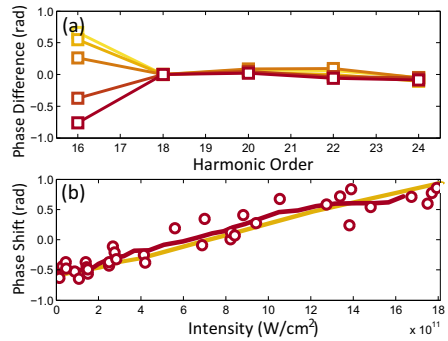

FIG. 4: (color online) Intensity dependence of the R2PI phase. (a) Harmonic phase differences at dressing intensities from 0.1 (dark red) to $2.2 \times 10^{12}\,\mathrm{Wcm}^{-2}$ (light orange), with attosecond chirp correction and normalization at sideband 18. (b) R2PI phase (circles) as a function of intensity, with a 6-point moving average (dark red line) and TDSE (light orange).

The cosine term leads to the modulation of the signal observed in the experiment. In general, the phase terms involved do not depend much on the photon energies. In two-photon ionization via a resonant state, however, the phase (φ_1^a) changes by π across the resonance. The study of the variation of φ_1^a as a function of detuning δ provides interesting information on the two-photon ionization process, e.g. on the relative importance of resonant and nonresonant contributions, AC Stark shift of the resonant state, depending on the spectral characteristics of the XUV and laser fields.

The variation of φ_1^a with the detuning can be experimentally obtained from $S_{f_1}(\varphi)$ provided the other phase terms φ_2^e, φ_1, φ_2 do not depend on δ and provided the phase delay φ is known in absolute value, which is generally not the case. $S_{f_1}(\varphi, \delta)$ is therefore referenced against $S_{f_2}(\varphi)$, assuming that the phase terms involved, φ_2^a and φ_3^e, are independent of the detuning and thus removing the need of knowledge of the absolute φ. When changing δ, the laser intensity used to generate the harmonics varies slightly, leading to a (small) variation of the group delay of the attosecond pulses and thus of $\varphi_1 - \varphi_2$. We correct for this effect and the harmonic spectral phase by removing a linear attosecond group delay function [20] and we set to zero the phase of sideband 18 (S_{f_2}) for all detunings. The results are presented in Fig. 3(a). As expected, the phases corresponding to all sidebands except the 16^{th} are almost superposed to each other and show no influence of detuning.

Figure 3(b) shows the variation of the R2PI phase as a function of detuning. We can tune only over half the resonance since for lower (negative detunings) sideband 16 moves progressively below the ionization threshold, thus making our phase measurement inaccurate. We also compare our measurements with the results of two different models (solid lines): The dark red line is obtained by time-dependent perturbation theory [21], only considering the resonant state. Gaussian envelopes were used for the IR and XUV pulses with FWHMs of 30 fs and 10 fs, respectively. The light orange curve shows the result of calculations performed by numerically integrating the TDSE in the single active electron approximation [14]. Our calculation uses a He pseudo-potential with the energy of the 1s3p state equal to 23.039 eV. The result is therefore shifted by 40 meV for comparison with the experiment. The result shown in Fig. 3(b) agrees very well with the experiment, thus confirming our detuning calibration.

In order to investigate how the 1s3p resonance behaves in a laser field, we measured the dependence of the R2PI phase on the dressing laser intensity. Figure 4(a) shows the R2PI phase determined similarly to Figure 3(a) but keeping the wavelength constant at 805.5 nm and gradually increasing the dressing intensity. We verified that even at the highest intensity, higher-order multi-photon transitions were still negligible [22], thus not affecting our phase determination. Increasing the intensity from 0.1 to $1.8 \times 10^{12}\,\mathrm{W/cm}^2$, the R2PI phase varies from -0.7 to 0.9 radians. Figure 4(b) presents the intensity dependence of all of the measured phases (circles). We find an almost linear increase of the phase with intensity, as indicated by the dark red curve obtained by averaging, with a saturation at around $1.3 \times 10^{12}\,\mathrm{W/cm}^2$, due to the suppression of R2PI when part of the two-photon excitation bandwidth moves partly below the ionization threshold. The

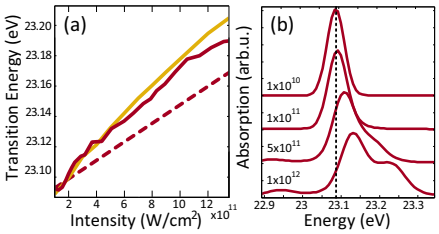

FIG. 5: (color online) (a) Measured transition energy of the 1s3p state. Experimental results (solid dark red), compared with $\Delta E_{1s^2} + U_p$ (dashed) and TDSE calculation (solid light orange). (b) TDSE calculation of XUV absorption for three different intensities with 50 meV resolution. The position of the 1s3p state is indicated by the dashed line.

light orange line obtained by TDSE calculations agrees well with our measurements.

Combining our previous phase measurements as a function of detuning for a fixed (low) intensity and as a function of intensity (for a fixed detuning) allows us to determine the intensity-dependence of the $1s^2 \rightarrow 1s3p$ transition energy. Both experimental (dark red solid) and TDSE (light orange solid) results are shown in Fig. 5(a). The dashed line is equal to $\Delta E_{1s^2} + U_p$, representing the variation of the transition energy if the 1s3p state was moving as a high-lying Rydberg state, following U_p [19]. The AC Stark shift of the fundamental state ΔE_{1s^2} is very small, equal to $-0.3I$eV where the intensity I is in units of 10^{14}Wcm^{-2} [23, 24] so that $\Delta E_{1s^2} + U_p \approx U_p$. We find that the measured transition energy increases about 40% more rapidly with the laser intensity than U_p, up to the saturation at 1.3×10^{12} Wcm^{-2}.

To better understand this faster than ponderomotive shift, we have calculated the XUV absorption cross-section for helium in the presence of an 800 nm field by numerically solving the TDSE as a function of both XUV wavelength and laser intensity [Figure 5(b)]. Using an XUV bandwidth of 50 meV or smaller we find that beyond 1×10^{11} Wcm^{-2}, the 3p resonance has at least two components the higher of which shifts significantly faster than the ponderomotive energy. With the experimental XUV bandwidth (150 meV), however, the different components cannot be resolved. As a result, we observe shifts exceeding $E_{1s^2}+U_p$. Experimentally, the predicted structure in the 3p resonance could be observed using longer fundamental laser pulses, leading to spectrally narrower harmonic peaks.

In conclusion, we have shown how well-characterized phase-locked high-order harmonics can be used to measure the phase of R2PI and we have applied it to the determination of the AC Stark shift of the 1s3p ^{1}P$_1$ state. Although our resolution was unsufficient to detect the splitting of the excited state, we observed a non-trivial, faster than ponderomotive, AC Stark shift. Our method, here demonstrated in He, could be applied to the study of numerous resonant or quasi-resonant processes in atoms and molecules.

We thank A. Maquet and R. Taïeb for fruitful suggestions at the beginning of this work. This research was supported by the Marie Curie Intra-European Fellowship ATTOCO, the Marie Curie Early Stage Training Site (MAXLAS), the European Research Council (ALMA), the Knut and Alice Wallenberg Foundation and the Swedish Research Council. Funding at LSU is provided by the National Science Foundation through grant numbers PHY-0449235 and PHY-0701372.

* Electronic address: anne.lhuillier@fysik.lth.se; URL: http://www.atto.fysik.lth.se

[1] A. Osterwalder and F. Merkt, Phys. Rev. Lett. **82**, 1831 (1999).
[2] E. G. Robertson and J. P. Simons, Phys. Chem. Chem. Phys. **3**, 1 (2001).
[3] U. Koster, V. Fedoseyev, and V. Mishin, Spectrochimica Acta B **58**, 1047 (2003).
[4] P. Ranitovic et al., New Journal of Physics **12**, 013008 (2010).
[5] M. Ferray et al., J. Phys. B **21**, L31 (1988).
[6] J. L. Krause, K. J. Schafer, and K. C. Kulander, Phys. Rev. Lett. **68**, 3535 (1992).
[7] P. B. Corkum, Phys. Rev. Lett. **71**, 1994 (1993).
[8] F. Brandi, D. Neshev, and W. Ubachs, Phys. Rev. Lett. **91**, 163901 (2003).
[9] L. H. Haber, B. Doughty, and S. R. Leone, Phys. Rev. A **79**, 031401 (2009).
[10] V. Véniard, R. Taïeb, and A. Maquet, Phys. Rev. A **54**, 721 (1996).
[11] P. M. Paul et al., Science **292**, 1689 (2001).
[12] K. Varjú et al., Laser Physics **15**, 888 (2005).
[13] S. Haessler et al., Phys. Rev. A **80**, 011404 (2009).
[14] K. J. Schafer and K. C. Kulander, Phys. Rev. Lett. **78**, 638 (1997).
[15] R. López-Martens et al., Phys. Rev. Lett. **94**, 033001 (2005).
[16] C. G. Wahlström et al., Phys. Rev. A **48**, 4709 (1993).
[17] M. B. Gaarde, M. Murakami, and R. Kienberger, Phys. Rev. A **74**, 053401 (2006).
[18] R. K. Freeman et al., Phys. Rev. Lett. **59**, 1092 (1987).
[19] K. Burnett, V. Reed, and P. Knight, J. Phys. B **26**, 561 (1993).
[20] Y. Mairesse et al., Science **302**, 1540 (2003).
[21] N. Dudovich, D. Oron, and Y. Silberberg, Phys. Rev. Lett. **88**, 123004 (2002).
[22] M. Swoboda et al., Las. Phys. **19**, 1591 (2009).
[23] M. D. Perry, A. Szoke, and K. C. Kulander, Phys. Rev. Lett. **63**, 1058 (1989).
[24] H. Rudolph et al., Phys. Rev. Lett. **66**, 3241 (1991).

PAPER VIII

Attosecond pump-probe electron interferometry

J. Mauritsson, T. Remetter, M. Swoboda, K. Klünder, A. L'Huillier, K. J. Schafer, O. Ghafur, F. Kelkensberg, W. Siu, P. Johnsson, M. J. J. Vrakking, I. Znakovskaya, T. Uphues, S. Zherebtsov, M. F. Kling, F. Lépine, E. Benedetti, F. Ferrari, G. Sansone and M. Nisoli.

(2010) *arXiv:1001.1085v1 [physics.atom-ph]*.

Attosecond pump-probe electron interferometry

J. Mauritsson,[1*] T. Remetter,[1] M. Swoboda,[1] K. Klünder,[1] A. L'Huillier,[1] K. J. Schafer,[2] O. Ghafur, [3] F. Kelkensberg,[3] W. Siu,[3] P. Johnsson,[3] M. J. J. Vrakking,[3] I. Znakovskaya,[4] T. Uphues,[4] S. Zherebtsov,[4] M.F. Kling,[4] F. Lépine,[5] E. Benedetti,[6] F. Ferrari,[6] G. Sansone,[6] M. Nisoli[6]

Attosecond science has as its goal the measurement and ultimately the control of electron dynamics on its natural time scale, the atomic unit of time, which is 24 attoseconds. The short pulses required to reach this time scale imply large bandwidths, leading to the excitation not of a single state but of a broad and coherent superposition of states, *i.e.*, a wave packet. In this paper we present a novel interferometric method that uses a free wave packet as a reference to measure a bound wave packet. The resulting interferogram contains both quantum beats as well as multi-path interference and provides precise and state-specific time-resolved amplitude and phase information about the bound electron wave packet. We demonstrate our method experimentally by measuring an attosecond wave packet in helium, prepared using an isolated 350 attosecond pulse with a central energy in the vicinity of the ionization threshold, but we also show that our approach can be applied to bound wave packets irrespective of the way they are created.

[1] Department of Physics, Lund University, P. O. Box 118, SE-221 00 Lund, Sweden
[2] Department of Physics and Astronomy, Louisiana State University, Baton Rouge, Louisiana 70803-4001, USA
[3] FOM-Institute AMOLF, Kruislaan 407, 1098 SJ Amsterdam, The Netherlands
[4] Max-Planck-Institut für Quantenoptik, Hans-Kopfermann-Strasse 1, D-85748 Garching, Germany
[5] Université Lyon 1; CNRS; LASIM, UMR 5579, 43 bvd. du 11 novembre 1918, F-69622 Villeurbanne, France
[6] National Laboratory for Ultrafast and Ultraintense Optical Science CNR Istituto Nazionale per la Fisica della Materia, Department of Physics, Politecnico di Milano, Piazza Leonardo da Vinci 32, 20133 Milano, Italy
[*] To whom correspondence should be addressed. E-mail: johan.mauritsson@fysik.lth.se (J.M.)

Background

The frequency of the periodic motion of a harmonic oscillator is inversely proportional to the mass of the oscillator. As a result, atomic motions at the heart of chemical processes typically occur on the femtosecond timescale, while the motion of electrons tends to occur on attosecond timescales. This motivates the current interest in the development of attosecond techniques for the time-resolved investigation of electron dynamics. Attosecond pulses were first produced in 2001[1,2], as the outcome of the process of high harmonic generation[3] (HHG). In HHG, an intense femtosecond infrared (IR) laser coherently drives atomic or molecular ionization, as well as subsequent electron acceleration and recombination[4,5]. This leads to the production of radiation in the extreme ultra-violet (XUV) or soft x-ray part of the spectrum with durations down to 100 as (refs 6, 7) or even below[8]. A unique aspect of attosecond pulses generated via HHG is that the XUV radiation is precisely synchronized to the electric field of the driving IR laser. Since 2001 intensive efforts have led to the first applications of attosecond pulses, and synchronization between the XUV pulses and the IR field has played a key role in each of them[9-12].

When attosecond pulses are used to excite atoms or molecules they create broad electron wave packets which are difficult to probe directly using a second attosecond pulse, as traditional pump-probe spectroscopy would have it. This limitation, which is due to the low intensity of the attosecond XUV pulses, can be circumvented by exploiting the XUV-IR synchronization inherent in the HHG process. Several methodologies that use this capability to extract information on sub-femtosecond electron dynamics have been demonstrated. The attosecond streaking technique exploits the momentum shift that a synchronized IR laser field imparts to electrons that have

been ejected from an atom into the field[13,14]. When applied to electrons that are directly ionized by an attosecond pulse, streaking enables the measurement of XUV and IR light fields, and was recently used in an investigation of atomic photo-ionization that directly imaged the interaction of low energy ionized electrons with the atomic core[15]. It has also been used to measure the time scale for Auger decay[9], where the "streaked electron" was the secondary electron emitted as a result of the attosecond photo-ionization event. A second method called attosecond chronoscopy exploits the sub-cycle nature of (multi-) photon ionization rates in a strong IR laser field[16,17] to study the ionization of individual bound states populated by means of a shake-up process accompanying the removal of an inner shell electron by an attosecond pulse. In the present study we use the XUV-IR synchronization to directly measure an attosecond electron wave packet composed of several bound states for the first time.

Principle of the measurement

When attosecond pulses are applied to atoms or molecules they excite broad coherent superpositions of bound states spread over several electron volts. This coherent superposition (and hence the electron dynamics that takes place) is completely characterized by a specification of the states (Ψ_i with energies E_i) that are part of the superposition, accompanied by their time-dependent amplitudes, $A_i(t)$ and phases, $\varphi_i(t)$

$$\Psi(t) = \sum_i A_i(t) e^{-i\left(E_i t/\hbar + \varphi_i(t)\right)} \Psi_i.$$

Here we present a method to determine the energies, amplitudes and phases of a bound electron wave packet excited by an attosecond pulse, and to subsequently follow the associated electron dynamics with attosecond time resolution.

The key idea is that coincident with the creation of the bound wave packet, a continuum wave packet that is coherent with it is also created. As we discuss below, there are several scenarios for doing this. In the current experiment we create one very broad wave packet that spans over the ionization threshold of the atom using one photon excitation with an attosecond pulse. The portion of the initial wave packet that is above the ionization threshold quickly disperses and moves away from the atom as a free wave packet leaving behind a bound wave packet. After a variable delay the bound wave packet is ionized by a short IR pulse that is locked in phase with the original attosecond pulse envelope (see Fig. 1). The free wave packet is unable to absorb energy or momentum from the IR field and so serves as a reference, and we observe interference fringes when measuring the photoelectron spectrum as a function of delay. These interference fringes result from the fact that we do not know, when observing an electron, whether it entered the continuum via the original attosecond pulse ("direct path") or after absorbing an additional IR photon ("indirect path"). As we will show, the interference fringes allow us to access the energies, amplitudes and phases of the states in the bound electron wave packet. As in Ramsey spectroscopy, the spectral precision is set not by the bandwidth of the excitation pulse, but by the delay between the pump and probe pulses[18-20] and by the experimental energy resolution of the photoelectron spectrometer used. In addition there is also a temporal resolution that is set by the duration of the excitation pulse as in traditional pump-probe spectroscopy.

Determining the amplitudes and phases of a wave-like object by interference with a reference wave is a well-known approach. It is the essence of holography, and has been used to great advantage in the characterization of optical fields[21]. The method has also been applied to vibrational and electronic wave

packets[22,23], but so far two bound wave packets have been used, one an object to be measured and the other a known reference wave packet that spectrally overlaps the unknown one. The challenge in attosecond science is to develop a similar technique without the reference wave packet needing to undergo the potentially very complicated dynamics that the electron wave packet under investigation experiences (which may include processes such as Auger decay and shake-up). In our method we solve this problem by having the reference be a free wave packet which does not interfere with the unknown wave packet during the evolution of the electron dynamics of interest, but only in the course of the detection step, when the bound wave packet is ionized by a coherent probe pulse and the resulting angle- and energy-resolved photoelectron spectrum is measured.

Figure 1 illustrates the principle of our measurement technique for the experimental scheme investigated in the present work (see Methods for more details). A linearly-polarized, few-cycle, phase-stabilized IR pulse is split into pump and probe pulses. The pump is used to generate an isolated attosecond pulse in xenon gas using the polarization gating technique[6,24]. At time t_0, the resulting XUV pulse, with 350 as duration and a central frequency of 24 eV, excites helium from its ground state to a coherent superposition of bound and continuum *p*-states. At a later time *t*, which is typically from zero up to a few tens of femtoseconds later, the bound wave packet is ionized by an IR probe pulse that has the same linear polarization as the XUV pulse. The ionized electrons are detected using a velocity map imaging spectrometer[25] (VMIS) which records angular-resolved momentum distributions.

Three experimental images, recorded at different delays between the XUV and IR fields are presented in Fig. 1c-e. The images are inverted[26] and a scan of the

photoelectrons emitted along the polarization axis of the fields (both up and down) is shown in Fig. 1b. When the two pulses overlap temporally, we get a normal streaking scan typical for photoionization by an isolated attosecond pulse in presence of a laser field[6,11], with a momentum shift either upward (Fig. 1c) or downward (Fig. 1d) depending on the relative timing between the pulses. In the region where the attosecond pulse precedes the IR probe (right side of the scan in Fig. 1b) interference fringes are observed both in the recorded images (Fig. 1c-e) and in the on-axis spectrogram (Fig. 1b). This interference pattern is due to the multiple pathways leading to the same final continuum energy. During the delay $\tau = t - t_0$, a continuum state with energy, E, and a bound stationary state ($A_i(t)$ and $\varphi_i(t)$ constant) with energy, E_i, accumulate a phase difference $(E - E_i)\tau/\hbar$. The interference fringes, defined as the curves of constant phase difference, are hyperboles, which become more closely spaced as the delay increases. In Fig. 1, owing to the resolution and short delays, these curves appear not as hyperboles but as tilted lines, appearing more horizontal with increasing delay. (See Fig. 2 and 4 for clearer hyperbolic variations).

To appreciate the role played by the reference wave packet, let us consider the case where the initial wave packet created by the attosecond pulse consists of a superposition of only bound states (*i.e.* if no reference wave packet is formed). In the delay between its creation by the attosecond pulse and its ionization by the IR probe pulse this purely bound wave packet would accumulate phase differences equal to $\left(E_j - E_i\right)\tau/\hbar$ where E_j and E_i stand for all of the possible combinations of states in the superposition. This would give rise to periodic structures known as *quantum beats* in the ionization probability as a function of delay, but no energy dependent interference fringes. In our experiment these quantum beats will of course be present, but as we will

show in the next section, the reference wave packet allows us to go beyond quantum beat spectroscopy.

Calculations and analysis

In Fig. 2, we present quantum calculations based on the single active electron approximation[28] under conditions that are close to those of the experiment. We have extended the maximum delay between the XUV and IR pulses beyond that shown in Fig. 1. The photoelectron spectrum emitted close to the polarization axis of the IR field in the upward direction is presented in Fig. 2a. Interference fringes appear as soon as the excitation of the bound states at t_0 is clearly separated in time from their ionization by the probe field at time t, meaning that we have two clearly delineated routes into the continuum, which we have called the "direct" and "indirect" pathways above. The hyperbolic shape of the fringes is clearly visible in the calculation and the fringe spacing decreases as the delay increases. The fringes have a rippled appearance because the attosecond pulse simultaneously excites several bound states, which leads to several sets of overlapping hyperbolic fringes. The superposition of these fringes creates *Moiré patterns*, when the constructive interference patterns from these sets of fringes overlap.

A strong quantum beat signal arising from the interference between states in the bound wave packet is also visible in Fig. 2a. The beat signal has a main periodicity of about 2 fs, corresponding to the beating between the 2*p* and the 3*p* states. This beating is also clearly observed in the red dashed curve in Fig. 2c, which is obtained by integrating over all photoelectrons emitted along the polarization axis in the upward direction. The periodicity of the beat signal carries information on the relative energy separation of the states involved, while the absolute timing of the beating depends on the relative phase of the pairs of states contributing to the signal.

The different components of the excited wave packet can be extracted by Fourier analysis of the time-dependent photoelectron signal $S(E,t)$ shown in Fig. 2a in black. The signal corresponding to one particular observation energy E_r (here at 4 eV) indicated by the horizontal red dashed line in Fig. 2a is shown as a line-out in Fig. 2c. The Fourier transform of this time-dependent signal $S(E_r,t)$, denoted $\mathcal{S}(E_r,E')$, shown in Fig. 2d, contains six prominent peaks which we will discuss below. Compiling the Fourier transform at all the possible observation energies yields a two dimensional function of the observation energy (E) and the Fourier frequency (represented as an energy E'). This function, $\mathcal{S}(E,E')$, is presented as a color plot in Fig. 2b. It encompasses both the quantum beat and the multiple interference signals generated by our technique.

The different contributions to $\mathcal{S}(E,E')$ can best be understood by examining the evolution of the six prominent peaks in Fig. 2d as we change the observation energy. The three lowest peaks (at approximately 1, 2 and 3 eV) are from the quantum beat between 3*p*-4*p*, 2*p*-3*p*, and 2*p*-4*p* pairs of states respectively. They are distinguished by the fact that their Fourier frequency does not change as a function of observation energy. As a result, they appear as vertical lines in Fig. 2b. The other peaks at 4.9, 5.55 and 7.4 eV in Fig. 2c are due to the interference between the direct and indirect pathways into the continuum. The indirect pathways involve the 4*p*, 3*p* and 2*p* states as intermediaries, in order of increasing energy. These peaks are distinguished by the fact that their Fourier frequency *increases* with increasing observation energy. This is because the accumulated phase difference between the direct and indirect ionization pathways is proportional to the difference between the bound state energy and the continuum energy where the observation is made. This linear relationship results in a line tilted at 45 degrees in Fig. 2b. The energies of the bound intermediate states (4*p*, 3*p*,

2*p*) in the wave packet can be read directly from the intersections of the 45 degree lines with the horizontal zero energy line. In addition, the relative strengths of the 45 degree lines relate the contributions from each bound state to the ionization signal.

Experimental results and analysis

In Fig. 3a, we present an experimental photoelectron spectrum, obtained with a maximum delay of 45 fs and with an attosecond pulse spectrum exciting the helium atom from the 3p state upwards. The low energy part of the photoelectron spectrum between 0 and 2 eV shows well resolved hyperbolic interference fringes, and a beating with a 13 fs periodicity can also be observed. In Fig. 3b a Fourier analysis of the experimental data similar to that presented above shows the characteristic 45-degrees lines for multi-path interferences through the 4*p* and 5*p* states, as well as with the 3*p* state which is just barely excited by the low frequency part of the XUV spectrum. A weak indication of the 4*p*-5*p* quantum beat can also be seen as a vertical line near 0.5 eV.

One notable feature of the energy and angle-resolved experimental measurement is that it allows us to separate out the two contributions to the ionization signal, those due to quantum beating, and those due to multi-path interference. We can do this by analyzing the full angular-resolved photo-electron distribution $F(E,\theta,t)$ as a function of time. Given the cylindrical symmetry of the problem, $F(E,\theta,t)$ can be expanded as a sum of Legendre polynomials

$$F(E,\theta,t) = \sum_{J=0}^{2L_{max}} \beta_J(E,t) P_J[\cos(\theta)],$$

where P_J is the Legendre polynomial of J^{th} order, β_J an expansion coefficient, and L_{max} the maximum angular momentum component of the ionized wave function, which

corresponds to the maximum absorbed angular momentum. After extraction of the individual expansion coefficients, $\beta_J(E,t)$, we apply the same analysis that was used for the photoelectron spectrum measured along the laser polarization axis. An example of this analysis is shown in Fig. 3c-f where the extracted expansion coefficients $\beta_1(E,t)$ and $\beta_2(E,t)$ are presented respectively as a function of time together with their Fourier transforms. Simple parity arguments dictate that interference between ionization processes that end in states of definite parity (either even or odd with respect to reflection along the polarization direction) will appear in the even *J* expansion coefficients, while interference between ionization processes that end in mixed parity states (both even and odd) will appear in the odd J expansion coefficients.

In our experiments, with moderately weak probe fields and low photo-electron energies, the direct-indirect interference process involves electrons that have absorbed different numbers of photons (one for direct, two for indirect since the bound states involved can be ionized by absorption of one IR photon) resulting in a mixed parity state. Indeed, we see that the characteristic hyperbolic interference fringes that denote this process appear more clearly in $\beta_1(E,t)$ and are strongly reduced in $\beta_2(E,t)$. This is confirmed by Fourier analysis (Fig. 3d). In contrast, the process that produces quantum beats (interference between states in the bound wave packet) results in states of definite parity. Accordingly, the quantum beat signal dominates $\beta_2(E,t)$ (Fig. 3e, f). Thus for a weak probe pulse, which can only induce single photon ionization from the excited states, the quantum beat signal and the bound-continuum interference should be strictly separated into even and odd *J* channels respectively. The strength of our probe pulse, however, allows for some absorption of extra photons and a weak signal is also seen from the direct-indirect interference in Figs. 3e, f. We emphasize that these multi-

photon effects are not a hindrance to the state-specific analysis that we have been discussing.

Perspective

Ideally a method for fully characterizing an attosecond electron wave packet should be able to (i) be applied to wave packets that are created either directly or indirectly by an attosecond pulse; (ii) supply the energies, amplitudes and initial phases of the states that comprise the wave packet; and (iii) follow the bound state dynamics which may include decay and/or de-phasing of the states. The experiment and the analysis we have presented thus far demonstrate that we can probe an attosecond electron wave packet using a coherent reference wave packet that is in the continuum. The wave packets that we have been discussing are created directly by our attosecond pulse, and the state amplitudes and phases are constant on a femtosecond time scale. With this proof of principle in hand, we now turn to a series of model calculations which demonstrate that our attosecond pump-probe interferometry can satisfy all three requirements that we have laid out.

The paradigmatic example of a wave packet that is indirectly created by an attosecond pulse is one formed from valence electrons when an inner shell electron is rapidly removed from an atom or molecule. These “shake-up” wave packets often span the ionization threshold and their continuum component is then called the “shake-off” wave packet. In general the components of the shake-up wave packet are not directly determined by the attosecond pulse, and the states that make up the wave packet may decay by, *e.g.*, Auger process.

To demonstrate the generality of our method we numerically simulated a shake-up/shake-off process in helium, using a sudden approximation in which one of the

helium electrons is removed while the remaining electron is left in the potential of the helium ion. This leads to excitation of all the *s*-states in the helium ion and also to significant ionization populating the continuum *s*-states. To illustrate how our method can be used to follow the time dependence of the state amplitudes $A_i(t)$ and phases $\varphi_i(t)$ we impose either an artificial lifetime of 5 fs or a variable phase shift on the 3s state and attempt to retrieve them from the interferogram. Our probe pulse is of 2 cycle duration and has a 200 nm wavelength.

In Fig. 4a we show the expansion coefficients $\beta_1(E,t)$, which contain information about the direct-indirect pathway interference. In the Fourier transform, $\mathcal{S}(E,E')$, (Fig. 4b) the contributions to the signal from excited states from 3s to 5s are clearly resolved (the 2s state cannot be ionized through one photon ionization with the probe field used). $A_i(t)$ and $\varphi_i(t)$ are retrieved by filtering the contribution from state *i* with a window function in the Fourier transform and then by inverse Fourier transforming back to the time domain. As an example, Fig. 4c shows the filtered expansion coefficient $\beta_1(E,t)$ after selecting only the contribution from the 3s state. Here the Moiré pattern disappears and the hyperbolic fringes appear more clearly. The amplitude of the oscillations is directly proportional to the amplitude of the state, $A_i(t)$, and in Fig. 4d, the extracted $A_i(t)$ is plotted for the states 3s (red lines), 4s (blue lines) and 5s (black lines), both for the case where the lifetime of the 3s state is infinite (dashed lines) and where it is artificially set to 5 fs (solid lines). The retrieval of the amplitudes is straight-forward, and the extracted lifetime matches the applied lifetime, but the extraction of the time-dependent phases, $\varphi_i(t)$, requires further analysis, which is briefly described below.

The phase of the oscillation measured at a given continuum energy E is the difference in phase between the two pathways, the direct: $\frac{E}{\hbar}(t-t_o)+\varphi_E$ and the indirect: $\varphi_i(t)+\frac{E_i}{\hbar}(t-t_o)+\varphi'_E$, where φ_E and φ'_E represent the phases gained by the electron in the direct and indirect ionization steps respectively. Assuming $\varphi_E=\varphi'_E$ the phase of the measured oscillation is given by:

$$\phi_{\mathrm{det}}(E,t)=\varphi_i(t)+(E_i-E)(t-t_o)/\hbar.$$

To correctly retrieve the phase, $\varphi_i(t)$, we need to know precisely the energy of the state, E_i, and the exact time of creation of the reference wave packet, t_0. This information can be obtained by utilizing the fact that we measure ϕ_{det} as a function of *both* delay and energy. E_i can be extracted from the Fourier transform (Fig. 4b), while t_0 is obtained by differentiating $\phi_{\mathrm{det}}(E,t)$ with respect to E, yielding t-t_0, from which t_0 can be determined. For the data shown in Fig. 4, such an analysis yields energies E_i =6.05, 3.41 and 2.18 eV for the 3s, 4s and 5s state, respectively, in excellent agreement with the energies of the states found in the potential used in the code. The ionization time for the reference wave packet, t_0, is determined to -0.66 fs, or one period of the probe field, which corresponds to the time when the sudden shake-up process takes place in the calculation. Finally, in Fig. 4e, the extracted initial phases, $\varphi_i(t_0)$ are plotted for the states 3s (black symbols), 4s (red symbols) and 5s (blue symbols), with phase shifts between 0 and π imparted on the 3s state. The retrieved phases are found to be in very good agreement with the imparted phases.

In conclusion, the method demonstrated in this article can be used to probe the temporal evolution of bound electron wave packets with high spectral and temporal resolution simultaneously. A further advantage is that our interferometric method does not rely on the use of intense probing fields, which is important when attosecond

techniques are applied to photo-induced processes that have a relevance to our natural environment. In this experiment we have created a broad electron wave packet in helium and demonstrated that it is a coherent superposition of bound and ionized states. Furthermore, we have demonstrated that the coherence between different components of the continuum wave packet created at different times and by different processes can be used to measure the amplitudes and phases of a bound attosecond electron wave packet.

Method summary

In the experiments, performed in Milan, a linearly polarized phase stabilized, few-cycle, IR laser pulse is divided into a central and annular part using a mirror with a hole in the center. The polarization gating technique is used on the central part to obtain a temporal window of linear polarization with a duration of less than half an optical cycle. This laser beam is focused into a xenon gas cell to generate XUV radiation via high order harmonic generation[24]. The low order harmonics and the collinear IR radiation are removed using a 100 nm thick aluminum filter. This metallic filter also provides partial dispersion compensation of the intrinsic positive chirp of the emitted pulse, compressing it to a duration of 350 attoseconds[6]. The attosecond pulses are focused using a grazing incidence toroidal mirror into the active region of a VMIS[25], used to record the photoelectron momentum distributions. The annular part of the initial IR beam is focused by a spherical mirror and collinearly recombined with the attosecond pulse using a second mirror with a hole in the centre. A piezoelectric stage inserted in the annular beam path allowed us to change the relative delay between the two pulses. The XUV and IR beams are crossed with an effusive He gas jet emerging from a capillary incorporated into the repeller electrode of the VMIS[26]. Using a set of electrostatic lenses, the electrons emitted in the two-color photo ionization process are accelerated onto a multichannel plate coupled to a phosphor screen detector. Two dimensional

images are acquired with a CCD camera and used for the retrieval of the 3D initial velocity distribution[29].

References

1. Paul, P. M., *et al.* Observation of a train of attosecond pulses from high harmonic generation. *Science* **292**, 1689-1692 (2001)

2. Hentschel, M., *et al.* Attosecond metrology. *Nature* **414**, 509-513 (2001)

3. Ferray, M, *et al.* Multiple-harmonic conversion of 1064 nm radiation in rare gases. *J. Phys. B*, 21, L31 (1988)

4. Schafer, K. J., *et al*. Above threshold ionization beyond the high harmonic cutoff. *Phys. Rev. Lett.* **70**, 1599-1602 (1993)

5. Corkum, P. B., Plasma perspective on strong-field multiphoton ionization. *Phys. Rev. Lett.* **70**, 1994-1997 (1993)

6. Sansone, G., *et al.* Isolated Single-Cycle Attosecond Pulses. *Science*, **314**, 443-446 (2006)

7. Gustafsson, E., *et al.* Broadband attosecond pulse shaping. *Opt. Lett.* **32**, 1353 (2007)

8. Goulielmakis, E., *et al*. Single-Cycle Nonlinear Optics. *Science* **320**, 1614 (2008)

9. Drescher, M., *et al.* Time-resolved atomic inner-shell spectroscopy. *Nature* **419**, 803-807 (2002)

10. Remetter, T., *et al.* Attosecond Electron Wave Packet Interferometry. *Nature Physics* **2**, 323 (2006)

11. Goulielmakis, E., *et al*. Direct Measurement of Light Waves. *Science*, **305**, 1267-1269 (2004).

12. Johnsson, P., *et al.*, Attosecond electron wave packet dynamics in strong laser fields, *Phys. Rev. Lett.* **95**, 013001 (2005).

13. Itatani, J., *et al*. Attosecond streak camera. *Phys. Rev. Lett.* **88**, 173903 (2002).

14. Kienberger, R., *et al.* Steering attosecond electron wave packets with light. *Science* **297**, 1144-1148 (2002)

15. Mauritsson, J., *et al.* Coherent Electron Scattering Captured by an Attosecond Quantum Stroboscope. *Phys. Rev. Lett.* **100**, 073003 (2008)

16. Uiberacker M., *et al.* Control Attosecond real-time observation of electron tunnelling in atoms. *Nature* **446**, 627 (2007)

17. Uphues, Th., *et al.* Ion-charge-state chronoscopy of cascaded atomic Auger decay. *New J. of Physics* **10,** 025009 (2008)

18. Jones, R. R., Schumacher, D. W., Gallagher, T. F. and Bucksbaum, P. H., Bound-state interferometry using incoherent light, *J. Phys. B* **28**, L405-L411 (1995).

19. Bellini, M., Bartoli, A. and Hänsch, T. W., Two-photon Fourier spectroscopy with femtosecond light pulses, *Opt. Lett.* **22**, 540-542 (1997)

20. Cavalieri, S., Eramo, R., Materazzi, M., Corsi, C. and Bellini, M., Ramsey-Type Spectroscopy with High-Order Harmonics, *Phys. Rev. Lett.* **89**, 133002 (2002)

21. Sandtke, M. and Kuipers, L., *Nature Photonics* **1**, 573 (2007)

22. Leichtle, C., Schleich, W. P., Averbukh, I. Sh. and Shapiro M., Quantum State Holography *Phys. Rev. Lett.* **80**, 1418 (1998)

23. Weinacht, T. C., Ahn, J. and Bucksbaum P. H., Measurement of the Amplitude and Phase of a Sculpted Rydberg Wave Packet *Phys. Rev. Lett.* **80**, 5508 (1998)

24. Sola, I. J., et al. Controlling attosecond electron dynamics by phase-stabilized polarization gating. *Nature Physics* **2**, 319-322 (2006).

25. Eppink, A. T. J. B. and Parker, D. H., Velocity map imaging of ions and electrons using electrostatic lenses. Application in photoelectron and photofragment ion imaging of molecular oxygen, *Rev. Sci. Instr.* **68**, 3477-3484 (1997).

26. Ghafur O., Siu W., Johnsson P., Kling M. F., Drescher M. and Vrakking M. J. J., A velocity map imaging detector with an integrated gas injection system, *Rev. Sci. Instrum.* **80**, 033110 (2009).

28. Johnsson, P., Mauritsson J., Remetter T., L'Huillier A. and Schafer K. J. Attosecond Control of Ionization by Wave-Packet Interference *Phys. Rev. Lett*. **89**, 173001 (2007).

29. Vrakking, M. J. J., An iterative procedure for the inversion of two-dimensional ion/photoelectron imaging experiments, *Rev. Sci. Instrum.* **72**, 4084-4089 (2001).

Acknowledgments: This research was supported by a Marie Curie Intra-European Fellowship, the Marie Curie Research Training Networks XTRA, the Marie Curie Early Stage Training Site MAXLAS, the Integrated Initiative of Infrastructure LASERLAB-EUROPE within the 6th European Community Framework Programme, the Swedish Research Council and the National Science Foundation. IZ, SZ, TU and MFK are grateful for support by the DFG through the Emmy-Noether program and the Cluster of Excellence: Munich Center for Advanced Photonics (www.munich-photonics.de). This work is part of the research program of the "Stichting voor Fundamenteel Onderzoek der Materie" (FOM), which is financially supported by the "Nederlandse Organisatie voor Wetenschappelijk Onderzoek" (NWO). KJS acknowledges support from the Ball Family Professorship.

Author Information Reprints and permissions information is available at www.nature.com/reprints. The authors declare no competing financial interests. Correspondence and requests for materials should be addressed to J.M. (johan.mauritsson@fysik.lth.se).

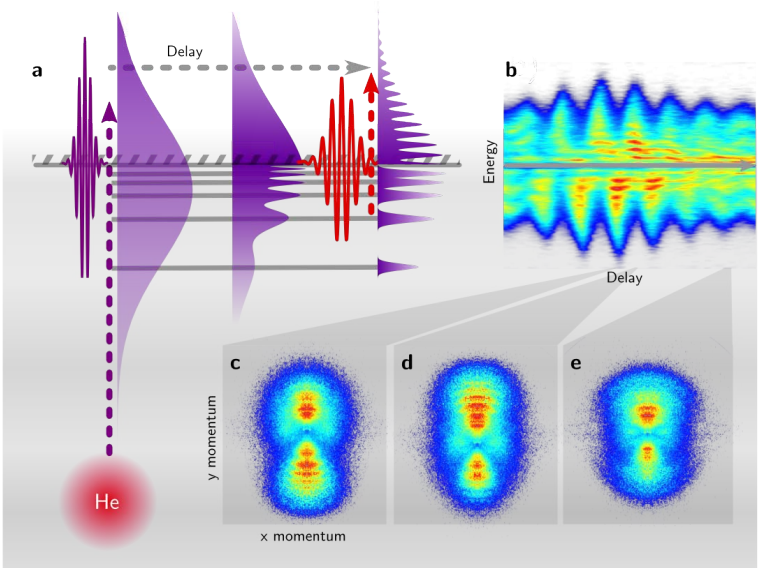

Figure 1: Principle of attosecond pump-probe interferometer. a, At time t_0, a broadband, isolated attosecond pulse centered on the ionization threshold of Helium is used to coherently excite an electron wave packet consisting of a superposition of bound and continuum *p*-states. After a delay, t-t_0, the bound part of the wave packet is ionized by a few cycle IR pulse, which is locked in phase to the attosecond pulse. The electron distribution is recorded using a velocity map imaging spectrometer (VMIS). Three VMIS images are shown for different delays in **c**-**e** and the on-axis electron energy is presented as a function of delay in **b**. The photoelectron spectra exhibit interference fringes owing to different pathways leading into the continuum allowing us to extract both phase and amplitude information about the excited states.

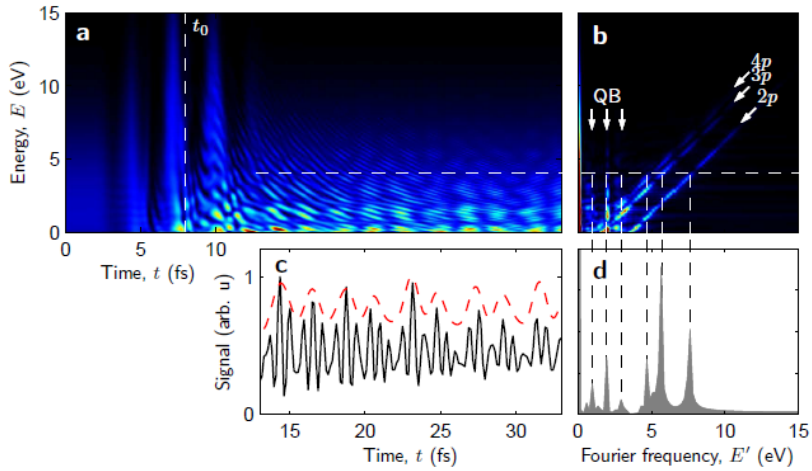

Figure 2: Analyzing the interferograms. a, Calculated photoelectron spectrum in He as a function of delay between the attosecond pump pulse and a two-cycle infrared probe pulse. The spectrum shows electrons emitted in the direction of the infrared and XUV polarization axis. Interference fringes are clearly seen at all delays where the attosecond pulse comes before the IR probe ($t<t_0$). **b**, Fourier transform of the photoelectron spectrum allowing the identification of the states that form the bound wave packet. The beat signals from the 2p, 3p and 4p states can be seen as vertical lines around 2 eV, while the interference between direct and indirect pathways give rise to contributions at an angle of 45 degrees. A lineout of the spectrogram at 4 eV is presented in **c** together with its Fourier transform (**d**). The red dashed line in **c** shows the integrated electron spectrum.

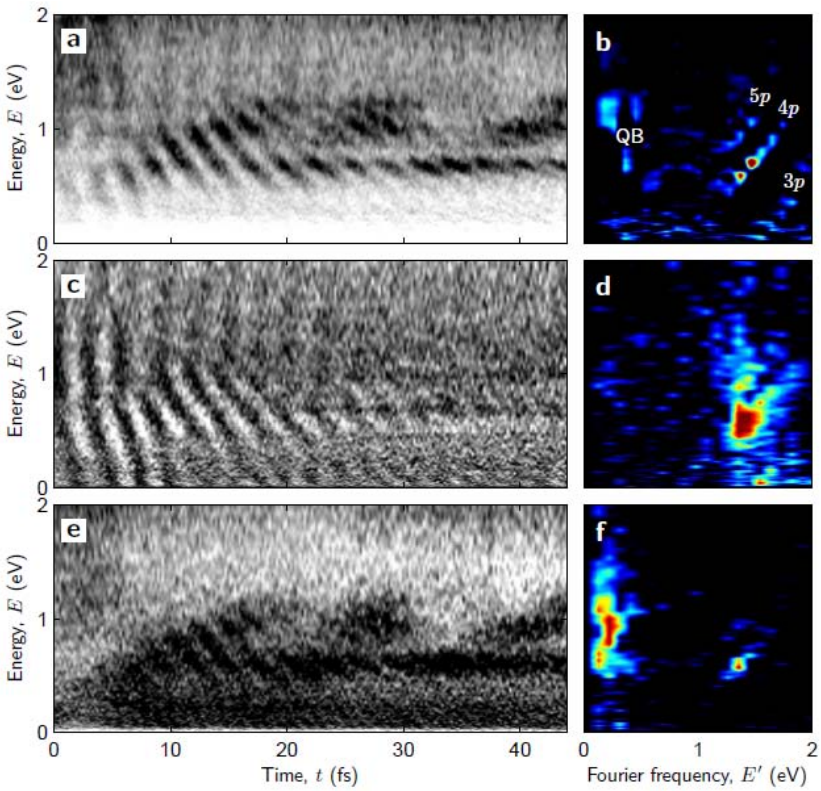

Figure 3: Partial wave analysis of the experimental angular distributions. a, Experimental interferogram obtained by recording the photoelectrons along the polarization axis and its Fourier transform (**b**). With mainly 4p and 5p excited the beating between the outgoing electron waves has a period of approximately 13 fs (three beat periods can be seen in **a**). From the Fourier analysis (**b**) we can resolve the two states and the beating between them, but also see a small hint of the 3p state, which was only weakly excited in this particular experimental scan. The different processes can be separated by a partial wave analysis where the direct – indirect interference appears primarily in the odd expansion coefficients, **c** and **d**, and the quantum beat signal appears exclusively in the even coefficients, **e** and **f**.

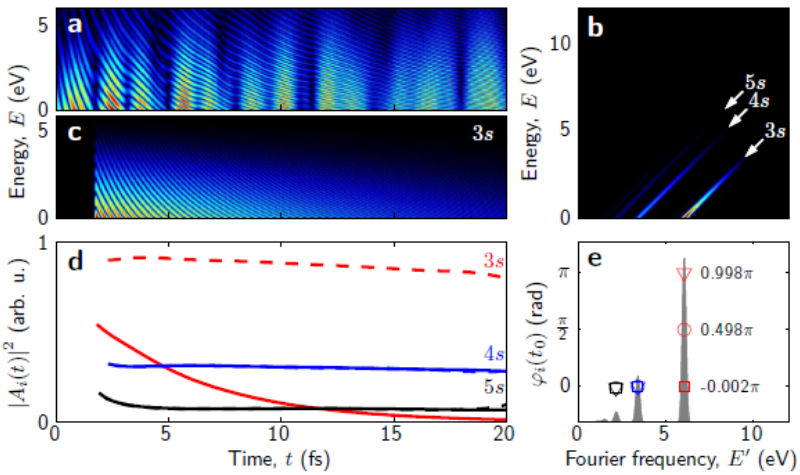

Figure 4: Amplitude and phase retrieval for shake-up/shake-off. a, Calculated spectrogram for the shake-up/shake-off process in helium ionized by a two cycle pulse [the presented data is the first odd expansion coefficient, $\beta_1(E,t)$]. The excited states can be clearly seen in the Fourier transform (**b**). **c**, Filtered spectrogram where only the contribution to $\beta_1(E,t)$ from the 3s state has been included, clearly showing the hyperbolic fringes. **d**, Time-dependent population of the states calculated by extracting the amplitude from the spectrogram in panel **c**, showing clearly the artificial lifetime of 5 fs that was imposed on the 3s state. **e**, Extracted phases at t_0 for the three states, presented for 3 different spectrograms where different phase shifts have been imposed on the 3s state. In the background, the Fourier spectrum at E=0 from panel **b** is plotted in gray.

PAPER IX

Ionization and Wave-Packet Dynamics Studied Using Two-Color XUV and IR Pump-Probe Spectroscopy

F. Kelkensberg, C. Lefebvre, W. Siu, O. Ghafur, T. T. Nguyen-Dang, O. Atabek, A. Keller, V. Serov, P. Johnsson, M. Swoboda, T. Remetter, A. L'Huillier, S. Zherebtsov, G. Sansone, E. Benedetti, F. Ferrari, M. Nisoli, F. Lépine, M. F. Kling and M. J. J. Vrakking.

Phys. Rev. Lett. **103**, 123005 (2009).

PRL 103, 123005 (2009) PHYSICAL REVIEW LETTERS week ending 18 SEPTEMBER 2009

Molecular Dissociative Ionization and Wave-Packet Dynamics Studied Using Two-Color XUV and IR Pump-Probe Spectroscopy

F. Kelkensberg,[1] C. Lefebvre,[2,3] W. Siu,[1] O. Ghafur,[1] T. T. Nguyen-Dang,[2] O. Atabek,[3] A. Keller,[3] V. Serov,[3] P. Johnsson,[1,4] M. Swoboda,[4] T. Remetter,[4] A. L'Huillier,[4] S. Zherebtsov,[7] G. Sansone,[5] E. Benedetti,[5] F. Ferrari,[5] M. Nisoli,[5] F. Lépine,[1,6] M. F. Kling,[1,7] and M. J. J. Vrakking[1]

[1]*FOM Institute for Atomic and Molecular Physics (AMOLF), Science Park 113, 1098 XG Amsterdam, The Netherlands*
[2]*Département de chimie, Université Laval, Québec, G1K 7P4, Qc, Canada*
[3]*Laboratoire de Photophysique Moléculaire, Bâtiment 213, Campus d'Orsay, Université Paris-Sud 11, 91405 Orsay, France*
[4]*Department of Physics, Lund University, PO Box 118, SE-221 00 Lund, Sweden*
[5]*CNR-INFM, National Laboratory for Ultrafast and Ultraintense Optical Science, Department of Physics, Politecnico of Milan, Piazza L. da Vinci 32, 20133 Milano, Italy*
[6]*Université Lyon 1, CNRS, LASIM, UMR 5579, 43 bvd. du 11 Novembre 1918, F-69622 Villeurbane, France*
[7]*Max-Planck Institut für Quantenoptik, Hans-Kopfermann Strasse 1, D-85748 Garching, Germany*

(Received 2 July 2009; published 17 September 2009)

We present a combined theoretical and experimental study of ultrafast wave-packet dynamics in the dissociative ionization of H_2 molecules as a result of irradiation with an extreme-ultraviolet (XUV) pulse followed by an infrared (IR) pulse. In experiments where the duration of both the XUV and IR pulses are shorter than the vibrational period of H_2^+, dephasing and rephasing of the vibrational wave packet that is formed in H_2^+ upon ionization of the neutral molecule by the XUV pulse is observed. In experiments where the duration of the IR pulse exceeds the vibrational period of H_2^+ (15 fs), a pronounced dependence of the H^+ kinetic energy distribution on XUV-IR delay is observed that can be explained in terms of the adiabatic propagation of the H_2^+ wave packet on field-dressed potential energy curves.

DOI: 10.1103/PhysRevLett.103.123005 PACS numbers: 33.80.Gj, 33.20.Tp, 42.50.Md, 82.53.Eb

With recent advances in laser technology, real-time imaging of ultrafast molecular phenomena has become possible. Femtosecond laser pulses have led to the development of transition state spectroscopy and femtosecond chemistry [1], and have been applied in pump-probe experiments to map out time-dependent nuclear motion in molecules [2]. The advent of attosecond pulses [3] has given rise to endeavours where it is the even faster electronic motion that is probed in a time-resolved manner [4]. The high-harmonic generation technique that is responsible for the formation of attosecond laser pulses has been exploited as a probe of molecular structure and dynamics, both with regards to the position or motion of the constituent atoms [5–7] and that of the electrons [6,8]. An important concern in these experiments is the question to which extent the structure and dynamics of the molecule(s) under investigation are influenced by the presence of the intense infrared (IR) laser field that drives the high-harmonic generation process [9]. Here we report experiments on the dissociative ionization of H_2 in a two-color extreme ultra-violet (XUV) + infrared (IR) laser field, where variation of the pulse duration of the IR field affects the adiabaticity of the strong-field dissociation, as manifested in the proton kinetic energy distributions that can be measured. More specific, we present a combined theoretical and experimental study of ultrafast wave-packet dynamics in the $1s\,\sigma_g^+$ potential of a H_2^+ molecular ion created by an ultrashort XUV pump pulse, with the initial H_2^+ geometry reflecting that of the neutral ground state. Subsequently, molecular dissociation by the process of bond softening (BS) [10–12] is induced by an IR pulse with different durations, ranging from 7 fs up to 35 fs. In the first case (experiment A, hereafter) the IR pulse is significantly shorter than the H_2^+ vibrational period, implying that the vibrational wave packet freely propagates on the H_2^+ ($1s\,\sigma_g^+$) potential energy curve until it finally dissociates under the influence of the IR pulse. By contrast, in experiment B, the duration of the IR laser pulse is comparable to or longer than the H_2^+ vibrational period. This implies that the IR field is present during the propagation of the wave packet before dissociation, which, depending on the XUV-IR delay, may or may not include the time at which the ionization by the XUV took place. In experiment A, few-cycle 750 nm laser pulses were obtained by means of hollow-core fiber compression [13] and were split into a central and an annular part. The central part (5 fs FWHM) was used to generate attosecond XUV laser pulses in a Kr gas cell. By using the polarization gating technique this resulted in isolated attosecond pulses with an estimated pulse duration of 400 as [14,15]. The attosecond pulses, which spanned an energy range from 15 to 35 eV, were collinearly recombined with the annular part (7 fs FWHM) of the few-cycle IR pulse (with a variable time delay) and focused into the active region of a velocity map imaging spectrometer [16]. The velocity and angular distribution of H^+ ions resulting from two-color excitation

 © 2009 The American Physical Society

of H_2 molecules were measured. Experiment B made use of a similar setup (previously described in Ref. [17]), except for the fact that the IR laser pulse was about 35 fs long. Consequently, the XUV pulse generated by high-harmonic generation then consisted of a train of attosecond pulses. This, and differences in the XUV spectrum, do not affect our observations significantly.

Figure 1 shows a comparison of the time-dependent H^+ kinetic energy (KE) distributions measured in experiments A and B. For delays $\tau > 0$ fs, the XUV pulse precedes the IR pulse. In experiment A, the yield of fragments with energies below 1.2 eV oscillates in time with a period of about 27 fs. The results for experiment B, where the IR pulse duration is somewhat longer than the vibrational period of the $H_2{}^+$ molecule, are radically different. The time dependence of the H^+ KE distribution evolves smoothly as a function of time. The most striking feature in measurement B is that the KE release shows a pronounced decrease when the peak of the IR pulse comes after the XUV pulse.

In order to simulate the experimental results, a one-dimensional model was used. The molecular system H_2, originally in its ground vibrational and electronic state, is considered to be ionized by an XUV pulse or a pulse train at time $t = 0$. The ionization occurs by a single XUV pulse in the presence of a 7 fs FWHM IR laser pulse (experiment A), or by an XUV pulse train consisting of 15 attosecond pulses in the presence of a 35 fs FWHM IR laser pulse (experiment B). The center of the laser pulse is positioned at a delay $t = \tau$ with respect to the XUV pulse(s). Based on the favorable Franck-Condon (FC) overlap between the neutral ground state and the ionic $|1s\ \sigma_g^+\rangle$ state and based on the fact that our energy-resolved detection allows us to selectively investigate the BS channel, we will consider that the attosecond pulse promotes the $v = 0$ vibrational state of the parent molecule vertically onto the $|1s\ \sigma_g^+\rangle$ state of the molecular ion. We consider the nuclear motion to occur on two electronic manifolds of the molecular ion $H_2{}^+$: the ground state $|1s\ \sigma_g^+\rangle$ and the first excited electronic state $|2p\ \sigma_u^+\rangle$. In the simulations, the molecule is assumed to be aligned along the laser polarization. Experimentally, the angle-resolved H^+ detection allows us to selectively observe fragments along the polarization axis. As it turns out, none of the observations reported here depend very strongly on the ejection angle of the H^+ fragment with respect to the polarization axis. The nuclear dynamics is obtained by solving the one-dimensional time-dependent Schrödinger equation using a wave-packet propagation procedure largely described in previous work (see [10] for complete details). The resulting kinetic energy spectra are compared with the experimental spectra.

Figure 2 displays the theoretical proton KE distributions as a function of the time delay between the XUV pump and the IR probe for experiments A and B at intensities of $1 \cdot 10^{13}$ W/cm^2 and $3 \cdot 10^{12}$ W/cm^2 respectively, which corresponds to the peak intensity in the experiments. The main observations of Fig. 1 are qualitatively reproduced.

In experiment A, the XUV laser pulse prepares a coherent superposition of vibrational states of $H_2{}^+$, which evolves under essentially field-free conditions, oscillating back and forth and spreading out on the $1s\ \sigma_g^+$ potential before encountering the IR pulse. The short durations of the IR pulse evokes a situation, in which the laser-molecule interaction opens a ''gate'' to dissociation at some internuclear distance. The dissociation yield, hence, depends on a synchronization between the wave packet and the opening of this gate at the maximum of the IR field. Stated differently, the oscillations in the dissociation yield are a result of the coherence between the various vibrational components of the initial wave packet [2]. This coherence is further explored in Fig. 3, which shows the Fourier transforms of the H^+ fragment yield integrated over the KE distribution in the range of 0–1.2 eV for the experimental [Fig. 3(a)] and the theoretical [Fig. 3(b)] results. This reveals that the oscillatory signal is composed of a series of two-level beats at frequencies that are given by the energy difference between adjacent vibrational levels centered around the level $v^+ = 9$ [18,19]. A correlation between frequency and kinetic energy is observed when the Fourier transform is shown as a function of the fragment KE (see insets in Fig. 3). This can be understood from the

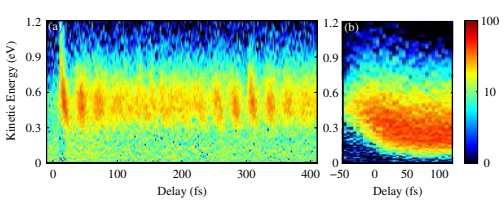

FIG. 1 (color online). Measured time-dependent H^+ kinetic energy distributions for two-color XUV + IR dissociative ionization of H_2, with 7 fs IR laser pulses (a) and 35 fs IR laser pulses (b). In the latter case the XUV pulse consisted of a train of attosecond laser pulses.

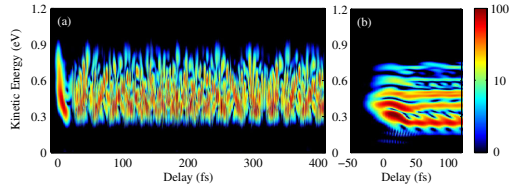

FIG. 2 (color online). Calculated time-dependent kinetic energy distributions resulting from model calculations for two-color XUV + IR dissociative ionization of H_2, making use of a 7 fs FWHM IR pulse (a) and a 35 fs FWHM IR pulse (b). In the latter case the XUV pulse consisted of a train of attosecond laser pulses.

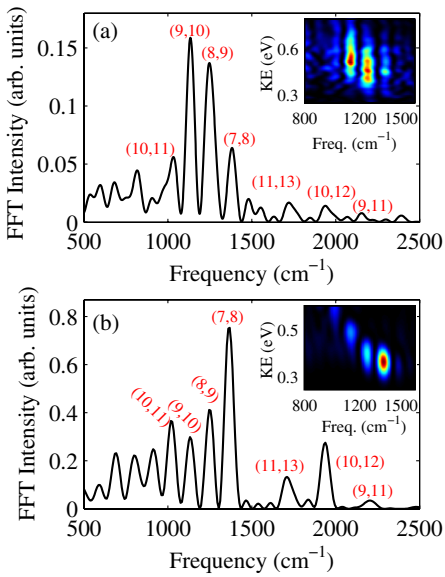

FIG. 3 (color online). Fourier transform of the H^+ fragment yield integrated over the energy range between 0 and 1.2 eV for the experimental (a) and theoretical (b) results, in the case of a 7 fs FWHM IR laser pulse. The spectra reveal the two-level beats that are responsible for the observed time dependence. The insets show an energy-resolved Fourier transformation and reveal a correlation between the fragment KE release and the vibrational level occupied prior to dissociation, observed both in the experiment and the simulations.

fact that higher vibrational levels, which lead to larger observed kinetic energies, have a smaller energy separation. Clearly, the calculations in Fig. 2(a) contain very detailed structures which are partially washed out by the volume averaging in the experiment and which arise from the simultaneous influence of several vibrational frequencies (see Fig. 3) corresponding to $\Delta v^+ = 1$ or $\Delta v^+ = 2$ at a given fragment kinetic energy. This indicates that more than 3 vibrational states contribute at a given kinetic energy, which is a manifestation of the nonadiabatic nature of the dissociation process.

When the H_2^+ vibrational wave packet interacts with the longer IR pulse, as in experiment B, little or no dependence of the KE spectrum on the time delay τ is expected when the XUV pulse precedes the IR without overlapping. This is indeed what is observed for time delays $\tau > 20$ fs. In contrast, for $\tau < 20$ fs the fragment KE is strongly delay dependent, where at near zero delay it reaches energy values similar to those encountered in experiment A.

The dependence of the H^+ kinetic energy on XUV-IR delay in experiment B can be understood in terms of the adiabaticity of the dissociation process, and the way the IR intensity affects both the preparation and the propagation of the wave packet. To understand this, it is useful to discuss the dissociation dynamics in terms of Floquet states. The probe pulse projects the various vibrational components of the wave packet onto Floquet resonances, whose widths and energies vary with the intensity of the IR pulse.

When the IR pulse follows the XUV pulse without overlapping [i.e., $\tau > 20$ fs, situation indicated in Fig. 4(a)] individual field-free vibrational states v^+ of the ion are, at first, transported adiabatically onto corresponding Floquet resonances. Each resonance gives rise to a characteristic contribution to the proton KE spectrum [18]. The magnitude of the kinetic energy is determined by the nonperturbative laser-induced modification of the dressed potential energy curves. On the way towards dissociation, the ion experiences an increasing IR pulse amplitude, lowering the BS barrier. The lowest barrier height is reached at the center of the pulse (maximum of intensity), resulting in most efficient dissociation when the lowest energy resonance can still tunnel before the barrier rises. Most protons contributing to the spectrum have a KE of about 0.3 eV, corresponding to the resonance issued from $v^+ = 8$. Higher energy resonances are also dissociative, but are not significantly populated by the XUV ionization step (through FC mapping of the vibrationless ground state of H_2).

This situation is in contrast with the case where the IR and XUV pulses are overlapping ($\tau < 20$ fs). The vibrational states of the ion are then shaken up by the sudden intense IR excitation and transferred onto a superposition of resonances with weighting coefficients in the wave

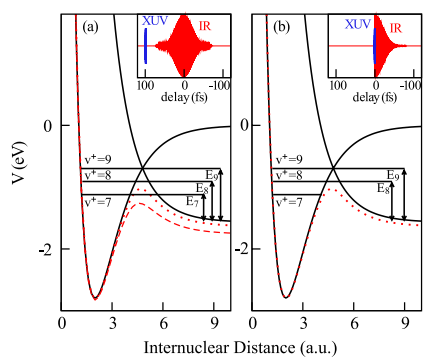

FIG. 4 (color online). Potential energy curves of H_2^+ in a 750 nm laser-dressed diabatic representation (black solid lines). Also indicated are the lower adiabatic curves resulting from the diagonalization of the radiative interaction for two intensities reached at the center of the pulse: $I = 3 \cdot 10^{12}$ W/cm^2 (dashed red line) and $I = 10^{12}$ W/cm^2 (dotted red line). E_7, E_8 and E_9 represent the kinetic energies issued from $v^+ = 7$, 8 and 9 for XUV-IR delays of 100 fs (a) and 0 fs (b).

packet that can noticeably differ from those resulting from a FC ionization step. In particular, higher energy resonances may temporarily be populated and play an important role in the dissociation step. Afterwards, as shown in Fig. 4(b), the ion experiences the falling edge of the IR pulse with a rising BS barrier which quenches the dissociation of low energy resonances. High energy over-the-barrier shape resonances, more populated than in the previous adiabatic case, are the ones which contribute most to the dissociation. The increasing role played by resonances issued from $v^+ = 9, 10$ explains the shift to higher energies of the proton KE distribution when the XUV pulse is close to the maximum of the IR probe. We note that at very short delays corresponding to the XUV-IR pulse overlap, the blueshift of the kinetic energy spectrum can also observed in experiment A.

Better quantitative experiment versus theory agreement would require the relaxation of some of our model assumptions. Among these approximations are a phenomenological description of the XUV ionization step [20], the neglect of rotational degrees of freedom [21] and also of the laser focal volume averaging [21].

In conclusion, we have shown that the dynamics of two-color dissociative ionization of H_2 under the influence of an XUV + IR pulse sequence depends considerably on the properties of the IR radiation and whether or not the IR laser is already present when the molecule is ionized by the XUV pulse. We have described two experimental situations in this Letter where the richness of the structural determination of molecules, their imaging and possible control rest on the sudden character of the strong IR excitation and the partial breakdown of the adiabatic approximation. In this way our study represents a departure from most intense field dynamics work where, ordinarily, only adiabatic laser excitation regimes result into spectral observables with finely resolved peak structures that can be interpreted in terms of isolated, nonoverlapping resonances [18]. Our experiment and numerical analysis show not only that the dynamics of a small molecule like H_2^+ is strongly dependent on the presence of a strong laser field, but moreover that the influence of the laser field is strongly dependent on its pulse duration, influencing whether any induced dynamics is adiabatic or not.

This work is part of the research program of the "Stichting voor Fundamenteel Onderzoek der Materie (FOM)", which is financially supported by the "Nederlandse organisatie voor Wetenschappelijk Onderzoek (NWO)". Support by MC-RTN XTRA (FP6-505138) is gratefully acknowledged. C. L. and TTND acknowledge the Natural Sciences and Engineering Research Council of Canada (NSERC) for financial support. M. S. was supported by the MC-EST MAXLAS. The Swedish Research Council and the Knut and Alice Wallenberg foundation are gratefully acknowledged. M. F. K. and S. Z. acknowledge support by the DFG.

[1] A. H. Zewail, J. Phys. Chem. A **104**, 5660 (2000).
[2] T. Ergler, A. Rudenko, B. Feuerstein, K. Zrost, C. D. Schröter, R. Moshammer, and J. Ullrich, Phys. Rev. Lett. **97**, 193001 (2006).
[3] F. Krausz and M. Yu Ivanov, Rev. Mod. Phys. **81**, 163 (2009).
[4] M. Drescher, M. Hentschel, R. Kienberger, G. Tempea, C. Spielmann, G. A. Reider, P. B. Corkum, and F. Krausz, Science **291**, 1923 (2001).
[5] H. Niikura, R. Légaré, M. Yu Ivanov, D. M. Villeneuve, and P. B. Corkum, Nature (London) **421**, 826 (2003).
[6] M. Meckel, D. Comtois, D. Zeidler, A. Staudte, D. Pavicic, H. C. Bandulet, H. Pepin, J. C. Kieffer, R. Dörner, and D. M. Villeneuve, *et al.*, Science **320**, 1478 (2008).
[7] S. Baker, J. S. Robinson, A. Haworth, H. Teng, R. A. Smith, C. C. Chirila, M. Lein, J. W. G. Tisch, and J. P. Marangos, Science **312**, 424 (2006).
[8] J. Itatani, J. Levesque, D. Zeidler, H. Niikura, H. Pépin, J. C. Kieffer, P. B. Corkum, and D. M. Villeneuve, Nature (London) **432**, 867 (2004).
[9] C. C. Chirila and M. Lein, Phys. Rev. A **77**, 043403 (2008).
[10] A. Giusti-Suzor, X. He, O. Atabek, and F. H. Mies, Phys. Rev. Lett. **64**, 515 (1990).
[11] P. H. Bucksbaum, A. Zavriyev, H. G. Muller, and D. W. Schumacher, Phys. Rev. Lett. **64**, 1883 (1990).
[12] A. D. Bandrauk, *Molecules in Laser Field* (M. Dekker, New York, 1994).
[13] M. Nisoli, S. De Silvestri, and O. Svelto, Appl. Phys. Lett. **68**, 2793 (1996).
[14] G. Sansone, E. Benedetti, F. Calegari, C. Vozzi, L. Avaldi, R. Flammini, L. Poletto, P. Villoresi, C. Altucci, and R. Velotta *et al.*, Science **314**, 443 (2006).
[15] I. J. Sola, E. Mével, L. Elouga, V. Strelkov, L. Poletto, P. Villoresi, E. Benedetti, J.-P. Caumes, S. Stagira, and C. Vozzi *et al.*, Nature Phys. **2**, 319 (2006).
[16] O. Ghafur, W. Siu, P. Johnsson, M. Kling, M. Drescher, and M. J. J. Vrakking, Rev. Sci. Instrum. **80**, 033110 (2009).
[17] T. Remetter, P. Johnsson, J. Mauritsson, K. Varju, Y. Ni, F. Lépine, E. Gustafson, M. Kling, J. Khan, and R. López-Martens *et al.*, Nature Phys. **2**, 323 (2006).
[18] K. Sändig, H. Figger, and T. W. Hänsch, Phys. Rev. Lett. **85**, 4876 (2000).
[19] M. Gruebele and A. H. Zewail, J. Chem. Phys. **98**, 883 (1993).
[20] T.-T Nguyen-Dang, F. Chateauneuf, S. Manoli, O. Atabek, and A. Keller, Phys. Rev. A **56**, 2142 (1997).
[21] V. Serov, A. Keller, O. Atabek, H. Figger, and D. Pavicic, Phys. Rev. A **72**, 033413 (2005).

PAPER X

Electron Localization following Attosecond Molecular Photoionization

G. Sansone, F. Kelkensberg, J. F. Pérez-Torres, F. Morales, M. F. Kling, W. Siu, O. Ghafur, P. Johnsson, M. Swoboda, E. Benedetti, F. Ferrari, F. Lépine, J. L. Sanz-Vicario, S. Zherebtsov, I. Znakovskaya, A. L'Huillier, M. Yu. Ivanov, M. Nisoli, F. Martín and M. J. J. Vrakking.

(2010) *Nature, accepted for publication*.

Electron Localization following Attosecond Molecular Photoionization

G. Sansone[1*], F. Kelkensberg[2*], J. F. Pérez-Torres[3*], F Morales[3*], M.F. Kling[4], W. Siu[2], O.Ghafur[2], P. Johnsson[2,5], M. Swoboda[5], E. Benedetti[1], F. Ferrari[1], F. Lépine[6], J. L. Sanz-Vicario[7], S. Zherebtsov[4], I. Znakovskaya[4], A. L'Huillier[5], M. Yu. Ivanov[8], M. Nisoli[1], F. Martín[3], M.J.J. Vrakking[2,9]

[1]CNR-INFM, National Laboratory for Ultrafast and Ultraintense Optical Science, Department of Physics, Politecnico of Milan, Piazza L. da Vinci 32, 20133 Milano, Italy; [2]FOM-Institute AMOLF, Science Park 113, 1098 XG Amsterdam, The Netherlands; [3]Departamento de Química, C-9, Universidad Autónoma de Madrid, 28049 Madrid, Spain; [4]Max-Planck Institut für Quantenoptik, Hans-Kopfermann Strasse 1, D-85748 Garching, Germany; [5]Department of Physics, Lund University, PO Box 118, SE-221 00 Lund, Sweden ; [6]Université Lyon 1; CNRS; LASIM, UMR 5579, 43 bvd. Du 11 Novembre 1918, F-69622 Villeurbanne, France ; [7]Grupo de Física Atómica y Molecular. Instituto de Física, Universidad de Antioquia, Medellín, Colombia; [8] National Research Council of Canada, Ottawa, Ontario K1A 0R6, Canada; [9]Max-Born-Institut, Max-Born Straße 2A, D-12489 Berlin, Germany

[*] *These people contributed equally to this work.*

The development of attosecond laser pulses allows one to probe the inner workings of atoms and molecules on the timescale of the electronic response [1-4]. In molecules, attosecond pump-probe spectroscopy enables investigations of the prompt charge redistribution and localization that accompany photo-excitation processes, where a molecule is lifted from the ground Born-Oppenheimer potential energy surface to one or more excited surfaces, and where subsequent photochemistry evolves on femtosecond timescales. Here we present the first example of a molecular attosecond pump-probe experiment. H_2 and D_2 are dissociatively ionized by the sequence of an isolated attosecond pulse and an intense infrared few-cycle pulse. A localization of the electronic charge distribution within the molecule is measured that depends – with attosecond time-resolution – on the delay between the pump and probe pulses. The localization is shown to rely on two mechanisms. In mechanism I, it arises due to quantum mechanical interference between dissociation channels involving the Q_1 $^1\Sigma_u^+$ doubly-excited states and ionization continua where the infrared laser alters the angular momentum of the departing electron. In mechanism II, the charge localization arises during dissociation of the molecular ion and is due to laser-driven population transfer between the $1s\sigma_g$ and the $2p\sigma_u$ electronic states. These results open the way for attosecond pump-probe strategies to investigate the complex molecular dynamics that result from the coupling between electronic and nuclear motions beyond the usual Born-Oppenheimer approximation.

Following the successful development of isolated attosecond (1 as = 10^{-18} s) laser pulses less than a decade ago,[5] pioneering work on their use in studies of atomic photo-excitation and –ionization,[6,7] and in studies of electron dynamics in solids,[8] has raised the prospects that the molecular sciences may similarly benefit from the introduction of attosecond techniques. While the timescale for chemical re-arrangements that involve elaborate motion of the constituent atoms is necessarily in the femtosecond (1 fs = 10^{-15} s) domain, the electronic re-arrangement that accompanies the sudden removal or excitation of a selected electron is intrinsically faster. Indeed the removal of electrons that are involved in chemical binding may result in hole dynamics on sub- or few-fs timescales in a wide range of systems including bio-molecules and bio-molecular complexes.[9,10] Extremely fast molecular dynamics involving electron correlation can also be initiated by the excitation of doubly-excited states and by subsequent auto-ionization processes.[11,12]

The application of attosecond laser pulses to molecular (auto)-ionization and electron localization requires suitable experimental diagnostics. Existing experimental implementations of attosecond techniques [13-16] do not readily lend themselves towards intra-molecular electronic re-arrangement processes. Here we introduce the measurement of angular asymmetries in the momentum distributions of fragments that result from dissociative ionization as a tool that is directly related to charge dynamics. As a benchmark, we investigate the dissociative ionization of hydrogen molecules (H_2, D_2). In the following we will mainly present experimental results for the case of D_2, where the highest quality data was acquired. Likewise, we present computational results for the case of H_2, where the close-coupling calculations presented below allow a more extensive exploration of the experimental conditions. To validate these calculations we will occasionally compare with H_2 measurements, whose quality is lower but which show analogous behavior to the D_2 measurements.

The choice of the hydrogen molecule as the subject of our investigation follows a rich tradition.[17,18] An attractive feature of H_2 is that its (intense field) dissociative ionization can frequently be understood in terms of the two lowest electronic states of the molecular ion, namely the $^2\Sigma_g^+(1s\sigma_g)$ and $^2\Sigma_u^+(2p\sigma_u)$ states (see Figure 1a). In our experiment (see Methods), the combination of an isolated attosecond XUV pulse[19] with a spectrum that extended from 20 to 40 eV and a (time-delayed) intense 6 fs FWHM IR pulse, with identical linear polarization, produced ionic fragments H^+ and D^+. The velocity and angular distribution were measured.[20] In D^+ ion kinetic energy spectra recorded without the IR beam (Figure 1b), a broad kinetic energy distribution is observed, consistent with earlier experimental and theoretical work.[21] To interpret these (see Figure 1c) and all later results, we have solved the time-dependent Schrödinger equation (TDSE) for H_2 by using a close-coupling method that includes the bound states, the $^2\Sigma_g^+(1s\sigma_g)$ and the $^2\Sigma_u^+(2p\sigma_u)$ ionization continua, and the doubly excited states embedded in them.[12] The calculations take into account all electronic and vibrational (dissociative) degrees of freedom, and include the effect of electron correlation and interferences between different ionization and dissociation pathways (see Methods). From here on, we will focus on the detection of fragments from molecules that are aligned parallel to the laser polarization axis. Therefore in the calculations only states of Σ symmetry were included.

Upon XUV excitation, several pathways lead to dissociative ionization. The relative weights depend on the photon energy and the observation angle of the ionic fragment with respect to the laser polarization.[21] Up to hν = 25 eV, direct ionization forms the $^2\Sigma_g^+(1s\sigma_g)$ state , and releases a small fraction (2%) of low kinetic energy (E_k < 1 eV) ionic fragments. Between hν = 25 eV and hν = 36 eV, a parallel transition preferentially excites molecules aligned along the polarization axis to the doubly-excited Q_1 $^1\Sigma_u^+$ states. Subsequent auto-ionization to the $^2\Sigma_g^+(1s\sigma_g)$ state produces fragments with a kinetic energy that spans the entire range of 0-10 eV, but lies primarily between 2 and 7 eV.[22, 23] Direct ionization to the repulsive $^2\Sigma_u^+(2p\sigma_u)$ state becomes possible at hν = 30 eV. Above hν = 38 eV the full range of internuclear distances sampled by the ground state of H_2 can participate in this channel, leading to high-energy fragments (E_k = 5 - 10 eV). Above 31 eV, a perpendicular transition preferentially excites molecules that are orthogonally aligned to the laser polarization axis to the Q_2 $^1\Pi_u$ doubly-excited states. These states auto-ionize to both the $^2\Sigma_g^+(1s\sigma_g)$ and the $^2\Sigma_u^+(2p\sigma_u)$ states, resulting in ionic fragments with kinetic energies of 1-5 eV and 5-8 eV, respectively.[21] Since the evaluation of the kinetic energy distributions in the experiment forces us to include ionic fragments within a 45 degree cone around the laser polarization axis, involvement of the Q_2 $^1\Pi_u$ states cannot *a priori* be ruled out.

When the molecule furthermore interacts with a few-cycle IR pulse, a number of changes occur in the fragment kinetic energy distributions. Experimental D^+ and calculated H^+ kinetic energy distributions are shown as a function of the relative delay τ between the attosecond and IR pulses in Fig. 1d and 1e. Note that in view of the very demanding nature of the computations, calculations could be performed for IR intensities up to $3\cdot10^{12}$ W/cm^2 and for XUV-IR delays of up to 12 fs. Experimentally we estimate the IR intensity may have been higher by as much as a factor of 2.

At low energy (E_k < 1 eV) bond-softening of the bound $^2\Sigma_g^+(1s\sigma_g)$ vibrational wave packet by the IR pulse is observed. The bond-softening peaks at τ = +10 fs, when the wave packet finds itself near the outer turning point of the potential energy curve.[24,25] When the XUV and IR pulses overlap ($\tau \approx 0$ fs), a strong increase of the ion signal at high energy (around 8 eV) is observed, accompanied by a decrease at intermediate energies (3 eV < E_k < 5 eV). Based on the close-coupling calculations, we believe this enhancement is due to an increase of the excitation cross-section of the $2p\sigma_u$ continuum due to IR-laser induced mixing of the $2p\sigma_u$ and $1s\sigma_g$ states. The increase may furthermore contain contributions from photo-ionization of the Q_1 $^1\Sigma_u^+$ doubly-excited states by the IR laser. For larger time delays (τ > 8 fs), the kinetic energy distribution above 1 eV does not change appreciably with delay and resembles the distribution obtained in the absence of the IR field (see Fig. 1b and 1c).

Dissociative ionization of H_2 lends itself to the observation of both laboratory-frame and molecular-frame asymmetries. The former corresponds to an asymmetry in the fragment ejection along the laser polarization axis, while the latter corresponds to a (anti-)correlation in the direction of emission of the ionized electron and the ionic fragment. Laboratory-frame asymmetries were previously observed in dissociative ionization of D_2 by a carrier-envelope phase (CEP)-locked infrared laser pulse,[26] while

symmetry-breaking in the molecular frame was observed in single-photon XUV dissociative ionization of H_2 and D_2, mediated by auto-ionization of the $Q_2\ ^1\Pi_u$ state.[27]

In the present experiment laboratory-frame asymmetries $A(E_k, \tau)$ were defined as

$$A(E_k, \tau) = \{N_L(E_k, \tau) - N_R(E_k,\tau)\}/\{N_L(E_k, \tau) + N_R(E_k,\tau) + \delta\} \quad (1)$$

where $N_{L,R}(E_k,\tau)$ indicates the number of ions arriving within 45 degrees from the polarization axis on the left and right side of the detector and δ is a small number that prevents a singularity when $N_L(E_k, \tau) + N_R(E_k,\tau)$ vanishes.

Over almost the entire kinetic energy range where D^+ resp. H^+ ions are formed, asymmetries are observed that oscillate as a function of τ, as shown in Figure 2a and 2c. Delaying the IR laser by one-quarter of the IR period (650 as) or by one-half of the IR period (1.3 fs) leads to a disappearance or reversal of the electron localization. The phase of the asymmetry oscillations strongly depends on the kinetic energy of the fragment that is measured.

The asymmetries can be understood by writing the two-electron wave function of singly-ionized H_2 as:

$$\Psi = c_1[1s\sigma_g(1)\ \varepsilon l_g(2)]_g + c_2[1s\sigma_g(1)\ \varepsilon l_u(2)]_u + c_3[2p\sigma_u(1)\ \varepsilon l_u(2)]_g + c_4[2p\sigma_u(1)\ \varepsilon l_g(2)]_u \quad (2)$$

where, for simplicity, the wave function has not been anti-symmetrized with respect to electrons 1 and 2, and the ionized electron 2 is described by a continuum orbital of well defined energy ε and angular momentum l_g or l_u. The observation of a fragment asymmetry relies on the formation of a mixed-parity superposition state that contains contributions (at the same fragment kinetic energy and for the same angular momentum l_u or l_g) from both the $1s\sigma_g$ and the $2p\sigma_u$ states. This can be recognized from the following expressions for wave-functions of $H_2^+ + e^-$ that have the bound electron localized on the left or right proton:

$$\Psi_L = [1s\sigma_g(1) + 2p\sigma_u(1)]\ \varepsilon l_{g,u}(2)$$

$$\Psi_R = [1s\sigma_g(1) - 2p\sigma_u(1)]\ \varepsilon l_{g,u}(2) \quad (3)$$

From equations (1-3), it is very easy to see that

$$N_L(E_k,t) - N_R(E_k,t) = 4\ \mathrm{Re}\ [c_1 c_4^* + c_2 c_3^*]$$

Thus a laboratory frame asymmetry is formed by a mixed-parity superposition where the continuum electron has the same angular momentum $l_{u/g}$ in both ionic states, ($c_1,c_4 \neq 0$) resp. ($c_2,c_3 \neq 0$).[26] In contrast, a molecular frame asymmetry is caused by an interference of the first (second) and the third (fourth) term in equation (2) ($c_1,c_3 \neq 0$ or $c_2,c_4 \neq 0$).[27]

$A(E_k,\tau)$ can be accurately evaluated from the two-electron wave function obtained in the close-coupling calculation. As can be seen in Figure 2b, the close coupling calculations reproduce the occurrence of oscillations in $A(E_k,\tau)$ with the periodicity of the IR laser. The asymmetry oscillations are very pronounced for delays up to 7 fs and kinetic energies above 5 eV and decrease in amplitude for delays beyond 7 fs and kinetic energies below 5 eV.

In the absence of the IR, the XUV photo-ionization produces a two-electron wave function where only c_2 and c_4 are non-zero, thereby precluding the observation of a laboratory-frame asymmetry. The IR laser can cause an asymmetry either by changing the wave function of the continuum electron or by changing the wave function of the molecular ion. The former occurs as a result of the influence of the IR laser during the photo-excitation process (this will henceforth be called: mechanism I, Fig. 3a), while the latter occurs as a result of the interaction of the molecular ion with the IR laser during the dissociation process (this will henceforth be called: mechanism II, Fig. 3c).

The asymmetry oscillations in Figure 2b in the region where the XUV and IR pulses overlap ($\tau < 8$ fs) occur under conditions where XUV-only ionization produces high-energy fragments (from excitation of the $2p\sigma_u$ state) accompanied by the emission of an s-electron ($c_4 \neq 0$). However, the interaction of the IR laser with this photoelectron redistributes the wave function over several angular momentum states, including the p-continuum ($c_3 \neq 0$, see figure in supplementary information). At the same time, auto-ionization of the $Q_1\ ^1\Sigma_u^+(1)$ state (and, to a lesser extent, direct ionization) leads to the formation of a dissociative wave packet on the $1s\sigma_g$ state that is primarily accompanied by the emission of a *p*-electron ($c_2 \neq 0$, see figure in supplementary information). Further support for the involvement of the $Q_1\ ^1\Sigma_u^+(1)$ state is suggested by results of a close-coupling calculation in which direct excitation to the $1s\sigma_g$ state by the XUV pump was artificially suppressed (see Fig. 3b): fringes in the region $\tau < 7$ fs and $E_k > 5$ eV are then still apparent, even though no wave packet is initially produced in the $1s\sigma_g$ state. To summarize, our mechanism I (Fig. 3a) explains the asymmetry oscillations that are observed for temporal overlap of the XUV and IR pulses in terms of the interference of a wave packet on the $1s\sigma_g$ state that is mainly formed by auto-ionization of the $Q_1\ ^1\Sigma_u^+(1)$ doubly-excited state with a wave packet on the $2p\sigma_u$ state that is formed by an XUV photo-ionization process where the continuum electron absorbs one or more photons from the IR field.

Mechanism I can only occur when the XUV and IR pulses overlap. In contrast, mechanism II requires that the IR has a high intensity during the dissociation of the molecule, irrespective of whether the IR and XUV pulses themselves overlap. The IR-laser can induce population transfer between a wave packet dissociating on the $2p\sigma_u$ state and the $1s\sigma_g$ state (see Fig. 3c). Since the close coupling calculations were restricted to intensities $\leq 3\text{x}10^{12}$ W/cm^2 and to the excitation of Σ-states, this mechanism is only weakly visible in Fig 2b. Nevertheless this mechanism is expected to be dominant at the intensities where the experiments were performed and clearly shows up in calculations performed by numerical integration of the 1D TDSE that describe the evolution of a vibrational wave packet initially placed in the $2p\sigma_u$ state of the H_2^+ (see Fig. 3d). Moreover, under our experimental conditions the potential involvement of the

Q_2 $^1\Pi_u$ doubly excited states implies a larger population of the $2p\sigma_u$ states than in the calculations and, therefore, a reinforcement of the asymmetry at long delays in the region $E_k > 5$ eV.

Similar results as in figure 3d are obtained by an even simpler semi-classical Landau-Zener (LZ) model (see Methods). In this model the IR-laser induced population transfer during dissociation can be understood in terms of so-called quasi-static states, which are the eigenstates of the $1s\sigma_g/2p\sigma_u$ two-level problem in the presence of a (static) electric field:

$$\Psi_1 = \cos\theta(t)\,(1s\sigma_g) + \sin\theta(t)\,(2p\sigma_u)$$

$$\Psi_2 = -\sin\theta(t)\,(1s\sigma_g) + \cos\theta(t)\,(2p\sigma_u) \qquad (4)$$

where $\theta(t)$ is related to the splitting $\omega_0(R)$ between the $1s\sigma_g$ and $2p\sigma_u$ states and to the IR laser-induced dipole coupling $V_{g,u}(R,t) = -\mu(R)E(t)$ by[28]

$$\tan 2\theta(t) = -2V_{g,u}(R,t)/\omega_0(R) \qquad (5)$$

Early on, when $\omega_0(R) >> \mu(R)E_0(t)$, the Landau-Zener transition probability is small and the nuclear wave packet remains in Ψ_2. When $\omega_0(R) \approx \mu(R)E_0(t)$, the nuclear wave packet breaks up into a coherent superposition of the quasi-static states, which now furthermore begin to resemble the localized states Ψ_L and Ψ_R. Towards the end of the dissociation, $\omega_0(R) << \mu(R)E_0(t)$, the nuclear wave packet switches between the two quasi-static states. This merely reflects the fact that the electron is no longer able to switch from left to right and ensures that the localization acquired in the intermediate region persists. The correlated dependence of the asymmetry on E_k and τ is caused by the dependence of the localization process on the internuclear distance where the nuclear wave packet is launched.

Rapid electronic processes on timescales extending down into the attosecond domain define our natural environment, and are at the heart of photo-physical, photo-chemical and photo-biological processes that sustain and enable life. In this work the first comprehensive experimental and computational effort has been presented aiming at and demonstrating the utility of attosecond pulses in molecular science thereby establishing a point of departure for the direct investigation of (multi)-electron dynamics in molecular systems, such as electron transfer/localization and auto-ionization, and of the coupling between electronic and nuclear degrees of freedom on timescales approaching the atomic unit of time.

Methods summary

Experimental methods. To generate both beams, linearly polarized few-cycle IR laser pulses with a controlled CEP were divided into a central and annular part using a drilled mirror. The polarization state of the central part was modulated in time using two birefringent plates in order to obtain a short temporal window of linear polarization around the center of the pulse. This laser beam was focused in a Krypton gas jet to generate an XUV continuum via high-order harmonic generation.[29] A 100 nm aluminum

filter was used to eliminate low-order harmonics and the IR radiation, and provided a partial dispersion compensation of the transmitted XUV light. In this way single attosecond pulse with a duration between 300-400 as were produced.[19] The attosecond pulses were focused using a grazing incidence toroidal mirror into the interaction region of a Velocity Map Imaging Spectrometer (VMIS). The annular part of the original IR beam was focused by a spherical mirror and collinearly recombined with the attosecond pulse using a second drilled mirror. The relative time delay between the two pulses was changed with attosecond time resolution using a piezoelectric stage inserted in the interferometric setup. The XUV and IR laser beams were crossed with an effusive H_2/D_2 gas jet that emerged from a 50 μm diameter capillary that was incorporated into the repeller electrode of the VMIS.[30] Ions generated in the two-color dissociative ionization were projected onto an MCP + phosphor screen detector. 2D ion images were acquired using a low-noise CCD camera, and allowed retrieval of the 3D velocity distribution of the ions.

Methods

Experimental methods. To generate both beams, linearly polarized few-cycle IR laser pulses with a controlled CEP were divided into a central and annular part using a drilled mirror. The polarization state of the central part was modulated in time using two birefringent plates in order to obtain a short temporal window of linear polarization around the center of the pulse. This laser beam was focused in a Krypton gas jet to generate an XUV continuum via high-order harmonic generation.[29] A 100 nm aluminum filter was used to eliminate low-order harmonics and the IR radiation, and provided a partial dispersion compensation of the transmitted XUV light. In this way single attosecond pulses with a duration between 300-400 as were produced.[18] The attosecond pulses were focused using a grazing incidence toroidal mirror into the interaction region of a Velocity Map Imaging Spectrometer (VMIS). The annular part of the original IR beam was focused by a spherical mirror and collinearly recombined with the attosecond pulse using a second drilled mirror. The relative time delay between the two pulses was changed with attosecond time resolution using a piezoelectric stage inserted in the interferometric setup. The XUV and IR laser beams were crossed with an effusive H_2/D_2 gas jet that emerged from a 50 μm diameter capillary that was incorporated into the repeller electrode of the VMIS.[30] Ions generated in the two-color dissociative ionization were projected onto an MCP + phosphor screen detector. 2D ion images were acquired using a low-noise CCD camera, and allowed retrieval of the 3D velocity distribution of the ions.

Numerical methods. The two-electron close-coupling calculations have been performed by using an extension of the method reported in Ref. [12]. Briefly, we have solved the seven dimensional (7D) time-dependent Schrödinger equation

$$\left(\hat{H}^0(\mathbf{r}_1, \mathbf{r}_2, R) + V(t) - i\frac{\partial}{\partial t} \right) \Phi(\mathbf{r}_1, \mathbf{r}_2, R, t) = 0$$

where $\mathbf{r}_1$, $\mathbf{r}_2$ are the position vectors of electrons 1 and 2, respectively (two times 3D), R is the internuclear distance (1D), $\hat{H}^0$ is the H_2 field-free non relativistic Hamiltonian, Φ is the time-dependent wave function, and $V(t)$ is the laser-H_2 interaction potential in the

dipole approximation which is a sum of two terms corresponding to the XUV and IR pulses separated by a peak-peak time delay τ, $V(t) = V_{XUV}(t) + V_{IR}(t+\tau)$, , with frequencies ω_{XUV} and ω_{IR}, and durations T_{XUV} and T_{IR}, respectively. Each pulse has a cosine square temporal envelope and is given by the analytical formula

$$V_k(t') = \begin{Bmatrix} \mathbf{p}\cdot\mathbf{A}_k^0 \cos^2\left(\dfrac{\pi t'}{T_k}\right) & for -\dfrac{T_k}{2} \le t' \le \dfrac{T_k}{2} \\ 0 & elsewhere \end{Bmatrix}$$

where $t'=t$ for the XUV pulse, $t'=t+\tau$ for the IR pulse, and **p** is the dipole moment. In all calculations we have used ω_{XUV} = 30 eV, T_{XUV} = 400 as, $I_{XUV} = \left(A_{XUV}^0\right)^2 \omega_{XUV}^2 = 10^9$ W/cm^2, ω_{IR} = 1.65 eV, T_{IR} = 16 fs (corresponding to a pulse duration of 6 fs FWHM), $I_{XUV} = \left(A_{XUV}^0\right)^2 \omega_{XUV}^2 = 3\cdot10^{12}$ W/cm^2, and τ has been varied from 0 up to 12 fs. The TDSE has been solved by expanding the time-dependent wave function Φ in a basis of fully correlated H_2 vibronic stationary states of Σ_g^+ and Σ_u^+ symmetries, which include the bound states, the non-resonant continuum states associated with the $1s\sigma_g$ and $2p\sigma_u$ ionization channels, and the lowest Q_1 and Q_2 doubly excited states. In doing so, the TDSE is effectively 6D and the results are exclusively valid for H_2 molecules oriented parallel to the polarization direction. The electronic part of the vibronic states is calculated in a box of 160 a.u. and the nuclear part in a box of 12 a.u.. The size of these boxes is large enough to ensure that there are no significant reflections of electronic and nuclear wave packets in the box boundaries for propagation times smaller than $\tau + (T_{XUV} + T_{IR})/2$. Non-adiabatic couplings and molecular rotations have been neglected.

The two-electron wave function that is obtained in the close-coupling calculation lends itself to a detailed analysis of the mechanisms that lead to the measurement of laboratory-frame asymmetries in the dissociative ionization of the molecule. As an example, the figure in the Supporting Information shows the angular momentum and electronic state-resolved delay dependence of H^+ ions with a fragment kinetic energy in the interval <7.5 eV, 8.5 eV>. Angular momentum l_g and l_u stand for $l_g = (1s\sigma_g \varepsilon l)_g$ and $l_u = (2p\sigma_u \varepsilon l)_u$ for l = 0 ($s_{g,u}$-wave), l = 2 ($d_{g,u}$-wave),…. and $l_g = (2p\sigma_u \varepsilon l)_g$ and $l_u = (1s\sigma_g \varepsilon l)_g$ for l = 1 ($p_{g,u}$-wave), l = 3 ($f_{g,u}$-wave),…. A (time-dependent) asymmetry is expected when for a given angular momentum a substantial population is simultaneously present in both the $1s\sigma_g$ and the $2p\sigma_u$ states (g and u).

In analyzing mechanism II, we have performed 1D TDSE calculations that describe the evolution of a wave packet initially located in the $2p\sigma_u$ state and centred at the H_2 equilibrium distance. In these calculations, only the $1s\sigma_g$ and $2p\sigma_u$ state were included and the IR pulse was launched at different times to simulate the delay τ between the pump and the probe pulses. We have also used the Landau-Zener model in which the transition probability between the two-dressed states of eq. (4) is given by [25]

$$W = \exp\left(\frac{-\pi\omega_0^2(R)}{4\omega_{IR}\mu(R)E_0(t)}\right)$$

where ω_{IR} is the carrier frequency of the laser and where $E_0(t)$ is the envelope of the laser pulse. This has been used to evaluate the probability for a diabatic transition and, hence, the population in the quasi-static states. This leads to an asymmetry parameter that is similar to that obtained from the 1D TDSE calculations.

1. Corkum, P. B. & Krausz, F. Attosecond science. *Nature Physics* **3**, 381-387 (2007).

2. Kapteyn, H., Cohen, O., Christov, I. & Murnane, M. Harnessing Attosecond Science in the Quest for Coherent X-rays. *Science* **317**, 775-778 (2007).

3. Kling, M. F. & Vrakking, M. J. J. Attosecond Electron Dynamics. *Annu. Rev. Phys. Chem.* **59**, 463-492 (2008).

4. Krausz, F. & Ivanov, M. Attosecond physics. *Rev. Mod. Phys.* **81**, 163-234 (2009).

5. Hentschel, M. et al. Attosecond metrology. *Nature* **414**, 509-513 (2001).

6. Drescher, M. et al. Time-resolved atomic inner-shell spectroscopy. *Nature* **419**, 803-807 (2002).

7. Uiberacker, M. et al. Attosecond real-time observation of electron tunnelling in atoms. *Nature* **446**, 627-632 (2007).

8. Cavalieri, A. L. et al. Attosecond spectroscopy in condensed matter. *Nature* **449**, 1029-1032 (2007).

9. Remacle, F. & Levine, R. D. An electronic time scale in chemistry. *PNAS* **103**, 6793-6798 (2006).

10. Kuleff, A.I. & Cederbaum, L.S. Charge migration in different conformers of glycine: The role of nuclear geometry. *Chem. Phys.* **338**, 320-328 (2007).

11. Wickenhauser, M., Burgdorfer, J., Krausz, F. & Drescher, M. Time Resolved Fano Resonances. *Phys. Rev. Lett.* **94**, 023002 (2005).

12. Sanz-Vicario, J. L., Bachau, H. & Martin, F. Time-dependent theoretical description of molecular autoionization produced by femtosecond xuv laser pulses. *Phys. Rev. A* **73**, 033410 (2006).

13. Kienberger, R. et al. Atomic transient recorder. *Nature* **427**, 817-821 (2004).

14. Uphues, T. et al. Ion-charge-state chronoscopy of cascaded atomic Auger decay. *New J. Phys.* **10**, 025009 (2008).

15. Remetter, T. et al. Attosecond electron wave packet interferometry. *Nature Physics* **2**, 323-326 (2006).

16. Mauritsson, J. et al. Attosecond Pump-Probe Electron Interferometry. (2009 (submitted for publication)).

17. Bucksbaum, P. H., Zavriyev, A., Muller, H. G. & Schumacher, D. W. Softening of the H_2^+ molecular bond in Intense Laser Fields. *Phys. Rev. Lett.* **64**, 1883-1886 (1990).

18. Frasinski, L. J. et al. Manipulation of Bond Hardening in H_2^+ by Chirping of Intense Femtosecond Laser Pulses. *Phys. Rev. Lett.* **83**, 3625-3628 (1999).

19. Sansone, G. et al. Isolated Single-Cycle Attosecond Pulses. *Science* **314**, 443-446 (2006).

20. Eppink, A. T. J. B. & Parker, D. H. Velocity map imaging of ions and electrons using electrostatic lenses: Application in photoelectron and photofragment ion imaging of molecular oxygen. *Rev. Sci. Instrum.* **68**, 3477-3484 (1997).

21. Ito, K., Hall, R. I. & Ukai, M. Dissociative photoionization of H_2 and D_2 in the energy region of 25-45 eV. *J. Chem. Phys.* **104**, 8449-8457 (1996).

22. Sanchez, I. & Martin, F. Origin of Unidentified Structures in Resonant Dissociative Photoionization of H_2. *Phys. Rev. Lett.* **79**, 1654-1657 (1997).

23. Sanchez, I. & Martin, F. Resonant dissociative photoionization of H_2 and D_2. *Phys. Rev. A* **57**, 1006-1017 (1998).

24. Rudenko, A. et al. Real-time observation of vibrational revival in the fastest molecular system. *Chem. Phys.* **329**, 193-202 (2006).

25. Kelkensberg, F. et al. Molecular Dissociative Ionization and Wave-Packet Dynamics studied using Two-Color XUV and IR Pump-Probe Spectroscopy. *Phys. Rev. Lett. 103, 123005 (2009).*

26. Kling, M. F. et al. Control of Electron Localization in Molecular Dissociation. *Science* **312**, 246-248 (2006).

27. Martin, F. et al. Single Photon-Induced Symmetry Breaking of H_2 Dissociation. *Science* **315**, 629-633 (2007).

28. Dietrich, P., Ivanov, M. Y., Ilkov, F. A. & Corkum, P. B. Two-Electron Dissociative Ionization of H_2 and D_2 in Infrared Laser Fields. *Phys. Rev. Lett.* **77**, 4150-4153 (1996).

29. Sola, I. J. et al. Controlling attosecond electron dynamics by phase-stabilized polarization gating. *Nature Physics* **2**, 319-322 (2006).

30. Ghafur, O., Siu, W., Kling, M., Drescher, M. & Vrakking, M. J. J. A velocity map imaging detector with an integrated gas injection system. *Rev. Sci. Instrum.* **80** (2009).

Supplementary Information is linked to the online version of the paper at www.nature.com/nature.

Acknowledgements This work is part of the research programs of the "Stichting voor Fundamenteel Onderzoek der Materie (FOM)", which is financially supported by the "Nederlandse organisatie voor Wetenschappelijk Onderzoek (NWO)", and of the Spanish Ministerio de Ciencia e Innovación, project no. FIS2007-60064 . Support by MC-RTN "XTRA" (FP6-505138), the MC-EST MAXLAS, Laserlab Europe (Integrated Infrastructure Initiative Contract RII3-CT-2003-506350, proposal cusbo001275), the European COST Action "CUSPFEL" (CM0702), the Mare Nostrum Barcelona Supercomputer Center (BSC), the Centro de Computación Científica UAM, the Netherlands National Computing Facilities foundation (NCF), Stichting Academisch Rekencentrum Amsterdam (SARA), the Alban Program for Latin-America (E07D401391CO), the Universidad de Antioquia, the COLCIENCIAS agency, the Swedish Research Council, the DFG via the Emmy-Noether program and the Cluster of Excellence: Munich Center of Advanced Photonics.

Author Contributions G.S., F.K., J.F.P.T. and F.M. contributed equally to this work. G.S. was responsible for the construction of the attosecond pump-probe set-up and the experiments on H_2 and D_2.

F.K. was responsible for the experiments on H_2 and D_2 and the development of the semi-classical model. J.F.P.T. and F.M. were responsible for the construction of the close-coupling code and the calculations using this code.

Author Information Correspondence and requests for materials should be addressed to M.V. (m.vrakking@amolf.nl).

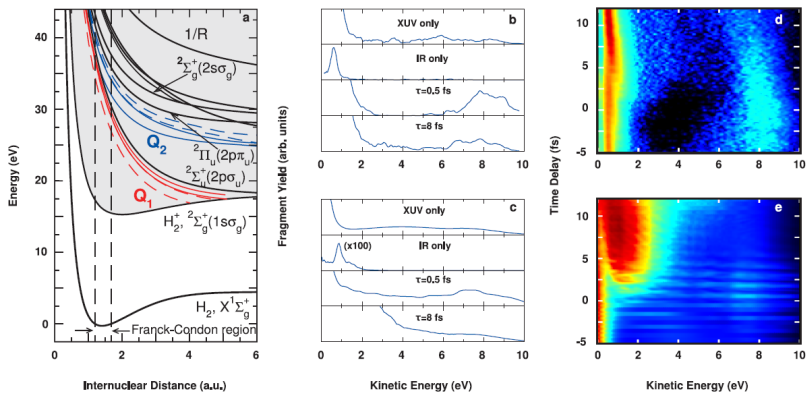

Figure 1: Dissociative ionization of hydrogen by an XUV-IR pulse sequence (a) Photo-excitation of neutral hydrogen leads to the excitation of the Q_1 (red) and Q_2 (blue) doubly-excited states and ionization to the $1s\sigma_g$ and $2p\sigma_u$ states, which can be followed by dissociation.; (b) experimental D^+ and (c) calculated H^+ kinetic energy distributions with only the isolated attosecond laser pulse present, with only the few-cycle IR laser pulse present, and for two delays between the XUV the IR pulse ; (d) experimental D^+ and (e) calculated H^+ kinetic energy distributions as a function of the delay between the attosecond pulse and the IR pulse.

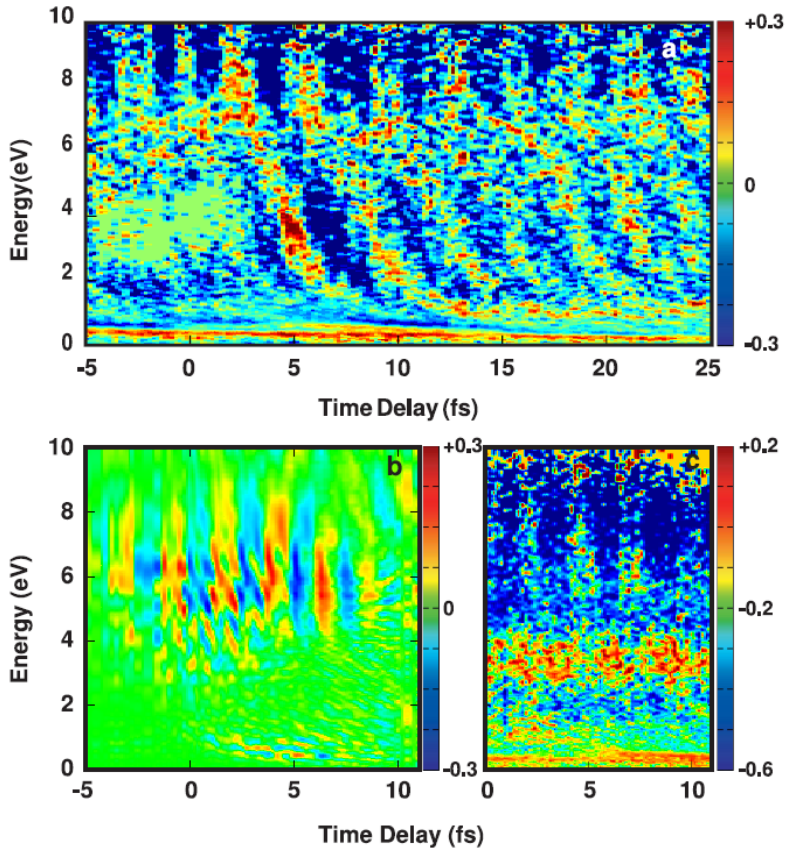

Figure 2: Asymmetry in XUV+IR dissociative ionization of hydrogen (a) Experimentally measured asymmetry parameter for the formation of D^+-ions in two-color XUV+IR dissociative ionization of D_2, as a function of the fragment kinetic energy E_k and the XUV-IR delay. A fragment asymmetry is observed that oscillates as a function of the XUV-IR delay and that strongly depends on the kinetic energy.; (b) Calculated asymmetry parameter for the formation of H^+ ions in two-color XUV+IR dissociative ionization of H_2 as a function of the fragment kinetic energy E_k and the XUV-IR delay, obtained using the close-coupling method described in the text; (c) similar to (a) but for H^+-ions

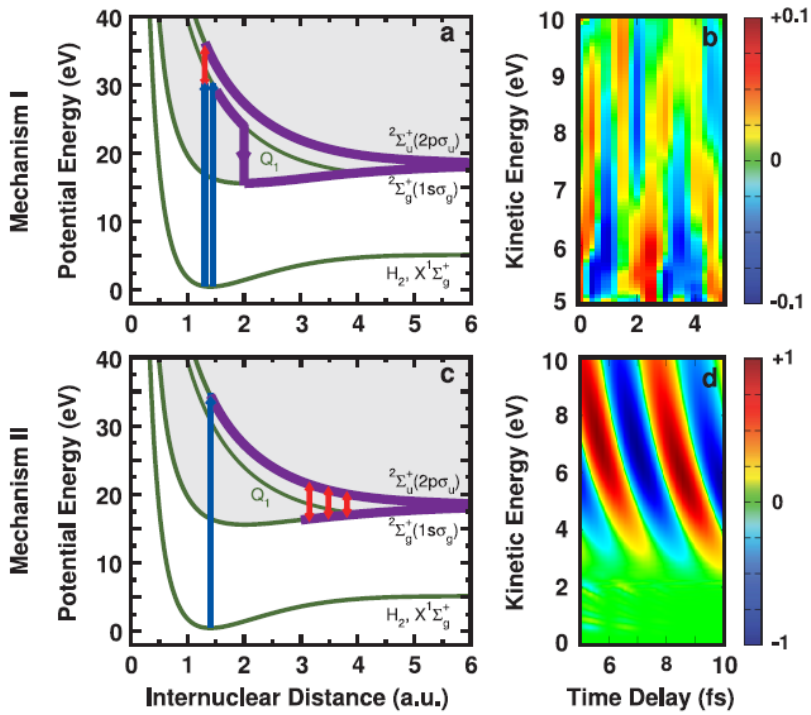

Figure 3: Mechanisms that lead to asymmetry in XUV+IR dissociative ionization. (a) asymmetry caused by the interference of a wavepacket launched on the $2p\sigma_u$ state by direct XUV ionization or rapid ionization of the Q_1 $^1\Sigma_u^+$ states by the IR, and a wavepacket on the $1s\sigma_g^+$ state resulting from autoionization of the Q_1 $^1\Sigma_u^+$ states. Blue arrows signify the role of the XUV pulse, and red arrows that of the IR pulse; purple lines and arrows signify dynamics that is intrinsic to the molecule; (b) close-coupling calculations where direct photo-excitation to the $1s\sigma_g$ state has been excluded, supporting the notion that the Q_1 autoionizing states play an important role in the localization dynamics; (c) asymmetry caused by the interference of a wavepacket that is launched on the $2p\sigma_u$ state by direct XUV ionization and a wavepacket on the $1s\sigma_g$ state that results from stimulated emission during the dissociation process; (d) time-dependent asymmetry calculated by a two-level calculation where the wave function of the dissociating molecule is considered as a coherent superposition of the $1s\sigma_g$ and $2p\sigma_u$ states.